



UNIVERSITE CATHOLIQUE
DE LOUVAIN
ECOLE POLYTECHNIQUE DE LOUVAIN
INSTITUTE OF MECHANICS, MATERIALS AND
CIVIL ENGINEERING

Blood flow modeling for patient-specific bypass surgery in lower-limb arteries

MARIE WILLEMET

Thesis submitted in fulfillment of
the requirements for the degree of
Docteur en Sciences de l'Ingénieur

Jury Members:

Prof. E. Marchandise (Supervisor)	Université catholique de Louvain
Prof. J.-F. Remacle (Supervisor)	Université catholique de Louvain
Prof. P. Flaud	Université Paris Diderot
Prof. R. Verhelst	Université catholique de Louvain
Prof. J. Alastruey Arimon	King's College London
Prof. A. Khir	Brunel University
Prof. V. Legat	Université catholique de Louvain
Prof. T. Pardoën (Chair)	Université catholique de Louvain

February 2012

*“Les passions sont les vents
qui enflent les voiles du navire;
elles le submergent quelquefois,
mais sans elles il ne pourrait voguer.”*

Voltaire

Acknowledgements

Writing this dissertation is the last step of quite a long solo journey. Hopefully, it was punctuated by many stopovers and encounters which made it worth it! I would like to take the opportunity here to gratefully acknowledge all of whom who supported me during these years.

First of all, I would like to express my sincere gratitude to my supervisor Prof. Emilie Marchandise for her guidance and support. I appreciated her energy and motivation, and the opportunity she gave me to drive this research according to my interests. I also would like to thank my supervisor Prof. Jean-François Remacle for his great enthusiasm, and for giving me the opportunity to carry out a PhD within the NHEMO project. Thank you for launching these bridges between the medical and engineering worlds five years ago.

This thesis would not have had the same interest without this close collaboration with the surgeon Dr. Valérie Lacroix. Valérie, I want to warmly thank you for your availability and patience, your will against all the experimental difficulties (and we have faced many...), and your passion in sharing your clinical knowledge.

I wish to thank the members of my PhD committee: Prof. Robert Verhelst and Prof. Patrice Flaud, for their pertinent comments during these four years, and their guidance in the experimental data acquisition. I also would like to express my gratitude to Prof. Ashraf Khir for his interest in my work about wave intensity analysis, his numerous advice and for welcoming me in Brunel University. I am thankful to the other members of the jury: Prof. Jordi Alastruey, Prof. Vincent Legat and Prof. Thomas Pardoën, for the time they dedicated to this dissertation and for their helpful and constructive comments.

I want to thank Alex Bertholet from the GC lab for his precious help in the set-up of the experimental protocol of data acquisition. I also would like to thank Prof. Kim Parker for the Matlab code of the reservoir-excess separation, and his advice about that matter. I want to acknowledge Prof. Patrick Segers for the hemodynamics data measured in healthy subjects, as well as Alessandra Borlotti for the wave intensity analysis of these signals. I also gratefully acknowledge the financial support of the FRIA, FNRS, and the NHEMO project.

Enormous thank you to all colleagues and friends of the Euler building, for the nice atmosphere, the boosting talks, the coffee breaks, the lunch debates,... Laurence, Gaetan and François, thanks for sharing the a.217 with me! Just on the other side of the corridor, thanks Vincent for your encouragements and your wonderful gazou-glouglouteries! Astrid and Gaetan D., thank you also for your help in logistics.

Merci à mes amis du 127.1, de la ligne 161, de Tawi-Tawi, de Méca et d'ailleurs, merci pour votre support, votre écoute et vos sourires! Mes chers parents, Merci! Merci de m'avoir transmis cet amour des choses bien faites, cette rigueur scientifique d'apothicaire... Merci à vous, à Nico et Juju et à la folle ménagerie, à Marraine, ainsi qu'à ma famille++, pour votre intérêt et votre soutien dans les projets que j'entreprends.

Last but not least, merci à mon petit moussaillon Olivier, pour tes encouragements, nos discussions et tes nombreux conseils lors de cette grande traversée!

Marie

Contents

Acknowledgements	iii
Abstract	ix
Notations and abbreviations	xi
1 Introduction	1
1.1 The cardiovascular system	2
1.2 The lower-limb bypasses	3
1.2.1 Atherosclerosis	5
1.2.2 Bypass characterisation	5
1.2.3 Medical criteria of success	6
1.2.4 Failure of bypasses	9
1.3 Data acquisition in pathological subjects	9
1.3.1 Morphology: lengths and diameter of the vessels	10
1.3.2 Pressure	13
1.3.3 Velocity and flow	14
1.4 Arterial hemodynamics modeling	15
1.5 Aim & outline of this thesis	17
2 In-vivo hemodynamics in bypasses	19
2.1 In-vivo data acquisition in pathological subjects	20
2.1.1 Data acquisition protocol	20
2.1.2 Processing of the information	22
2.1.3 Subjects	23
2.2 Waveform analysis	24
2.2.1 Hemodynamics in healthy lower-limb arteries	25
2.2.2 Influence of aging and atherosclerosis disease	26
2.2.3 Hemodynamics in occluded lower-limb arteries	28
2.2.4 Hemodynamics in bypassed lower-limb arteries	30
2.2.5 Influence of the data acquisition protocol	31
2.3 Patient-specific parameters computation	31
2.3.1 Vessel wall elasticity	32
2.3.2 Distal arterial sub-network	46
2.4 Bypass patency	54
2.5 Conclusion	55

3	A coupled 1D-0D numerical model	59
3.1	The mathematical model	61
3.1.1	The one-dimensional model	61
3.1.2	Characteristic analysis	63
3.1.3	Wave separation	64
3.2	The numerical resolution	67
3.3	The boundary conditions	69
3.3.1	Inflow boundary conditions	69
3.3.2	Outflow boundary conditions	71
3.3.3	Bifurcation and discontinuity treatment	73
3.4	Applications of the forward absorbing inlet boundary condition	74
3.4.1	Test case 1: Arterial tree vs upper- and lower-limb . . .	74
3.4.2	Test case 2: An in-vivo lower-limb patient-specific appli- cation	75
3.5	Discussion	82
4	Validation and sensitivity analysis of the 1D-0D model	85
4.1	Validation of the model	87
4.1.1	Materials and methods	89
4.1.2	Results (1): General observations	93
4.1.3	Results (2): Clinical cases	98
4.2	Sensitivity analysis of the model	104
4.2.1	Methods	104
4.2.2	Results	106
4.3	Discussion	117
5	Wave Intensity Analysis	121
5.1	Materials and methods	122
5.1.1	Theoretical background of the WIA	122
5.1.2	In-vivo data acquisition	124
5.1.3	1D-0D numerical model	125
5.1.4	Statistical analysis	125
5.2	In-vivo wave intensity in bypassed and occluded lower-limbs . .	125
5.2.1	Results	125
5.2.2	Discussion	129
5.3	Patient-specific results analysed with a numerical tool	136
5.3.1	Reflections	136
5.3.2	Leakage	137
5.4	Conclusion	139

6	Reservoir-excess separation	143
6.1	Algorithm for pressure separation in an arbitrary artery	145
6.2	Pressure separation in bypassed lower-limbs	147
6.2.1	Assumptions	147
6.2.2	The reservoir components	148
6.2.3	The excess components	150
6.2.4	Pressure components distribution	150
6.2.5	Reflection coefficient	153
6.3	WIA applied to the excess component	154
6.4	Conclusion	155
7	Conclusion and perspectives	157
7.1	Summary and concluding remarks	157
7.1.1	In-vivo data acquisition	157
7.1.2	Validation of the 1D-0D model	159
7.1.3	Sensitivity analysis of the 1D-0D model	160
7.1.4	Origin and propagation of waves	161
7.1.5	From a clinical point of view	162
7.2	Outlook	163
A	Basic laws of hemodynamics	169
B	In-vivo parameters, waveforms and results of simulations	173
C	Additional results of the sensitivity analysis	197
	Bibliography	205
	Publications related to this thesis	221

Abstract

In western countries, 1% of the population older than 70 years will undergo a bypass surgery in the lower-limb arteries. Even though this intervention is very common, failure of this treatment within five years reaches up to 60%. In order to improve our understanding of the causes of bypass failure, one approach is to study the local hemodynamics in these vessels, as this factor strongly influences the initiation and progression of arterial diseases.

This thesis addresses this objective by modeling the patient-specific arterial hemodynamics. As each patient is characterised by his own physiology and is treated with a bypass graft of fixed characteristics, each clinical case needs to be considered individually.

In the first part of our work, blood pressure, velocity and flow rate are modeled with a one-dimensional model of the arteries and lumped windkessel models of the secondary and distal vessels. The 18 parameters of this coupled model are then computed in order to reflect the pathological condition of the patient. Thanks to the set-up of an experimental protocol of data acquisition, we have been able to acquire in-vivo measurements of hemodynamics in 25 patients operated with bypass surgery. The comparison of these in-vivo signals with numerical simulations enabled us to improve and validate our patient-specific numerical model.

In the second part of this thesis, the dynamic of blood is considered as impulses of waves generated by the contractions of the heart, which propagate throughout the arterial network. By using the wave intensity analysis, we analysed and characterised these waves in the pathological arteries of the leg, and emphasized the effects of the bypass.

Notations and abbreviations

Abbreviations

ABI	Ankle-Brachial Index
AH	Arterial Homograft
AK	Above-Knee
AT	Anterior Tibial
AV	Absorbing Velocity
AV-Fwd	Absorbing forward component of velocity
BC	Boundary Condition
BCW	Backward Compression Wave
BEW	Backward Expansion Wave
BK	Below-Knee
BP	Bypass
CF	Common Femoral
CT	Computed Tomography
DA	Dacron [®]
DBP	Diastolic Blood Pressure
DF	Deep Femoral
DG	Discontinuous-Galerkin
EDV	End-Diastolic Velocity
FCW	Forward Compression Wave
FEW	Forward Expansion Wave
GT	Gore-Tex [®]
ISV	In-Situ Vein
LV	Left Ventricle
MIH	Myointimal Hyperplasia
MRI	Magnetic Resonance Imaging
ODE	Ordinary Differential Equation
PAOD	Peripheral Arterial Occlusive Disease
PET	Polyethylene Teraphthalate (Dacron [®])
PO	Popliteal
PP	Pulse Pressure
PSV	Peak Systolic Velocity
PT	Posterior Tibial

PTFE	Polytetrafluorethylene (Gore-Tex [®])
PVR	Peripheral Vascular Resistance
RMSE	Root-Mean-Square Error
RK	Runge-Kutta
RV	Reflected Velocity, Reflected Vein
RV-Fwd	Reflecting forward component of velocity
SA	Sensitivity Analysis
SBP	Systolic Blood Pressure
SD	Standard Deviation
SF	Superficial Femoral
WSS	Wall Shear Stress

Hemodynamic variables

A	(cm^2)	Area
A_0	(cm^2)	Diastolic area
A^c	(cm^2)	Upwind area
c	(m/s)	Pulse wave velocity
C	$(cm^4 g^{-1} s^2)$	Compliance
C_{exp}	$(cm^4 g^{-1} s^2)$	Compliance computed with the exponential fitting method
C_{ODE}	$(cm^4 g^{-1} s^2)$	Compliance computed with the ODE method
C_A	$(cm^4 g^{-1} s^2)$	Area compliance
C_D	$(cm^4 g^{-1} s^2)$	Diameter compliance
C_r	$(cm^4 g^{-1} s^2)$	Radial compliance
d	/	Derivative
∂	/	Partial derivative
D	(cm)	Diameter
D_0	(cm)	Diastolic diameter
dI	$(W m^{-2} s^{-2})$	Wave intensity
dI_f	$(W m^{-2} s^{-2})$	Forward component of wave intensity
dI_b	$(W m^{-2} s^{-2})$	Backward component of wave intensity
E	(N/m^2)	Elastic Young's modulus
f	(N/m)	Friction force
\mathbf{F}^e	/	Numerical upwind flux
f_{acq}	(s^{-1})	Acquisition frequency
h_0	(mm)	Wall thickness
I	$(kJ m^{-2} s^{-2})$	Cumulative intensity
$I_{i,k}$	/	Relative sensitivity index
$\bar{I}_{i,k}$	/	Mean relative sensitivity index

K_R	(m^2/s)	Viscous resistance of flow per unit length
L	(cm)	Length of the bypass
l	(cm)	Length of a vessel
p	$(mmHg)$	Blood pressure
p_f	$(mmHg)$	Forward component of pressure
p_b	$(mmHg)$	Backward component of pressure
p_0	$(mmHg)$	Diastolic pressure
p_{out}	$(mmHg)$	Venous pressure
P	$(mmHg)$	Reservoir pressure
P_∞	$(mmHg)$	Pressure at which flow through the microcirculation ceases (reservoir-excess separation)
\tilde{p}	$(mmHg)$	Excess pressure
p^*	$(mmHg)$	Pressure at one third of diastole
\dot{p}	$(mmHg/s)$	Slope of pressure increase during systole
Q	(cm^3/s)	Flow rate
\bar{Q}	(cm^3/s)	Mean flow rate
r	(cm)	Radius
R	$(cm^{-4} g s^{-1})$	Resistance
R_{mean}	$(cm^{-4} g s^{-1})$	Resistance computed with the ratio of means
R_{ODE}	$(cm^{-4} g s^{-1})$	Resistance computed with the ODE method
Re	/	Reynolds number
R_f	/	Reflection coefficient (ratio of characteristic admittances)
$R_{ p }$	/	Reflection index (ratio of amplitudes of backward to forward pressure waves)
R_p	/	Reflection coefficient (ratio of peaks of backward to forward pressure waves)
t	(s)	Time
t^*	(s)	Time at one third of diastole
t_N	(s)	Time of closure of the aortic valve
u	(cm/s)	Blood velocity
u_f	(cm/s)	Forward component of velocity
u_b	(cm/s)	Backward component of velocity
u_0	(cm/s)	Diastolic velocity
U	(cm/s)	Reservoir velocity
\tilde{u}	(cm/s)	Excess velocity
u^*	(cm/s)	Velocity at one third of diastole
u^c	(cm/s)	Upwind velocity
V	(cm^3)	Volume
W_f	(m/s)	Forward characteristic variable
W_b	(m/s)	Backward characteristic variable
x	(m)	Position
Y	$(m^4 kg^{-1} s)$	Characteristic admittance of a vessel
Z_c	$(m^{-4} kg s^{-1})$	Characteristic impedance

α	/	Womersley parameter
β	$(m^{-2} kg s^{-2})$	Stiffness of the arterial wall
Δ	/	Difference
ϵ_p	$(mmHg)$	Root-mean-square error of pressure waveforms
ϵ_u	(cm/s)	Root-mean-square error of velocity waveforms
γ	/	Proportionality constant
ζ	/	Arbitrary scaling factor
θ	$(m^{-2} kg s^{-1})$	Slope of the linear part of the PU-loop
$\lambda_{f,b}$	(m/s)	Eigenvalues
μ	$(cm^{-1} g s^{-1})$	Dynamic viscosity of blood
ν	(cm^2/s)	Kinematic viscosity of blood
π	/	3.1415...
ρ	(g/cm^3)	Blood density
σ	/	Poisson's ratio
τ	(s)	Exponential diastolic decay
τ_{area}	(s)	τ computed with the area method
τ_{exp}	(s)	τ computed with the exponential fitting method
τ_{ODE}	(s)	τ computed with the ODE method
τ_{RW}	(s)	τ computed with the reservoir-excess separation theory
$\hat{\phi}$	/	Test function
χ	$(W m^{-2} s^{-2})$	Net wave energy
Ω	/	1D Domain
Ω_e	/	Element of the 1D domain
$\partial\Omega$	/	Interface of the 1D Domain

CHAPTER 1

Introduction

In western countries, 1% of the population older than 70 years will need a lower-limb bypass surgery (Norgren et al., 2007). In Belgium alone, this represents about 100 interventions a year in each major clinical center (Daenens et al., 2009; Bosiers et al., 2006; Peeters et al., 2006). Though, while bypass surgery is one of the most common type of vascular intervention, failure of this treatment within five years reaches up to 60% (Norgren et al., 2007).

If you were to be diagnosed for a long arterial occlusion in your thigh, the insertion of a bypass conduit in your leg arteries would allow blood to flow downwards of this blockage, towards your feet and distal tissues. Without this revascularization, gangrene or even amputation might be your fate.

Because patients present different levels of pathology and different characteristics of their treatment (e.g. bypass dimensions and structure), it is essential to consider a patient-specific approach. Thanks to the development of medical imaging and data acquisition techniques in a clinical setting, the patient-specific characterisation has become possible.

Nowadays, it is widely accepted among clinicians that the initiation and progression of disease in the arteries are strongly influenced by the local hemodynamics. Because the insertion of the bypass graft changes the morphology of the arterial path in the leg, the local hemodynamics undergoes modifications, which are furthermore function of the nature of the bypass. The evaluation of these variations in function of the bypass nature and the patient characteristics would be a useful indication for the vascular surgeons.

In this work, we intend to study this problem by using one-dimensional models of the arterial hemodynamics in bypassed legs. Nevertheless, the application of the patient-specific approach to this model is not straightforward, in view of the various degrees of the pathology amongst patients. Parameters of the model need to be defined and computed in order to represent the observed pathological hemodynamics.

Thanks to a close collaboration with surgeons and clinicians, a hemodynamical dataset from patients treated with lower-limb bypass surgery has been

set up. On basis of these in-vivo data, we investigate the efficiency of patient-specific simulations of waveforms in the bypassed lower-limb.

In this introductory chapter, the cardiovascular system will be briefly presented, while emphasis will be put on the description of the pathology of lower-limb bypasses. Current available techniques for measuring hemodynamics in pathological arteries are discussed in Section 1.3. An overview on the computational methods for the modeling of the arterial hemodynamics are then presented. From thereon, the objectives of this work will be stated and the outline of this thesis will be presented.

1.1 The cardiovascular system

The cardiovascular system of the human body consists of the heart interacting with the systemic and pulmonary vascular systems. While the heart acts as a pump, the vascular system consists of a dense network of ducts transporting blood into and from the tissues, organs and muscles of the body. In the systemic circulation, arteries transport the oxygenated blood from the heart towards their subdivisions in arterioles and capillaries where the exchange of nutrients, oxygen, carbon oxide and other solutes takes place through the very thin capillary wall. Venules collect the desoxygenated blood and progressively reunite into larger veins. The dense network of veins convey the blood back to the heart, where it is again oxygenated into the pulmonary circulation.

The heart propels blood around the circulatory system by contraction and relaxation of the cardiac muscle. During the systolic phase, high-pressure blood is ejected by the left ventricle through the aortic valve into the main artery, the aorta. The diastolic phase starts at the closure of the aortic valve and finishes at its opening at the beginning of the next systole. During the diastolic phase, the heart does not generate any impulsion into the vascular system. The presence of these two phases induce the pulsatility of the cardiac waveform.

Because blood in the arterial circulation is transported at a high-blood pressure, the arterial wall is much thicker than the walls of the venous system, where blood is transported under much lower pressures. The wall of the large arteries is composed of three main layers of different structures and cell types: the internal layer or tunica intima (composed of the endothelial cells), the middle layer or tunica media (composed of elastic fibers and smooth muscle cells), and the outer layer or adventitia (elastic and collagenous fibers).

During each heartbeat, the left ventricle ejects on average 70 ml of blood in the aorta. The created wave propagates into the arteries, from the aorta towards the distal arterioles, at a finite speed thanks to the elasticity of the arterial wall (in a rigid tube, the speed would be infinite). The velocity of this pulse wave ($c \simeq 10\text{ m/s}$) is much higher than the velocity of blood in the arteries ($u \simeq 1\text{ m/s}$). While the wave propagates, it can be reflected at arterial bifurcations or distal networks. The reflected wave travels backwards towards

the heart and interacts with the forward-propagating pulse, generating an inflection point (the dicrotic notch) on the aortic pressure waveform (Fig. 1.1).

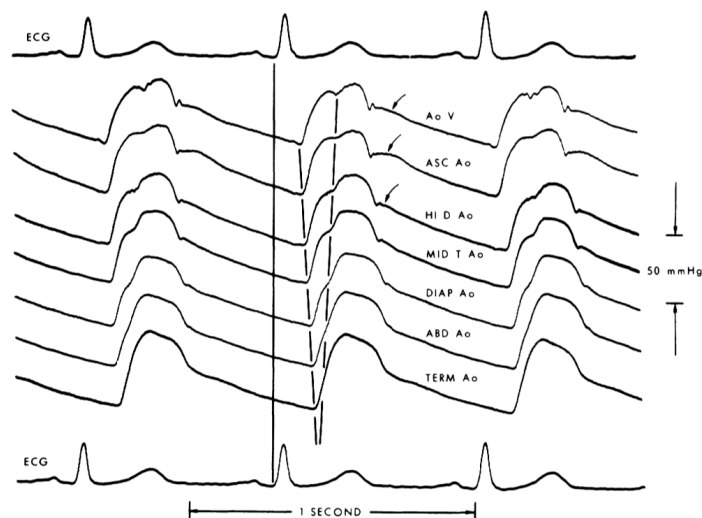


Figure 1.1 – Evolution of pressure wave contours with transmission of the wave from the ascending aorta (top) to the distal circulation (the iliac bifurcation, bottom) in one patient. The effect of the reflected wave on the pressure waveform is emphasized in the second cardiac cycle using dashed lines. From Murgu et al. (1980).

1.2 The lower-limb bypasses

When atherosclerosis affects a patient, its arterial network suffers from physiological changes due to the deposit of proteins and fat: e.g. increase of the rigidity of the arterial wall or of its thickness. When not treated, this can lead to arterial narrowing (i.e. stenosis) or occlusions of the vessel, and as a clinical consequence to the lack of vascularization of downwards tissues and muscles (which might result in gangrene). If the stenosis is shorter than 5 cm, the zone can be treated by balloon angioplasty and stenting. But if the diseased arterial segment is too long, a bypass remains the main surgical procedure to overcome the lesion: a new conduit which goes around the arterial occlusion is inserted in the surrounding tissues, and allows blood flow to *bypass* the obstruction.

In the arterial circulation, bypass surgery is mostly performed on the coronaries arteries around the heart, the cerebral arteries and on the lower-limb

arteries. This work focuses on the lower-limb bypasses: the occlusion of the superficial femoral artery is bypassed from the femoral to the popliteal or tibial arteries (Fig. 1.2).

Femoro-popliteal bypasses are one of the most common types of vascular surgery: 1% of the population older than 70 years will need surgical treatment because of the occlusion of the native femoral artery. Even though this surgery is frequently performed, a high failure rate (up to 60%) is still observed within the five years following the surgery (Norgren et al., 2007).

In this section, we aim at familiarizing the reader with this specific type of clinical intervention. After a brief reminder of the atherosclerosis disease, i.e. the pathological cause of occlusion, the main characteristics of bypasses are presented. Once a bypass surgery is realized, surgeons assess the success of the bypass by referring to some medical criteria, presented in subsection 1.2.3. The main causes of failure of bypasses after a few years are finally discussed.

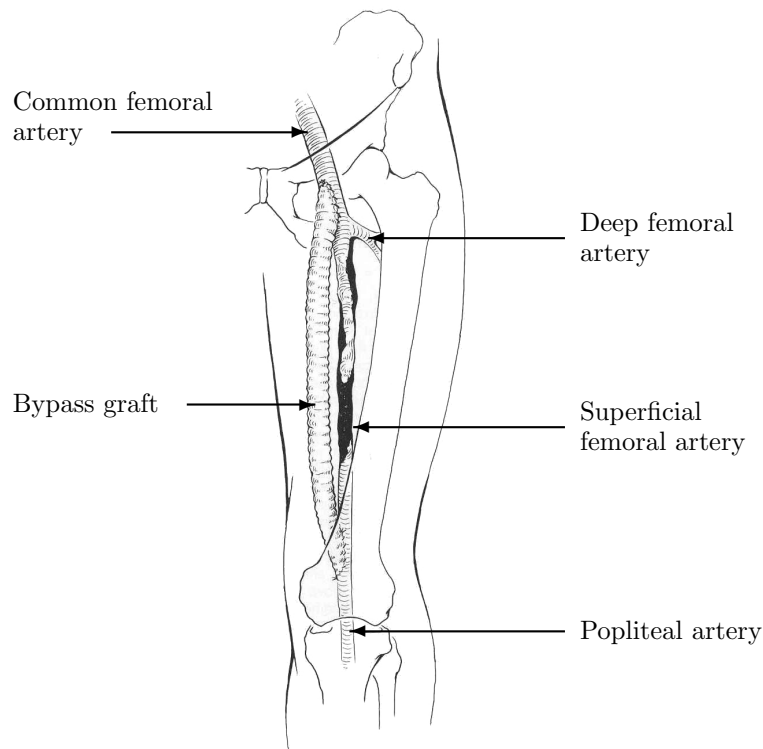


Figure 1.2 – Bypassed lower-limb arteries. The occlusion of the superficial femoral artery is treated with femoro-popliteal bypass.

1.2.1 Atherosclerosis

Atherosclerosis is a widespread cardiovascular disease in our western world: it is the most common cardiovascular cause of death and disability (Nichols and O'Rourke, 2005).

Atherosclerosis is primarily an intimal disease of large and medium-sized arteries. It is characterised by formation of intimal plaques consisting of lipid accumulation, smooth muscle and inflammatory cells, connective tissue fibers and calcium deposits (Nichols and O'Rourke, 2005). Its main effects include arterial narrowing and reduction of blood flow in the downwards tissues. It also weakens the wall locally, alter endothelial function, vascular tone, cell adhesion molecules and platelets adhesion.

Risk factors for atherosclerosis include age and male sex, hypertension, hypercholesterolemia, cigarette smoking, diabetes, physical inactivity, adiposity and race (Nichols and O'Rourke, 2005).

1.2.2 Bypass characterisation

In practice, surgeons need to define patient-specific bypass characteristics: the bypass material and dimensions, the proximal and distal location of the bypass sutures on the patent arteries (i.e. the anastomoses), and the types of these anastomoses.

Different types of materials are available when designing the bypass surgery: either vessels from the human being or synthetic materials.

Among human vessels, surgeons can use arterial or venous homografts, mammary arteries, but in most cases, they use a vein from the patient when available in good quality. The greater saphenous vein is generally used as it offers the best match in size and quality. Other venous tissues including contralateral long saphenous vein, femoral vein or arm vein have also been used. The vein can be used in a reversed configuration (the vein is extracted from the tissues, fistulae are ligated and it is reversed in order to allow blood to flow through the venous valves) or in-situ configuration (the vein remains in the surrounding tissues, but its valves are removed in order to allow blood to flow downwards and side branch fistulae are ligated to avoid leakages). Though, no difference in patency rates have been observed between these two configurations (Norgren et al., 2007).

Grafts in synthetic materials (polyethylene terephthalate, PET (polyester or Dacron[®]) or polytetrafluorethylene, PTFE (Gore-Tex[®])) are available for medical practice with a constant diameter (6, 7, 8 *mm*) (Figs. 1.3, 1.4). Tapered diameter grafts (6-8 *mm*, 4-8 *mm*) are currently not used for peripheral vascular surgery. Depending on the commercial provider, synthetic grafts offer different designs and characteristics. For example, polyester grafts might be coated with a layer of silver on the surface in order to avoid microbial adhesion. Others are impregnated with absorbable modified gelatin to reduce the initial

porosity of the graft. PTFE grafts might also be reinforced with rings on the external surface. Some models present a cuff at the graft tip in order to enhance flow at the anastomosis.

In femoro-popliteal bypasses, the proximal anastomosis is located on the common femoral artery a few *cm* from the deep femoral arterial junction. The distal anastomosis is located on the popliteal, anterior or posterior tibial, or even peroneal artery depending on the patient's disease. Surgeons usually classify this distal anastomosis site as above or below-knee position (Fig. 1.5): medical statistics indicate that this morphological feature seems to be related to the patency of the bypass graft and to its material (Albers et al., 2003; Norgren et al., 2007).

At the distal anastomosis, in order to reduce the compliance-mismatch between prosthetic graft and native artery, different surgical techniques modify the anastomosis geometry by using autologous vein cuffs and patches (Fig. 1.6). In-vitro studies showed that different stagnation points seem to be observed with different cuff and patch configurations (Noori et al., 1999). Even though, the benefits associated with the cuffed grafts are controversial. Numerical studies conclude that aspects of the anastomotic hemodynamics are worsened when a cuff is employed (Cole et al., 2002).

When surgeons define these patient-specific bypass characteristics, they rely on morphological images, on the patient's pain, on medical literature and on their own experience. Their goal is to maximize the bypass patency in time, i.e. design a bypass that maintains a sufficient distal arterial run-off as many years as possible.

1.2.3 Medical criteria of success

One classical clinical approach to evaluate the success of the bypass is to measure its hemodynamics after surgery. Velocity and blood flow can be easily measured intraoperatively and postoperatively a few days, weeks and months after the surgery. These measurements can be compared with medical criteria established on basis of hemodynamical observations. Four indicators of early graft failure (3 to 12 months) are presented in the medical literature (Lundell and Bergqvist, 1993; Stirnemann et al., 1994; Bandyk et al., 1985; Johnson et al., 2000; Miller et al., 1990):

- a low mean flow in the bypass ($\bar{Q} < 50 \text{ ml/min}$),
- a low peak systolic velocity ($PSV < 45 \text{ cm/s}$),
- a low end-diastolic velocity ($EDV < 8 \text{ cm/s}$),
- a high peripheral vascular resistance
($PVR > 66 \text{ mmHg s ml}^{-1}$ or $8.8e^4 \text{ cm}^{-4} \text{ g s}^{-1}$).

In practice, the first three indicators can be easily measured by Doppler ultrasound. The fourth, the peripheral vascular resistance, can be computed from pressure and flow measurement but is not used by surgeons in medical practice.



Figure 1.3 – Examples of synthetic bypasses commercially available. Top: polyester (Dacron[®]). From left to right: Silver graft, BRAUN / Impregnated knitted, BRAUN / Intergard silver ultrathin, MAQUET. Bottom: PTFE (Gore-Tex[®]). From left to right: Interling, GORE / VascuGraft, BRAUN / Unity, with ring reinforcement, VASCUTEK.

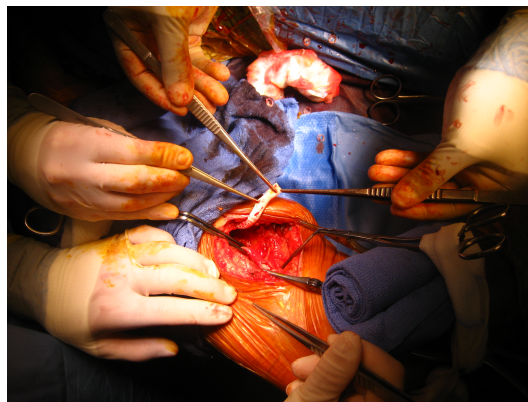


Figure 1.4 – Distal extremity of a synthetic Gore-Tex graft during bypass surgery. The native popliteal artery can be seen between clamps.

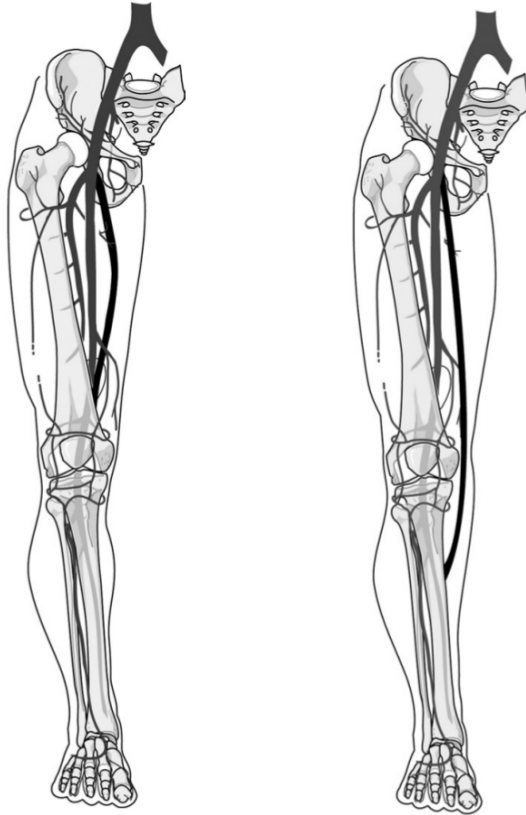


Figure 1.5 – Above-knee femoro-popliteal bypass (left) and below-knee femoro-tibial bypass (right). From Norgren et al. (2007).



Figure 1.6 – Different types of cuffs used at the distal anastomosis. From left to right: Miller-cuff, Taylor- and Linton-patch. From Noori et al. (1999).

Studies have pointed out that venous grafts present better patency rates than prosthetic materials thanks to their ability to develop an endothelium along their inner wall (Albers et al., 2003; Sottiurai et al., 1983). Indeed, in grafts constructed with a vein, five-year assisted patency rates reach 60%, while those constructed with prosthetic material are usually less than 35% (Norgren et al., 2007). There is no clear evidence of the advantage of one synthetic bypass material over the other (Roll et al., 2008).

1.2.4 Failure of bypasses

Despite the efforts of clinicians, early-graft failure often happens: the complete obstruction of the bypass within 3 months is not so rare (Rzucidlo et al., 2002).

One of the most important causes of graft failure is due to the development of myointimal hyperplasia (MIH) at the anastomosis, especially in the distal location (Taylor et al., 1987; Sottiurai et al., 1983). This is seen as a cause of failure in both autogenous and prosthetic bypass grafts. MIH was found predominantly at the heel of the graft and on the floor of the artery. The triggers for its formation are injury, circulating blood components, abnormal hemodynamics or impedance mismatch between the native vessel and the graft material (Toes, 2002). Three-dimensional modeling studies have also shown that abnormal hemodynamics may create zones of high or low wall shear stress that contribute to the development of plaque along the graft wall or at the distal anastomosis (Leuprecht et al., 2002; Pousset et al., 2006).

When occlusion of the graft occurs, dilatation of the occluded zone can be realized if treated early. Otherwise, a new bypass surgery might be realized while the occluded graft remains in the leg. In the worst cases, in patients with severe arterial disease, amputation of the distal limb might be required.

1.3 Data acquisition in pathological subjects

As previously described, the success of a bypass surgery depends on the characteristics of the bypass and the patient's condition. It is therefore important to be able to characterise patient-specific information in each lower-limb bypass.

In this section, we present a brief review of existing current techniques for the acquisition of in-vivo data in human arteries: i.e. arterial morphology (diameter D and length L) and hemodynamics (pressure p and velocity u). Emphasis will be put on the particular application of these techniques to the pathological arteries of occluded and bypassed lower-limbs.

1.3.1 Morphology: lengths and diameter of the vessels

Thanks to the development of medical imaging, clinicians have efficient and accurate techniques at their disposal to study the morphology of the arterial network. In the routine of vascular surgery, the occluded and bypassed vascular network of the patient's lower-limb are depicted using some of the following exams.

Magnetic resonance imaging (MRI)

MRI instrument uses powerful magnets to polarize and excite hydrogen atoms in human cells. The excited atoms emit a detectable signal which is spatially encoded, resulting in images of the body. With injection of contrast agents to enhance the appearance of blood vessel, MRI produces two-dimensional (2D) images of slices of the vessels along a defined direction. These images can then be used in a segmentation process in order to generate a three-dimensional (3D) geometry of the arterial network. MRI exams are performed on the patient's leg a few days before and after surgery in order to depict the lower-limb arterial network (Fig. 1.7). Lengths of the bypass graft can be measured accurately on these images. Though, this type of exam is preferably not used for diameter measurement, because of the limited level of precision of the MRI at our disposal in the Cliniques St-Luc (1.5T Philips, low resolution (0.84 mm/voxel) applied to small distal arteries (~ 3 voxels per diameter)).

Arteriography or angiography

This radiographic imaging technique allows to visualise the lumen of blood vessels and organs. It is performed by injecting a radio-opaque contrast agent into the blood vessel while images are recorded using X-ray based techniques. Fig. 1.8 presents three successive angiography images of the distal anastomosis of a venous bypass. Peripheral angiography is commonly used to identify vessel narrowing or occlusions. It is also used during vascular surgery as a tool to assess qualitatively the success of the bypass grafting.

Computed Tomography scan (CT Scan)

Using X-rays, CT scans produce a large series of 2D images taken around an axis of rotation (Fig. 1.9, left). With these images, a three-dimensional reconstruction of the bones and vessels can be performed (Fig. 1.9, right). CT scan images look similar to MRI but they do not present the same level of details in the soft tissues. Indeed, MRI has the ability to change the contrast of the images and therefore highlight different types of tissue. This type of exam is also not used for diameter measurement, similarly to MRI images. CT scan images at our disposal present almost the same resolution than MRI images (0.68 mm/voxel, 4 voxels per vessel diameter).

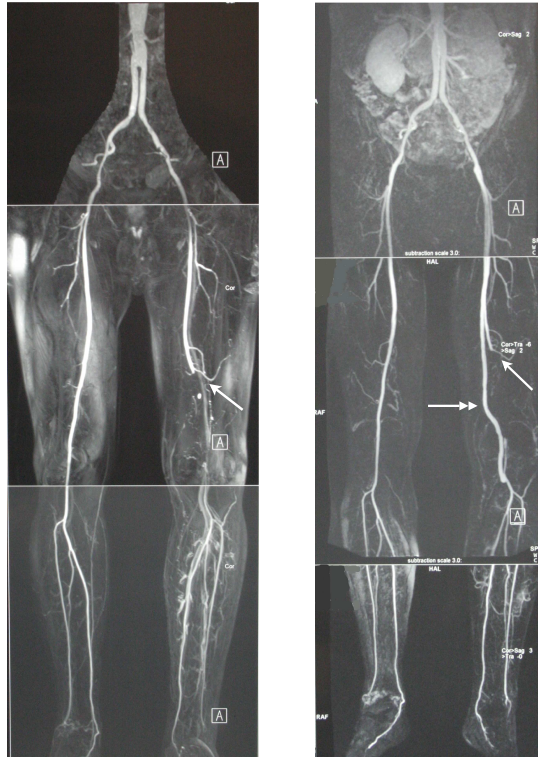


Figure 1.7 – MRI images of the lower-limb arterial network of a patient before (left) and after (right) surgery. The occlusion of the superficial femoral artery is indicated by a simple arrow. After surgery, the bypass graft (reversed vein) is marked by a double arrow.

Ultrasound

Ultrasound exams involve the use of high-frequency sound waves which are reflected on body structures (organs, vessels). By using different types of transducers, sound waves can be emitted at different tissue depth and within different tissues.

B-mode ultrasound is used in clinical practice (PHILIPS, ALOKA, GE). It allows to depict a two-dimensional image representing a plane of the human body. For example, Fig. 1.10 represents a longitudinal view of the common femoral artery. These static images allow to measure the arterial lumen with a good level of precision. Combined with Doppler measurements, arterial lumen detection is enhanced.

M-mode ultrasound allows to measure motion by the emission of successions

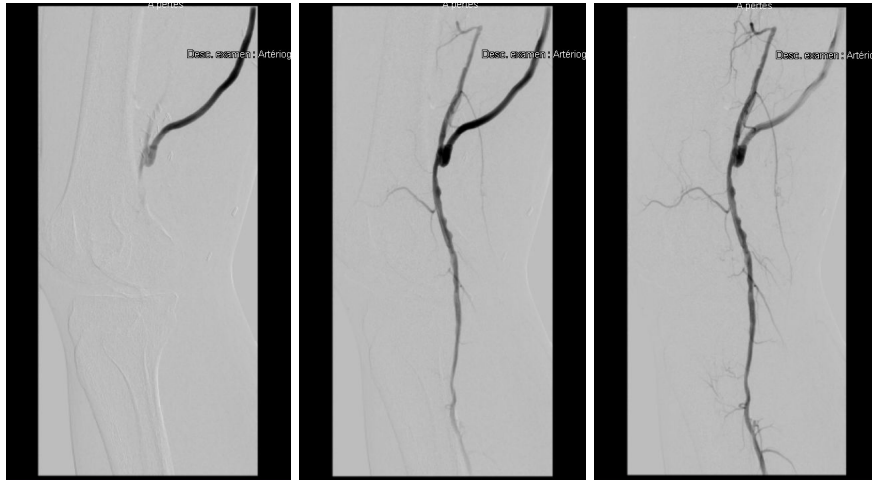


Figure 1.8 – Angiography images of a distal anastomosis of a venous bypass at three different times. The displacement in time of the contrast agent is clearly visible.

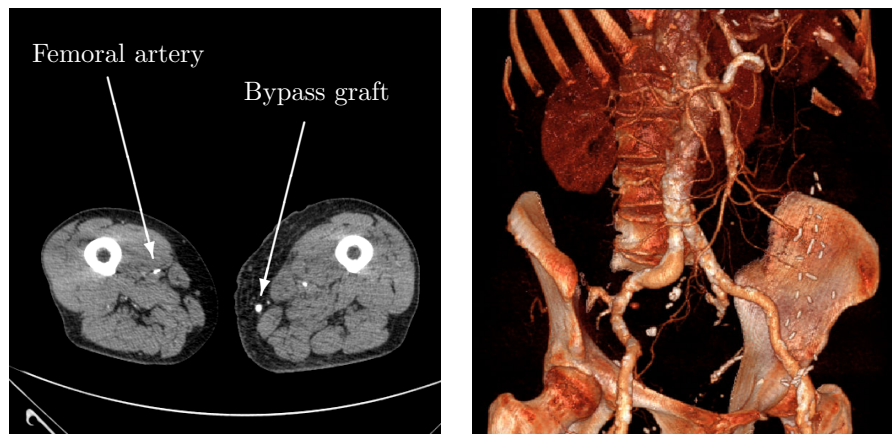


Figure 1.9 – Images obtained with CT Scan. Left: 2D image of the legs of a patient. Note the femoral artery on the healthy left leg and the bypass graft (in-situ vein) on the right leg. Right: 3D reconstruction from the abdominal aorta to the left and right iliac arteries (realised with the software DirectView-V5CR[®], Kodak Carestream).

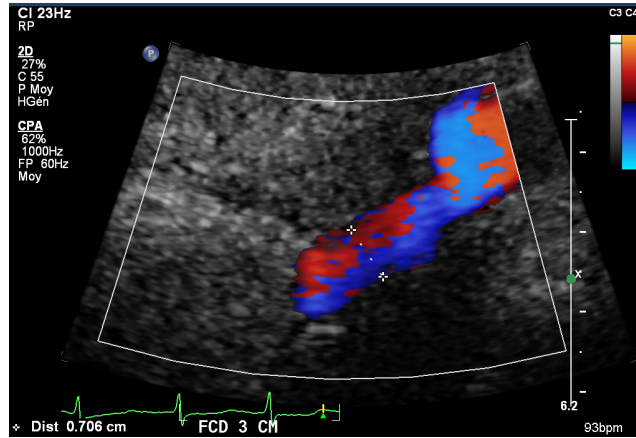


Figure 1.10 – B-mode Doppler ultrasound image of the common femoral artery. Diameter is measured manually during diastole. Red and blue areas indicate the zones where flow moves towards and away from the transducer.

of ultrasound pulses and recording of B-mode images. Combined with a high temporal resolution, this mode allows to measure vessel wall distension waveform ($D(t)$) (Meinders and Hoeks, 2004). Nevertheless, these high-resolution echotracking devices are not available in clinical practice and are developed for clinical research usage (ESAOTE).

1.3.2 Pressure

Blood pressure waveforms in arteries can be measured by the following invasive and non-invasive techniques.

Catheter-tip pressure manometer

Arterial blood pressure is accurately measured invasively using a pressure catheter, directly inserted into the artery of interest (MILLAR, CORDIS). The pressure sensor is mounted at the tip of the cardiovascular catheter, which are available in different shapes and dimensions (from 0.67 to 2.67 mm external diameter).

Pressure guide wire

Pressure guide wires allow to measure high-fidelity pulsatile pressure in small arteries (RADI, VOLCANO). The fiber optic pressure sensor is located laterally and a few cm from the distal tip of the thin wires (0.014 inch = 0.36 mm diameter).

Applanation tonometry

This non-invasive technique uses a large band piezoelectric probe as pressure transducer (SPHYGMOCOR). This instrument permits accurate registration of arterial pressure waves (contour and amplitude of the pressure pulse). Though, it requires scaling by systolic and diastolic values at the same arterial location (measured for example with stethoscope and sphygmomanometer). This method requires to appanate the artery and to compress overlying structures: it is limited to superficial arteries. Accurate measurements can therefore be obtained on superficial arteries such as the carotid or radial arteries. Though, this method is inefficient if applied on deep arteries of the leg or on calcified and atherosclerosed arteries.

Distension waveforms

An indirect and non-invasive way to measure pressure waveforms is by scaling vessel wall distension waveforms with systolic and diastolic blood pressures, assuming a linear or exponential pressure-area relationship (Vermeersch et al., 2008; Meinders and Hoeks, 2004). This method has been applied to healthy superficial arteries but is currently not developed for distal arteries.

1.3.3 Velocity and flow

The following methods focus on the velocity waveform measurement. The flow Q is obtained as the product of the velocity and the cross-sectional area of the conduit (the vessel or the probe).

Doppler ultrasound

Combined with the Doppler measurements, ultrasounds wave emission and reflection allow to assess if blood cells are moving towards or away from the probe, as well as the relative velocity of blood flow. The Doppler information is displayed graphically using spectral Doppler (Fig. 1.11), or as an image using color Doppler (Fig. 1.10).

Ultrasonic flowmeter

This invasive method uses an ultrasonic probe which measures the instantaneous blood flow by averaging the difference in measured transit time between the pulses of ultrasound propagating into and against the direction of the flow (TRANSONIC). The main disadvantage of this technique is that the flow probes have a fixed diameter which do not corresponds perfectly to the arterial diameter.

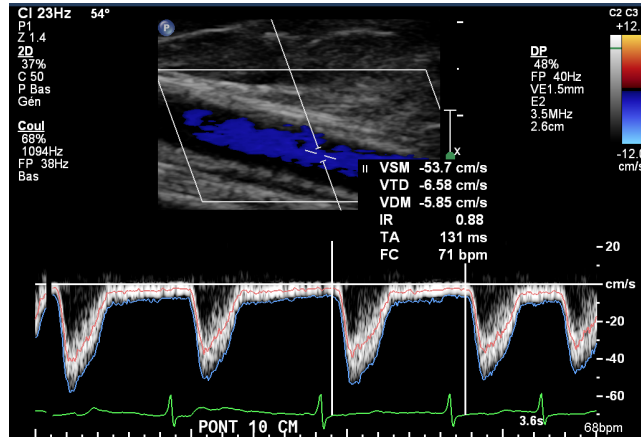


Figure 1.11 – B-mode Doppler ultrasound in a bypass vessel with measurement of the centerline velocity in the central region of the artery delimited by the two cursors.

Intravascular velocity transducer

This invasive and accurate technique is similar to the pressure guide wire: the velocity sensor (an ultrasound transducer or electromagnetic flow probe) is mounted at the tip of the 0.014 *inch* diameter wire (VOLCANO). This technique involves the knowledge of the distribution of the velocity profile across the artery.

1.4 Arterial hemodynamics modeling

Nowadays, the efficiency of computational models of the human physiology is not doubted. Either one considers models of the respiratory system, skeletal solid mechanics or the ocular biomechanics, these mechanical models are able to reproduce and explain the observed human physiology (Ethier and Simmons, 2007). In the modeling of the cardiovascular system, different aspects can be considered: the modeling of the heart, of the venous system, or of the arterial hemodynamics. This work will focus on this last point: modeling of blood flow in large arteries.

The human arterial system can be mathematically described with different levels of precision. From three-dimensional models (3D) models to lumped zero-dimensional (0D) models, many applications have taken benefits from the efficiency of these different models.

The most complex ones, the 3D models, offer great level of details of the hemodynamic variables inside the arteries. For example, they allow to detail

blood flow recirculation in an arterial junction (Fig. 1.12, right), or to compute the friction at the arterial wall (wall shear stress, WSS) (Giordana et al., 2005; Loth et al., 2008). Though, besides the high computational costs, they require the definition of a realistic fluid-structure interaction between the blood and the vessel walls (Crosetto et al., 2011; Hron and Mádlík, 2007) as well as the set-up of the 3D geometry of interest, which results for in-vivo geometries of an arterial section, from a complex segmentation process (Fig. 1.12, left) (Marchandise et al., 2010).

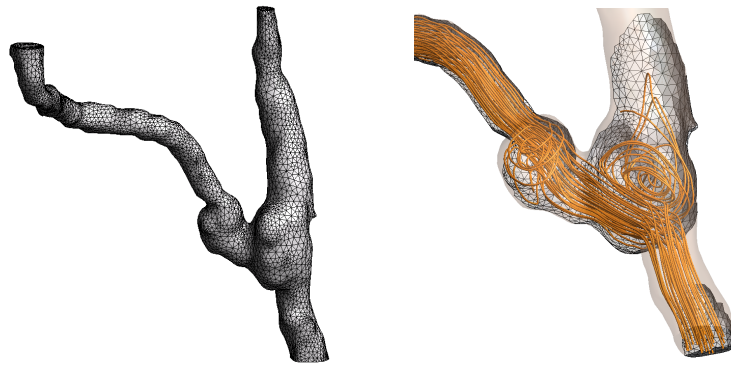


Figure 1.12 – Left: 3D geometry of the distal anastomosis of a venous bypass. Right: 3D simulation results (streamlines) in that geometry. See Marchandise et al. (2010) for further details about the generation of the geometry and the 3D simulation.

If one is interested in the axial distribution and evolution of hemodynamics along the arterial tree, one-dimensional (1D) models provide efficient and fast-computing results. 1D models of the arterial tree have shown their ability to capture the main features of pressure and velocity waveforms in large arteries (Reymond et al., 2009; Sherwin et al., 2003a). Though, as this approximation considers mean values of the hemodynamic variables across the arterial section, it requires the simplification of the velocity profile by an average value. Depending on the hypothesis used to represent the velocity profile (e.g. flat or Poiseuille velocity profile), an average WSS can be computed. One-dimensional models of the arterial tree have been widely used for simulating wave propagation in the entire arterial tree (Stergiopoulos et al., 1992; Avolio, 1980; Reymond et al., 2009; Sherwin et al., 2003a; Olufsen et al., 2000; Mynard and Nithiarasu, 2008) or in part of it (Alastruey et al., 2006; Bessems, 2006; Leguy et al., 2010; Raines et al., 1974) under physiological or pathological conditions (Alastruey et al., 2007; Steele et al., 2003; Kolachalama et al., 2008).

Zero-dimensional models of the circulatory network are based on electrical analog of a hydraulic description of the system. These models predict blood pressure and flow in and between compartments representing various parts of the cardiovascular system. From complex non-linear systems describing the pulsatile pumping of the heart (Olufsen et al., 2005) to simple windkessel models of an arterial network (Westerhof et al., 2009), they provide mean values of hemodynamic variables and require the determination of a number of parameters.

An interesting approach consists of coupling these different models in order to benefit from their respective advantages. Coupling between 3D, 1D and 0D models allows for example to study the hemodynamics in arterial section with great precision using 3D modeling, while waves propagate in the large arteries of the cardiovascular system using 1D models, and small and distal arterial networks are described using windkessel models (Urquiza et al., 2006; Blanco et al., 2009; Nobile, 2009). Another example is the coupling of the 1D model of the arteries to a lumped model of the heart, in order to provide a realistic impulsion of waves (Formaggia et al., 2006; Mynard and Nithiarasu, 2008).

In this work, we will consider the coupling between 1D and 0D models. Simple, efficient and fast-computing, this coupling gives physiological waveforms of pressure and velocity in different parts of the human body while taking into account the effect of the distal vasculature. This type of model presents a limited number of parameters, which can be evaluated on basis of in-vivo data.

1.5 Aim & outline of this thesis

The aim of the present research is to enhance our understanding of the hemodynamics in bypassed legs, by using numerical modeling of this arterial hemodynamics. Bypasses present high failure rates within 5 years, caused among others by the development of intimal hyperplasia and vessel occlusion. As the local hemodynamics greatly influences the initiation and progression of the disease, it is essential to better understand it if one intends to improve the long-term patency of lower-limb bypasses.

This work is part of the NHEMO project (which stands for *Numerical HEMO*dynamics). The goal of the NHEMO project is to build a predictive, patient-specific, fast and easy-to-use tool to help surgeons plan the bypass surgery on basis of commonly used non-invasive medical exams. The NHEMO tool would provide the surgeon with advices on the best bypass characteristics as a function of the patient's pathology.

The main aim of this research consists of studying the one-dimensional aspect of the wide-ranging NHEMO project. Furthermore, thanks to a close collaboration with clinicians and surgeons, this research aims at evaluate and set-up an efficient in-vivo data acquisition protocol, and design a patient-specific characterisation.

In particular, this work will focus on the application of the coupled one-dimensional and zero-dimensional numerical model of the arterial hemodynamics to the particular configuration of bypassed legs. It will furthermore consider the patient-specific validation of the model on basis of in-vivo clinical exams. Therefore, let us emphasize here that this validation step does not address the predictive objective of the NHEMO project. Besides the model validation, a detailed study of the sensitivity of the model to its parameters will be conducted.

Also, this research considers the point of view of wave quantification and propagation through the arteries with the analysis of wave intensity and the decomposition of waves into reservoir and excess components. Emphasis is put on the influence of the pathological condition and the insertion of the bypass graft in the arterial lower-limb network.

This work starts by a thorough description of the arterial in-vivo hemodynamics in bypassed lower-limbs (Chapter 2). In that chapter, the data acquisition protocol is defined; pressure and velocity waveforms are described, together with the evaluation of the patient-specific parameters of the model. Chapter 3 describes the mathematical and numerical model used in this work, with emphasis on the definition of an improved inlet boundary condition. Validation and sensitivity analysis of the model are conducted in Chapter 4 on basis of in-vivo measurements from 9 patients, performed during bypass surgeries. In Chapter 5, these in-vivo signals are analysed using the wave intensity analysis approach, and the influence of the pathology on the pattern of waves is demonstrated. Using the database of in-vivo measurements, Chapter 6 presents the application of the reservoir-excess theory in the practical application of pathological lower-limbs. Finally, Chapter 7 brings a summary, general discussion and outlook of this thesis.

CHAPTER 2

In-vivo hemodynamics in bypasses

Since the palpation of the arterial pulse by Galen, a Greek physician who lived during the second century common era, clinicians have developed numerous methods to characterise and understand the hemodynamics in the human body. Much efforts have been dedicated to the measurement of pressure since almost 100 years ago, and to the measurement of flow for the last 60 years. With time, works based on these measurements have directed attention to different indicators of cardiovascular disease: e.g. the pulse pressure, the systolic blood pressure, the wave speed or the arterial wall stiffness. Over the past 30 years, much interest has also been devoted to the study of contours of pressure and flow waveforms in human arteries, and to the understanding of the origin and transmission of these waves to peripheral vessels. This has led to the development of new models explaining some of these observations. Let us mention two major ones: the one-dimensional wave propagation theory and the Windkessel model of the arterial system.

In this chapter, we intend to follow a similar approach: in a first part, define the in-vivo data acquisition in arteries of bypassed lower-limbs, and characterise the subjects under study. In a second part, observe and analyse the hemodynamic waveforms acquired, and explain the origin of the contours observed. Based on the literature and our observations (25 patients studied during 4 years), we focus on the description of pressure and velocity contours in lower-limb arteries in different pathological conditions: healthy subjects, old and atherosclerosed subjects and subjects with arterial occlusion operated with bypass surgery. In a third part, we derive some indicators of the disease from hemodynamical measurements. We discuss and apply different methods for evaluating arterial properties from in-vivo measurements. We particularly focus on the vessel wall elasticity and the characterisation of the distal networks in the arterial leg. This database of parameters is then discussed, compared with healthy data, and comparison between pre- and post-operative conditions is performed. Finally, characteristics, performances and patencies of surgeries analysed during this work are presented.

2.1 In-vivo data acquisition in pathological subjects

The characterisation of the patient's condition and of the bypass is achieved through measurements of the morphology and hemodynamics. After studying different alternatives of measuring techniques (cfr the Introduction), we have elaborated an experimental protocol of data acquisition in close collaboration with the Cliniques Universitaires St-Luc (UCL, Bruxelles, Belgium). Our choice is motivated by the efficiency of the application of the technique to the pathological arteries of the leg, as presented in the first subsection. The post-processing used to transform the raw data into representative signals over a cardiac cycle is then described in details. Finally, this section presents the clinical characteristics of the patients considered in this work.

2.1.1 Data acquisition protocol

The following data acquisition protocol has been defined within the framework of the NHEMO project in order to acquire the morphology and hemodynamics in the lower-limb arteries of our subjects.

The length

The length L of synthetic bypasses is evaluated during surgery as the difference between the complete graft length and the excess piece of graft. For the other types of bypasses, L is acquired on MRI images taken a few days after surgery.

Within the numerical application, lengths of the arteries correspond to the distance between the point of measurement and the downstream or upstream arterial junction (e.g. the common femoral length is measured from the catheter tip to the proximal anastomosis).

The diameter

The diameter D of arteries and bypass graft is acquired using B-mode Doppler ultrasound by a skilled operator. The diameter of the lumen of the artery is manually selected during the diastolic phase, and is considered representative of the diameter over the arterial length. Notice that this manual measurement might be subject to some error and imprecision (e.g. selection of the intima layer). This technique only allows to measure the mean diastolic diameter D_0 . Ultrasound measurements are acquired using the Philips iU22[®] (xMATRIX ultrasound system, Philips, Drachten, The Netherlands). This device computes the velocity averaged over a region defined by the user and highlights the maximal velocity at this location.

The synthetic bypasses are of constant diameter along their length. The morphology of the venous bypass is described as a nearly constant diameter vessel, based on MRI images and angiogram exams.

Hemodynamic variables

The pressure p and velocity u are acquired invasively during bypass surgery, while patients are under anaesthesia. Patients are in a stable hemodynamical state and no vasodilatory drug is injected at least 30 *min* before measurements. For all patients, measurements are performed after the suture of the graft, at four different locations in the leg: in the proximal common femoral artery (CF), the proximal deep femoral artery (DF), the proximal bypass graft (BP) and in the popliteal artery (PO) (Fig. 1.2). For some patients, data is also acquired before insertion of the graft, with occlusion of the superficial femoral artery. Measurements are then taken at the same three arterial sites.

Two different acquisition protocols have been used, each patient is analysed by one of them.

In the first one, pressure profiles are acquired invasively with a pressure catheter (acquisition frequency f_{acq} of 1000 *Hz*). Even if the presence of the needle (0.6 *mm* diameter) alters the flow pattern, the resulting increase of pressure is limited to a few *mmHg* (< 5 *mmHg* for a 0.6 *mm* needle diameter in an artery of 3 *mm* diameter) (Torii et al., 2007). Centerline velocity waveforms are measured using B-mode Doppler ultrasound. These measurements are not realized simultaneously, though they present a constant heart rate. Their acquisition frequency is 100 or 250 *Hz*, depending on the ultrasound device used.

In the second acquisition protocol, pressure and velocity profiles are acquired invasively and simultaneously using a 0.014 *inch* diameter guide wire with pressure and velocity sensors both located at the tip of the wire (ComboWire[®] and ComboMap[®], Volcano Corporation, Rancho Cordova, CA, USA). The acquisition frequency of the pressure sensor is 200 *Hz*, while velocity is acquired at 100 *Hz*. Combined use of angiography might be necessary to determine precisely the position of the wire in arteries.

Notice that, due to the configurations of the medical devices in the surgery rooms, the ECG signal could not be acquired simultaneously to both pressure and velocity measurements.

Invasive in-vivo data acquisition and local or general anaesthesia may alter blood hemodynamics. Notice though that this type of data acquisition has been used and validated in multiple studies (Parker and Jones, 1990; Khir et al., 2001a; Sun et al., 2000; Penny et al., 2008; Hollander et al., 2001; Koh et al., 1998).

Because the physiological network is very sensitive to the condition of the subject, it might be influenced by various external factors such as stress or medication. Ideally, measurements of the hemodynamics should be performed while the patient is in a resting state. Nevertheless, small variations of the

hemodynamical condition (central pressure, vasomotor tone, vasoconstrictor tone) might be observed in the hemodynamical observations in the following analysis.

2.1.2 Processing of the information

Signals are post-processed within the Matlab[®] programming environment (MathWorks, Natick, USA).

In order to obtain representative cardiac cycles of the patient's hemodynamics, ensemble average and filtering is applied to the raw pressure and velocity signals. Furthermore, the analysis of velocity measured by B-mode Doppler requires an assumption on the velocity profile.

Ensemble average

As raw signals of pressure and velocity are recorded over at least 5 to 10 cardiac cycles, ensemble averaging is performed in order to provide representative pressure and velocity waveforms. Because the cardiac cycle duration might not be perfectly constant over the sample of data, there is a need for an algorithm determining the optimal lag between the systolic upstrokes.

As the ECG signal is not recorded simultaneously to pressure and velocity, the reference signal of the heart can not be used to synchronise the systolic upstrokes. Following Zambanini et al. (2005), ensemble averaging is performed by maximizing the cross-correlation coefficient between each waveform using the first 100 *ms* of rapid rise in p and u .

Filtering

Ensemble average signals are smoothed using a Savitzky-Golay filter (17-points third-order), which reduces signal noise with minimal influence on peak magnitudes (Savitzky and Golay, 1964). This method performs a local polynomial regression on a series of values to determine the smoothed value at each point. Its main advantage is to act as a filter to smooth the noise fluctuations without introducing distortion into the recorded data.

Finally, as the frequency of data acquisition differs between pressure and velocity, signals are discretized at the lowest frequency, the frequency of the ultrasound measurement.

Velocity profile

The velocity spectrum acquired with Doppler ultrasounds corresponds to the maximal velocity at the center of the artery. We considered the assumption of a Poiseuille velocity profile in the arteries; therefore the mean velocity is computed as the maximal envelope u_{max} divided by 2. In view of the Womersley

parameter α in the leg arteries, the assumption of a Poiseuille profile is acceptable. The Womersley parameter α expresses the relative importance of inertial effects over viscous effects: $\alpha^2 = r^2\omega\rho/\mu$ with r the internal radius of the vessel, $\omega = 2\pi/T$ the circular frequency (T the cardiac period), ρ the blood density and μ the blood dynamic viscosity (Westerhof and Stergiopulos, 2005). For low values of α ($\alpha < 3$), the profile becomes parabolic as in Poiseuille flow; while for large values of α ($\alpha > 10$), the profile becomes flat. In this study, the average Womersley parameter is around 3 in the small leg arteries and is in the low to medium range in the common femoral artery and bypass vessel (Table 2.1), which confirms that the Poiseuille hypothesis is reasonable.

Notice also that compared to the assumption of a pulsatile Womersley model, Poiseuille profiles under-estimate the maximum blood volume flow by 19% (Leguy et al., 2009).

	CF	DF	BP	PO
α (/)	4.8 ± 0.7	3.2 ± 0.6	3.9 ± 0.9	2.7 ± 0.8

Table 2.1 – Average values \pm standard deviation of the Womersley parameter α in the main vessels of the bypassed leg. Average is performed over the 9 patients analysed in this study.

Regarding the analysis of the velocity acquired with guide wire, we assume that the measured signal corresponds to the average velocity across the artery. As the velocity is acquired punctually at the wire tip, there is a large uncertainty about the position of the sensor at the center of the vessel.

2.1.3 Subjects

During the four years of this work, 25 patients in an advanced stage of atherosclerosis and suffering from occlusion of the superficial femoral artery have been followed for lower-limb bypass surgery (femoro-popliteal or femoro-tibial). All patients gave their full agreement for taking part into the study. Nine of them have been analysed with an efficient data acquisition protocol and are considered in the following of this analysis. (Patients #14, #15, #16, #19, #21, #22 analysed with the first protocol and patients #23, #24, #25 with the second.) Notice that, among the 16 other patients, 13 of them have been analysed with an inefficient data acquisition protocol (non-similar physiological conditions for p and u recordings) and 3 of them have been analysed with a Doppler ultrasound device of poor resolution ($f_{acq} = 50$ Hz).

In the 9 patients considered, materials used for the bypass are either a synthetic material of 6 mm diameter (Dacron[®], Gore-Tex[®]), or the native saphenous vein used in-situ. Distal anastomosis is either located above or below the knee.

The severity of the peripheral arterial disease is characterised with the ankle-brachial index (ABI) before surgery. Values of the ABI after surgery are also given, as an indicator of the success of the surgery. The ABI is computed as the ratio of the systolic blood pressure at the ankle to the systolic blood pressure at the arm. Table 2.2 presents the interpretation of the ABI scores (Al-Qaisi et al., 2009), mean scores of the patients considered are displayed in Table 2.3. Before surgery, patients presented a severe disease, close to critical ischemia. After surgery, thanks to the bypass graft, their ABI index increased to a normal range with moderate disease.

Resting ABI	Severity of disease
> 1.4	Calcification
0.81 - 1.4	Normal range
0.5 - 0.8	Moderate disease
< 0.5	Severe disease
< 0.3	Critical ischemia

Table 2.2 – Interpretation of the ankle-brachial index (ABI), from Al-Qaisi et al. (2009)

The clinical parameters of the subjects are listed in Table 2.3. Morphology and hemodynamical waveforms of the 9 patients are displayed in Appendix B.

2.2 Waveform analysis

Analysis of waveforms tells the observer many information about the physiological and pathophysiological condition of the organism. At the generation of waves by the left ventricle, the complete arterial vasculature applies some load on the heart which influences the blood ejection. While waves propagate in the arterial network, they interact with the surrounding tissues and the morphology of the arterial network, creating wave reflection and damping. The shape of the arterial pressure wave is dependent on a number of factors, including the duration of systole, the mean arterial pressure, the vasomotor tone, the pulse wave velocity and wave reflections. Therefore, considering the complexity of the cardiovascular system, analysis of pressure and velocity contours at an arterial site of interest is a first clue to understand the medical condition of the subject considered.

In order to highlight the modifications in hemodynamics induced by the bypass surgery in the lower-limbs, we summarize observations from the literature about hemodynamics in healthy lower-limbs, in old and atherosclerosed subjects and in subjects with arterial occlusion. The following descriptions are based on the works of Nichols and O'Rourke (2005); Vlachopoulos and O'Rourke (2000);

<i>Clinical parameters of the patients:</i>		
Gender		6 men, 3 women
Age	(year)	72.9 ± 11.0
Heart rate	(beats/min)	69.8 ± 14.1
Common Femoral SBP	(mmHg)	112.1 ± 24.3
Common Femoral DBP	(mmHg)	55.8 ± 9.7
Body Mass Index	(kg/m^2)	24.1 ± 2.8
ABI before surgery*	(/)	0.35 ± 0.05
ABI after surgery**	(/)	0.79 ± 0.17
Distal anastomosis		4 BK, 5 AK
Type of bypass graft		5 GT, 2 DA, 2 ISV
Length of AK bypass graft	(<i>cm</i>)	35.0 ± 4.1
Length of BK bypass graft	(<i>cm</i>)	50.8 ± 6.1
Acquisition protocol		6 (#1), 3 (#2)

Table 2.3 – Clinical characteristics of the 9 pathological subjects of this study (mean data \pm standard deviation). SBP: systolic blood pressure; DBP: diastolic blood pressure; ABI: Ankle-Brachial Index; AK/BK: Above/Below-Knee; GT: Gore-Tex, DA: Dacron, ISV: in-situ saphenous vein. Acquisition protocol (#1) uses catheter and Doppler ultrasound measurements, while protocol (#2) uses a guide wire. In ABI computation, data available for 5* and 8** subjects.

Kelly et al. (1989); O’Rourke and Avolio (1980); Avolio (1980). These studies only consider the common femoral artery from the lower-limb. Notice that few information about distal leg arteries, such as the tibials, is available due to their distal location and difficult access.

2.2.1 Hemodynamics in healthy lower-limb arteries

In healthy lower-limb arteries, the femoral pressure wave presents a single systolic wave. In comparison with upwind arteries such as the aorta, the peak pressure is increased, even though the mean pressure falls slightly. Contrary to the aorta (see Fig. 1.1 in Section 1.1 of the Introduction), the dicrotic notch is not apparent and the diastolic decay is nearly exponential with a shallow diastolic wave (Fig. 2.1). Following Murgó’s classification of aortic waves, the femoral wave corresponds to a wave of type D (Murgó et al., 1980). This type of pressure waves does not present any inflection point because the reflected wave arrives early in systole and merges with the incident wave.

As described with Doppler waveform contour in the common femoral artery, a healthy velocity waveform presents a triphasic contour (Shaanan et al., 2003): a sharp, narrow and tall systolic upstroke and two or three waveform phases including an element of reverse diastolic flow (Fig. 2.2). Compared with the aorta, peak velocity and amplitude of the lower-limb flow are reduced.

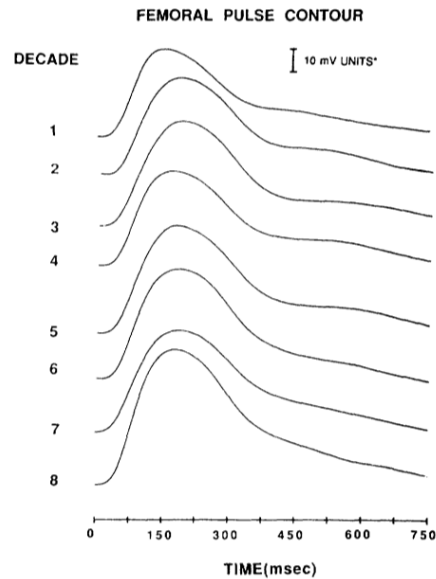


Figure 2.1 – Evolution of femoral pressure wave contours with age. From Kelly et al. (1989).

Similarly to the ascending aorta, the peak pressure occurs after the peak flow. Because of the arrival of the reflected pressure waves, the pressure increases furthermore while the velocity wave has reached her systolic peak and starts to decrease.

2.2.2 Influence of aging and atherosclerosis disease

Age

With aging, the structural components of the arteries change, leading to alterations in function and geometry of the arteries. Arterial stiffness increases, which creates increased pulse wave velocity and progressively earlier wave reflections. The femoral pressure waveform shows a progressive rise in the systolic wave; the single diastolic wave becomes less prominent (Kelly et al., 1989) (Fig. 2.1).

In older subjects, the peripheral and lower body arteries show none of the diastolic flow fluctuations characteristic of younger subjects. Arterial flow contours come to resemble what is observed in the ascending aorta.

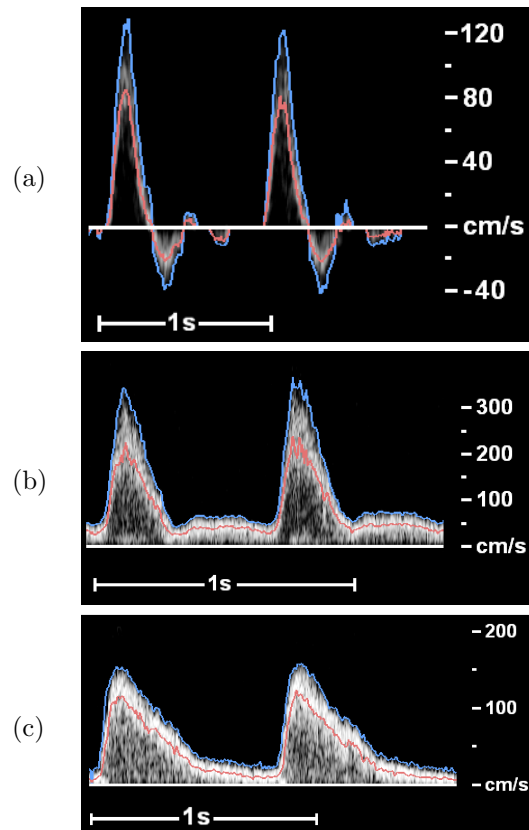


Figure 2.2 – Examples of tri- (a), bi- (b) and mono-phasic (c) velocity waveforms measured in the common femoral artery.

Atherosclerosis

As described in Section 1.2 of the Introduction, the most common effect of atherosclerosis is the narrowing of the arterial lumen, leading to stenosis and eventually to arterial occlusion. This narrowing causes a reduction of blood flow supplying the distal tissues. With the development of ischemic symptoms, pressure pulses may disappear completely. Also, atherosclerosis appears to increase stiffening of major arteries.

It can be considered that the effects of a stenosis on the hemodynamics are similar, to a lesser extent, to what is observed in occluded arteries, as described in the following paragraphs.

2.2.3 Hemodynamics in occluded lower-limb arteries

Proximal to the obstruction

Peripheral arterial obstructions produce little effects on the pressure pulse proximal to the obstruction. According to Vlachopoulos and O'Rourke (2000), this is explained by the peripheral nature of the obstruction, the normally occurring high degree of wave reflection from the peripheral vascular bed and the presence of the other patent peripheral arteries. Indeed, in the femoral vascular bed, the arteriolar tone is already high, resulting in a high reflection coefficient that is increased marginally by arterial obstruction (Nichols and O'Rourke, 2005).

Pressure measurements performed invasively during bypass surgeries (see Section 2.1) present similar observations. Proximal to the obstruction, waves measured before the suture of the bypass show little variations in shape and intensity with waves measured after the graft suture. This observation takes into account the possible small fluctuations of the central pressure induced by the surgery in progress (Fig. 2.3).

The flow contour is markedly altered by arterial obstruction. When the obstruction is close, mean flow may be eliminated. When the flow is measured at some distance upstream of the occlusion, changes in the flow include a fall in the entire flow wave: reduction of mean flow and creation of backflow, but with little change in wave contour (Nichols and O'Rourke, 2005). The presence of an arterial occlusion changes the blood distribution in the arterial network of the leg. When the main vessel gets occluded, blood travels to the arteries below the occlusion by perfusion through small collateral arteries. Therefore, the resistance measured above the occlusion increases largely and the flow proximal to the occlusion decreases in comparison with a non-occluded artery.

In 70 % of the bypasses analysed in this work, we observed that the blood flow measured in the artery proximal to the occlusion was decreased because of occlusion, when compared with the flow measured after bypass surgery (with measurements taken with Doppler ultrasound a few days before and after surgery).

Distal to the obstruction

Downstream of a short obstruction or stenosis, pressure waves present a decreased amplitude, with damped contour and damped peak. In the case of a long arterial occlusion, the pressure drop and damping is enhanced distal to the occlusion.

Fig. 2.4 presents pressure measurements proximal and distal of a stenosed superficial femoral artery, before and after treatment (dilatation and stenting) of the artery. Measurements were taken invasively during an arteriography, using a Volcano guide wire (see Section 2.1). Below the stenosis, the pressure is strongly reduced, while its intensity remains quite constant above

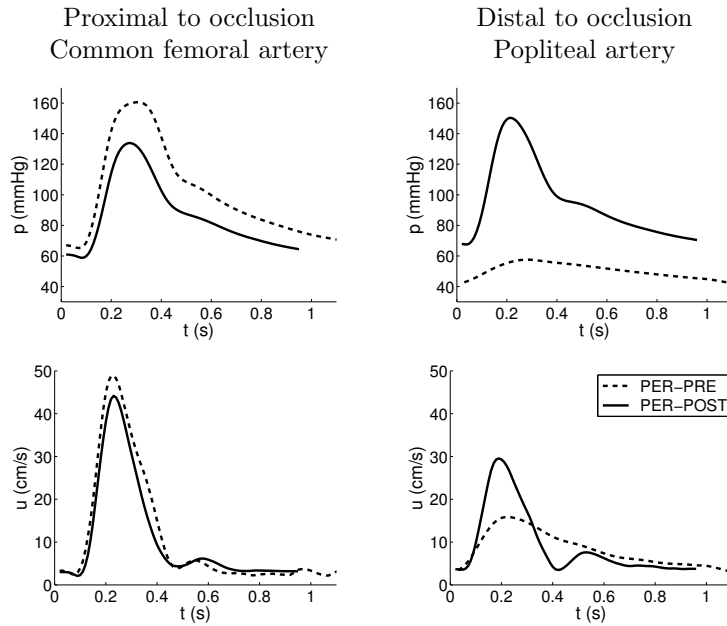


Figure 2.3 – Pressure p and velocity u waveforms, proximal (left, common femoral artery) and distal (right, popliteal artery) to a long arterial occlusion of the superficial femoral artery. p and u measurements are realized simultaneously during bypass surgery, in pre-operative (dashed line) and post-operative state (continuous line).

the stenosis. Notice that, above the stenosis, the pressure is particularly high (120-200 $mmHg$); this might be induced by the local anaesthesia or the condition of the patient (hypertension). During the pre-operative state of a bypass surgery, a strongly damped pressure waveform, hardly pulsed is observed distal to the occlusion, in the popliteal artery (Fig. 2.3).

In the presence of arterial stenoses or occlusions, flow waveforms present important alterations of their contour. In his study, Shaalan et al. (2003) showed that the distal flow presents an abnormal waveform. Abnormal common femoral waveform contours includes biphasic or monophasic waveforms. Biphasic waveform is characterised by sharp, tall, narrow systolic upstroke but absent reverse diastolic flow component, with continuous forward flow during diastole. A monophasic flow waveform is characterised by blunt, short, widened systolic upstroke and continuous forward flow during diastole (Fig. 2.2). The damping of the flow wave also increases with the severity of the disease (Cossman et al., 1989).

In the presence of a long arterial occlusion, blood flow in the distal arteries

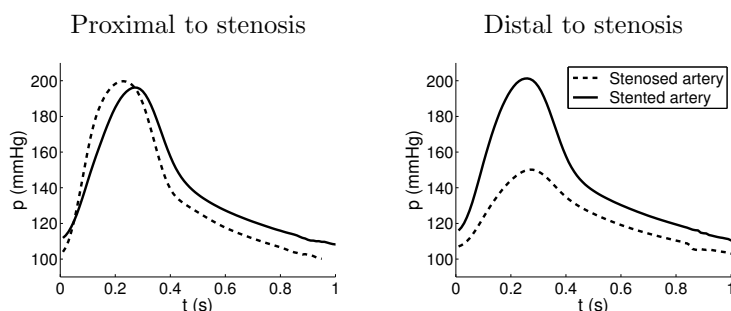


Figure 2.4 – Pressure proximal and distal to a stenosed superficial femoral artery, before (dashed line) and after (continuous line) stenting.

does not completely vanish. Blood flow of weak intensity is observed in distal arteries thanks to blood perfusion through collateral networks (e.g. distal of the deep femoral artery). Fig. 2.3 illustrates the velocity waveforms in the common femoral artery during the pre-operative state of a bypass surgery. Proximal to the occlusion, the velocity presents a biphasic waveform, which becomes monophasic distally.

2.2.4 Hemodynamics in bypassed lower-limb arteries

The insertion of a graft vessel in order to bypass the long arterial occlusion influences the waveforms. Whether the bypass graft is made of a synthetic material or of a patient's vein, the stiffness of this new vessel is usually greater than the stiffness of healthy arteries. As a result, propagating waves are reflected earlier and the pressure waveform presents a single systolic wave without diastolic fluctuation, similarly to what is observed proximal to an occlusion. Nevertheless, thanks to the new conduit, the pressure pulse is not damped anymore in the distal arteries (Fig. 2.3). Notice though, that a slight decrease of the pressure pulse is sometimes observed distally, probably as a result of the mismatch compliance induced by the insertion of the graft.

The graft vessel modifies the peripheral arterial network of the leg by reducing the load on the collateral network responsible for blood perfusion. Thanks to this decrease in resistance, mean blood flow is increased through the upper leg. The distal run-off flow is also increased: it reaches values at least greater than 50 ml/min , as required by literature advices for limiting the risk of early graft failure (Stirnemann et al., 1994). A few days after the bypass surgery, the flow waves in the upper- and lower-leg present a triphasic contour with reversed flow and diastolic waves, representative of normal (non-occluded) arteries.

After bypass surgery, the waves observed in the lower-limb do not present the characteristics of an occluded network anymore, though they still differ

from waves in healthy leg arteries. See, for example, Fig. 5.2 in Chapter 5: it presents a comparison of pressure and velocity signals from a healthy subject and a subject treated with bypass surgery. Because of the increased wall stiffness, and thus increased velocity of propagation of waves, reflected waves arrive earlier. The pressure peak is observed earlier in systole and, unlike the healthy condition, we observe that peak pressure and peak flow occur nearly simultaneously.

2.2.5 Influence of the data acquisition protocol

Our choice of invasive data acquisition protocol implies that measurements are taken during surgery, while the patient is under general or local anaesthesia. One known consequence of the anaesthetic drug is vasodilatation (Robinson et al., 1997; Chang and Davis, 1993). The effects on pressure and flow wave contours of arteriolar vasodilatation in a vascular bed have been studied by intra-arterial injection of acetylcholine (O'Rourke and Taylor, 1966). They comprise a rise in mean flow, a disappearance of back flow and a change of inflow wave. The pressure wave shows less diastolic fluctuations (Nichols and O'Rourke, 2005). These changes are explained by decreased peripheral wave reflection.

Notice that, in surgical practice, these effects might be emphasized by injection of papaverine in order to further dilate the atherosclerosed vessels.

Comparison of the flow waveforms measured during bypass surgery and a few days before or after surgery (on an awake and resting patient) illustrate these observations (Fig. 2.5). The rise in mean velocity and, if we assume a constant cross-sectional area of the vessel, the rise in mean flow, is apparent on the measurements realized under anaesthesia, both before and after insertion of the bypass graft. Also, these waves do not present any back flow, while this characteristic is present on velocity waveforms measured on the arteries of an awake and resting patient.

2.3 Patient-specific parameters computation

We have shown in the previous section that the analysis of the pressure and velocity waveforms is a source of information about the condition of the patient. Additionally, by extracting some parameters from the curves, i.e. by describing the in-vivo curves with some indices, the patient can be further characterised.

One objective of this work is to validate results from a 1D-0D numerical model of the arterial hemodynamics, that simulates in particular the hemodynamics of bypassed lower-limbs from a specific patient. The patient-specific characterisation of the model is achieved through its model parameters, computed on basis of in-vivo measurements from the subject (e.g. the arterial diameter and elasticity, the length of arteries). Among those parameters, the vessel wall

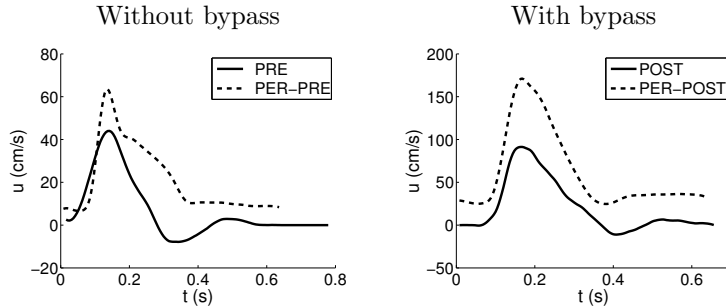


Figure 2.5 – Velocity waveforms in the common femoral artery of a leg without (left) and with (right) a bypass graft. Comparison between the per-operative state while the patient is under anaesthesia (PER-PRE/PER-POST, dashed line), and an awake and resting state a few days before or after surgery (PRE/POST, continuous line).

elasticity and the resistance and compliance of the distal arterial sub-system are not directly determined and need further computation. In this section, we describe different methods and algorithms that approximate their values and we focus on the influence of the pathological condition of the subjects analysed. We compare results from the different methods considered and interpret the physiological values.

Let us notice that, while the validation of the numerical model applies to a post-operative state (once the bypass graft is inserted in the leg), the computation of the patient-specific parameters can be performed on the pre-operative condition of the patient as well, as long as in-vivo measurements are available.

2.3.1 Vessel wall elasticity

The elasticity, or stiffness, of the vessel wall is a material property of the tissue and is described with the elastic Young's modulus E . If the wall thickness h is known, E can be computed directly using the pressure-diameter relation derived from Laplace's law (Eq. (A.10), Appendix A). With this method, E is assessed locally. Though this method requires the evaluation of the transmural pressure as well as a high level of precision in the diameter evaluation during a cardiac cycle. Another indirect approach consists of measuring the influence of the wall elasticity on the propagation of a wave in the vessel. The higher the stiffness of the vessel wall, the less the radial distension of the wall while the wave travels, and therefore the higher the wave speed. This behaviour is described with the Moens-Korteweg equation (Eq. (A.12), Appendix A), relating the pulse wave velocity (PWV), the elastic modulus, the blood density, the vessel diameter and the wall thickness.

In this work, we developed the PWV approach rather than the pressure-diameter relation. Thanks to its ease of application, PWV measurement has been largely developed and used in clinical practice in recent years (Laurent et al., 2006; Boutouyrie et al., 2009). Many epidemiological studies have characterised the arterial wall elasticity of different populations using the PWV (Laurent et al., 2001; Cruickshank et al., 2002). Here, the direct evaluation of the arterial elasticity was not considered due to practical concerns. In our partnership with the Cliniques Universitaires St-Luc, we did not have at our disposal high-precision ultrasound scanners to measure distension waveforms. Furthermore, as we are measuring calcified and atherosclerosed arteries (rigid arteries a priori), variations of the cross-sectional area might be strongly reduced and difficult to measure.

Different methods have been developed in order to measure the velocity of propagation of waves (Rabben et al., 2004; Feng and Khir, 2010; Horváth et al., 2010; Harada et al., 2002; Davies et al., 2006b). Considering our practical and technical limitations, we focused on studying and applying three of them. The most direct and common method in clinical practice is the foot-to-foot method. In the following, we discuss its practical application to our pathological subjects. The PU-loop and the single-point methods are derived from the 1D formulation of the blood flow equations and present the advantage to compute a local PWV.

As described in Section 1.2 of the Introduction, different types of vessels can be used as graft in femoro-popliteal bypasses: vessels made of synthetic materials (Gore-Tex[®] or Dacron[®]), a patient’s vein or an arterial homograft. In view of their different origins, these vessels should be associated with different material stiffnesses, and could differ from the elasticity of the surrounding arteries. In addition to the PWV approaches, we describe two other methods for the estimation of the bypass wall elasticity: a method based on in-vitro results for estimating the elasticity of synthetic materials, and a method based on the structural properties of venous conduits.

The foot-to-foot method

Waves generated by the heart propagate along the arterial tree. By estimating the time (Δt) it takes for a wave (pressure, distension or velocity wave) to travel a known distance apart between two arterial sites (ΔL), the PWV c between these two measurement sites can be computed as follows

$$c = \frac{\Delta L}{\Delta t}. \quad (2.1)$$

Fig. 2.6 illustrates the evaluation of the carotid-femoral PWV, the “gold standard” measurement of arterial stiffness in clinical practice. Measurements of the waves at the two sites can either be realized simultaneously, or recorded successively with both signals being synchronised with the same time basis (the ECG R wave).

It is generally accepted that the time delay Δt should be calculated from the foot or early upslope of the wave rather than its systolic part. Indeed, the systolic peak is altered by wave reflections and the arterial stiffness increases non-linearly with blood pressure. The foot of the wave is defined at the end of diastole, when the steep rise of the wavefront begins and should be identified by automatic algorithms in order to avoid imprecisions (Millasseau et al., 2005).

The distance between the two sites ΔL represents an estimation of the pathway of the waves and can be evaluated using different methods (Vermeersch et al., 2009a). If the arterial pulse moves in opposite ways (such as from the sternal notch to the carotid and to the femoral), the computation of ΔL should be obtained by subtracting pathway distances in opposite directions.

Different pulse waves have been used in practice to assess the PWV: pressure waves, distension waves and velocity waves. Although these waves are different in nature, they are theoretically in phase at the beginning of the cardiac cycle, so could be used alternatively.

The most often used signal in clinical practice is the pressure wave. Different devices based on the acquisition of this signal are commercially available. For example, the Complior System[®] (Artech, Les Lilas, France) uses two mechanotransducer probes simultaneously; while the Sphygmocor[®] (ArtCor, Sydney, Australia) uses a single high-fidelity applanation tonometer (a large band piezoelectric probe) with ECG synchronisation. Both of these devices require the application of a pressure transducer and are therefore limited to superficial arteries, such as the common carotid, common femoral or radial arteries. While these methods are well accepted for carotid-femoral PWV measurement (Asmar et al., 1995; Wilkinson et al., 1998), they present some limitations. The femoral pressure waveform may be difficult to record accurately in patients with peripheral arterial disease (Van Bortel et al., 2002): in the presence of stenoses, the pressure signal may be attenuated and delayed; in calcified arteries, the pressure signal may be too weak and non-pulsatile. Within the framework of the NHEMO project, we tested these two devices on calcified, occluded and bypassed lower-limb arteries and met the problems described hereover.

PWV can also be measured using distension waveforms, acquired using high-definition echotracking devices. Some devices have been commercialized (Art.Lab[®] (Esaote, Maastricht, The Netherlands), WallTrack[®] (Pie Medical, Maastricht, The Netherlands)) and used in clinical studies (Hoeks et al., 1990; Brands et al., 1998; Pannier et al., 2002). This type of measurement does not present technical limitations and could be applied to pathological lower-limb arteries. Though, this expensive equipment was not at our disposal within the framework of the NHEMO project.

Finally, PWV can be measured using the sharp systolic upstroke from velocity waveforms acquired with Doppler ultrasound techniques (Wright et al., 1990). Even if this technique presents some imprecision in the exact location of the measurement, it presents the advantage to be applicable to all arteries.

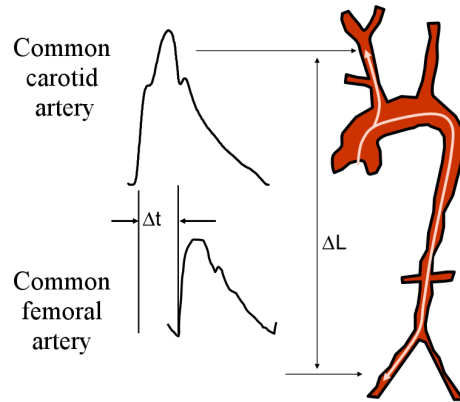


Figure 2.6 – Measurement of the carotid-femoral pulse wave velocity using the foot-to-foot method. From Boutouyrie et al. (2009).

With appropriate probes, velocity waveforms can be measured on deeper and calcified arteries, as well as on weakly pulsatile arteries. Furthermore, this type of equipment produces similar results than with the standard tonometry (Jiang et al., 2008) and is easily available in medical centers.

Therefore, we developed an application in Matlab[®] (MathWorks, Natick, USA) in order to compute the foot-to-foot PWV from velocity waveforms of peripheral atherosclerosed arteries. Velocity waveforms were measured with the B-mode colour Doppler ultrasound Philips iU22[®] (xMATRIX ultrasound system, Philips, Drachten, The Netherlands) and saved as DICOM images. Measurements were taken successively at two arterial sites, with synchronisation by the ECG R wave (Fig. 2.7). Arterial distance was measured directly on the patient's leg; this could introduce imprecisions in cases of arterial occlusions considering the complex arterial path through collaterals. The foot of the velocity waveform was determined manually using a mouse driven graphical interface. The algorithms for determining the foot of pressure waveforms were not always efficient when applied to velocity signals because of the shivering of the systolic increase, and small fluctuations in velocity contours. A manual selection might nevertheless induce a relatively important error if ΔL is small. On a leg for example, if $\Delta L = 30 \text{ cm}$ and the arterial wall elasticity is characterised by $c = 10 \text{ m/s}$, with a DICOM resolution of 250 Hz , a deviation of 1 pixel induces an error of about $\pm 1.5 \text{ m/s}$. For comparison, with an arterial length $\Delta L = 1 \text{ m}$, the deviation of PWV is reduced to $\pm 0.4 \text{ m/s}$. The distance between the measurement sites is limited in its lower bound by the need for higher temporal resolution.

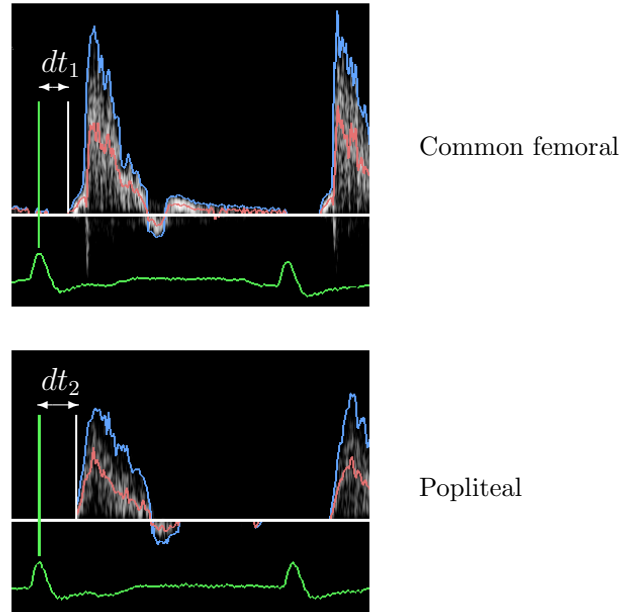


Figure 2.7 – PWV computation in the leg with the foot-to-foot method. Measurements of the delay between the ECG peak and the foot of the velocity waveform in two arteries of the leg (common femoral and popliteal). The PWV is then computed as $c = \Delta L / (dt_2 - dt_1)$, with ΔL the distance between the two arterial sites.

As the foot-to-foot PWV is an average wave speed for the entire arterial pathway traveled by the wave, this method does not allow to distinguish specifically the elasticities of arteries of different calibers, or the elasticities of vessels made of different materials. Therefore, the foot-to-foot method will not give an accurate estimation of the wave speed in the graft: for example, the femoral-popliteal PWV is calculated as an average of the wave speeds in the bypass graft and in the arterial segments above (the common femoral) and below (the popliteal) the bypass.

We used the foot-to-foot method to compare the central (carotid-femoral) PWV with the peripheral (femoral-distal) PWV in patients suffering from peripheral arterial disease (Lacroix et al., 2011). Our results showed that, in subjects with peripheral pathology, the central PWV can be used as a good estimator of the distal PWV.

The pressure-velocity loop method

The pressure-velocity loop (PU-loop) method allows the determination of the local wave speed (i.e. the wave speed at one arterial location) using simultaneous measurements of pressure and velocity (Khir et al., 2001b). The theoretical origin of this method is based on the solution of the one-dimensional equations for blood flow in elastic arteries using the method of characteristics (Parker and Jones, 1990). The mathematical background will be detailed in Section 3.1.3 of Chapter 3, we only recall the main results here.

The relationship between the changes in pressure and velocity across any wavefront is given by the water hammer equation:

$$dp_{f,b} = \pm \rho c du_{f,b} \quad (2.2)$$

where dp and du are the pressure and velocity variations during one sampling interval, and the f and b subscripts refer to their forward and backward components. When there are no backward waves, e.g. at the start of systole, the water hammer equation indicates that there is a linear relationship between the changes in pressure and velocity. Thus, in a plot of pressure versus velocity over a cardiac cycle, the part of the PU-loop at the start of the systole should be linear, with a slope equal to ρc (Fig. 2.8).

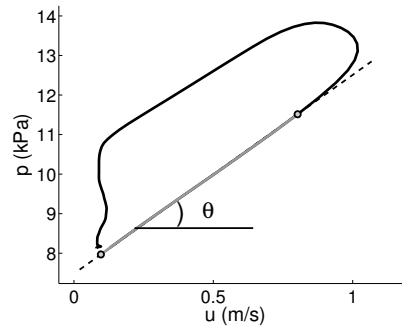


Figure 2.8 – Computation of the PWV with the PU-loop method: $\rho c = \tan(\theta)$, where θ is the angle of the linear part of the PU-loop at early systole (in grey).

The PU-loop method has been validated in-vitro (Khir and Parker, 2002) and in-vivo (Khir et al., 2004) with the foot-to-foot method and has been widely used to determine the PWV in various systemic arteries of healthy subjects (Zambanini et al., 2005) and in patients with cardiovascular diseases (Khir et al., 2001a; Curtis et al., 2007).

In order to obtain significant results with the PU-loop method, pressure and velocity need to be acquired simultaneously. During the bypass surgery of some patients though, pressure was measured a few minutes after velocity (non-simultaneous data acquisition protocol, see Section 2.1). Nevertheless, measurements were realized while the patient was under anaesthesia and in a stable hemodynamical state. Patients presented a constant heart rate during both measurements. We therefore assumed that these measurements might be considered for this analysis. In the case of non-simultaneous measurements, the alignment of pressure and velocity in time needs to be carefully adjusted in order to provide the optimal linear slope of the loop. This is also applicable to signals measured simultaneously since the response of pressure and velocity transducers might involve different delays. In order to resolve this time lag, we used the algorithm described by Swalen and Khir (2009): while shifting the velocity backwards and forwards in time steps equal to the sampling interval, the correlation factor between p and u at early systole is computed. The highest correlation factor indicates the optimal time shift between waveforms.

The value of the slope of the initial part of the PU-loop can be determined manually by eye. More objectively, this slope can be obtained using the algorithm of Khir et al. (2007). Starting from the start of systole, the deviation of the curve from linearity is computed. Until this value exceeds a defined threshold, the curve representing the systolic upstroke is increased by time steps. When the curve deviates from linearity, the slope is calculated between this last point and the begin of systole.

The single-point method

Derived from the theory of the wave intensity analysis, the single-point method allows the derivation of wave speed with simultaneous measurements of pressure and velocity at a single location (Davies et al., 2006b). It was initially introduced to measure the wave speed in the human coronary arteries, as none of the previous methods were suitable for these arteries. The foot-to-foot method can not be applied, considering the short length of these tortuous arteries. The PU-loop method is inefficient as well, as it requires unidirectional waves during part of the cycle. Because of the influence of the aortic and microcirculatory vessels creating multiple reflections and hemodynamic interactions, the coronaries do not present a single wave impulse. The linearity of the pressure-velocity relation is altered and this approach can not be used.

The single-point method derives the PWV by minimizing the net wave energies over a complete cardiac cycles. Following Davies et al. (2006b), the derivation of the method formula is based on the observation that the propagation of individual wave fronts is discrete, characterised by changes in pressure and velocity, with no summation of energy from one beat to the next. The idea is to find the wave speed that minimizes the total wave intensity over the cardiac cycle in order to reduce wave energy summation. The net wave energy is defined

as the sum of the absolute values of the forward (dI_f) and backward (dI_b) wave intensities, where the backward wave intensity is defined negative

$$\chi = \sum (\|dI_f\| + \|dI_b\|) = \sum (dI_f - dI_b) \quad (2.3)$$

and where the sum is taken over the sampling intervals of the cardiac cycle. The background of the wave intensity analysis (WIA) will be detailed further on in Chapter 5. By deriving the expressions for dI_f and dI_b from the forward and backward pressure and velocity components

$$dI_f = dp_f du_f \quad dI_b = dp_b du_b \quad (2.4)$$

and by substituting definitions of $dp_{f,b}$ and $du_{f,b}$ as a function of dp and du (see Eqs. (3.23) and (3.24) from Chapter 3)

$$dI_f = \frac{\rho c}{4} \left(du + \frac{dp}{\rho c} \right)^2 \quad dI_b = -\frac{\rho c}{4} \left(du - \frac{dp}{\rho c} \right)^2, \quad (2.5)$$

χ can be written in terms of the changes in pressure and velocity:

$$\chi = \frac{\sum (dp)^2}{2 \rho c} + \frac{\rho c \sum (du)^2}{2}. \quad (2.6)$$

The minimization of χ as a function of ρc requires $\frac{d\chi}{d(\rho c)} = 0$, i.e.

$$-\frac{\sum (dp)^2}{2 (\rho c)^2} + \frac{\sum (du)^2}{2} = 0 \quad (2.7)$$

which simplifies to:

$$c = \frac{1}{\rho} \sqrt{\frac{\sum (dp)^2}{\sum (du)^2}} \quad (2.8)$$

This method also requires simultaneous measurements of p and u but, on the opposite to the PU-loop, it presents no restrictions about the wave travel direction. In their study, Davies et al. (2006b) obtain a good correlation for the aortic PWV measured with the foot-to-foot method and with the single-point method. Though, to our knowledge, this method has not been applied to pulse wave velocity evaluation in other long systemic arteries. Notice that this method has been criticized for its application in the coronary arteries: according to Kolyva et al. (2008), due to the short length of the arteries, it yields erroneous predictions of changes of the local wave speed induced by a proximal stenosis and distal vasodilation.

In-vitro compliance of synthetic bypass materials

Besides PU-loop and single-point methods, the characterisation of the prosthetic vessels can also be performed using in-vitro experimental results. In Daniele et al. (2003), samples of different synthetic bypass materials were subjected to dynamic cyclic vessel loading under physiological pressure with measurement of diameter variations. The radial compliance $C_R = \frac{\Delta r}{\Delta p}$ was estimated, with Δr the changes in the vessel radius. Table 2.4 presents the values of C_R/r measured within the pressure interval of 80-120 *mmHg* in some commercial grafts tested in the study. Notice that these in-vitro results fluctuate significantly with the pressure interval considered, the cyclic loading, and the dimension of the graft.

Model	Material	Type	D [<i>mm</i>]	C_R/r [<i>mmHg</i> ⁻¹]	c [<i>m/s</i>]
Intervascular	PTFE	Ultrathin	6	$3.440e-4$	13.6
Gore	PTFE	Extensible	6	$0.579e-4$	33.1
Sorin Carbograft	PET	Knitted	6	$2.510e-4$	15.9
Bard soft woven	PET	Woven	6	$2.314e-4$	16.6
Bard soft woven	PET	Woven	8	$1.685e-4$	19.4

Table 2.4 – Radial compliance C_R/r , pulse wave velocity c and properties of some commercial bypass grafts. D is the vessel diameter, PTFE stands for polytetrafluoroethylene (Gore-Tex[®]), PET for polyethylene terephthalate (polyester or Dacron[®]). Data for the Intervascular graft (first line) courtesy of the Datascope Intervascular society (now Maquet Getinge Group). Data for Gore, Sorin and Bard (lines 2-5), published in Daniele et al. (2003), are measured in-vitro within a pressure interval of 80 to 120 *mmHg*.

By using the Bramwell-Hill equation (Eq. (A.13) of Appendix A), the PWV can be related to the vessel area compliance $C_A = \Delta A/\Delta p$ and thus to the radial compliance C_R :

$$c = \sqrt{\frac{A}{\rho C_A}} = \sqrt{\frac{A \Delta p}{\rho \Delta A}} = \sqrt{\frac{\pi r^2 \Delta p}{\rho 2\pi r \Delta r}} = \sqrt{\frac{r}{2\rho C_R}}. \quad (2.9)$$

This in-vitro study gives an estimation of the order of magnitude of the PWV in the prosthetic bypasses: for 6 *mm* diameter grafts, the PWV varies from 13 to 33 *m/s*, depending on the synthetic material considered.

Within the framework of the NHEMO project, surgeons at Cliniques Universitaires St-Luc use PTFE grafts from Gore and Vascutek, and PET grafts from Intervascular and Vascutek.

Properties of venous bypasses

A comparison of the arterial and venous elasticities can be performed on basis of the properties of veins. Considering that the vein used as bypass graft should be affected by the disease similarly than the native artery, a relation between venous and arterial wave speeds can be established on basis of the following observations obtained during in-vitro experiments (Pukacki et al., 2000). (1) The elastic modulus E of the venous wall is about twice the elastic modulus of the arterial wall: $E_v \simeq 2 E_a$. (2) The wall thickness h of the vein is about half the wall thickness of arteries: $h_v \simeq \frac{1}{2} h_a$.

Using the Moens-Korteweg relation (Eq. (A.12) in Appendix A, with σ the Poisson's ratio), the PWV of the vein (c_v) can be related to the PWV of the surrounding arteries (c_a) and to the ratio of arterial to venous diameters:

$$c_v = \sqrt{\frac{h_v E_v}{D_v \rho (1 - \sigma^2)}} \simeq \sqrt{\frac{1}{D_v} \frac{h_a}{2} \frac{2 E_a}{\rho (1 - \sigma^2)}} = \sqrt{\frac{D_a}{D_v}} c_a . \quad (2.10)$$

This formulation is established from in-vitro observations, while the venous bypass is not inserted in the surrounding tissues of the leg. We assume that they are still valid when measurements are performed during surgery, after insertion of the vein in the patient's leg. Furthermore, it is assumed that the Poisson's ratios of venous and arterial tissues are similar, i.e. that these tissues present a similar behaviour under deformation. In view of these hypotheses, the relation (2.10) should be carefully considered, as an evaluator of the relation between PWV in veins and arteries.

It should be noticed that after insertion in the leg as arterial bypass, the venous tissue will undergo structure modification for a few weeks after surgery. When inserted into the high-pressure, high-flow environment of the arterial system, the vein adapts itself such that the thickening of the venous graft wall increases until its ratio to the vessel diameter h/D reaches the ratio observed in the arteries (Wilson et al., 2003): $\frac{h_v}{D_v} \simeq \frac{h_a}{D_a}$. Notice that the previous relation simplifies then to $c_v = \sqrt{2} c_a$.

Comparison of methods

Bland and Altman (1986) showed that in order to assess the agreement between two methods of clinical measurement, the use of correlation is misleading. Even if this technique is still often used in the literature, this statistical operator is inappropriate as it measures the strength of a relation between two variables, not the agreement between them. Results should instead be plotted against each other with the identity line; and in a Bland-Altman plot. This last plot presents the difference between the methods against their mean. It allows to assess between-method differences and to investigate any possible relationship between the measurement errors and the true value (Bland and Altman,

1986). It also includes the 95 % confidence interval for a normal distribution, $[\mu - 2SD; \mu + 2SD]$, where μ is the mean of the differences, and SD its standard deviation. The relative difference between two methods can also be calculated as the mean ratio of the difference to the average of both results.

– *PU-loop versus foot-to-foot*

Because the foot-to-foot method is computed along an arterial path, there is only one value of PWV that can be compared along the leg with the PU-loop method. We only have here 14 measurements at our disposal. For this comparison, the PU-loop value was computed as an average value of wave speeds in the leg vessels, weighted by the length of the vessel. Fig. 2.9 presents these results. We observe some correspondence between results at low wave speeds and dispersion at higher wave speeds. The relative difference of the foot-to-foot PWV minus the PU-loop PWV is equal to 12.3% so that the foot-to-foot method overestimates the PU-loop method. This observation is similar to results of Khir et al. (2004) in the ascending aorta: the wave speed measured by the foot-to-foot method is systematically higher than the wave speed determined by the PU-loop, though results were much closer in that study. The dispersion of our results can be explained as follows. Measurements at the base of both methods are not realized at the same time: for the PU-loop, pressure and velocity are realized during surgery, while for the foot-to-foot method, DICOM images are taken a few days before or after surgery. Variations of the central pressure and condition of the patient might influence the results. Furthermore, the distance between the common femoral and popliteal or tibial arteries is rather limited (about 60 cm), which reduces the accuracy of the foot-to-foot measurement.

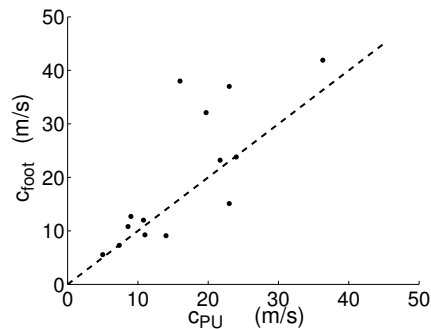


Figure 2.9 – Comparison of wave speeds derived by PU-loop (c_{PU}) and foot-to-foot (c_{foot}) methods in the upper leg. Plot of results from both methods with line of identity (dashed line).

– *PU-loop versus single-point*

Fig. 2.10 presents the comparison between the single-point (c_{SP}) and PU-loop (c_{PU}) methods for the computation of the PWV in all lower-limb vessels analysed (i.e. arteries and bypasses), at different times during surgery (i.e. before and after insertion of the bypass). There is a general good agreement between the two methods and the relative difference is 7.5 % (single-point minus PU-loop). There is no obvious relation between the difference ($c_{SP} - c_{PU}$) and the mean $(c_{SP} + c_{PU})/2$ of the two methods (Fig. 2.10, right).

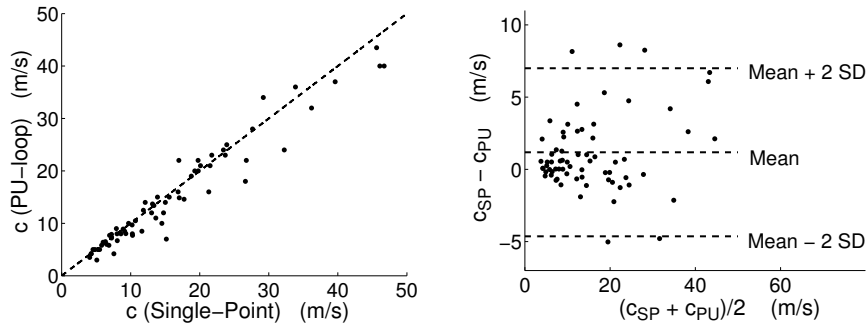


Figure 2.10 – Comparison of lower-limb wave speeds derived by PU-loop (c_{PU}) and single-point (c_{SP}) methods. Plot of results from both methods with line of identity (dashed line) (left) and Bland-Altman plot (right).

Because the single-point method has not been much discussed for large systemic arteries, we also mention here the results from a numerical comparison of methods. The PU-loop and the single-point methods (as well as other methods for estimating the local PWV not considered in this work) have been compared by using a one-dimensional numerical model (Alastruey, 2011). While the theoretical values of the PWV along the arterial tree are calculated from the model parameters, estimations of the wave speeds are obtained by applying the different techniques to the numerically generated pressure and velocity waveforms at different arterial locations. The results show that, in comparison with the single-point method, estimates of the PWV given by the loop methods were closer to the theoretical values and more uniform within each arterial segment.

On basis of this analysis and our results, we will use preferably the PU-loop for evaluating the vessel elasticity.

– *Synthetic bypass stiffness*

Amongst the previous PWV methods, the foot-to-foot will not be considered for estimating the stiffness of bypass vessels. The PU-loop method estimates a local PWV; therefore it can be applied to the bypass vessel,

whatever the graft material. As the analysis of the single-point method showed a good correspondence with the PU-loop, we will only retain the PU-loop result.

Fig. 2.11 presents the values of measured PWV in prosthetic bypasses, as a function of the pressure in the vessel. From our few observations, we see that within the same pressure range, the PWV in the Dacron bypasses seems to be higher than in the Gore-Tex bypasses. Furthermore, the PWV is positively related to the blood pressure, as was shown by the Bramwell-Hill equation (Eq. (A.13), Appendix A) and the study of Avolio et al. (1983).

Our results lie within the range of PWV values for synthetic bypasses suggested by the in-vitro approximation. Because the PU-loop considers the synthetic vessel in its tissue and muscle environment and takes into account the physiological condition of the patient, we will consider these results in the rest of this work.

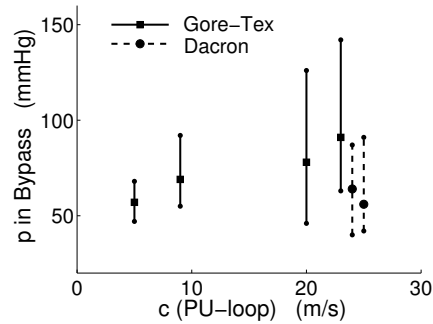


Figure 2.11 – PWV in prosthetic Gore-Tex[®] and Dacron[®] bypasses as a function of the pressure in the bypass. Each vertical line represent the range of the pressure in the bypass (diastolic to systolic pressures; the mean pressure symbolized by a square or circle).

– *Venous bypass stiffness*

Our theoretical estimation of the venous bypass stiffness could only be tested on two patients operated with in-situ venous bypass. We used arterial data from the common femoral artery because vessels are close in the leg morphology. Using Eq. (2.10), the approximation produced a reasonable approximation in the first case (Table 2.5). Similarly than in prosthetic bypasses, results from the PU-loop will be considered in the continuation of this work.

Patient #		Artery	Vein
16	D (mm)	0.81	0.37
	c_{PU} (m/s)	8.5	11.0
	c_v (m/s)		12.6
19	D (mm)	0.615	0.43
	c_{PU} (m/s)	5.8	15.0
	c_v (m/s)		7.0

Table 2.5 – Estimation of the PWV of in-situ venous bypasses

Interpretation of physiological results

Values of wave speeds observed in the arteries of the leg are slightly higher than in healthy patients due to the presence of the pathology. For healthy leg arteries, the average PWV measured by foot-to-foot method is about 8.3 m/s (from femoral to dorsalis pedis arteries) (O’Rourke et al., 2002; Kingwell et al., 1997). In subjects with high prevalence of hypertension, the wave speed is about 12 m/s (O’Rourke et al., 2002; Avolio et al., 1985). In our data about pathological leg arteries, we observe PWV values from 10 to 16 m/s (Table 2.6). These values correspond well with observations from literature.

We also observe an increase of wave speeds along the leg of the patients, because of the reduction in arterial caliber (cfr Moens-Korteweg Eq. (A.12), Appendix A). Measurements in the deep femoral artery present a larger deviation than in other arteries. We suppose that this is due to less accurate measurements because of their less accessible location in the thigh.

As expected, PWV in bypasses is larger than in arteries of similar diameter; this observation is further emphasized for synthetic grafts.

In the four patients with measurements before and after bypass suture, we observe a decrease of the pulse wave velocity from the pre-operative to the post-operative state in the common femoral artery ($\bar{\Delta}c_{PRE-POST} \simeq 4.8$ m/s). The

Vessel	\bar{c} (m/s)	\bar{D} (mm)
Common femoral	8.5 ± 4.6	7.0 ± 1.0
Deep femoral	16.9 ± 13.3	4.6 ± 0.8
Popliteal	14.6 ± 10.8	4.2 ± 1.2
Synthetic Bypass	17.7 ± 8.5	5.9 ± 0.7
Venous Bypass	13.0 ± 2.8	4.0 ± 0.5

Table 2.6 – Mean values \pm SD of the post-operative PWV c (measured with the PU-loop) and of the diameter D in the vessels of bypassed legs.

opposite variation is observed in the popliteal ($\bar{\Delta}_{C_{PRE-POST}} \simeq -9.6 \text{ m/s}$); the low PWV observed in these distal arteries before surgery is probably due to the reduced flow, downstream of the occlusion. These observations are based on a very reduced number of patients and should need to be further studied in order to draw any further conclusion.

Values of all parameters for all patients can be found in Appendix B.

2.3.2 Distal arterial sub-network

Our leg model focuses on the arteries from the upper-leg, from the femoral to the popliteal arteries: these arteries are modeled as 1D segments and are characterised. This is not the case for distal sub-networks composed of smaller arteries (e.g. peroneal artery, plantar arch, perforating arteries in the thigh), arterioles, collaterals and the venous system. Even though, their influence on the 1D hemodynamics need to be taken into account. This is done through lumped models. In our model of the upper-leg, we will consider two distal sub-systems: the network distal to the popliteal artery, including the lower-leg and the foot, as well as the network distal to the deep femoral artery, embedded into the thigh. The behavior of each of them is modeled at its entrance with a three-element windkessel model, composed of resistive and compliant elements (Fig. 2.12). The mathematical modeling of this windkessel model will be derived and described in details in Section 3.3.2, Chapter 3.

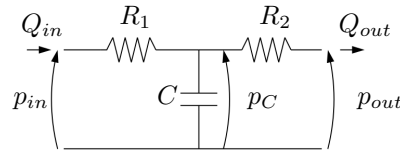


Figure 2.12 – The three-element windkessel model, with its two resistances R_1 and R_2 and its compliance C . At the entrance of the model, the pressure (p_{in}) and flow rate (Q_{in}) correspond to the pressure and flow in the adjacent 1D arterial segment. p_C is the pressure across C . At the outlet of the windkessel model, p_{out} and Q_{out} characterise the venous circulation.

Several methods have been proposed in order to compute the value of the two parameters of a distal peripheral network, namely the total resistance R ($R = R_1 + R_2$) and compliance C . Considering the limitations of our data acquisition protocol (mainly, we do not have distension waveforms at our disposal), we applied the following three methods to our data: exponential fitting, area method and windkessel ODE.

Exponential fitting

Because the windkessel model can be seen as an electrical circuit, the value of the total resistance of the vascular bed can be evaluated by using the hemodynamical analogy of Ohm's law:

$$R = \frac{\bar{p}_{in} - p_{out}}{\bar{Q}_{in}}, \quad (2.11)$$

where \bar{p}_{in} and \bar{Q}_{in} are respectively the mean pressure and mean flow over the cardiac cycle at the entrance of the windkessel. p_{out} is the venous pressure and its value is fixed to 20 *mmHg* for all peripheral outlets (Marieb, 2005; Alastruey et al., 2008).

As observed by Otto Frank (1920), when flow is zero during diastole, the pressure decay can be described by an exponential curve of time constant τ . τ is defined as the product of the peripheral resistance and the total arterial compliance: $\tau = RC$. The larger the resistance, the slower the blood leaves the system, and the longer the time constant is. Also, the larger the compliance the more blood is stored, and the longer the time constant is. Knowing R and τ , the compliance C can then be deduced.

In practice, the exponential fitting is applied on the last two third of diastole. τ is calculated by minimizing the sum of the squares of the following difference (obtained as the solution of the ODE describing a 2-element RC windkessel):

$$\left(p(t) - p_{out} \right) - \left((p^* - p_{out}) \exp\left(\frac{-(t - t^*)}{\tau}\right) \right) \quad \text{with } t \in [t^* : t_{end}], \quad (2.12)$$

with t^* and p^* the time and pressure at one third of diastole (Fig. 2.13).

Area method

In this method, the decay time τ is computed as the area under the diastolic pressure, divided by the pressure difference between the start (t_1) and endpoint (t_2) of the decay (Liu et al., 1986):

$$\tau = \int_{t_1}^{t_2} \frac{p}{p(t_1) - p(t_2)} dt. \quad (2.13)$$

The start of the decay is taken at one third of diastole: $t_1 = t^*$ (Fig. 2.13).

The resistance is also calculated as the ratio of the mean pressure and mean flow; the compliance is then $C = \tau/R$.

Winkessel ODE

The following method calculates the optimal values of the parameters of the 3-element windkessel model from its governing ODE and by using the complete

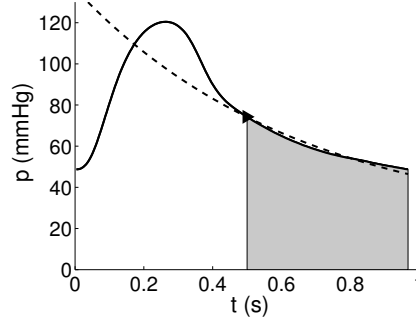


Figure 2.13 – Illustration of the exponential fitting method and the area method on a pressure curve. The exponential fit is in dashed line. The area under the diastolic pressure is in grey. The triangle represents the pressure at one third of diastole.

profiles of flow and pressure measurements (Toorop et al., 1987; Stergiopoulos et al., 1995).

The ordinary differential equation of the 3-element windkessel will be derived in Section 3.3.2. We neglect here the output pressure p_{out} .

$$p_{in} + R_2 C \frac{dp_{in}}{dt} = (R_1 + R_2) Q_{in} + R_1 R_2 C \frac{dQ_{in}}{dt} \quad (2.14)$$

By approximating the derivatives using forward finite differences of first order, the equation can be written in terms of $Q_{in}(t)$, $Q_{in}(t + \Delta t)$, $p_{in}(t)$ and $p_{in}(t + \Delta t)$:

$$Q_{in}(t + \Delta t) + Q_{in}(t) \underbrace{\left(\frac{(R_1 + R_2) \Delta t - 1}{C R_1 R_2} \right)}_{a_1} = p_{in}(t + \Delta t) \underbrace{\frac{1}{R_1}}_{b_1} + p_{in}(t) \underbrace{\left(\frac{\Delta t}{C R_1 R_2} - \frac{1}{R_1} \right)}_{b_2}. \quad (2.15)$$

In order to obtain $R = R_1 + R_2$ and C , the parameters a_1 , b_1 and b_2 need to be determined. Knowing the flow profile, the idea is to estimate the best pressure curve governed by the equation

$$p_{in}(t + \Delta t) = -p_{in}(t) \frac{b_2}{b_1} + \frac{1}{b_1} Q_{in}(t + \Delta t) + \frac{a_1}{b_1} Q_{in}(t). \quad (2.16)$$

The optimal estimation is obtained by minimizing the difference between the measured and the estimated pressure profile using least squares. In Matlab, this function is implemented using ARX models.

In order to assess the accuracy of the estimation, the measured pressure curve can be plotted against its estimate. Similarly, an estimated flow curve can be obtained from the estimate of pressure and compared with the measured one.

Comparison of methods

Similarly to the PWV analysis, we will use the Brand-Altman analysis for comparing methods two by two. Additionally, when a linear relation can be drawn between the two sets of data, we will assess the strength of the linear relation between them by using a Pearson product-moment correlation coefficient r . A P-value < 0.001 is taken statistically significant.

The comparison of methods is assessed for the three methods on 11 patients, at 2 arterial sub-network in pre- and post-operative states (when available), i.e. 3 sets of 32 points.

– Exponential versus area methods

In Fig. 2.14, the exponential fitting method is compared to the area method for the computation of the time delay τ : there is a significant linear regression of equation $\tau_{area} = 1.71 \tau_{exp} - 0.063$ between the two sets of data ($r = 0.71$, $P < 0.005$). The area method overestimates the exponential fitting method. Notice that, as the resistance is computed similarly for both methods, this relation only affects the compliance derivation.

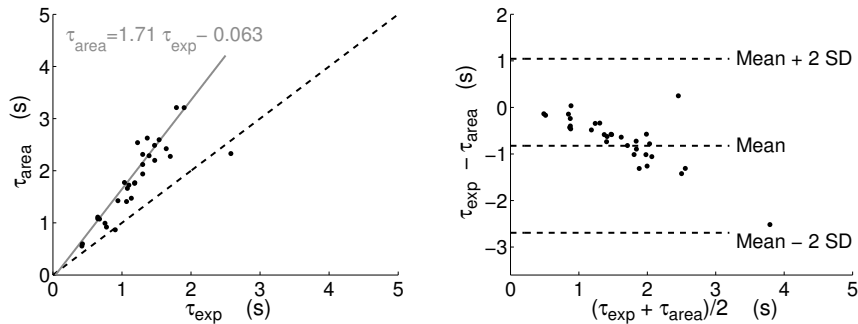


Figure 2.14 – Comparison of values of τ between the exponential method (τ_{exp}) and the area method (τ_{area}). Left: a linear regression can be found between the two evaluations of τ ($\tau_{area} = 1.71 \tau_{exp} - 0.063$) (grey line), with a correlation coefficient $r = 0.71$ ($P < 0.005$). The line of identity is in dashed black. Right: Bland-Altman plot.

Our observations differ from the conclusions of Stergiopoulos et al. (1995). Their study used results from a numerical 1D model and compared the total arterial compliances computed using different methods. Unlike our

observations, they observe that the exponential and area methods yielded similar results, accurate within 10% of the exact value. They also pointed out that these methods are sensitive to the choice of the diastolic period.

– *Exponential versus ODE methods*

In Fig. 2.15, the exponential fitting method is compared to the ODE windkessel method for the computation of the time delay τ . There does not seem to have a direct relation between both variables. Though, the Bland-Altman plot shows that the exponential fitting method seems to slightly overestimate the ODE method. Interestingly, the resistance estimated with the ODE method is strongly correlated by a linear regression to the resistance estimated as the ratio of means (R_{mean} , Eq. (2.11)): $R_{ODE} = 1.41 R_{mean} - 258$ ($r = 0.993$ $P < 0.005$). The resistance obtained with the ODE method overestimates R_{mean} . Therefore, it is the evaluation of C that introduces scatter in the comparison of τ (Fig. 2.16). In the study of Stergiopoulos et al. (1995), the ODE method is also used to compute the total arterial compliance: their results indicate that the ODE method tend to strongly overestimate the compliance of the model (in comparison with the exact numerical value), though they do not compare it with the exponential fitting method.

Because of its ease of application and coherence of results, the resistance and compliance of the arterial network will be estimated in the following of this work using the exponential fitting method.

Interpretation of physiological results

Table 2.7 presents average values of resistances and compliances measured in the two peripheral networks distal to the deep femoral and popliteal arteries in bypassed legs. When analysing results from each patient individually, there is no clear relation between parameters R and C of these two networks.

These values can be compared with observations from literature. Compliance in patients with peripheral arterial occlusive disease (PAOD) was found to be about 0.023 ± 0.012 $ml/mmHg = 1.73 \pm 0.9 e5$ $cm^4 g^{-1} s^2$ in the distal circulation (Duprez et al., 2001), which is of the same order than our observations. Furthermore, they observed that the compliance was correlated with markers of severity of vascular disease (ABI, pulse pressure). Notice also that the compliance in large arteries is greater than the compliance of the distal circulation, and that compliance is reduced with hypertension (Duprez et al., 2001; Simon et al., 1979).

Resistances and compliances of a healthy subject have also been estimated in Stergiopoulos et al. (1992) where a complete arterial tree composed of 55 arteries is simulated with a 1D model. The resistance and compliance distally to the deep femoral are given in Table 2.7. We estimated R and C distally to the popliteal artery from the anterior and posterior tibial values. The average resis-

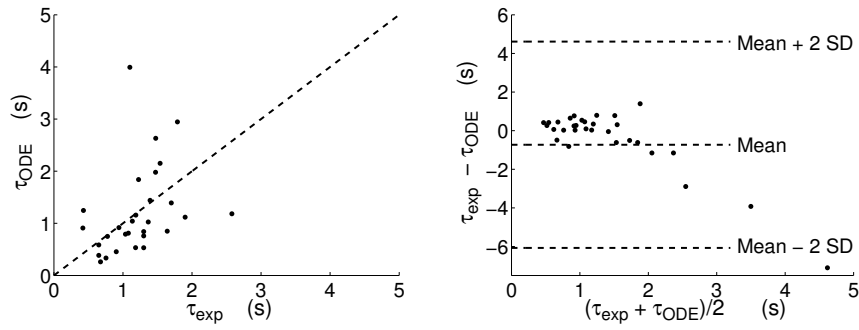


Figure 2.15 – Comparison of values of τ between the exponential method (τ_{exp}) and the windkessel ODE method (τ_{ODE}). Plot of results from both methods with line of identity (dashed line) (left) and Bland-Altman plot (right).

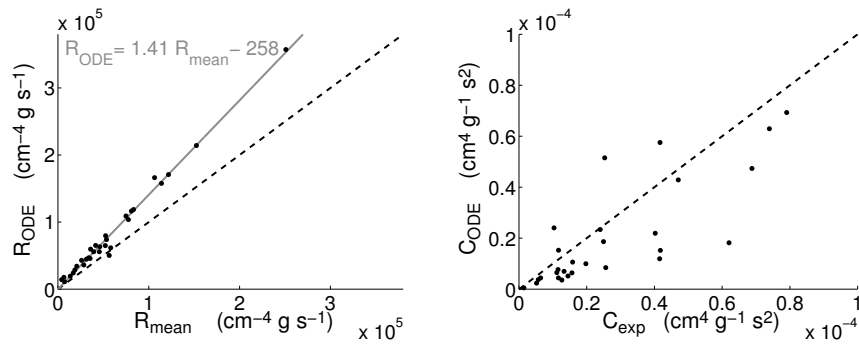


Figure 2.16 – Comparison of values of R (left) and C (right) computed by the exponential method (R_{mean} , C_{exp}) and the windkessel ODE method (R_{ODE} , C_{ODE}). Plot of results from both methods with line of identity (dashed line). Left: a linear regression can be found for the two evaluations of R ($R_{ODE} = 1.41 R_{mean} - 258$) (grey line) with a correlation coefficient $r = 0.993$ ($P < 0.005$).

tance observed in bypassed legs is slightly larger than the value representative of a healthy state. This observation seems coherent considering the pathological distal network of our old subjects. The increase in peripheral resistance results from vascular rarefaction and decrease in arterial cross-sectional area. On the opposite, results for the compliance are unexpected: we observe that the compliance of bypassed arteries is largely higher than data from Stergiopoulos et al. (1992). Notice that these values result from indirect estimations and approximations; they might be inaccurate and their comparison should be considered with caution. These discrepancies in observations support our approach of computing parameters on a patient-specific basis.

We have too few accurate data at our disposal to evaluate the relation between pre-operative and post-operative conditions. It seems though that the resistance of the peripheral networks increases after bypass surgery, while the compliance decreases with the insertion of the bypass (Fig. 2.17). Notice that these few results are opposed to our expectations: i.e. an improvement of the peripheral vascular system with the insertion of the bypass (reduced peripheral resistance and increased arterial compliance). In the distal popliteal artery, this increase of R might result from a proportionally more important increase of pressure than increase of flow ($R = \frac{p \uparrow}{Q \uparrow}$). Indeed, we have seen in Section 2.2.3 that flow increases thanks to the bypass surgery, though this increase is limited to 20 to 50%. In distal arteries, pressure is very damped, nearly unpulsated; the introduction of the bypass increases pressure back to a healthy value (more than 100% increase). Because of the damped popliteal signal, the ratio p/Q might therefore result in an increase of R . Compliance might decrease as a result of the increase of resistance, under the assumption that the exponential pressure decay remains nearly identical. Notice that τ increases to the most of 40% in damped pressure signals.

All values of parameters for all patients are listed in Appendix B.

	Bypassed arteries	PAOD	Stergiopulos (1992)
R ($10^4 \text{ cm}^{-4} \text{ g s}^{-1}$)			
Deep femoral	6.4 ± 3.1	-	4.77
Popliteal	5.0 ± 2.8	-	2.57
C ($10^{-5} \text{ cm}^4 \text{ g}^{-1} \text{ s}^2$)			
Deep femoral	1.7 ± 0.7	1.73 ± 0.9	0.39
Popliteal	2.6 ± 1.6		0.72

Table 2.7 – Mean values \pm standard deviation of the post-operative resistance R and compliance C of distal networks. Comparison with values of a subject with peripheral arterial occlusive disease (PAOD) (Duprez et al., 2001) and with values from Stergiopulos et al. (1992) representative of an healthy condition.

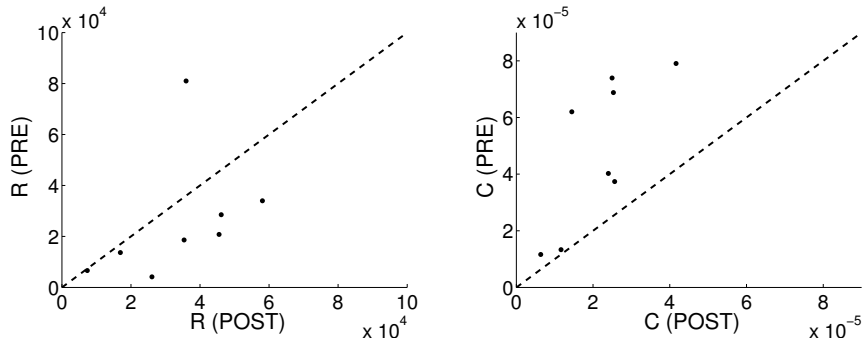


Figure 2.17 – Comparison between pre-operative and post-operative values of parameters R (left, in $(\text{cm}^{-4} \text{ g s}^{-1})$) and C (right, in $(\text{cm}^4 \text{ g}^{-1} \text{ s}^2)$) of peripheral networks of bypassed legs. Line of identity is represented (dashed line).

2.4 Bypass patency

This section aims at presenting the population analysed during this 4-year study. Table 2.8 gathers details about the bypass surgeries: surgery date, date of last check-up of the bypass of the patients, duration of the observation period, the status of the bypass at the last observation and the type of material used for the graft as well as the location of the distal anastomosis.

Table 2.8 also presents the evaluation of the criteria of early bypass failure for each patient, as presented in Subsection 1.2.3 of the Introduction. To recall, indicators of failure are low mean flow ($\bar{Q} < 50 \text{ ml/min}$), low peak systolic velocity ($PSV < 45 \text{ cm/s}$), low end-diastolic velocity ($EDV < 8 \text{ cm/s}$), and high peripheral vascular resistance ($PVR > 8.8e^4 \text{ cm}^{-4} \text{ g s}^{-1}$). Measurements are taken in the bypass graft, during bypass surgery or a few days after surgery, depending on the patient. PVR corresponds to the resistance of the peripheral network distal to the popliteal artery. Both PSV and EDV are measured on the maximum centerline velocity (i.e. the external envelope of the ultrasound spectrum).

On the 23 patients with available information, 4 patients have suffered from the occlusion of their bypass after one or two years, 16 patients still present patent lower-limb bypass and among them, 3 had dilatation of the distal anastomosis. Notice that these dilatation have all been performed on below-knee in-situ venous bypasses. As the observations about bypass patency are taken over short duration, shorter than the 4-year index, they are expected to be better than the patency statistics from the literature.

In most cases, the criteria of early failure are confident indicators of the current status of the bypass. In a few cases though, predictions are not met. For 4 subjects (#4, #17, #20, #21), while 2 or 3 criteria predicted early graft failure, the patients did not present occlusion of the bypass after 9 or 41 months. On the opposite, occlusion of patients #12 and #13 was observed after 13 and 11 months, though it was not markedly foreseen by the criteria (notice though that the PVR criteria were not available for these patients).

2.5 Conclusion

In this chapter, we have defined the protocol of data acquisition in the pathological arteries of our subjects. In the following, we have presented observations about the hemodynamics in bypassed lower-limb arteries. These observations have focused, in the first part, on the analysis of waveform contours, from a healthy condition to a bypassed one. In the second part, hemodynamics is described through some indices (PWV, peripheral resistance and compliance) extracted from the measured signals; methods of evaluation have furthermore been described in details.

In total, measurements have been performed on 25 patients. Notice though that only 9 of them presented accurate simultaneous pressure and velocity measurements necessary for the parameters computation. The following points summarize our observations.

- Pressure waveforms in bypassed lower-limb arteries are largely influenced by the increased vessel wall stiffness. Because of earlier arrival of reflected waves, the pressure waveform presents a single systolic wave with earlier peak, without diastolic fluctuations. Even if pressure in distal arteries might be slightly decreased in comparison with proximal vessels, the insertion of the bypass graft ensures a pulsed signal distally.
- Velocity waveforms in bypassed lower-limb arteries are less influenced than pressure. Thanks to the bypass vessel, velocity waveforms present triphasic contours representative of normal waveforms. Flow is distributed again towards distal arteries.
- Measurements that we will analyse in the major part of this work have been realized during surgery, under vasodilatation effects. This induces an increase of mean flow and disappearance of backflow.
- Pulse wave velocity in bypassed lower-limb arteries is increased in comparison with a healthy condition. Furthermore, we observe that PWV increases distally in the leg, as a result of arterial diameter diminution. PWV measured in the bypass graft is larger than in arteries; especially in synthetic grafts.
- In the pathological arteries of our subjects, the most accurate and efficient method for measuring PWV is the PU-loop. It allows PWV evaluation locally to the vessel of interest (artery or bypass graft) and presents great accuracy, even in presence of atherosclerosed vessels.
- Resistance and compliance of peripheral networks are easily and efficiently evaluated using ratio of means and exponential fitting methods. Because of the pathology, the peripheral compliance is reduced while the resistance is slightly increased.

Patent number	Surgery date	Check-up date	Duration	Bypass material	Anastomosis	Status	\bar{Q}	PSV	EDV	PVR
01	26/05/2008	07/2010	26	ISV	BK	Deceased	150	80	7	NA
02	11/06/2008	09/2011	40	GT8	AK	Patent	84	55	1.5	NA
03	25/03/2008	07/2011	40	ISV	BK	Patent	344	140	30	NA
04	26/03/2008	08/2011	41	GT8	AK	Patent	34	55	0	NA
05	31/08/2007	03/2011	43	RV	BK	Patent	131	100	19	NA
06	14/11/2008	08/2011	34	GT6	BK	Patent	446	80	14	NA
07	15/09/2008	06/2010	21	D6	AK	Occluded	107	40	0	NA
08	19/09/2008	03/2009	6	ISV	BK	Patent*	174	70	20	NA
09	16/01/2009	08/2011	31	ISV	BK	Patent*	196	70	20	NA
10	20/01/2009	06/2010	17	AH	AK	Deceased	444	145	17	NA
11	23/01/2009	06/2011	29	D8	AK	Occluded	223	35	7.0	NA
12	06/02/2009	03/2010	13	ISV	BK	Occluded	210	95	5	NA
13	23/02/2009	01/2010	11	ISV	BK	Occluded	103	105	20	NA
14	21/10/2009	07/2011	21	GT6	BK	Patent	585	114	18.5	$5.3e^4$
15	26/10/2009	10/2009	12	GT6	BK	Deceased	90	100	-2.3	$11.4e^4$
16	04/11/2009	07/2011	9	ISV	BK	Patent*	74	60	10	$3.13e^4$
17	23/12/2009	09/2011	9	GT6	BK	Patent	370	50	6	$25.1e^4$
18	21/12/2009	NA	NA	NA	AK	NA	NA	56	0	NA
19	07/01/2010	NA	NA	ISV	AK	NA	158	90	19	$3.9e^4$

Table 2.8 – Continued on next page

Patient number	Surgery date	Check-up date	Duration	Bypass material	Anastomosis	Status	\bar{Q}	PSV	EDV	PVR
20	08/02/2010	10/2011	9	GT6	BK	Patent	74	25	2	$1.34e^4$
21	16/11/2010	09/2011	10	D6	AK	Patent	63	40	-0.6	$3.6e^4$
22	24/11/2010	08/2011	9	GT6	AK	Patent	288	NA	NA	$5.2e^4$
23	13/12/2010	09/2011	10	GT6	AK	Patent	106	80	10	$4.6e^4$
24	29/06/2011	08/2011	2	D6	BK	Patent	92	44	9	$2.6e^4$
25	31/08/2011	10/2011	2	GT6	AK	Patent	334	100	15	$0.7e^4$

Table 2.8 – Characteristics of the bypass surgeries and evaluation of the medical criteria of early graft failure for our 25 patients. The first six columns describe the bypass interventions: patient number, surgery date, date of last check-up, duration of the observation period (in months), bypass graft material, location of the anastomosis. The status of the bypass at the last observation and the four medical criteria of early graft failure of bypass are then displayed: mean flow \bar{Q} (ml/min), peak systolic velocity PSV (cm/s), end diastolic velocity EDV (cm/s), peripheral vascular resistance PVR ($cm^{-4}g s^{-1}$). Criteria which indicate failure are in red. Notice that criteria for patients 1 to 13 and 18 are evaluated a few days after surgery, and, for the other patients, during surgery after bypass grafting. ISV: In-Situ Vein. RV: Reversed Vein. AH: Arterial Homograft. GT6/8: Gore-Tex 6/8 mm . D6/8: Dacron 6/8 mm . AK: Above-Knee. BK: Below-Knee. NA: Information not available. Patent*: Patent with dilatation of the distal anastomosis.

- Very few sets of data allow us to describe precisely the evolution of the parameters from the pre- to the post-operative states. We will limit this conclusion to the following general observations: with the insertion of the bypass graft, the rigidity and the peripheral compliance decrease while the peripheral resistance increases. Notice that these variations of the peripheral network are not reflecting an improvement of the distal vascular networks. They might be a result of the damped wave contour in the distal arteries. Additional studies should be carried on in order to confirm these findings.

Variations induced by the pathological condition of the subjects differ in magnitude from one subject to the other. This supports the need of determining parameters patient-specifically.

The uncertainty in assessing the evolution from the pre- to the post-operative conditions of the network parameters shows the current limitations of the predictive feature within the NHEMO project.

A coupled 1D-0D numerical model

Nowadays it is widely accepted that there is a strong correlation between local hemodynamics and the initiation and progression of arterial diseases (Nichols and O'Rourke, 2005; Ku, 1997). The human arterial system can be mathematically described with different levels of precision. From the detailed three-dimensional models (3D) to the efficient one-dimensional models (1D) or the simple lumped parameters models (0D), many applications have taken benefits from the efficiency of these models (see Section 1.4 of the Introduction).

In this work, we focus on the coupled 1D-0D models: simple, efficient and fast-computing, they give good global hemodynamical results in different parts of the human body. While one-dimensional equations of blood flow result from the integration of the Navier-Stokes equations along the length of the artery together with an elastic relation for the artery, lumped zero-dimensional models of the circulatory network are based on electrical analog of a hydraulic description of the system. These 1D-0D models have been widely used to efficiently simulate wave propagation in the arterial system.

Besides the dimension of the model, the efficiency of computational models is based on the quality of its inlet and outlet boundary conditions (BC). Those boundaries act as artificial interfaces with the remaining parts of the cardiovascular system which are not included in the model. They are particularly important when the simulation (either 3D, 2D, 1D or 0D) considers only a truncated arterial tree, which is the case for most of the patient-specific computations.

Outlet boundary conditions determine the way the distal network, not included in the model, influences the arterial model: their effect range from a com-

The content of this chapter is based on results published in: Willemet M., Lacroix V., Marchandise E., 2011. Inlet boundary conditions for blood flow simulations in truncated arterial networks. *Journal of Biomechanics*, **44**(5), 897-903.

plete absorption of the outgoing waves to their physiological reflection. These boundary conditions are well discussed in Olufsen (1999); Vignon-Clementel and Taylor (2004); Vignon-Clementel et al. (2006).

When defining the inlet BC, a classification depending on the geometry of the model may be realized. It can include the complete arterial tree (Stergiopoulos et al., 1992) or a network limited to some arteries, such as the arm (Balar et al., 1989), the leg (Raines et al., 1974) or the carotid artery (Zhao et al., 2000). In the model of the complete arterial tree, the inlet BC intends to reproduce the impulsion from the heart. It can be achieved by a simple model of the behavior of the aortic valve (Sherwin et al., 2003b; Matthys et al., 2007; Blanco et al., 2009), by a model of the ventricle (Mynard and Nithiarasu, 2008) or by a coupling with a lumped model of the heart (Reymond et al., 2009; Formaggia et al., 2006).

When modeling only a truncated arterial tree, the inlet boundary may be located at the heart, such as in Alastruey et al. (2007) where the cerebral circulation is modeled. This is not the case when the arteries of interest are peripheral to the heart: for example, in the modeling of the arm hemodynamics (Leguy et al., 2010; Alastruey et al., 2006), the inlet BC is located at the brachial artery.

Using this truncated geometry presents many advantages. It allows to focus on one particular site of interest ruled by complex mechanisms (e.g. circle of Willis (Alastruey et al., 2007)). When designing patient-specific models for clinical applications, it greatly reduces the number of parameters to be determined. It is also used, most of the time, in three-dimensional modeling, considering the high computational costs.

Nevertheless, as the upstream vessels are not included in the model, their effects need to be modeled with relevant boundary conditions. Indeed, the behavior of the waves at the artificial inlet completely differs from their behavior at the heart or at the aortic valve. Different mathematical tools have been developed in order to prescribe an absorption or reflection of the waves at the inlet BC (Thompson, 1987; Hedstrom, 1979; Sherwin et al., 2003a). They need to be used according to the physics of the problem. For example, prescribing a complete reflection of the inflow signal at the inlet of the truncated tree may lead to unphysiological high pressures.

Waves propagate in the arterial tree in the forward and backward directions (Parker and Jones, 1990). While forward waves result from the contraction of the ventricle and ejection in the aorta, backward waves are created by the reflection at the bifurcations, discontinuities and peripheral resistive networks. Once reflected, they interact with the forward waves to produce a total signal.

In this description of the numerical model, we put to the fore the importance of prescribing the forward component of the desired signal at the inlet BC of truncated models. In this way, the numerical model creates the artificial computed reflected waves that interact with the prescribed forward ones in

order to generate the desired physiological total signal. Mynard and Nithiarasu (2008) have used this kind of inlet boundary condition in the ventricle, at the inlet of a complete arterial tree. We show here that its application to the inlet of one-dimensional truncated models is effective and improves the correspondence between the computed and measured signals.

This chapter is divided in 5 sections. We firstly describe the mathematical one-dimensional model and some mathematical tools that allow a complete understanding of the prescription of inlet BC for 1D models. More precisely, the 1D equations of blood flow, the method of characteristics and the wave separation technique are recalled. The numerical resolution using the discontinuous Galerkin method is described in Section 3.2. Thereafter, a complete description of the inlet and outlet boundary conditions is performed (Section 3.3). In Section 3.4, we compare the application of different types of inlet BC using a truncated arterial tree and a patient-specific lower-limb model of a femoral bypass. We show that with this new boundary condition, a much better fitting is observed on the shape and intensity of the simulated pressure and velocity waves.

3.1 The mathematical model

Subsection 3.1.1 presents the one-dimensional model of the human arterial network, which is a system of non-linear partial differential equations. In order to present different inlet boundary conditions, we briefly recall the characteristic analysis of the 1D blood flow equations (Subsection 3.1.2). It shows that the solution of the system may be seen as the sum of forward and backward components of the waves, as detailed in the theory of wave separation in Subsection 3.1.3.

3.1.1 The one-dimensional model

The equations of arterial blood flow, derived by Euler in 1775 (Euler, 1775), consider an incompressible and Newtonian fluid within an elastic tube. Their derivation in variables (A, u, p) can be found in several articles (Olufsen et al., 2000; Sherwin et al., 2003b). We only recall here their main assumptions: the arterial curvature is neglected; the structural arterial properties are constant over a section; the blood in reasonable large vessels is considered as incompressible and Newtonian (so that density ρ and viscosity ν are constant); the flow is assumed to be laminar, as the Reynolds number based on the mean blood velocity u and vessels diameter D ($Re = uD/\nu$) is below 2000 in all arterial vessels.

The equations of conservation of mass and momentum of blood flow read as follows:

$$\frac{\partial A}{\partial t} + \frac{\partial(Au)}{\partial x} = 0 \quad (3.1)$$

$$\frac{\partial u}{\partial t} + \frac{\partial(\alpha u^2/2)}{\partial x} + \frac{1}{\rho} \frac{\partial p}{\partial x} + \frac{f}{\rho A} = 0 \quad (3.2)$$

where x is the axial coordinate along the vessel, t is the time, $A(x, t)$ is the cross-sectional area, $u(x, t)$ is the mean blood axial velocity, $p(x, t)$ is the blood pressure over the cross section and ρ is the blood density. The second term of the momentum equation represents the convective acceleration with α the momentum correction coefficient which is a function of the velocity profile on each section. In the viscous term of Eq. (3.2) (i.e. $f/\rho A$), f represents the friction force per unit length, and can be developed as $f = (\rho K_R u)$ where K_R represents the viscous resistance of the flow per unit length of tube and is also a function of the velocity profile. With the assumption of a flat velocity profile, which is a quite realistic assumption for large arteries, α equals 1 and K_R takes the value $22\pi\nu$ (Quarteroni and Formaggia, 2003), where ν is the constant kinematic blood viscosity. Blood parameters are considered constant in the model: $\nu = 3.8e^{-2} \text{ cm}^2/\text{s}$, $\rho = 1.055 \text{ g/cm}^3$ (Westerhof and Stergiopoulos, 2005). This assumption of constant viscosity is acceptable: effects of red blood cells are mainly found in the microcirculation at low shear and small diameters, and are of little importance for the hemodynamics in large arteries.

With the assumption of a flat velocity profile, Eqs. (3.1) and (3.2) can be rewritten in a conservative form:

$$\frac{\partial \mathbf{U}}{\partial t} + \frac{\partial \mathbf{F}(\mathbf{U})}{\partial x} = \mathbf{S}(\mathbf{U}), \quad (3.3)$$

with

$$\mathbf{U} = \begin{bmatrix} A \\ u \end{bmatrix}, \quad \mathbf{F} = \begin{bmatrix} Au \\ \frac{u^2}{2} + \frac{p}{\rho} \end{bmatrix}, \quad \text{and} \quad \mathbf{S} = \begin{bmatrix} 0 \\ -K_R \frac{u}{A} \end{bmatrix}. \quad (3.4)$$

To close the system of equations, those equations are coupled with a given pressure-area relationship $p = \mathcal{F}(A(x, t))$, which describes how vessel area varies with pressure and thus deals with the fluid-structure interaction of the problem. In this work, as the effects of wall inertia and wall viscosity are generally assumed to be small, we will use an algebraic relation which assumes a thin, homogeneous, incompressible and elastic arterial wall (Formaggia et al., 1999, 2002):

$$p(x, t) = p_0 + \beta(x) \left(\sqrt{A(x, t)} - \sqrt{A_0(x)} \right) \quad (3.5)$$

with

$$\beta(x) = \frac{\sqrt{\pi} h_0(x) E(x)}{(1 - \sigma^2) A_0(x)} \quad (3.6)$$

where p_0 is the diastolic transmural pressure, E is the elastic Young's modulus and h_0 is the wall thickness. The subscript 0 indicates that the variables are at the diastolic state. σ is the Poisson's ratio, typically taken to be $\sigma = 1/2$ since biological tissue is practically incompressible. $\beta(x)$ accounts for the material properties of the elastic vessel.

A tube law relation is derived from a mechanical model of the vessel wall displacement. Here, Eq. (3.5) is derived by assuming instantaneous equilibrium by Laplace's law. Other relations may be adopted as well (Quarteroni and Formaggia, 2003), such as an exponential relationship between pressure and area (Hayashi, 1980) or an arctangent model (Langewouters et al., 1984). Though, in the range of physiological values of pressure and cross-sectional area, these relations are quite close (Marchandise et al., 2009).

The pulse wave velocity (PWV) c is defined as

$$c(x) = \sqrt{\frac{A}{\rho} \frac{\partial p}{\partial A}}, \quad (3.7)$$

and, by using the Moens-Korteweg equation (Eq. (A.12), Appendix A), can be related to the material properties $\beta(x)$:

$$c(x) = \sqrt{\frac{\beta(x)}{2\rho}} A^{1/4}(x). \quad (3.8)$$

3.1.2 Characteristic analysis

In order to explain the computation of the upwind flux and the implementation of the presented inlet BC, it is necessary to recall some main results of the characteristic analysis of Eq. (3.3). Let us rewrite system (3.3) in quasi-linear form:

$$\frac{\partial \mathbf{U}}{\partial t} + \mathbf{H}(\mathbf{U}) \frac{\partial \mathbf{U}}{\partial x} = \mathbf{S}(\mathbf{U}), \quad (3.9)$$

where,

$$\mathbf{H} = \begin{bmatrix} u & A \\ c^2/A & u \end{bmatrix}, \quad \mathbf{S} = \begin{bmatrix} 0 \\ -K_R \frac{u}{A} - \frac{1}{\rho} \left(\frac{\partial p}{\partial \beta} \frac{\partial \beta}{\partial x} + \frac{\partial p}{\partial A_0} \frac{\partial A_0}{\partial x} \right) \end{bmatrix}. \quad (3.10)$$

The matrix \mathbf{H} has two real eigenvalues $\lambda_{f,b} = u \pm c$ and can be written as $\mathbf{H} = \mathbf{L}^{-1} \mathbf{\Lambda} \mathbf{L}$, with:

$$\mathbf{L} = \zeta \begin{bmatrix} \mathbf{l}_1^T \\ \mathbf{l}_2^T \end{bmatrix} = \zeta \begin{bmatrix} c/A & 1 \\ -c/A & 1 \end{bmatrix}, \quad \mathbf{\Lambda} = \begin{bmatrix} \lambda_f & 0 \\ 0 & \lambda_b \end{bmatrix}, \quad (3.11)$$

with an arbitrary scaling factor ζ . For typical values of blood velocity u and PWV encountered in arteries under physiological conditions ($u \ll c$), we have

that $\lambda_f = u + c > 0$ and $\lambda_b = u - c < 0$. Pressure and velocity waveforms propagate forwards at speed λ_f and backwards at speed λ_b . At any point of the arterial system, the pressure, velocity and flow measurements are a combination of many forward and backward running fronts.

Results of the characteristic analysis will be used to compute the numerical flux at the boundaries and interfaces (\mathbf{F}^e), as described in Section 3.2. At these points, we make the reasonable assumption to cancel the spatial derivatives of β and A_0 and to neglect the viscous resistance ($\mathbf{S} = \mathbf{0}$ in Eq. (3.9)). This is a reasonable assumption as it only applies at a few discretisation points: at the inlet and outlet of the 1D model as well as at the few interfaces between the discrete elements representing the 1D geometry (Sherwin et al., 2003b). We recall that these assumptions are not applied in the global resolution on every element Ω .

By defining the characteristic variables as:

$$d\mathbf{W} = \mathbf{L} d\mathbf{U}, \quad (3.12)$$

the system of equations (3.9) may be decoupled in two equations of the characteristic variables (Sherwin et al., 2003b):

$$\frac{\partial W_{f,b}}{\partial t} + \lambda_{f,b} \frac{\partial W_{f,b}}{\partial x} = 0. \quad (3.13)$$

The characteristic variables $W_{f,b}$ can be determined by integrating the differential system. For a particular choice of integration domain and using the pressure-area law defined in Eq. (3.5), we can derive an explicit form of W :

$$W_{f,b}(x, t) = u \pm 4c = u(x, t) \pm 4\sqrt{\frac{\beta(x)}{2\rho}} A^{1/4}(x, t). \quad (3.14)$$

Finally, the primitive variables A and u can be computed using the information from the characteristic variables (denoted with the upper-script c):

$$A^c = \left[\frac{(W_f - W_b)}{4} \right]^4 \left(\frac{\rho}{2\beta} \right)^2, \quad u^c = \frac{W_f + W_b}{2}. \quad (3.15)$$

3.1.3 Wave separation

Waves are composed of forward- and backward-propagating components. The interaction of these wavefronts creates the observed velocity and pressure (or area) waves:

$$dp = dp_f + dp_b, \quad du = du_f + du_b, \quad (3.16)$$

On basis of the work of Parker and Jones (1990) presented following the approach of Alastruey (2006), we will recall the derivation of the equations governing these forward and backward components of pressure and velocity.

According to Eq. (3.12) the variation of the characteristic variables $d\mathbf{W}$ is related to the variation of area and velocity ($d\mathbf{U}$):

$$d\mathbf{W} = \mathbf{L} d\mathbf{U} = \begin{bmatrix} c/A & 1 \\ -c/A & 1 \end{bmatrix} \cdot d \begin{bmatrix} A \\ u \end{bmatrix} = \begin{bmatrix} \frac{c}{A}dA + du \\ -\frac{c}{A}dA + du \end{bmatrix} \quad (3.17)$$

If one considers that β and A_0 are constant in the neighborhood of the measurement site, Eq. (3.7) yields $c = \frac{A}{\rho c} \frac{dp}{dA}$, so that Eq. (3.17) produces:

$$dW_{f,b} = du \pm \frac{dp}{\rho c} \quad (3.18)$$

This equation can be solved for dp and du :

$$dp = \rho c \frac{dW_f - dW_b}{2} \quad (3.19)$$

$$du = \frac{dW_f + dW_b}{2}. \quad (3.20)$$

The characteristic variable propagates information in a unique direction: as $\lambda_f > 0$, W_f propagate changes in pressure and velocity in the forward direction, while W_b propagate them backwards ($\lambda_f < 0$). Therefore, based on Eq. (3.19), the forward dp_f and backward dp_b contributions to dp are

$$dp_f = \rho c \frac{dW_f}{2} \quad dp_b = -\rho c \frac{dW_b}{2} \quad (3.21)$$

Similarly, from and Eq. (3.20), the forward du_f and backward du_b contributions to du are

$$du_f = \frac{dW_f}{2} \quad du_b = \frac{dW_b}{2} \quad (3.22)$$

By substitution of Eq. (3.18) into the four previous relations, the forward and backward time changes in pressure and velocity can be computed:

$$dp_{f,b} = \pm \frac{\rho c}{2} \left(du \pm \frac{dp}{\rho c} \right) \quad (3.23)$$

$$du_{f,b} = \frac{1}{2} \left(du \pm \frac{dp}{\rho c} \right) \quad (3.24)$$

Comparison of Eqs. (3.23) and (3.24) gives the very simple water hammer equation,

$$dp_{f,b} = \pm \rho c du_{f,b} \quad (3.25)$$

previously used in the application of the PU-loop method for PWV estimation (Chapter 2, Section 2.3.1).

Finally, the forward and backward components of the pressure and velocity waveforms can be determined by summing the instantaneous differences of Eqs. (3.23) and (3.24) over a time t :

$$p_f(t) = p_0 + \sum_0^t dp_f \quad , \quad p_b(t) = \sum_0^t dp_b, \quad (3.26)$$

$$u_f(t) = u_0 + \sum_0^t du_f \quad , \quad u_b(t) = \sum_0^t du_b, \quad (3.27)$$

where the integration constants are the pressure and velocity at diastolic state, p_0 and u_0 respectively.

The opposite signs of the incremental backward components dp_b and du_b (Eqs. (3.23) and (3.24)) explain why pressure and velocity waves present different shapes. Pressure components add to generate the complete wave, while the backward velocity component is subtracted from the forward one in order to generate the velocity wave. This is illustrated on Fig. 3.1 with the wave decomposition of in-vivo pressure and velocity waves into their forward and backward components. The physiological signals, described in Section 3.4.2, have been measured on the common femoral artery of a patient operated for lower-limb bypass surgery.

The separation method is based on the linearising assumption that intersecting forward and backward waves are additive. Furthermore, it neglects the viscous dissipation. These assumptions have been relaxed by Pythoud et al. (1996) who showed that the friction and fully non-linear corrections were small ($\sim 5\%$) and compared well with the accuracy of in-vivo measurements.

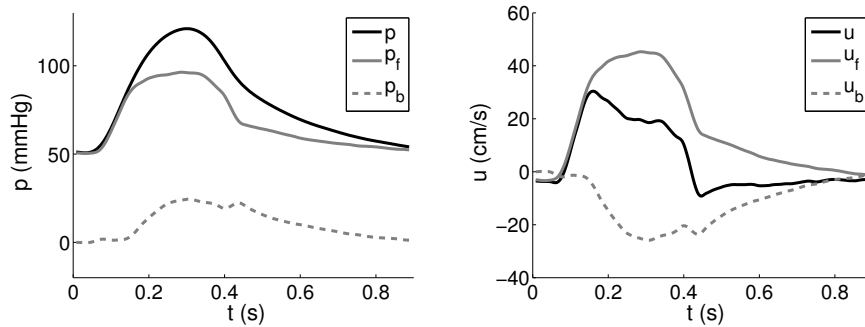


Figure 3.1 – Decomposition of in-vivo pressure (left) and velocity (right) signals (in black line) into their forward (grey) and backward (dashed grey) components.

3.2 The numerical resolution

The discrete model of the blood flow equations can be established using different numerical schemes, e.g. finite differences, finite volumes, continuous or discontinuous Galerkin finite elements. Whatever the method, similar steps need to be achieved. For the sake of clarity, we recall those briefly hereunder.

The weak form of the system is obtained by multiplying Eq. (3.3) by a test function¹ $\hat{\phi}$, integrating over the domain Ω and using the divergence theorem:

$$\int_{\Omega} \frac{\partial \mathbf{U}}{\partial t} \hat{\phi} dx - \int_{\Omega} \mathbf{F} \frac{\partial \hat{\phi}}{\partial x} dx + \int_{\partial \Omega} \mathbf{F} \hat{\phi} \cdot \mathbf{n} = \int_{\Omega} \mathbf{S} \hat{\phi} dx \quad \forall \hat{\phi}, \quad (3.28)$$

where $\partial \Omega$ is the boundary of the domain Ω and \mathbf{n} is its normal vector. The domain Ω is subdivided into a mesh of N elements $\Omega_e = [x_e, x_{e+1}]$, $e = 0, \dots, N$ on which d_i^e discrete nodes (degrees of freedom) are defined. As an example, Fig. 3.2 shows the 1D discretization for the discontinuous Galerkin finite element method (DG), with a polynomial test function $\hat{\phi}$ of order $p = 2$ and $p + 1 = 3$ degrees of freedom per mesh element. For this method, the variables can be discretized in each element using the test functions $\hat{\phi}$: $\mathbf{U}^e = \sum_{i=0}^p U_i^e \hat{\phi}_i^p$.

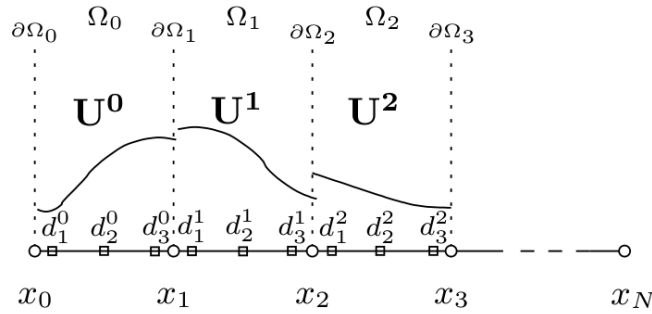


Figure 3.2 – One dimensional discretization for the discontinuous Galerkin method. Mesh of N elements $\Omega_e = [x_e, x_{e+1}]$ ($e = 0, \dots, N$), on which the unknowns \mathbf{U}^e are discretized with a polynomial test function of order $p = 2$ and 3 discrete nodes d_i^e per mesh element.

Let us consider more specifically the third term of Eq. (3.28). This term needs to be computed at the inlet and outlet boundaries. When using numerical methods for which the flux \mathbf{F} is not uniquely defined at the mesh interfaces $\partial \Omega_e$, this term also needs to be computed at all the mesh interfaces. In order

1. In the case of finite differences, the test function $\hat{\phi} = \delta(n)$, with $\delta(n)$ being the Dirac distribution, for finite volumes $\hat{\phi} = 1$ and for Galerkin finite elements $\hat{\phi}$ are the basis function of Lagrange type.

to compute this third term, we have to supply a numerical flux formula \mathbf{F}^e at these particular interfaces:

$$\mathbf{F}^e = \left[\begin{array}{c} A^e u^e \\ \frac{(u^e)^2}{2} + \frac{p(A^e)}{\rho} \end{array} \right], \quad (3.29)$$

where A^e and u^e are the variables computed at the interfaces. Different methods can be used to compute this numerical flux \mathbf{F}^e at the interfaces: e.g. Lax flux, characteristic-based upwind flux, approximate Roe's Riemann solver (Marchandise and Flaud, 2010; Marchandise et al., 2006). In this work, the numerical flux \mathbf{F}^e is computed as a characteristic-based upwind flux. As described in Subsection 3.1.2, some assumptions are required in order to solve the characteristic system (Eq. (3.9)). These assumptions are reasonable and only apply at a few discretisation points: at the inlet and outlet of the 1D model as well as at the few interfaces between the discrete elements representing the 1D geometry (discontinuities, junctions) (Sherwin et al., 2003b). We recall that these assumptions are not applied in the global resolution on every element Ω .

In this work, we have discretized the system (3.3) along with the pressure-area relationship (Eq. (3.5)) with a high order discontinuous Galerkin finite element method with a characteristic-based upwind flux and a Runge-Kutta time-integration scheme. The RK-DG scheme is suitable for the hyperbolic blood flow equations because it can propagate waves of different frequencies without suffering from excessive dispersion and diffusion errors. Further details on this numerical method can be found in Marchandise et al. (2006).

Framework of computation

The numerical resolution of this problem is integrated into the numerical platform ARGO, developed jointly at the UCL (Louvain-la-Neuve, Belgium) and at CENAERO (Gosselies, Belgium). Our biofluid application consists of a 1D application of this fluid mechanics code, developed in C++ language. The generation of the 1D mesh is performed in the open-source software GMSH (Geuzaine and Remacle, 2009).

The time step of computations was 10 ms. Arterial segments were divided into non-overlapping elements of length equal to 2 cm (when physically possible) and were given a polynomial order of 3. The running time for one simulation is less than 5 minutes.

Finally, let us notice that we have collaborated in the integration of this 1D biofluid application into the platform GMSH (under development) which offers the resolution of numerous applications in computational fluid dynamics.

3.3 The boundary conditions

The characteristic analysis and the fact that blood flow in arteries is sub-critical ($u \ll c$) lead to the conclusion that only one BC has to be imposed at each end of the 1D model. In the following, values that are prescribed are represented with an over-bar (e.g. velocity $\bar{u}(t)$).

This section describes the different types of boundary conditions encountered in our 1D model: the inlet, outlet and junction elements. In this study, we particularly emphasize on the computation of the inlet boundary condition for a truncated arterial network. Based on the previous characteristic analysis, we introduce the reflecting and absorbing inlet BC with either a prescribed total wave or forward wave.

3.3.1 Inflow boundary conditions

Fig. 3.3 depicts the implementation of two different types of inlet BC. The inlet boundary is represented by a double line that separates the first element Ω_0 on the right and, on the left, outside the arterial domain, a virtual region Ω_* . At each time step of the resolution, (A_1, u_1) represents the current value of the variables at the first degree of freedom of Ω_0 (d_1^0). At the interface, the numerical flux $\mathbf{F}^{e=0}$ is computed using some specific values for the variables at the interface $A^{e=0}$ and $u^{e=0}$. These variables can be computed using the information carried by the two characteristic variables W_f and W_b joining at the interface. Two different ways of computing those specific values define two different weak boundary conditions: reflecting or non-reflecting BC, also called absorbing BC. In the following, we describe how these two ways can be implemented and combined with different prescribed values.

Prescribing *reflecting* boundary conditions

This is achieved by imposing one of the two variables at the inlet as follows: $A^{e=0} = \bar{A}(t)$ or $u^{e=0} = \bar{u}(t)$ or $A^{e=0} = A(\bar{p}(t))$, the other variable being taken from the interior of the computational domain. Fig. 3.3(a) shows an example of reflecting velocity (RV) boundary condition that is defined by taking $u^{e=0} = \bar{u}(t)$ and $A^{e=0} = A_1$. With this reflecting BC, waves arriving at the inlet interface are reflected back into the computational domain. This type of BC permits to model aortic valve closure (Matthys et al., 2007; Urquiza et al., 2006) but is also used by default in many truncated arterial domains (Raines et al., 1974; Balar et al., 1989; Alastruey et al., 2007; Bertolotti and Deplano, 2000; Leguy et al., 2010).

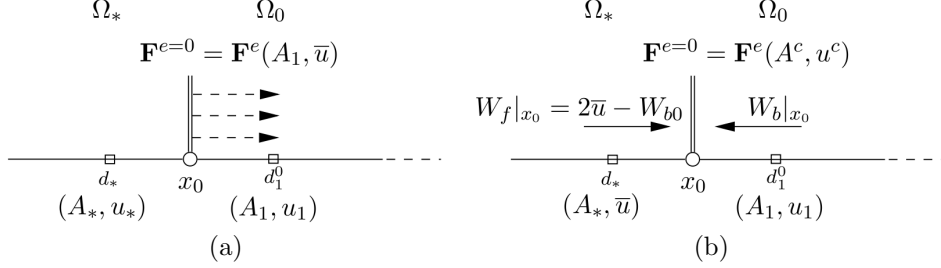


Figure 3.3 – Implementation of the inlet boundary condition. The double line represents the inlet boundary that separates the virtual region Ω_* and the first element Ω_0 . (A_1, u_1) represents the current value of the variables at the first degree of freedom of Ω_0 (d_1^0). $\mathbf{F}^{e=0}$ is the numerical upwind flux computed on the boundary $x = x_0$. (a) Reflecting velocity BC: the prescribed velocity \bar{u} is directly imposed at the inlet interface. Spurious reflections (dashed arrows) are observed at the interface. (b) Absorbing velocity BC: the prescribed velocity \bar{u} is weakly enforced through the forward characteristic $W_f|_{x_0}$.

Prescribing *absorbing* boundary conditions

In this type of BC, the interface variables $A^{e=0}$ and $u^{e=0}$ will be computed from an imposed forward characteristic variable W_f and a computed backward characteristic variable W_b using Eq. (3.15). Imposing a prescribed value through the forward characteristic variables W_f can be achieved as follows. Following Hedstrom (1979), W_f should be computed as a constant incoming characteristic variable in order to ensure absorption of the waves:

$$\left. \frac{dW_f}{dt} \right|_{x_0} = 0. \quad (3.30)$$

A constant value for W_f can be achieved by computing W_f as a function of the prescribed variable and as a function of a constant backward characteristic $W_{b0} = W_b(t = 0)$. For example (see Fig. 3.3(b)), prescribing an absorbing velocity BC (AV) can be done by re-arranging Eq. (3.15) and imposing the forward characteristic as follows:

$$W_f(t)|_{x_0} = 2\bar{u}(t) - W_{b0}. \quad (3.31)$$

It should be noted that even if the incoming characteristic at the inlet W_f still varies in time (\bar{u} is a function of time), it can be considered as constant since $|\bar{u}(t)| \ll |W_{b0}|$ (Thompson, 1987). In Eq. (3.31), the constant outgoing characteristic W_{b0} is computed with Eq. (3.14) using the variables at the interior of the computational domain (A_1, u_1) at time $t = 0$. The backward characteristic $W_b(t)|_{x_0}$ is also computed from (A_1, u_1) but taken at time t .

With this absorbing BC, the resulting numerical velocity at the inlet is not equal to the prescribed velocity \bar{u} : the velocity is imposed through the forward characteristics. However, waves coming from the distal regions will be perfectly absorbed in the numerical simulations without any spurious reflections. This absorbing BC is used for modeling the open condition of the aortic valve in Sherwin et al. (2003b); Formaggia et al. (2006).

It should be mentioned that the procedure to prescribe an absorbing pressure, area or flow rate instead of the velocity is identical (Mynard and Nithiarasu, 2008; Marchandise et al., 2009). As prescribing a flow rate is a classical way to define inlet boundary conditions for 3D-FSI blood simulations, the presented method can be easily extended for those 3D simulations. For example, in order to prescribe an absorbing flow rate, the imposed forward characteristic could be computed using the assumption of a constant area at the inlet $A(t) = A_1$:

$$W_f(t)|_{x_0} = 2 \frac{\bar{Q}(t)}{A_1} - W_{b0}. \quad (3.32)$$

Prescribing the *forward component* of the variable in an *absorbing* way

Considering that the model produces physiological reflected waves at outlets, bifurcations and discontinuities, prescribing the forward component of a variable in an absorbing way presents great improvements in the shape of the computed waves. Indeed, the reflected waves computed by the model superpose with the prescribed forward wave to give the total initial wave. This BC can be implemented easily by replacing \bar{u} by the forward component of the velocity \bar{u}_f in Eq. (3.31), while \bar{u}_f is computed from given velocity and pressure fields (\bar{u}, \bar{p}) using Eqs. (3.24) and (3.27). The imposed forward characteristic W_f then reads as follows:

$$W_f(t)|_{x_0} = 2 \bar{u}_f(t) - W_{b0}. \quad (3.33)$$

This approach has been recently used in the work of Mynard et al. as inlet BC in the ventricle (Mynard and Nithiarasu, 2008; Mynard et al., 2010) but is still not very common for most of the blood flow simulations presented in the literature. We intend to put to the fore the importance of this BC through some 1D-0D applications (cfr Section 3.4).

3.3.2 Outflow boundary conditions

Because the complete arterial network is too large and complex to be modeled with one-dimensional elements, zero-dimensional equations are used to describe the behaviour of secondary networks such as small arteries, arterioles and capillaries. These lumped models also represent the interface with the venous network. In this work, we use an electrical analog model which models the

effect of the wall compliance and the fluid resistance of the distal vessels on the propagating waves: the 0D windkessel model.

Originally introduced by Otto Frank, windkessel models are lumped models of the entire systemic arterial tree and mimic the load on the heart (Frank, 1920; Westerhof et al., 2009). Based on the observation that the diastolic decay of aortic pressure can be described by an exponential curve when flow is zero, the two-element windkessel model is initially composed of a resistance R and a compliance C in series. The time constant of the pressure decay is then described by $\tau = RC$. The resistance characterises the opposition of the distal vasculature to blood flow. The compliance is determined by the elasticity of the arterial wall and represents the capacitive effect of the distal network to regulate flow variation.

This two-element model explained the decay in diastole but fell short in systole. Thanks to developments in frequency analysis, the characteristic impedance of the aorta Z_c was introduced as a third element of the windkessel model (Westerhof et al., 1971). Z_c accounts for the local inertia and local compliance of the very proximal ascending aorta. This characteristic impedance can be seen as a link between the lumped windkessel model and the wave travel aspects of the arterial system. Z_c equals $\rho c/A$ and has the same dimension as a resistor ($m^{-4} kg s^{-1}$). It is therefore often represented as the resistor R_1 . This representation causes error in the estimation of the resistance $R + Z_c$, which is relatively small though (Stergiopoulos et al., 1994), and error in the low frequency range of the input impedance.

This three-element windkessel model ($R_1 C R_2$) has been largely used as outlet boundary condition to model distal parts of the arterial network (Raines et al., 1974; Olufsen, 1999; Stergiopoulos et al., 1992). It accounts for the cumulative resistive and compliant effects of all distal vessels (small arteries, arterioles and capillaries) beyond a terminal site. It is composed of the resistance R_1 in series with a parallel combination of the resistance R_2 and the compliance C (Fig. 2.12, Chapter 2). The total resistance R of the vascular bed is given by $R_1 + R_2$.

Let us define p_{in} and Q_{in} as the pressure and flow rate at the entrance of the windkessel model, which values are given by the 1D formulation. p_C is the pressure across C . The pressure at the outlet of the windkessel model, p_{out} , represents the venous pressure. Each compartment of this analog circuit can be described by electrical relations. The first resistance R_1 is governed by:

$$Q_{in} = \frac{p_{in} - p_C}{R_1}, \quad (3.34)$$

and the second compartment CR_2 by equations:

$$\begin{cases} C \frac{dp_C}{dt} + Q_{out} - Q_{in} = 0 \\ R_2 Q_{out} + p_{out} - p_C = 0. \end{cases} \quad (3.35)$$

These relations can be summarized into the following differential equation:

$$p_{in} + R_2 C \frac{dp_{in}}{dt} = p_{out} + (R_1 + R_2) Q_{in} + R_1 R_2 C \frac{dQ_{in}}{dt}. \quad (3.36)$$

The coupling between the RCR model to the 1-D terminal branch requires to determine p_C by solving a first-order time discretisation of the conservation of mass in the capacitance (Alastruey, 2006).

Furthermore, the value of the first resistance R_1 is fixed to the characteristic impedance $R_1 = \rho c_0 / A_0$, in order to allow incoming waves to reach R_2 and C without being reflected by R_1 (Alastruey et al., 2008).

3.3.3 Bifurcation and discontinuity treatment

While arterial bifurcations are largely present in the complete arterial network, discontinuities in material properties are less frequent in healthy arteries. Though, in the particular application of bypasses, the introduction of a synthetic rigid graft induces important mismatch in the geometry and elastic properties of the vessels. Both cases, bifurcation and discontinuity, require the resolution of a specific system of equations at these boundaries.

Consider the arterial bifurcation on Fig. 3.4 where we denote the parent vessel by index 1 and the daughter vessels by the indexes 2 and 3. We need to determine the values of the six variables (A, u) in all vessels: (A_1, u_1) , (A_2, u_2) , (A_3, u_3) . Therefore, a system of six equations need to be solved.

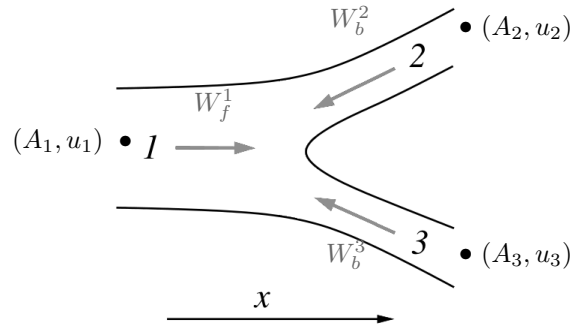


Figure 3.4 – Layout of an arterial tree bifurcation

From its decomposition (3.13) into characteristic variables W_b and W_f , the system can be described in terms of forward and backward waves. Information from the characteristic can only reach the bifurcation from within the vessel, i.e. within the parent vessel, information will reach the bifurcation by a forward-travelling wave W_f^1 , while within the daughter vessels information will reach

the bifurcation by a backward-travelling wave W_b^2 or W_b^3 . The first three equations of the Riemann problem are obtained by imposing that these incoming characteristic variables in each vessel remain constant (Sherwin et al., 2003b):

$$W_f^1 = u_1 + 4c_1 = u_1 + 4\sqrt{\frac{\beta_1}{2\rho}}A_1^{1/4} \quad (3.37)$$

$$W_b^2 = u_2 - 4c_2 = u_2 - 4\sqrt{\frac{\beta_2}{2\rho}}A_2^{1/4} \quad (3.38)$$

$$W_b^3 = u_3 - 4c_3 = u_3 - 4\sqrt{\frac{\beta_3}{2\rho}}A_3^{1/4} \quad (3.39)$$

Three independent equations are obtained from the conservation of mass and continuity of the total pressure $P_t = p + \frac{1}{2}\rho u^2$ at the interface:

$$Q = u_1A_1 = u_2A_2 + u_3A_3 \quad (3.40)$$

$$P_t = p_1 + \frac{1}{2}\rho u_1^2 = p_2 + \frac{1}{2}\rho u_2^2 \quad (3.41)$$

$$P_t = p_1 + \frac{1}{2}\rho u_1^2 = p_3 + \frac{1}{2}\rho u_3^2 \quad (3.42)$$

This non-linear system of 6 equations is resolved using a Newton-Raphson method. The solution of this Riemann problem is used to calculate an upwind flux \mathbf{F}^e at this junction in the numerical discretisation, as described in Section 3.2.

Similarly, in case of discontinuities between the arterial properties of two consecutive segments (elasticity or area), constant incoming characteristics are enforced and the conservation of mass and continuity of total pressure are prescribed. A non-linear system of four equations is then resolved and allows the computation of an upwind flux.

3.4 Applications of the forward absorbing inlet boundary condition

In both test cases presented in this section, we have chosen to prescribe a velocity profile at the inlet BC. This choice does not influence the conclusions about the most adequate type of BC. Similar results are obtained when pressure or area are prescribed.

The first example compares the hemodynamics in a complete arterial tree and in parts of it, when different types of BC are used. The second example is a clinical application that emphasizes the influence of the inlet BC on the shape and intensity of the computed hemodynamic waves.

3.4.1 Test case 1: Arterial tree vs upper- and lower-limb

In this first test case, we show that a truncated geometry of a human arterial model is able to reproduce similar results as a complete arterial tree does; as

long as appropriate inlet BC is chosen. Two truncated arterial networks are considered: the lower-limb and the upper-limb. The approach is described for the lower-limb network and is identically applied to the upper-limb.

We compare here the waveforms computed with two different models: the complete 1D model with 55 arteries developed by Stergiopoulos et al. (1992) and part of this arterial tree (the left lower-limb) (Fig. 3.5). In both models, properties of the arteries (geometry, elasticity) and outlet BC (0D Windkessel models) are taken from the literature (Stergiopoulos et al., 1992; Reymond et al., 2009). Following Sherwin et al. (2003b), a periodic half sine wave is imposed in a reflecting way at the inlet of the arterial tree, the ascending aorta. At the inlet of the leg, the external iliac (point (a) in Fig. 3.5), different ways of imposing an inlet velocity BC are compared. They are all based on the computed hemodynamics at the external iliac of the complete arterial model. The four inlet BC of the reduced model are:

- the total velocity imposed in an absorbing way (AV),
- the total velocity imposed in a reflecting way (RV),
- the forward component of the velocity imposed in an absorbing way (AV-Fwd),
- the forward component of the velocity imposed in a reflecting way (RV-Fwd).

Fig. 3.6 compares the computed pressure and velocity waves at the posterior tibial artery in the leg (point (b) in Fig. 3.5) and in the arterial tree (considered as the reference). Imposing the velocity wave in AV or RV does not accurately reproduce the reference signal. Instead, imposing an AV-Fwd boundary condition gives a much more accurate fitting in shape and intensity. The last BC, RV-Fwd, gives results that over-estimate the reference signal as waves are reflected back again at the inlet.

Similar results are obtained with the upper-limb arterial network, truncated at the subclavian artery. Comparisons of computed pressure and velocity waves at the ulnar artery are shown on Fig. 3.7. The efficiency of the forward absorbing inlet BC is also observed for this arterial site, more proximal to the heart.

3.4.2 Test case 2: An in-vivo lower-limb patient-specific application

The second test case focuses on a patient-specific application with in-vivo pressure and velocity measurements. The lower-limb network of a pathological subject suffering from atherosclerosis is studied. Due to the occlusion of the superficial femoral, popliteal and anterior tibial arteries, the patient was treated with a femoro-posterior tibial bypass surgery (6 mm diameter Gore-Tex synthetic graft).

The 1D-0D model of the lower-limb includes four vessels modeled as one-dimensional segments: the common femoral artery (CF), the deep femoral

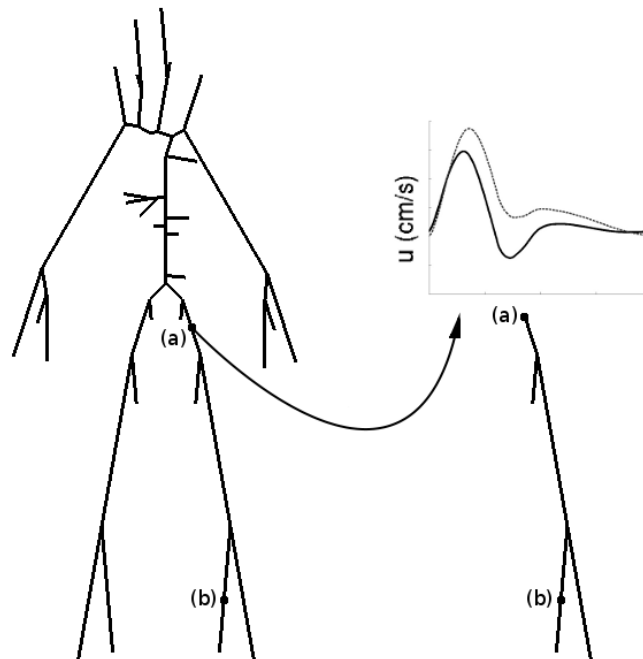


Figure 3.5 – Sketch of the two models: the arterial tree made of 55 arteries (left) and the lower-limb with identical parameters (right). The velocity waveforms from the external iliac (a) are depicted: the velocity wave (black line) and its forward component (grey line). They are inserted as inlet boundary condition in the model of the leg. Comparison of the hemodynamics is performed in the posterior tibial (b).

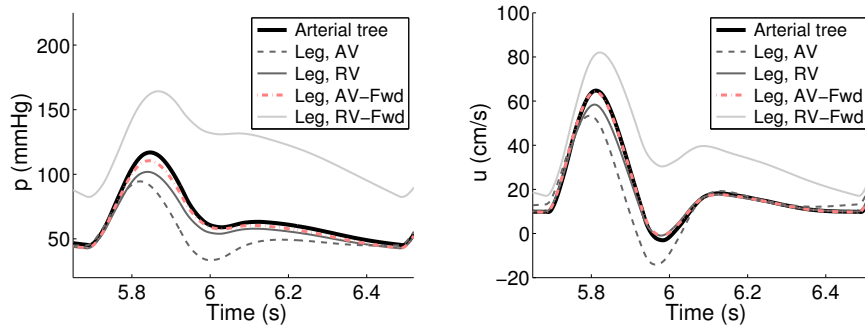


Figure 3.6 – Comparison of the pressure p (left) and velocity u (right) in the posterior tibial artery. The waves computed in the arterial tree are considered as the reference (black solid line). They are compared with the results obtained in the model of the leg with four different inlet BC: the velocity imposed in an absorbing way (AV) (dark grey dashed line) or in a reflecting way (RV) (dark grey solid line), the forward component of the velocity imposed in an absorbing way (AV-Fwd) (red dash-dot line) or in a reflecting way (RV-Fwd) (light grey solid line). The AV-Fwd inlet boundary condition presents a perfect fitting with the reference waves.

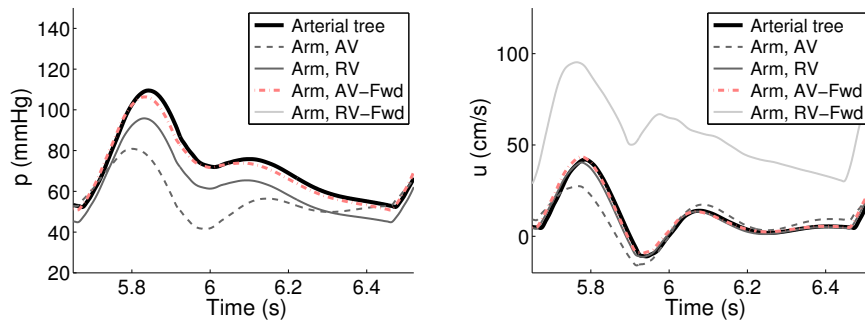


Figure 3.7 – Pressure p (left) and velocity u (right) in the ulnar artery: comparison between the complete arterial network and the truncated model of the arm with four different inlet BC. See Fig. 3.6 for the legend of curves. The AV-Fwd inlet boundary condition presents a perfect fitting with the reference waves.

artery (DF), the bypass conduit (BP) and the posterior tibial artery (PT) (Fig. 3.8). As outlet BC, zero-dimensional *RCR*-windkessel models represent the peripheral arterial networks: one is distal to the deep femoral and the other is distal to the posterior tibial artery. The inlet BC, a velocity profile, is prescribed at the CF.

Physiological data

In order to evaluate the properties of the patient-specific model, measurements were performed during the surgery just after the bypass was implanted, on the four vessels of the leg (red points in Fig. 3.8). The patient (male, 79 years old, patient #15) gave his full agreement for taking part into this study. For this subject, the first protocol of data acquisition was used, as described in Section 2.1 of Chapter 2. Pressure profiles were acquired invasively with a pressure catheter. Velocity profiles and mean diastolic diameters were measured using B-mode Doppler ultrasonography. The rigidity of the vessel walls was described with the PWV using Eq. (3.8), and PWV was computed using the PU-loop method. For outlet BC, resistances were computed as the ratio of mean pressure to mean flow while compliances were obtained using the exponential fitting method. All the methods for the determination of the parameters are described in Section 2.3, Chapter 2.

All parameters describing the patient-specific model for the subject considered here (Patient #15) are displayed in Appendix B.

Inlet boundary condition

Similarly to the first test case, we have run our 1D-0D model with four different kinds of velocity BC: the in-vivo velocity u imposed in an absorbing way (AV), in a reflecting way (RV), the forward component u_f imposed in an absorbing way (AV-Fwd) and in a reflecting way (RV-Fwd). Fig. 3.1 presents the decomposition of the in-vivo pressure and velocity waveforms in the CF artery into their forward (u_f, p_f) and backward (u_b, p_b) components. It shows the velocity waveforms used as inlet BC : u , the in-vivo velocity and u_f , its forward component. These two waveforms differ remarkably in intensity and in shape. The forward waveform does not present the fluctuations observed in the complete velocity wave, such as the negative backflow at the end of the diastole. Furthermore, we may observe that its shape is very close to the pressure waveform p .

The RV-Fwd BC does not converge after several cardiac cycles: due to added up reflections at the inlet, pressure signals increase towards infinite values (Fig. 3.9, left). The RV BC converges but does not produce physiological pressure results: after stabilization (around 10 cycles), pressure reaches 150 to 300 *mmHg* (Fig. 3.9, right).

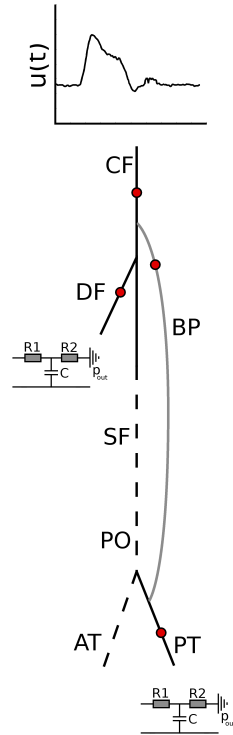


Figure 3.8 – The 1D-0D model of the lower-limb arterial network of subject #15. The main arteries of the leg are depicted: the common femoral (CF), the deep femoral (DF), the superficial femoral (SF), the popliteal (PO), the anterior tibial (AT) and the posterior tibial arteries (PT). The occluded arteries (in dashed line) are bypassed by the synthetic graft (BP, in grey). Blood pressure and blood velocity, arterial diameter are measured at the CF, DF, PT and in the bypass (red points). The 1D model (including the four arteries CF, DF, BP and PT) is bounded at its outlets by RCR-windkessel models. Velocity waveform is applied at the inlet of the arterial network.

Results obtained with the two absorbing BC are shown in Fig. 3.10. The AV-Fwd model produces waveforms that fit the in-vivo measurements very well. This is especially true for the intensity and shape of the pressure results. With the AV model, the shape of the pressure result reproduces the shape of the velocity waveform imposed at the inlet.

In-vivo velocity measurements are also better reproduced when the AV-Fwd model is used. Though, some discrepancies between curves can be observed in the DF and BP. These differences may come from uncertainties in in-vivo measurements and parameters computation.

In comparison to the classical absorbing inlet boundary condition, imposing the forward component of velocity, area or pressure for the inlet BC manages to produce physiological pressure and velocity waveforms and should be used for truncated 1D models. The main reason for this comes from the fact that reflected pressure waves are positive while reflected velocity waves are negative. Addition or subtraction of the reflected waves from the forward waves permits to create various shapes and intensities of the resulting waves. Furthermore, as every reflected wave is absorbed while it arrives at the inlet of the arterial path, their effect is taken into account only once in our model. For partial arterial tree model, this is closer to the reality. Notice that some smaller reflections may travel through the whole arterial path and be reflected again at the aortic valve or iliac bifurcation (Alastruey et al., 2009). Even though, these re-reflected waves only induce limited difference in the lower-limb results, as observed in the test case 1 (Fig. 3.6).

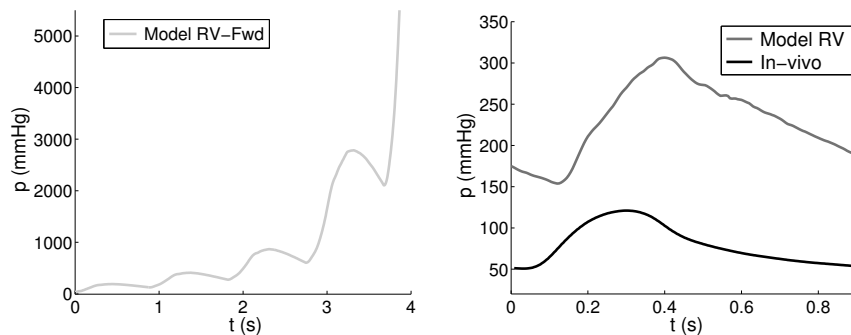


Figure 3.9 – Pressure signal in the CF produced by the model with different inlet BC. Left: non-convergence of the model when forward velocity component is imposed in a reflecting way (RV-Fwd). Right: non-physiological results when velocity is imposed in a reflecting way (RV)

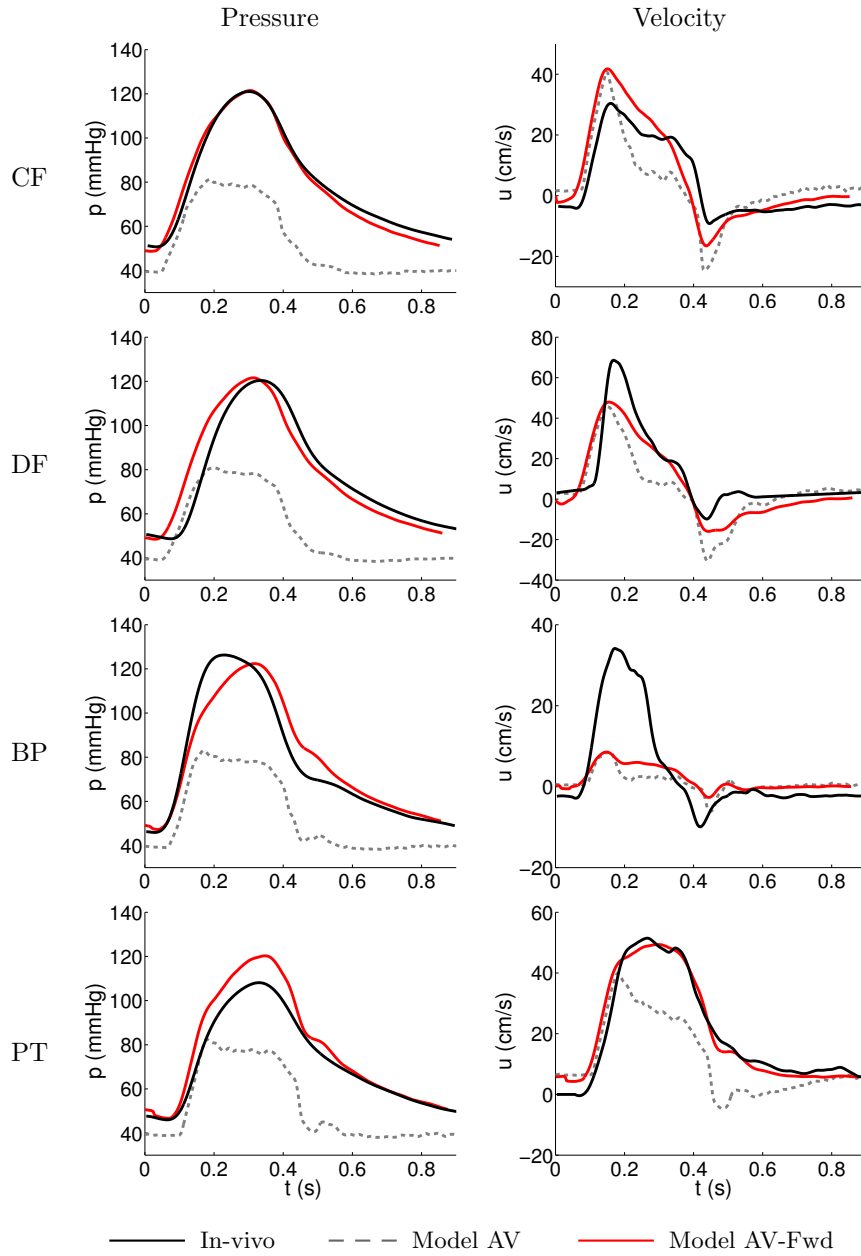


Figure 3.10 – Model results compared to in-vivo measurements of pressure (left) and velocity (right) in the four arteries of the leg model. In-vivo measurements are plotted in black. Model results with an AV inlet BC are in dashed grey. Model results using an AV-Fwd inlet BC are in continuous red line. The 10th cycle of numerical result is selected.

3.5 Discussion

This chapter has presented the coupled 1D-0D mathematical and numerical model used in this work for blood flow simulation. Furthermore, it has focused on the prescription of the inlet boundary condition. Different formulations to prescribe inlet boundary conditions have been presented together with two applications of one-dimensional blood flow simulations. Specific attention has been devoted to truncated arterial networks models that do not include the heart as wave generator. We have shown that, in such truncated models, the most relevant inlet BC is the following: prescribing the forward component of the variable of interest (velocity, pressure or flow), while enforcing the absorption of the backward waves arriving at this inlet. Waveforms computed in this way present physiological shapes and intensities that compare very well with in-vivo pressure and velocity measurements.

While the implementation of the numerical method is simple, a difficulty may arise in the data acquisition. Indeed, pressure and velocity signals need to be acquired simultaneously at the location of interest in order to compute the forward components by wave separation. In practice, velocity measurements may easily be acquired using Doppler ultrasound and pressure signals with tonometry. Another non-invasive method is to use a combined Doppler and echo-tracking system and to consider a linear or exponential relation between arterial diameter and pressure (Vermeersch et al., 2008). Nevertheless, this method should be applied with care as this assumption may not be true at distal sites and in pathophysiological conditions.

Despite these acquisition constraints, we are convinced that, when modeling subject-specific hemodynamics, it is preferable to impose this local inlet BC rather than to model the whole arterial tree (i.e. this implies computing all its parameters and imposing the inlet BC at the heart). Indeed, modeling the whole arterial tree increases the computational complexity as well as the amount of patient-specific parameters.

In the applications, we have focused on the lower-limb region and have shown the efficiency of the method at that distal site. Extrapolation of the method to sites that are proximal to the heart is also shown for the arm and presents similar conclusions. As the geometry at the level of the heart is quite complex, the shape of the hemodynamic waves fluctuates greatly from the aorta to its children vessels. This indicates that backward reflections are already of importance, suggesting the use of the inlet BC described in this work.

Enforcing the complete absorption of the waves at the level of the inlet has proven more efficient than enforcing their reflection. Though, it does not take into account the fact that reflected waves exiting the domain might be reflected again at the closed aortic valve and might re-enter the computational domain (Alastruey et al., 2009).

Considering its efficiency to describe the wave propagation in the arterial

network, this work focuses on the 1D-FSI model of blood flow. It should be noted however that the inlet BC we suggest is general and could be used for 3D-FSI blood flow simulations as well. Indeed, we observe similar results in terms of wave propagation. As long as pertinent outlet BC are chosen in the 3D model, physiological reflected waves will be created and will propagate towards the inlet of the domain. Their behavior will be similar to the one observed in 1D-0D models. By applying the inlet BC described in this work, forward and backward waves will interact and produce a physiological behavior at the inlet.

Validation and sensitivity analysis of the 1D-0D model

Mathematical and numerical models are designed in order to help scientists better understand an observed phenomena, whatever its nature (e.g. physical, meteorological or economical). Once the model is defined, its performances need to be assessed. The validation of the model aims at evaluating its efficiency and accuracy by comparing its numerical results with a set of observed data from the studied phenomena. This validation is successful if the model reproduces these observations within the limits of the objectives and hypotheses defined beforehand. Then, once a model is validated, it becomes a useful tool to evaluate the behaviour of the studied phenomena while it is subjected to some modifications, as long as those remain within the given hypotheses.

A mathematical model is composed of relations between variables of interest. Terms of these equations might be balanced by some parameters which values need to be fixed when running the model. In order to better understand the model developed, the sensitivity of the model to these parameters can be studied. Furthermore, this analysis allows to determine the most sensitive parameters which value should be determined more precisely.

The first aim of this chapter is to validate the coupled 1D-0D model of blood flow in arteries presented in Chapter 3. The hemodynamical simulations from the model will be confronted with in-vivo measurements performed in the arteries of bypassed legs of patients. As the hemodynamics in pathological arteries greatly fluctuates between subjects, the model is designed to produce patient-specific results. This characteristic is achieved by fixing the value of the model parameters so that they are representative of the physiological condition of the patient. The inlet boundary condition of the model is also derived from

The content of this chapter will be submitted in: Willemet M., Lacroix V., Marchandise E., Validation and sensitivity analysis of a coupled 1D-0D model of the arterial hemodynamics in bypassed lower-limbs. *Medical Engineering & Physics*.

in-vivo measurements. Because measurements we have at our disposal focus on the lower-limb, we will consider a truncated arterial model; the 1D model will be limited to the arteries of the upper leg. Another hypothesis of the validation is to consider only post-operative conditions, i.e. once the bypass is inserted in the patient's leg and that blood flows to the distal arteries. The modeling of a pre-operative condition (with a long section of the arterial path occluded) is indeed different as it is based on other modes of blood displacement (perfusion) through small collateral arteries and arterioles, and will not be considered in the framework of this work.

In recent years, coupled 1D-0D models of the arterial hemodynamics have been largely developed. Though, the study of their validation has been mostly restrained to healthy data. Assessment of a 1D numerical model against in-vitro measurements was performed in Matthys et al. (2007); Bessems et al. (2008); Alastruey et al. (2011) and showed the ability of the 1D time-domain formulation to capture the main features of pulse wave propagation. The ability of the 1D model to produce pressure and flow waveforms agreeing well with healthy in-vivo measurements was shown in Reymond et al. (2009). In their work, results from a 1D-0D model of a complete arterial tree (including the heart, cerebral arteries and coronaries) were compared against in-vivo measurements performed on healthy subjects with values of parameters taken from the literature. Simulations on local parts of the arterial network were also validated against in-vivo data, with parameters computed from in-vivo measurements (Olufsen et al., 2000; Leguy et al., 2010). Besides these healthy validation, few studies have focused on model validation of subjects under pathological conditions: Steele et al. (2003) validated a 1D model of a stenosis with thoraco-thoraco bypass in pigs by comparing flow measurements. In this work, we intend to validate a 1D-0D model of the hemodynamics (velocity and pressure) in atherosclerosed bypassed lower-limb arteries using patient-specific parameters computed from in-vivo data.

The second aim of this chapter is to perform a sensitivity analysis (SA) of the coupled 1D-0D model of the bypassed lower-limb. We will study the sensitivity of patient-specific models, i.e. use values computed from in-vivo data. This approach has been followed in Leguy et al. (2010, 2011) when studying the sensitivity of a coupled 1D-0D model of blood flow in arteries of the arm. In Ellwein et al. (2008), SA of a lumped parameter model of the cardiovascular system is performed on basis of in-vivo data from one healthy subject, and in Pope et al. (2009), SA is also performed in a lumped cerebrovascular model on basis of in-vivo data from 24 healthy subjects.

This chapter is organised as follows. The first aim of this chapter, the validation of the model, is described in Section 4.1; it firstly summarizes the options of the model considered and presents the methodology followed to assess the similarity between simulated and in-vivo curves. Validation results from patients are then described, and results from some subjects are detailed. The second

aim of this chapter, the sensitivity analysis is the main interest of Section 4.2. Sensitivity indexes, variation ranges of the input and output parameters are described, then global sensitivity results are presented with a focus on the influence of arterial location. The influence of some assumptions of the model (constant viscosity, velocity profile, arterial tapering) is also detailed. The last section of this chapter summarizes and discusses results and observations.

4.1 Validation of the model

When assessing a model based on experimental data, one must consider the entire process of transformation of the data: from their acquisition to the generation of the simulations. Indeed, new hypotheses, data acquisition errors, approximations or manual interactions are present at each step of the process. The evaluation of the performance of the numerical model requires to consider all of these inputs. The process of transformation of the in-vivo lower-limb raw data to the numerical simulations is presented in Fig. 4.1. In this schema, the different inputs and outputs of the process are identified. Boxes on the left represent the origin of the data (measurements or literature), the central panel represents the process of transformation of the raw data towards inputs of the model. The 1D-0D model appears in the box on the right. Variables are represented on arrows. We use the notation $[.]$ to represent a variable in the four vessels (the common femoral artery (CF), the deep femoral artery (DF), the bypass conduit (BP) and the popliteal artery (PO)), and the notation $\langle.\rangle$ to represent a variable relative to the DF and PO only. All variables are defined in the legend of Fig. 4.1.

In this work, we aim at presenting honest results, i.e. results generated by the model without any manual fitting to improve the validation. Some results might therefore be disappointing. In these cases, we will discuss the differences observed and suggest methods to improve the comparison.

We have at our disposal in-vivo data from 9 subjects in order to perform the validation of the model. Average clinical parameters of the subjects are presented in Subsection 2.1.3 of Chapter 2. For each patient analysed, in-vivo measurements, bypass characteristics, computed values of the parameters as well as simulations from the numerical model are presented in Appendix B.

This section firstly presents the materials and methods used in the validation process: the numerical model and its parameters, the physiological data and the tools introduced to compare in-vivo and simulated waveforms. Secondly, global results are presented and discussed. In the third part, we analyse a few clinical cases of patients; we detail the success or failure of the simulated waveforms in comparison with in-vivo data.

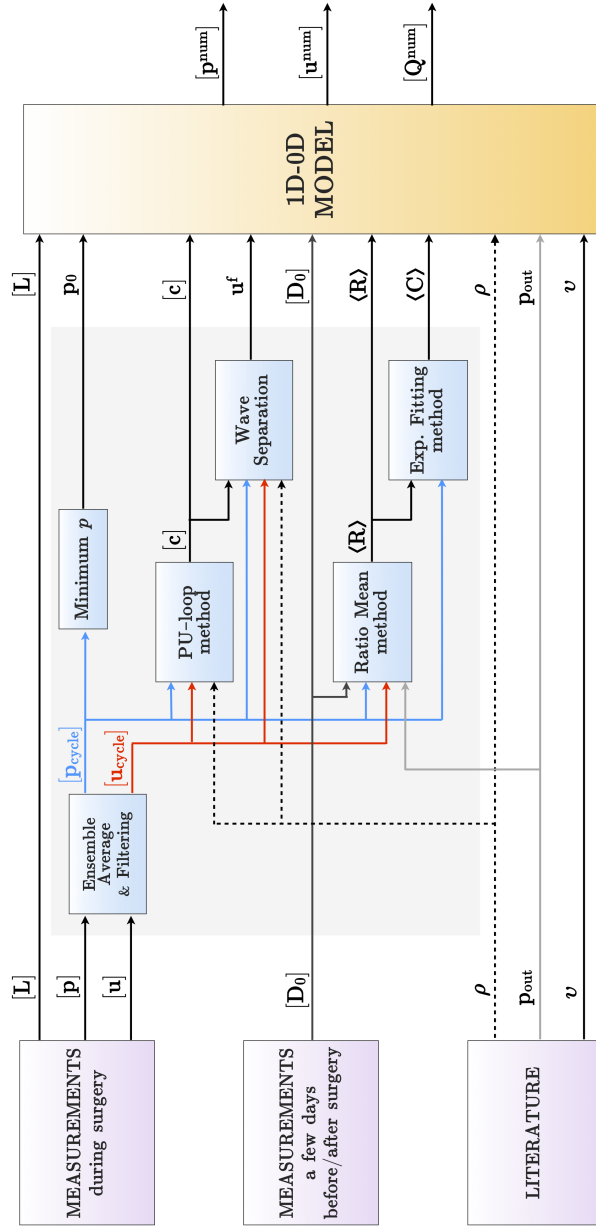


Figure 4.1 – Process of transformation of the in-vivo raw data to the numerical simulations. Boxes represent methods of acquisition or computation. Arrows represent variables. The notation $[\]$ represents a variable in the four vessels, and $\langle \ \rangle$ a variable relative to the DF and PO only. L : arterial length. p : pressure. u : velocity. p_{cycle} and u_{cycle} : mean p and u over a cardiac cycle. D_0 : diastolic diameter. ρ : blood density. p_{out} : venous pressure. v : blood kinematic viscosity. c : pulse wave velocity. R : resistance. C : compliance. u^f : forward component of velocity. p^{num} , u^{num} and Q^{num} : numerical simulations of p , u and Q .

4.1.1 Materials and methods

The 1D-0D model

The coupled 1D-0D model considered in this work (see Chapter 3) focuses on a truncated arterial network of the lower-limb. It comprises four vessels of the leg, modeled as one-dimensional segments: the common femoral artery, the deep femoral artery, the bypass conduit and the popliteal artery (Fig. 4.2). For ease of presentation, even if the distal vessel corresponds effectively to the tibial or peroneal artery, it will be referenced to as the popliteal artery. For example, the distal anastomosis might be located below the knee on one of the tibial arteries when the other one is occluded.

The arterial truncated model is limited to the popliteal artery and does not include the two tibial and peroneal arteries for practical reasons: in-vivo data are difficult to acquire precisely in these small and distal arteries, even with invasive methods. Even though, lumping arteries beyond the first generation of bifurcations into matched RCR outflow models induces a small error ($< 3\%$) (Alastruey et al., 2008). As outlet boundary conditions, zero-dimensional *RCR*-windkessel models represent the peripheral arterial networks: one is distal to the deep femoral and the other is distal to the popliteal artery. As inlet boundary condition, a velocity profile is prescribed at the common femoral: the forward component of the velocity is prescribed in an absorbing way. Notice that the 10th cycle of the numerical simulation is selected for comparison. Also, in simulated waveforms, the start of systole is delayed of about 0.1s in order to correspond to the similar delay applied to in-vivo signals (to ease pressure and velocity systolic synchronization).

Parameters of the model

In this work, the value of the venous pressure of the windkessel models is fixed ($p_{out} = 20 \text{ mmHg}$) (Marieb, 2005; Alastruey et al., 2008). We also prescribe the blood density $\rho = 1.05 \text{ g/cm}^3$ and kinematic viscosity $\nu = 3.8e^{-2} \text{ cm}^2/\text{s}$ (equivalently blood dynamic viscosity $\mu = 0.04 \text{ g/(cm s)}$).

We count 18 parameters describing our 1D-0D model: the length L , diameter D_0 , and pulse wave velocity c of the three arteries and of the bypass graft, the windkessel resistance $R = R_1 + R_2$ and compliance C of the two outlet lumped models, and the diastolic pressure p_0 . Even if it does not take a finite value, the velocity waveform prescribed at the inlet can also be considered as a parameter which is prescribed patient-specifically.

The value of these parameters is computed on basis of in-vivo measurements performed during the bypass surgery just after bypass grafting on the four vessels of the leg (see red points in Fig. 4.2). Details about the data acquisition protocol have been described in Section 2.1 of Chapter 2. Methods to evaluate the value of some of the parameters have been described in Section 2.3, Chapter 2. We summarize these results here.

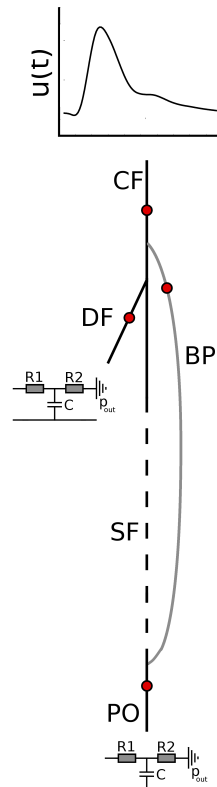


Figure 4.2 – The 1D-0D model of the lower-limb arterial network includes four vessels: the common femoral (CF), the deep femoral (DF), the bypass (BP) and the popliteal (PO). The occluded superficial femoral artery (SF, in dashed line) is bypassed by the synthetic graft (in grey). Blood pressure, velocity and arterial diameter are measured at the CF, DF, PO and in the BP (red points). The 1D model is bounded at its outlets by RCR-windkessel models. Forward component of the velocity waveform is applied at the inlet of the arterial network.

- Length of the bypass vessel corresponds to the length of the synthetic graft inserted in the leg, or is measured on MRI images.
- Lengths of the arteries in the model are evaluated during data acquisition as the distance from the catheter tip to the proximal or distal anastomosis.
- Mean diastolic diameters are measured using B-mode Doppler ultrasonography.
- Pulse wave velocities of arteries and bypass graft are evaluated locally using the PU-loop.
- Windkessel resistances are evaluated as the ratio of mean pressure to mean flow.
- Windkessel compliances are evaluated with the exponential fitting method.
- The diastolic pressure is evaluated as the minimum of the pressure cycle over a cardiac cycle.

These methods of acquisition and computation of data appear in the summary of the process of transformation of raw data in Fig. 4.1.

Physiological data

Results from the model will be compared to in-vivo measurements of pressure and velocity realized invasively during surgery, after suture of the bypass graft. Comparison will be performed in the four arteries of the leg considered. Ensemble average and filtering of the data is performed on the measured signals in order to obtain a representative set of simultaneous signals for each artery (see Subsection 2.1.2 of Chapter 2).

Comparison of curves

We intend to validate our model by comparing the hemodynamic curves of pressure and velocity in the four vessels of interest. Therefore, each clinical subject presents 8 couples of curves to compare. We will not consider flow rate curves for comparison because in-vivo flow measurements are not accurate. As we do not have distension waveform measurements at our disposal, flow is computed as $Q(t) = u(t) A_0$, with A_0 the diastolic cross-sectional area. The comparison with the simulated flow ($Q(t) = u(t) A(t)$) would lead to conclusions almost similar to the comparison of velocities.

Pressure and velocity waveforms along the cardiac cycle are complex as they result from lots of interactions between forward and backward waves. Comparing two curves objectively is not obvious in view of their many features during systole and diastole. Furthermore, as we are considering a pathological population, we expect to observe a wide range of physiological pressures and velocities between subjects. Unlike in Reymond et al. (2009) where healthy data are considered, computing average values of variables on the complete population is not pertinent.

In this work, we will objectively describe the similarity between curves using the following indicators.

- The vertical distance between the two curves computed as the root-mean-square error (RMSE) ϵ between the in-vivo (meas) and numerical (num) waveforms (Reymond et al., 2009; Segers et al., 1997):

$$\epsilon_p = \frac{1}{N} \sum_i^N \sqrt{(p_i^{\text{meas}} - p_i^{\text{num}})^2} \quad \epsilon_u = \frac{1}{N} \sum_i^N \sqrt{(u_i^{\text{meas}} - u_i^{\text{num}})^2} \quad (4.1)$$

where each curve is discretised by $N = 150$ points during one cardiac cycle.

Even if this index gives an estimation of the similarity between curves, it does not allow to detect the features of the curves which are not well simulated by the model. Furthermore, this index is influenced by the time synchronization of the curves.

- In order to describe the results of the simulation more precisely, we define particular attributes, or criteria, of pressure and velocity curves. The criteria describing a pressure curve are (see Fig. 4.3, left):

1. the pressure pulse $PP = p_{sys} - p_{dias}$ defined as the difference between the systolic and diastolic pressures,
2. the slope of the pressure increase during systole: $\dot{p} = \frac{dp}{dt}|_{\text{systole}}$, computed as the average slope during 40% of the systolic increase $([0.2T_{sys} - 0.6T_{sys}])$ with T_{sys} the duration of the systolic phase).

The criteria of a velocity curve are (see Fig. 4.3, right):

3. the peak systolic velocity PSV ,
4. the end diastolic velocity EDV ,
5. the value of velocity at one third of the diastolic phase $u^* = u(t^*)$ where t^* is the time at one third of diastole,
6. the time of the peak systolic velocity $t(PSV)$.

Furthermore, we compare :

7. the time-averaged flow rate \bar{Q} over the complete cycle.

From the values of these 7 extracted criteria of the in-vivo and simulated curves, we compute their difference (criteria^{meas} - criteria^{num}). Average \pm standard deviation (SD) of the absolute value of these differences is also computed in each artery. Notice that we consider the absolute value because differences might be positive or negative if the numerical simulation respectively under- or over-estimates the in-vivo measurement. Notice also that we could have used the relative difference (as defined by Bland-Altman) instead of the simple difference between criteria. Though, this evaluator is not efficient when considering criteria of small amplitude and close to zero, such as the EDV . Furthermore, it does not help the clinical interpretation of the criteria.

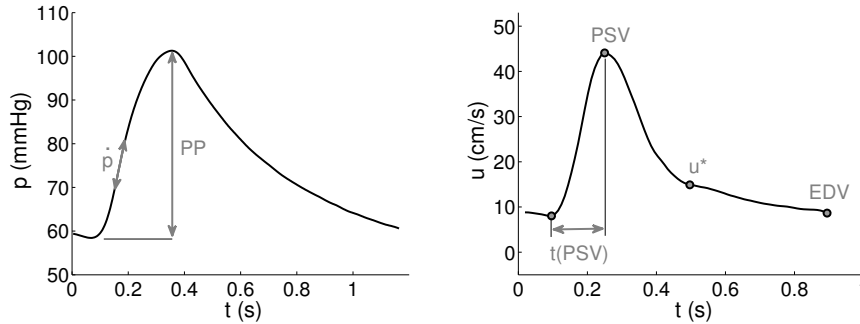


Figure 4.3 – Extracted criteria from the pressure (left) and velocity (right) curves. PP is the pressure pulse, \dot{p} is the slope of the pressure increase during systole, PSV is the peak systolic velocity, $t(PSV)$ is the time of the PSV , u^* is the velocity at one third of diastole, EDV is the end diastolic velocity.

4.1.2 Results (1): General observations

Comparison of pressure and velocity waveforms between numerical simulations and in-vivo measurements are shown for all patients in Appendix B. We will describe and analyse waveforms from a few representative patients in the next subsection. Here, general observations about the performance of the model are presented on basis of the evaluators defined above.

Data

The root-mean-square error gives information about the similarity between simulated and in-vivo curves. In Table 4.1, averages of the pressure and velocity RMSE by arteries are presented. Quantification of the RMSE for the four vessels of each patient individually is shown in Fig. 4.4.

In Table 4.2, we describe the error performed by simulations from the point of view of each criteria in the four vessels.

In order to easily evaluate the amplitude of the differences, and because some indexes are not commonly used in practice, Table 4.3 presents the average value of the indexes extracted from in-vivo curves of the lower-limb arteries.

As we have considered the absolute value of the difference between criteria, we have lost the information about the direction of this difference: is the simulation under- or over-estimating the in-vivo measurement? Furthermore, these averages do not allow to quantify the performance of the model for each patient individually. In Figs. 4.5 and 4.6, we plot for each criteria the difference in the four vessels for the 9 patients considered.

RMSE:

		CF	DF	BP	PO
ϵ_p	(<i>mmHg</i>)	5.8 ± 4.1	10.1 ± 6.4	10.6 ± 9.1	14.5 ± 10.3
ϵ_u	(<i>cm/s</i>)	16.5 ± 17.1	7.0 ± 4.6	8.9 ± 7.1	9.7 ± 6.1

Table 4.1 – Average \pm SD in all 9 patients of the root-mean-square error (RMSE) between measurements and simulations in the four vessels of the leg.

Average difference of criteria:

		CF	DF	BP	PO
PP	(<i>mmHg</i>)	14.8 ± 16	22.2 ± 23.3	16 ± 19.9	28.3 ± 21.3
\dot{p}	(<i>mmHg/s</i>)	182 ± 216	295 ± 265	187 ± 176	306 ± 326
PSV	(<i>cm/s</i>)	35.3 ± 33.3	17.8 ± 12.5	16.2 ± 9.5	18.5 ± 18.1
EDV	(<i>cm/s</i>)	11.7 ± 13.2	2.2 ± 1.7	6.2 ± 7.9	6.3 ± 7.9
u^*	(<i>cm/s</i>)	12.7 ± 15.5	7.6 ± 6.4	8.7 ± 8.7	3.6 ± 3.8
$t(PSV)$	(<i>ms</i>)	33.2 ± 36.4	29.1 ± 25.5	43.3 ± 50.1	31.5 ± 23.4
\bar{Q}	(<i>cm³/s</i>)	6.3 ± 8.4	0.3 ± 0.3	2.2 ± 2.7	0.8 ± 1.3

Table 4.2 – Average \pm SD in all 9 patients of the absolute values of the differences between measurements and simulations for the 7 criteria in the four vessels of the leg: $\text{mean}_{\text{vessel}}(\|\text{criteria}^{meas} - \text{criteria}^{num}\|)$.

Average in-vivo criteria:

	Lower-limb arteries
PP	(<i>mmHg</i>) 49 ± 18.9
\dot{p}	(<i>mmHg/s</i>) 400 ± 184
PSV	(<i>cm/s</i>) 49.1 ± 30.8
EDV	(<i>cm/s</i>) 6.4 ± 8.3
u^*	(<i>cm/s</i>) 11.6 ± 10.8
$t(PSV)$	(<i>ms</i>) 140 ± 38.8
\bar{Q}	(<i>cm³/s</i>) 4.3 ± 6.0

Table 4.3 – Average \pm SD in all 9 patients of the 7 criteria extracted from in-vivo measurements in the leg.

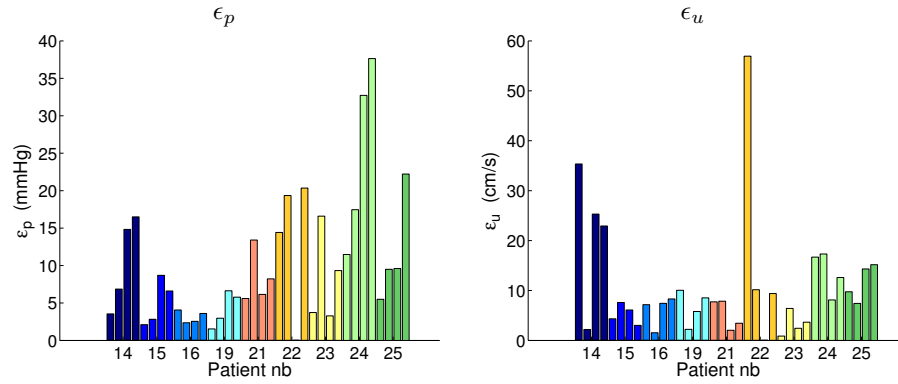


Figure 4.4 – Root-mean-square error (RMSE) for pressure (ϵ_p) and velocity (ϵ_u) in the four vessels of the 9 patients analysed. Results in the four arteries of each patient (from left to right: CF, DF, BP, PO) are represented using the same color.

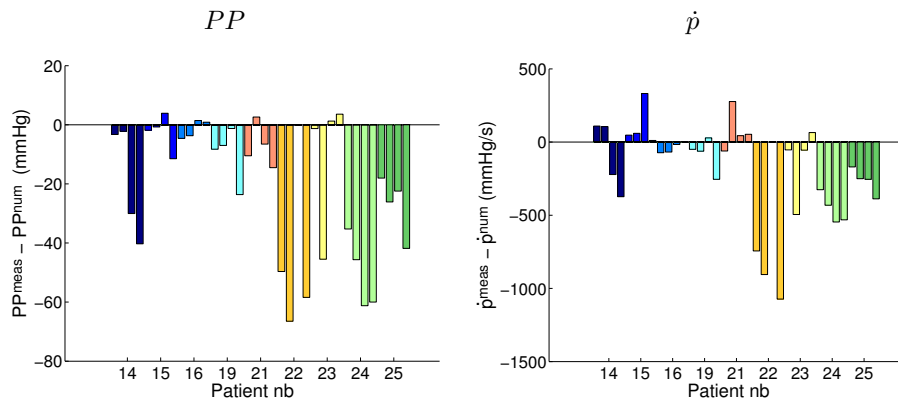


Figure 4.5 – Differences between measurements and simulations (criteria^{meas} – criteria^{num}) for the 2 pressure criteria (PP , \dot{p}) in the four vessels of the 9 patients analysed. Results in the four arteries of each patient (from left to right: CF, DF, BP, PO) are represented using the same color.

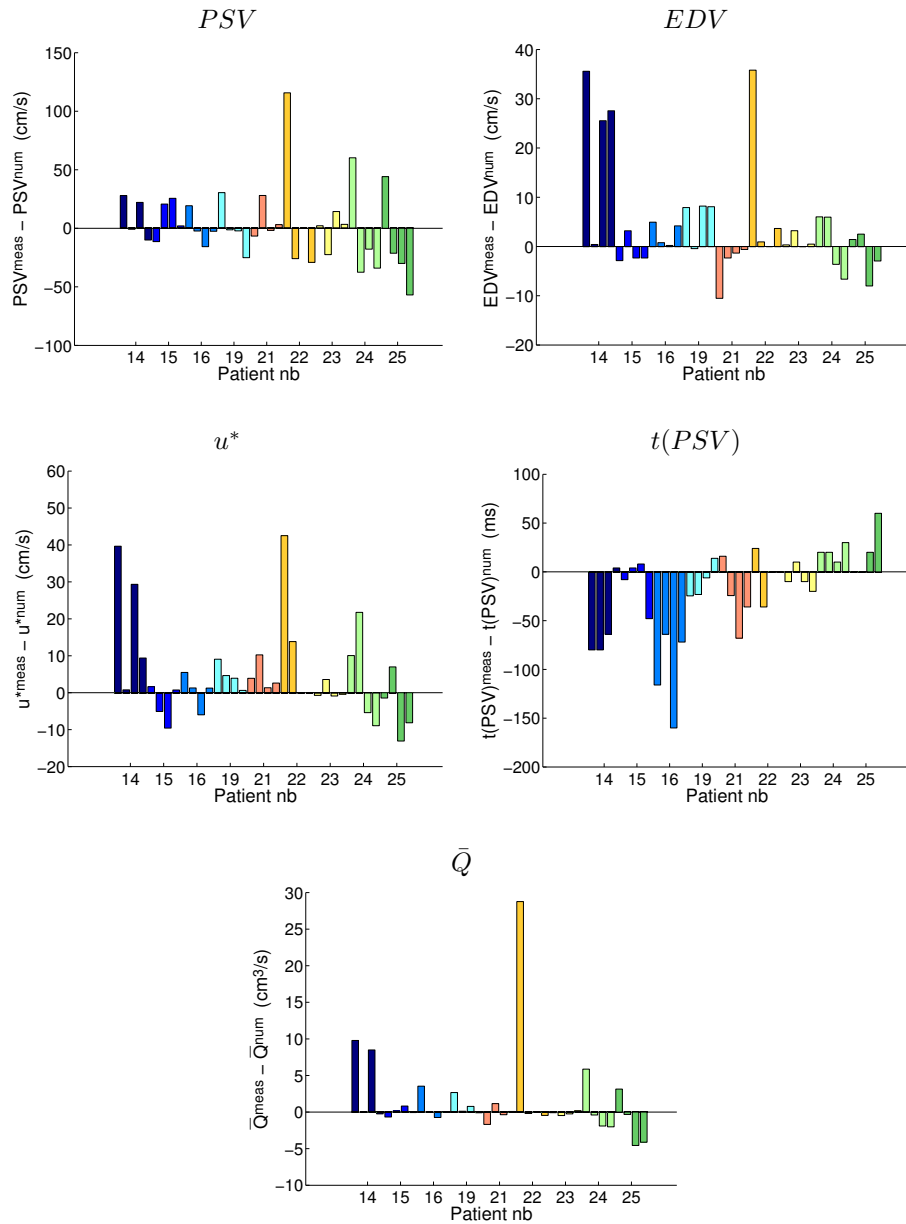


Figure 4.6 – Differences between measurements and simulations (criteria^{meas} – criteria^{num}) for the 4 velocity criteria (PSV , EDV , u^* , $t(PSV)$) and the flow criteria (\bar{Q}) in the four vessels of the 9 patients analysed. Results in the four arteries of each patient (from left to right: CF, DF, BP, PO) are represented using the same color.

Interpretation

A first general observation of Tables 4.1, 4.2 and 4.3 is that all the results lie within a physiological range. (To recall, we observed non-physiological values of pressure when considering an inappropriate inlet boundary condition, cfr Section 3.4.2 of Chapter 3.)

Simulation of pressure gives better results in the CF and BP rather than in the small DF and PO arteries: averages of pulse pressure and pressure slope criteria are both smaller in the CF and BP than in the DF and PO. These indexes are indeed related: a greater PP implies a steeper slope. The average RMSE is also smaller in the CF than in the other arteries (more than a double increase of the RMSE from the CF up to the PO). Fig. 4.5 also shows that the simulation tends to over-estimate in-vivo measurements, as PP criteria are almost all negative. When comparing pressure waveforms, in most cases, the error in pressure curves generated by the model is localised in the systolic phase; the diastolic exponential decrease is rather well simulated, at the exception of some results in the popliteal artery.

Unlike pressure, simulation of velocity is not as good in the CF compared to the other vessels: the velocity RMSE is greater in the CF than in the other arteries. Furthermore, PSV , EDV and u^* criteria differences present a larger mismatch in the CF than in the other arteries (Table 4.2). Also, the differences in the PSV are larger than those for the EDV criteria. When comparing velocity waveforms with great mismatch, the simulated curve appears to be translated from the measurement with elongation of the systolic peak. Regarding the time of the PSV, this criteria is almost similar in the three arteries and slightly increased in the bypass. Unlike pressure, there is no clear direction of the differences between velocity simulations and measurements (Fig. 4.6): the numerical model does not systematically over- or under-estimate in-vivo measurements.

The root-mean-square error gives the mean value of the vertical distance between the simulated and in-vivo curves; it is a good indicator of the global efficiency of the model for a specific patient. We see for example that the model seems to be efficient for patients 15, 16 or 19. On the opposite, it is not for patients 14, 22 or 25. As introduced in the process of transformation of data (Fig. 4.1), the simulated curves are the results from many steps, each step inducing some imprecisions. Therefore, we should not expect a perfect matching between simulations and measurements. Nevertheless, similar features of erroneous simulation can be observed amongst patients. We describe three of them in the following.

4.1.3 Results (2): Clinical cases

Depending on the patient considered, results from the numerical model do not perfectly match the in-vivo measurements. In those cases, when comparing waveforms from simulations and measurements, we observe recurrent features of errors: e.g. an important mismatch in the distal artery or disagreement of peak systolic velocity and pressure. We explain the cause of these unexpected results of simulation and we suggest some modification of the model and parameters in order to improve them. We consider 3 different cases that we describe on basis of the result from a specific patient, namely the mismatch in popliteal pressure and velocity (patient #19), the mismatch in *PSV* in the bypass (patient #23), the mismatch in pulse pressure and velocity in all arteries (patient #25).

Clinical case #1: Pressure and velocity drop in the popliteal

Let us consider the in-vivo results from patient #19 (Fig. 4.7). Important pressure and velocity drops are observed in the popliteal artery and are not reproduced by the model.

This particular feature results from blood leakage at the level of the bypass. The bypass used for this patient is made of in-vivo material: the saphenous vein has been used in-situ. The vein is not removed from its natural surrounding but its valves are extracted in order to allow blood to flow downwards. Furthermore, side branch fistulae of the vein need to be ligated in order to avoid leakages to the collateral or venous circulation. In this case, small collateral arteries and side branch fistulae have not been properly ligated during surgery, inducing blood leakage. This was confirmed by surgeons a few days after surgery. We indeed observe that the in-vivo flow distribution through the upper-leg shows a drop of 33% of the local flow at the CF bifurcation and at the distal anastomosis (see Patient #19 in Appendix B). Notice that a pressure drop in the popliteal is also observed in patient #14. As the bypass of this patient is made of Gore-Tex, no leakages are expected inside the graft. Though, a large flow decrease is observed between the bypass and popliteal which might be due to leakages through the anastomosis or small collateral arteries.

To model leakages, we follow Leguy's approach (Leguy et al., 2010) and insert two extra side branches at medium length of the CF and venous BP. Parameters of the two side branches are computed as follows (Table 4.4): the rigidity is taken identical to the parent vessel (the CF and BP respectively), the area is reduced by half, in order to allow 33% flow leakage through each collateral. The windkessel outlets represent the resistive and compliant condition of the parent vessel.

In addition to the introduction of two leakage vessels, we manually modified the diameter and PWV of the popliteal artery ($D_{PO} = 0.43 \text{ cm}$; $c_{PO} = 14 \text{ m/s}$) and we increased the resistance of the BP leakage ($R_{BP \text{ leakage}} = 8.0 \text{ e}^4$) in order to obtain a better fitting between simulations and measurements.

		CF leakage	BP leakage
L	(cm)	1	1
D_0	(cm)	0.43	0.3
c	(m/s)	5.8	15
R	($cm^{-4}gs^{-1}$)	$3.62e^4$	$4.2e^4$
C	($cm^4g^{-1}s^2$)	$3.29e^{-5}$	$2.9e^{-5}$

Table 4.4 – Geometry (length L and mean diastolic diameter D_0), pulse wave velocity c , peripheral resistances R and compliances C characterising the additional vessels modeling leakages in patient #19.

Fig. 4.7 presents the improved results from this simulation with fittings of the model and parameters. Despite the introduction of leakages, the numerical simulation does not capture the systolic damping observed in the measured popliteal pressure. This pressure drop might result from energy losses and damping effects due to the arterial wall viscoelasticity. This effect is indeed not taken into account in our model which considers the arterial wall as an elastic material.

Clinical case #2: Peak systolic velocity in the bypass

Let us now consider the results from patient #23 (Fig. 4.8). We firstly notice that in-vivo measurements in the deep femoral artery present unexpected large pressure and velocity drops. This result is probably due to an error in the data acquisition: signals are measured simultaneously with an invasive guide wire, which might have been too close to the arterial wall. Indeed, velocity waveforms measured a few days after surgery do not present any particular drop.

Besides the DF artery, results are very satisfactory in the other arteries, at the exception of the velocity in the bypass. In all arteries, pressure waveform contours are well reproduced and lie within the same physiological range. The biphasic velocity contour propagates also well towards distal arteries, even if its diastolic fluctuations are not emphasized in the numerical result. Though, in the bypass, the in-vivo PSV is under-estimated of about 20 cm/s . Notice that this inefficiency of the model is also observed in patient #15.

Improved results of simulation were obtained by parameter fitting. In this case, we only reduced the bypass diameter by 17% ($D_{0BP} = 0.5\text{ cm}$). As we will see in the next sensitivity analysis, the BP diameter has only a significant influence on the velocity in the BP, and does not influence the other hemodynamic variables much. Results from this fitted simulation are displayed in Fig. 4.8: the simulation of velocity in the BP is close to the in-vivo observations, while simulations in the other arteries remain similar.

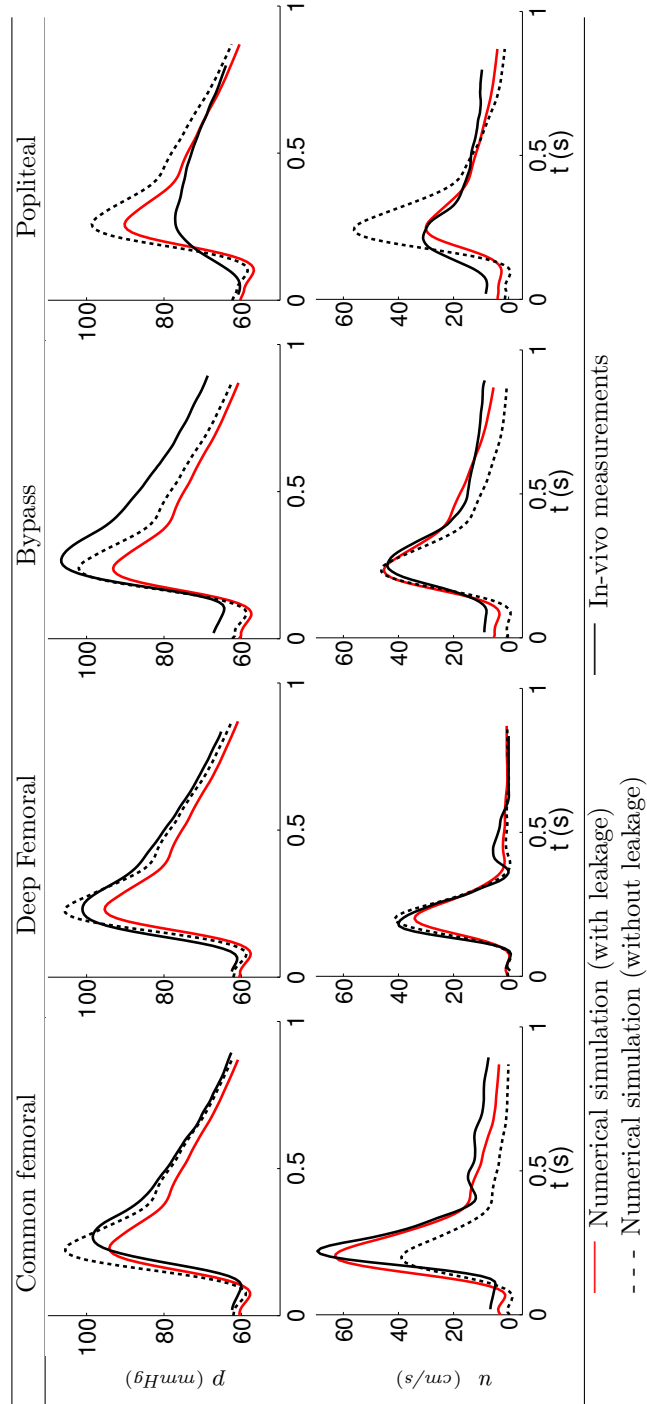


Figure 4.7 – Comparison of in-vivo measurements and numerical results for patient #19 using the initial model and the model with leakages and manual fittings.

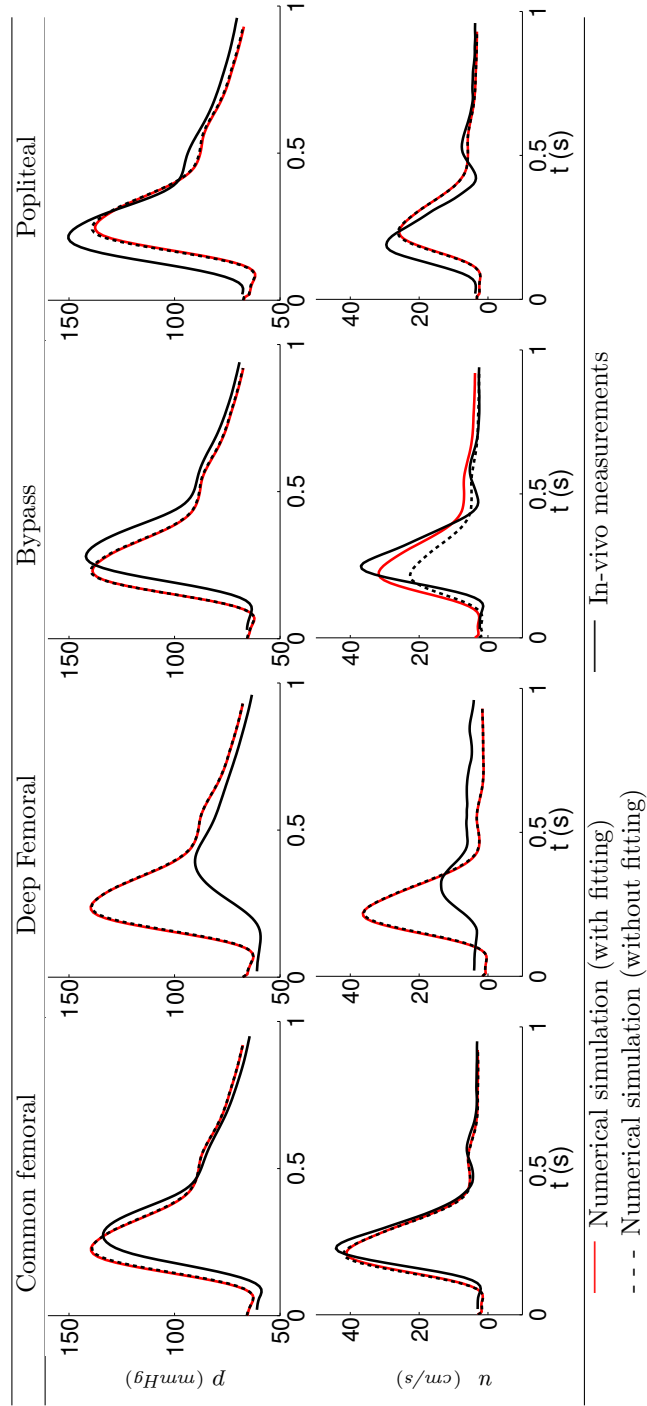


Figure 4.8 – Comparison of in-vivo measurements and numerical results for patient #23 using the initial model and the model with manual fitting.

Clinical case #3: Pulse pressure and velocity

Fig. 4.9 presents the results for patient #25. In this clinical case, large differences in the pressure and velocity pulses are observed between simulations and in-vivo data. Notice that this model inaccuracy is also observed in patients #22 and #24. Furthermore, for patient #25, we observe large pressure and velocity drops in the popliteal artery. Let us assume that these popliteal drops result from blood leakages through small collateral arteries, similarly to the clinical case #1. We will focus here on the differences in systolic pulses and will present parameters fitting in order to reduce those.

Improvement of the simulated pulses is obtained by modifying mainly the pulse wave velocities and, to a lesser extend, the vessel diameters. Table 4.5 presents these fittings and expresses them as a percentage of the initial parameter value. As we will show in the next sensitivity analysis, the PWV is the parameter of the model that influences the most the pulse pressure. Regarding velocity in a vessel, it is mostly influenced by the diameter of the vessel considered. Depending on the direction of the difference, we adjusted D_0 in each vessel (e.g. as velocity is under-estimated in the CF, we decreased D_{CF}). Notice that modifying the PWV in the three distal vessels (c_{DF} , c_{BP} and c_{PO}) was sufficient to obtain an appropriate pressure pulse reduction in the CF. Pressure modifications are transmitted throughout the arterial network while velocity adjustments have a local effect.

Artery	D_0 (cm)		c (m/s)	
CF	0.7	-15%	5.0	±0%
DF	0.55	+10%	5.8	-40%
BP	0.7	+17%	5.4	-40%
PO	0.53	±0%	3.8	-40%

Table 4.5 – Mean diastolic diameter D_0 and pulse wave velocity c characterising the fittings in patient #25.

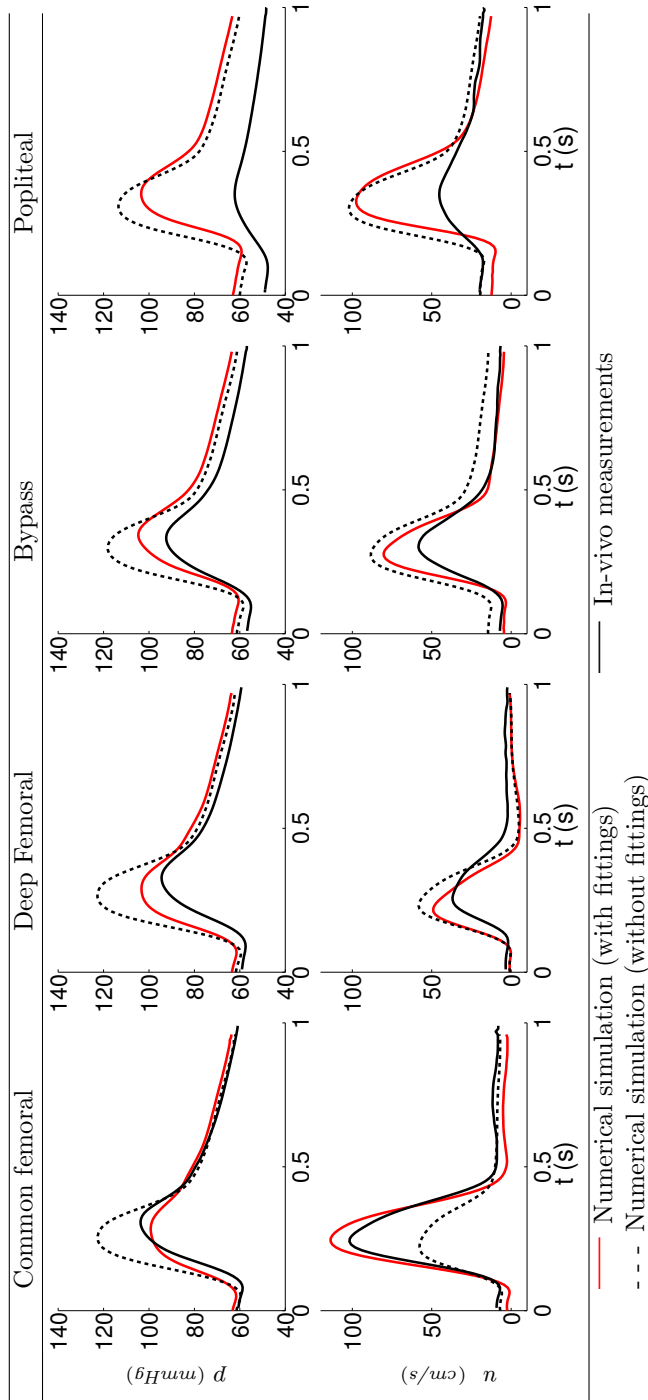


Figure 4.9 – Comparison of in-vivo measurements and numerical results for patient #25 using the initial model and the model with manual fittings.

4.2 Sensitivity analysis of the model

A sensitivity analysis (SA) aims at studying the effect of parameter uncertainty on the results from a model. Two types of analysis can be defined (Saltelli et al., 2004). A local SA evaluates the effect of one parameter varying around its initial value, while all other input parameters remain unchanged. In a global SA, all input parameters are changed simultaneously within their uncertainty range, and interactions between model parameters can be studied.

In this work, we restrain to a local SA as we do not have computing facilities for global SA at our disposal. Even if results of a local SA are only valid around an initial state and do not consider the interactions between input parameters, this standard method allows to give a first insight of the sensitivity of our arterial lower-limb model.

One particularity of this work is that the initial value used in the local SA corresponds to in-vivo patient-specific parameters. Therefore, one might expect different results if another patient is considered. In this chapter, we present the results of the local SA applied to data from patient #23 (initial data without manual fitting).

In a first part, this subsection defines the input and output variables of our model, the mathematical index used to evaluate the influence of parameters and the framework developed. Its second part aims at presenting the results of the local sensitivity analysis: it puts to the fore the global significance of each input parameter, and describes the way each parameter and assumption of the model influences the results of the model.

4.2.1 Methods

Input and output variables

In a first step, from the 18 parameters of the model, we will only retain 6 of them as inputs for this sensitivity analysis: the bypass length, the diameter and PWV of the four vessels, the resistance and compliance of the peripheral windkessels and the diastolic pressure. We do not consider the length of the three arteries, as in our model, these values do not represent any physiological distance. Table 4.6 presents the uncertainty range considered for each of these inputs, expressed in the input unit and as a percentage of variation. Each interval is chosen in order to reflect the measurement errors. Notice that the variation range of R is computed on basis of its definition as a ratio of pressure to flow: $\Delta R = \frac{\pm 30 \frac{mmHg}{cm^3/s}}{\pm 0.5 \frac{cm^3}{s}}$. The range of peripheral compliance $C = \tau/R$ follows from the variation of R with a variation of τ of $\pm 0.2 s$ (Leguy et al., 2011). In this work, a range of variation of one input variable is sampled by 10 simulations equally distant.

<i>Input</i>					<i>Output</i>		
Parameters	In-vivo value	Range	Range (%)		Parameters		
L_{BP}	(<i>cm</i>)	34.0	± 2.0	$\pm 6\%$	\Rightarrow	PP	(<i>mmHg</i>)
D_0	(<i>cm</i>)	0.59	± 0.1	$\pm 17\%$		\dot{p}	(<i>mmHg/s</i>)
c	(<i>m/s</i>)	25.0	± 5.0	$\pm 20\%$		PSV	(<i>cm/s</i>)
R	($cm^{-4}gs^{-1}$)	$4.55e^4$	$\pm 2.23e^4$	$\pm 50\%$		EDV	(<i>cm/s</i>)
C	($cm^4g^{-1}s^2$)	$2.5e^{-5}$	$\pm 2.0e^{-5}$	$\pm 80\%$		u^*	(<i>cm/s</i>)
p_0	(<i>mmHg</i>)	59.0	± 10.0	$\pm 17\%$		$t(PSV)$	(<i>s</i>)
						\bar{Q}	(cm^3/s)
						$\tilde{\epsilon}_p$	(<i>mmHg</i>)
						$\tilde{\epsilon}_u$	(<i>cm/s</i>)

Table 4.6 – Input and output parameters used in the first step of the sensitivity analysis. Input variables are presented with their range of variation in units and %.

In a second step, once the sensitivity of each type of input has been described, we will detail their sensitivity in the different vessels of the arterial network: diameter and PWV in the four vessels (D_{CF} , D_{DF} , D_{BP} , D_{PO} , c_{CF} , c_{DF} , c_{BP} , c_{PO}), peripheral resistance and compliance in the DF and PO windkessel models (R_{DF} , R_{PO} , C_{DF} , C_{PO}). Similar variation ranges are considered by arteries.

As output variables of the SA (Table 4.6), we consider the 7 criteria (defined in Subsection 4.1.1), as well as the pressure and velocity differences between simulated waveforms under input variation (var) and simulated waveforms at initial state (init):

$$\tilde{\epsilon}_p = \frac{1}{N} \sum_i^N \sqrt{(p_i^{\text{var}} - p_i^{\text{init}})^2} \quad \tilde{\epsilon}_u = \frac{1}{N} \sum_i^N \sqrt{(u_i^{\text{var}} - u_i^{\text{init}})^2} \quad (4.2)$$

with $\tilde{\epsilon}$ is the root-mean-square error (RMSE), and each curve is discretised by $N = 150$ points during one cardiac cycle. These 9 parameters describe the main characteristics of pressure and velocity waveforms.

Relative sensitivity index

The analysis aims at estimating the rate of change in the model outputs with respect to change in a system parameter. Following Leguy et al. (2010); Ellwein et al. (2008), we evaluate the sensitivity of each parameter by computing

the relative sensitivity index $I_{i,k}$ of output variable y_k to model parameter x_i ($i \in [1 : n]$). $I_{i,k}$ is defined as

$$I_{i,k} = \frac{\partial y_k}{\partial x_i} \frac{x_i}{y_k}, \quad (4.3)$$

with

$$\frac{\partial y_k}{\partial x_i} = \frac{y_k(x_1, \dots, x_{i-1}, x_i + \Delta x_i, x_{i+1}, \dots, x_n) - y_k(x)}{\Delta x_i}. \quad (4.4)$$

Notice that as $I_{i,k}$ is divided by the value of the output criteria y_k , this might induce particularly high values of this index when the output criteria is close to zero (e.g. EDV , u^*).

The definition of the sensitivity index of the RMSE outputs needs to be adapted, in view of their definition:

$$I_{i,\tilde{\epsilon}_p} = \tilde{\epsilon}_p \frac{x_i}{\Delta x_i} \quad I_{i,\tilde{\epsilon}_u} = \tilde{\epsilon}_u \frac{x_i}{\Delta x_i}. \quad (4.5)$$

Also, notice that, similarly to the Bland-Altman study (Chapter 2), using a correlation coefficient is not efficient here. Indeed, it would indicate if an output varies linearly with an input, instead of quantifying the relative importance of a parameter over another.

Framework of computation

The framework used in this analysis is based on a routine written in Matlab[®] (MathWorks, Natick, USA) which interacts with the ARGO code used for the numerical resolution of the coupled 1D-0D model. The routine writes the input text file for the C++ code (considering the variation $j \in [1, 10]$ of the input variable $i \in [1, 6]$); it launches the simulation run (i, j) and follows on with the next variations and the other input variables. Once all simulations are performed, the routine extracts the outputs out of the results and computes subsequent indexes.

4.2.2 Results

For each of the 6 input criteria (i) varying within their uncertainty range over 10 points, a sensitivity index $I_{i,k}$ can be computed for each of the 9 outputs (k) in the four arteries. In order to simplify these large amount of results, we will consider the average of the sensitivity indexes ($\bar{I}_{i,k}$) of each input variable over their uncertainty range. We observe that $I_{i,k}$ keeps a constant value within the range of variations for almost all input variables, i.e. there is a linear relation between the input variation and the effect on the output. In some outputs, this relation deviates from linearity for the resistance R and the diameter D_0 inputs (Fig. 4.10). For example, the sensitivity of the mean flow to the resistance increases with smaller values of R . Notice that, when $I_{i,k}$ is constant for

all variations, the amplitude of the range of variation does not matter for its computation.

Notice also that comparing values of $\bar{I}_{i,k}$ between different outputs might not be efficient, as outputs are computed differently. For example, an equal sensitivity of the pressure slope \dot{p} and of the *EDV* outputs ($\bar{I}_{i,\dot{p}} = \bar{I}_{i,EDV}$) has no physiological meaning. On the opposite, comparing values of $\bar{I}_{i,k}$ for one output highlights the importance of the different inputs.

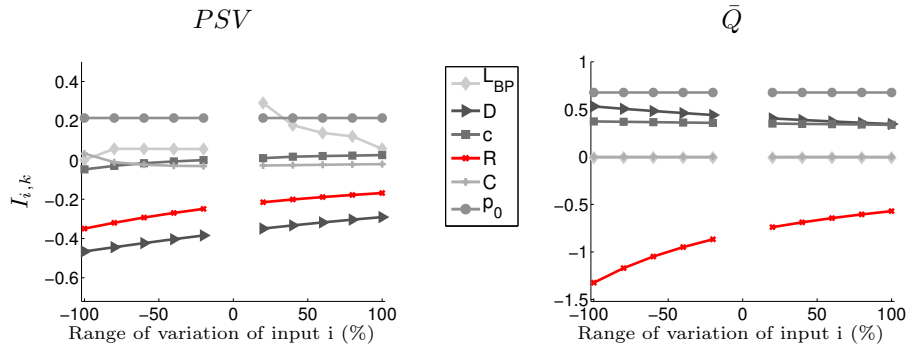


Figure 4.10 – Evolution of the relative sensitivity index $I_{i,k}$ of the outputs *PSV* (left) and \bar{Q} (right) within the uncertainty range of all input variables.

We present results in bar plots (Figs. 4.11 and 4.12): one figure looks at one output variable. For each output variable, the average relative sensitivity index is plotted as a function of the 6 input criteria. Four bars appear for each input criteria: each vessel is plotted individually (one color by vessel). We only present here the outputs $\tilde{\epsilon}_p$, $\tilde{\epsilon}_u$, *PP* and *EDV* as they are representative of pressure and velocity observations; results for the other outputs (\dot{p} , *PSV*, u^* , $t(\textit{PSV})$) can be found in Appendix C, Fig. C.1.

General observations

Fig. 4.11 presents the sensitivity of the RMSE outputs. Because these outputs are representative of the complete pressure and velocity waveforms, they are a good indicator of the influence of all inputs considered. In all vessels, the most significant inputs are the diameter, the diastolic pressure, the resistance and PWV, with a different influence intensity between pressure and velocity. Length of the bypass and compliance of the windkessel seem to have a reduced effect on both pressure and velocity. With the variation of input parameters, pressure waveforms change similarly in all vessels, while velocity waveform fluctuations are more affected by the location of the vessel. Pressure variations are transmitted throughout the arterial network while velocity variations have more a local impact.

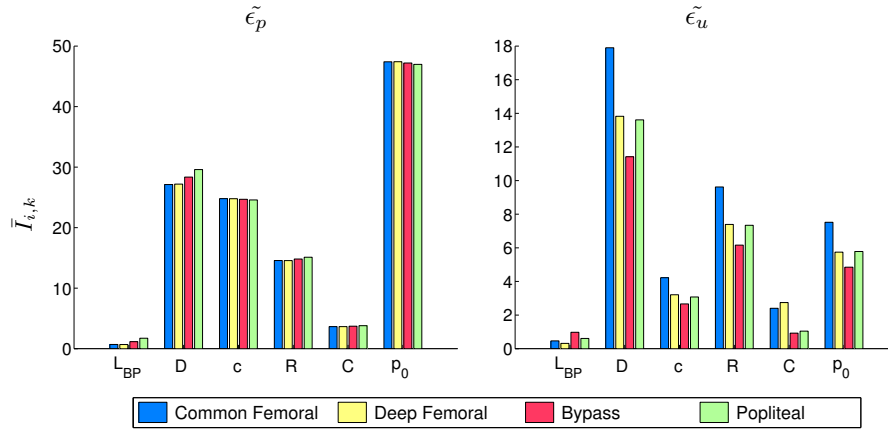


Figure 4.11 – Mean relative sensitivity index $\bar{I}_{i,k}$ of the outputs $\tilde{\epsilon}_p$ and $\tilde{\epsilon}_u$ as a function of the 6 input variables in the four leg vessels.

Even if RMSE outputs give a good idea of the influence of the inputs, these variables represent an absolute difference and do not allow to identify the “direction of the sensitivity” (i.e. does an input increase generate an increase or a decrease of the output?) Fig. 4.12 presents the relative sensitivity indexes of three punctual output variables: PP , EDV and \bar{Q} . If $\bar{I}_{i,k}$ is positive (negative), an increase of the input generates an increase (decrease) of the output value. For example, the mean flow intensity decreases with resistance augmentation (as $R = p/Q$).

Like pressure, variations of mean flow are similar in all vessels. As this behaviour is not observed in velocity (see also PSV and u^* plots in Appendix C), this highlights the importance of the cross-sectional area determination, as well as the arterial location.

What is the variation induced by each input?

In order to better understand the model, it is interesting to look in details into the variations induced by each input on the pressure, velocity and flow waveforms. The following resume is based on the relative sensitivity index results, as well as the evolution of variables in time, in the bypass vessel of patient #23.

Length of the bypass L_{BP} : The length of the BP vessel has nearly no influence on the hemodynamic results. Mean sensitivity indexes are insignificant. Observed pressure and velocity variations are smaller than 0.5 mmHg and 0.2 cm/s .

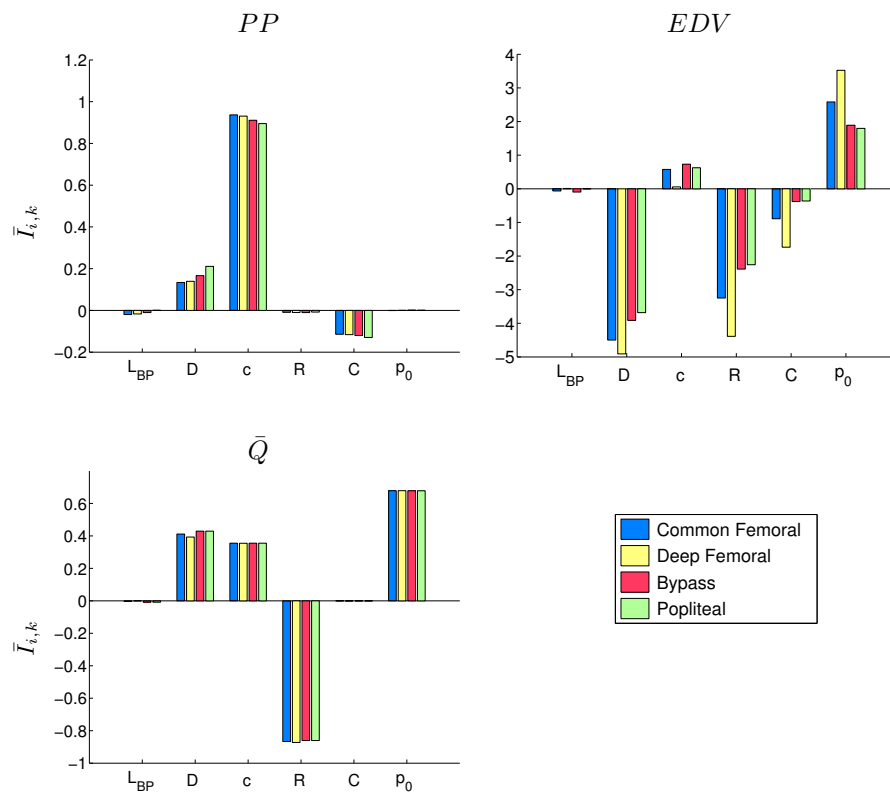


Figure 4.12 – Mean relative sensitivity index $\bar{I}_{i,k}$ of the outputs PP , EDV and \bar{Q} as a function of the 6 input variables in the four leg vessels.

The diameter D_0 : The effect of diameter variation on pressure and velocity consists of a translation of the curve enhanced during the systolic phase. Therefore, PP sensitivity is not nul, and velocity outputs (EDV , PSV and u^*) are largely influenced by this input with an inversed relation (if D_0 increases, u decreases). Amplification of the sensitivity to D_0 during the systolic phase is clearly marked on flow rate variations (Fig. 4.13).

The pulse wave velocity c : The vessel rigidity is especially influent on pressure and induces an extension of this waveform with increasing c . The variation of p is proportional to its value: it is emphasized during systole, inducing the important sensitivity of PP and \dot{p} to this input. On the opposite, velocity and flow are weakly influenced by the vessel rigidity, and the effect of c is visible only during diastole (Fig. 4.13).

Peripheral resistance R : The effect of resistance variation is visible on both pressure and velocity waveforms. With the increase of R , curves are translated upwards for p and downwards for u and Q (Fig. 4.13). Mean sensitivity index of outputs $\tilde{\epsilon}_p$, $\tilde{\epsilon}_u$ and \tilde{Q} are indeed significant compared to other inputs. Also, because of the effect of translation, $\bar{I}_{i,k}$ of PP is close to zero. Unlike all other inputs, resistance does not vary linearly in its variation range (as previously described in Fig. 4.10). A decrease of resistance has a much larger effect than an increase of the same amplitude. As we considered the mean $I_{i,k}$ on the variation range, this observation is not represented in bar plots but can be visualised in time plots.

Peripheral compliance C : Even if its range of variation reaches $\pm 80\%$, the effect of peripheral compliance variation is very small, and modifies only the shape of the waveform. Like resistance, compliance variation is not linear: a decrease of C is more pronounced than an increase. Compliance variation is well representative of the windkessel effect: if C is reduced, more fluctuations are observed in diastolic velocity and flow, the systolic velocity decreases earlier, and the systolic pressure continues to increase to a higher peak. These observations correspond to the definition of the compliance of a system (regulate hemodynamic variations). Increase of compliance corresponds to a very weak cushioning of the wave (Fig. 4.13). Notice that as compliance shortens or extends the systolic upslope, this input has a positive direct effect on the timing of the waves.

The diastolic pressure p_0 : The effect of p_0 is quite important on pressure and mean flow as it induces a translation of the whole pressure curve and as a consequence, a variation of mean pressure. Indeed, the pulse pressure is not sensitive at all to diastolic pressure variation. Velocity curves are also translated, but to a lesser extend (Fig. 4.13).

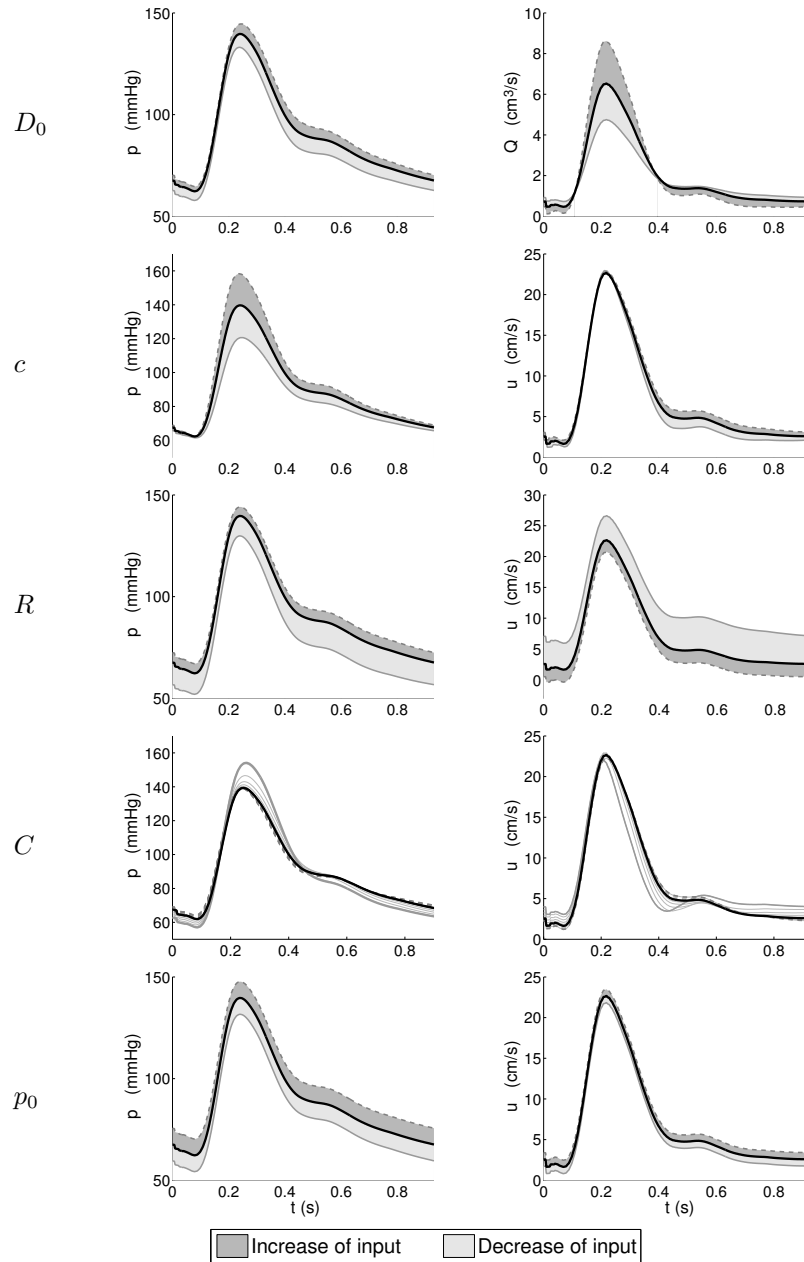


Figure 4.13 – Effect of input variation on p , u and Q waveforms over a cardiac cycle in the bypass, according to variations in Table 4.6. Waveforms generated by an increase (decrease) of the input variable form the dark (light) grey shaded area, bounded by a dashed (continuous) line. The input variable stands on the left of the plots. For the input C , areas are not shaded for ease of visualisation.

Influence of the arteries

These previous results describe the influence of an input when it is modified in the four vessels. Though, as we will describe in the following, vessels do not have the same influence on results.

Diameter D_0 and PWV c input variables are detailed in the four vessels, while parameters R and C from the DF and PO windkessel outlets are also considered separately. In Fig. 4.14, we present results from the sensitivity analysis of PP , $\tilde{\epsilon}_u$ and \bar{Q} outputs with inputs modified individually in each vessel. Other output results are presented in Appendix C on Figs. C.2 and C.3.

Notice that the presentation of results does not intend to compare the influence of inputs against each other (D_0 , c , R and C), but to compare the importance of arteries. Therefore, the scale of the graphs is adapted for each $\bar{I}_{i,k}$.

The observation of sensitivity indexes of PP and \bar{Q} outputs under the variation of diameters and PWV shows a marked importance of the CF artery. Flowrates in all vessels of the network are almost only dependant of the structural properties of this inlet artery. Pulse pressure is about two times more sensitive to the diameter and PWV of the CF than to the other arteries (DF and PO). Rigidity and dimension of the bypass present a very small influence on the pressure waveforms. Notice also that the direction of variation of the PP as a function of the diameter depends on the artery considered: an increase of the CF diameter induces an increase of the PP while an increase of the DF and PO diameters induce a reduction of PP . These opposite effects might explain the smaller amplitude of $\bar{I}_{i,k}$ when all vessel diameters are varied simultaneously ($\bar{I}_{D,PP} \simeq 0.2$ while $\bar{I}_{D_{CF},PP} \simeq 0.9$ and $\bar{I}_{D_{DF},PP} \simeq -0.4$).

Regarding the velocity as a function of the vessel diameter, u in a vessel is largely influenced by the diameter of this vessel, as shown by the four colored bars standing out in the plot of $\tilde{\epsilon}_u$ as a function of diameters. Furthermore, the relation between u and D_0 is negatively related, by conservation of flow. Regarding u as a function of the PWV, we observe that the velocity in an artery is also more influenced by the PWV of this artery, at the exception of the bypass. c_{BP} has a smaller effect on velocities than the PWV of the arteries, even if the BP is the central vessel in our arterial model.

Unlike diameter and PWV, pressure results are similarly influenced by both windkessel outlets: resistance results are identical and pressure seems more sensitive to the compliance of the DF network. The influence of the windkessel model is more pronounced on the local velocity, especially in a distal vessel: resistance and compliance of the DF influence more u in the DF, while R_{PO} and C_{PO} influence more u_{PO} . Notice that the BP velocity is largely influenced by the distal popliteal windkessel.

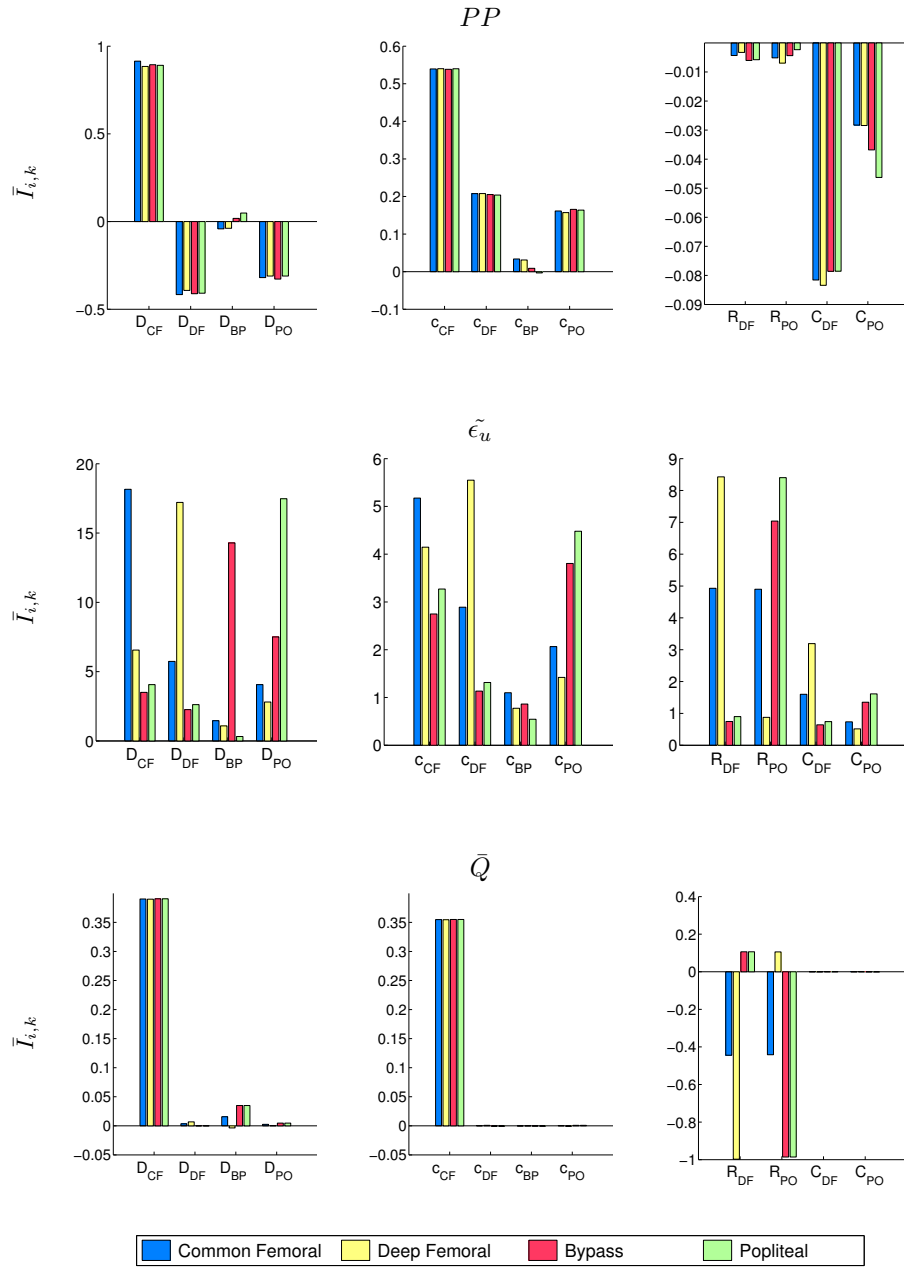


Figure 4.14 – Mean relative sensitivity index $\bar{I}_{i,k}$ of the outputs PP (1st line), $\tilde{\epsilon}_u$ (2nd line) and \bar{Q} (3rd line) as a function of the inputs D_0 (1st column), c (2nd column), R and C (3rd column) of the different arteries.

And around another initial state?

One important consequence of using a local sensitivity analysis is that results depend on the initial state. In this analysis, the initial state consists of the values of the patient-specific parameters, i.e. the parameters of subject #23.

In order to gain confidence that the previous observations could be generalised to all subjects studied, let us discuss the similarities and differences observed when an identical sensitivity analysis is applied to another subject. We applied the SA to subject #15, as results from the coupled 1D-0D model for this subject present a good correspondence with in-vivo data. All bar plots of relative sensitivity indexes can be found in Appendix C.

Similarly to subject #23, inputs p_0 , R , c and D_0 have a significant influence on the pressure and flowrate outputs: similar amplitude of mean relative sensitivity indexes are observed for these inputs. The sensitivity of velocity results is less marked for subject #15 than for subject #23. Depending on the velocity output considered, one vessel seems to be much more sensitive to a vessel than the others: $\bar{\epsilon}_u$ is more influenced by the PO, EDV by the CF and u^* by the BP. Notice also that the very high values of $\bar{I}_{i,k}$ for EDV and u^* outputs (which are probably due to the values of these outputs close to zero) extend the scale of $\bar{I}_{i,k}$ such that other indexes are not visible.

The sensitivity plots of outputs by arteries also show a predominance of the CF diameter and PWV regarding pressure and flowrate results. Velocity in an artery is also largely influenced by its arterial diameter (as observed on the $\bar{\epsilon}_u$ and PSV bar plots). While the effect of the windkessel resistance is also more pronounced on the velocity in the local artery, the pressure is more sensitive to the compliance of the DF windkessel.

To summarize, the main results of the SA regarding pressure and flow are similar to those observed in subject #23. Observations on the individual influence of the arteries are reproduced. The main difference comes from the analysis of velocity signals which fluctuate much between arteries. Additional analysis of other subjects should be performed in order to confirm these observations.

Influence of some assumptions of the model

The numerical model used in this work has been established using some basic assumptions. We will discuss the influence of three of them on the hemodynamical results, namely the constant viscosity, the assumption of a flat velocity profile and the fixed diameter of the bypass vessel.

In this work, we use the classical assumption of newtonian fluid with constant viscosity. Though, it has been shown that blood behaves as a non-newtonian and shear-thinning fluid (Nichols and O'Rourke, 2005). Many models have been suggested in order to take this behaviour into account (e.g. Einstein, Cross, Casson), inducing though increased complexity and additional parameters. In order to evaluate the influence of this assumption, we computed the variation

induced by a decrease and increase of the viscosity by a factor 2: in the case of patient #23, the RMSE $\tilde{\epsilon}$ in pressure and velocity in the bypass vessel do not vary significantly (Table 4.7).

	$\mu/2$	$\mu \cdot 2$
$\tilde{\epsilon}_p$ (mmHg)	0.26	0.51
$\tilde{\epsilon}_u$ (cm/s)	0.07	0.13

Table 4.7 – Root-mean-square error in pressure ($\tilde{\epsilon}_p$) and velocity ($\tilde{\epsilon}_u$) between results of simulation with initial viscosity ($\mu = 0.04 \text{ g/(cms)}$) and with a variation of μ by a factor 2.

In Chapter 3, the assumption of a flat velocity profile is used to fix the value of model parameters. Though, this choice contradicts the hypothesis taken in the analysis of the Doppler ultrasound exams, where a Poiseuille profile is used (cfr Subsection 2.1.2 of Chapter 2). Even though, in the numerical model, the difference between flat or Poiseuille profiles is rather limited. Indeed, in the case of patient #23, the RMSE in the bypass are negligible: $\tilde{\epsilon}_p = 0.87 \text{ mmHg}$ and $\tilde{\epsilon}_u = 0.22 \text{ cm/s}$ (Figure 4.15).

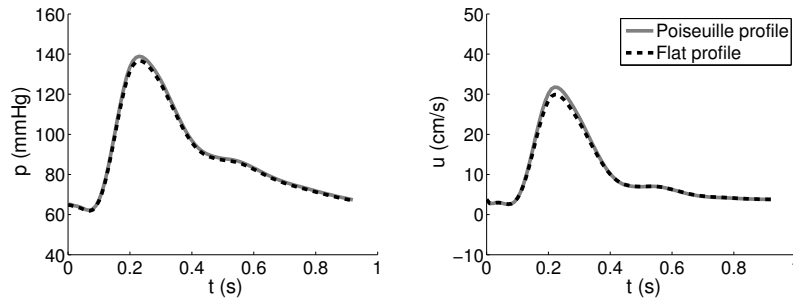


Figure 4.15 – Negligible influence of the velocity profile assumption on the numerical model. Comparison of numerical results (pressure, left and velocity, right) in the bypass of patient #23 between a Poiseuille profile (continuous grey line) and a flat velocity profile (dashed black line).

In view of the limited accuracy in the acquisition of the morphology of arteries, we have simply modeled arteries as cylindrical vessel, without tapering. Furthermore, in most clinical cases (7 out of 9), the bypass graft is made of synthetic material, which is of constant diameter. Though, introduction of tapering might be needed when a vein is used as bypass, or when one is interested to plan the effect of a new prototype of tapered graft. We introduced a linear tapering of the bypass vessel for patient #23 ($D = 0.6 - 0.4 \text{ cm}$) and compared the hemodynamic results of the numerical simulations (Figure 4.16). Variations

of pressure are negligible, while velocity decreases at the proximal BP and increases at the distal BP in order to ensure conservation of mass. From the point of view of the clinical efficiency, using a tapered bypass might be favorable as it increases the peak systolic velocity at the distal anastomosis, and it reduces the mismatch in geometry between the bypass graft and the native arteries. Though, it also increases the wall shear stress at that point, which is a contributing factor for the development of intimal hyperplasia (Leuprecht et al., 2002).

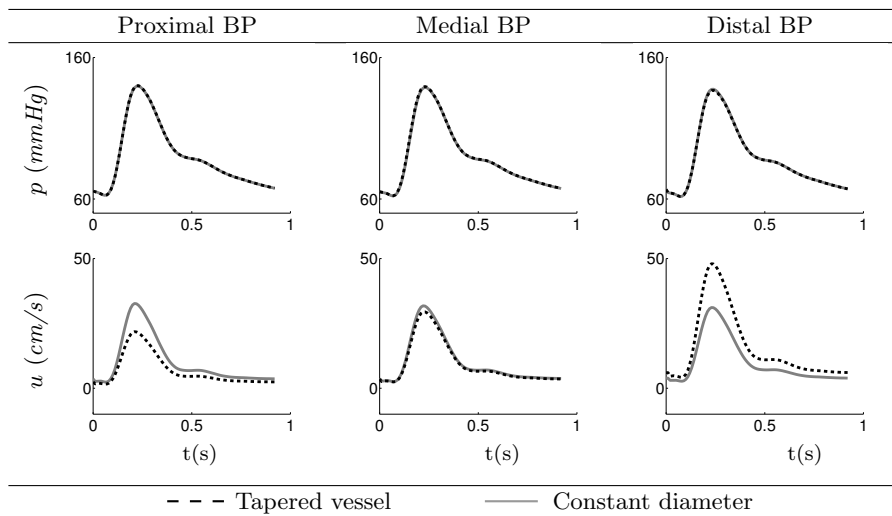


Figure 4.16 – Influence of the tapering of the bypass vessel on the pressure (top) and velocity (bottom) at three locations along the bypass: proximal, medial and distal. Numerical results with a constant diameter vessel ($D = 0.5 \text{ cm}$) are in continuous grey line, while numerical results with a tapered vessel ($D = 0.6 - 0.4 \text{ cm}$) are in dashed black line.

4.3 Discussion

In this chapter, we have studied the behaviour of a coupled 1D-0D model of the arterial blood flow in the lower-limb, using a validation study and a sensitivity analysis based on in-vivo data.

Validation

This work presents a first validation of a coupled 1D-0D model of the lower-limb focusing on pathological conditions of the subjects. Comparison of the model simulations against in-vivo measurements gives satisfactory results for most of the subjects, but still need some improvements for some of them in order to obtain an optimal reproduction of the in-vivo data. We showed, for example, that the introduction of blood leakages seems to be required in patients presenting a large flowrate drop in the distal popliteal artery. According to Steele et al. (2003), accurate modeling of collateral flow is crucial in surgical bypass planning as disease and treatment methods alter blood flow distribution amongst alternate pathways. Furthermore in our model, some parameters seem to present an inexact value, and therefore, their determination should be enhanced in precision (either during their measurement or their computation). In the few clinical cases considered, the validation study has stressed the importance of the diameter and PWV in all vessels.

The main imprecisions of the results of the model are summarized as follows. While the pressure results over-estimate the in-vivo measurements, there is no marked direction of deviation of velocity results in all patients. Compared to the other vessels, pressure results in the common femoral artery are more accurate, with discrepancies increasing towards distal arteries. On the opposite, velocity results are particularly less accurate in the common femoral artery.

In our model, we only include the energy losses from the viscous resistance of flow (K_R , see Chapter 3). As suggested in Steele et al. (2003), 1D models of pathological conditions should account for energy losses associated with secondary flows due to curvature, branching and stenoses. While these losses are generally small, they could play an important role in flow distribution, in the presence of collateral vessels and bypass grafts.

Our model considers the arterial wall as elastic and incompressible, and assumes a flat velocity profile in arteries. These assumptions are discussed in Reymond et al. (2009), where a viscoelastic constitutive law for arterial wall is introduced, and an improved description of the wall friction and convective acceleration term is considered using the Witzig-Womersley theory (in order to model pulsatile effects on the velocity profile). The results from this study show that the combined effects of viscoelasticity, improved wall shear stress and convective acceleration formulation induce a considerable variation of pressure and flow rate, especially in the peripheral sites (7.2% of p variation, 5.1% of u variation in the common iliac artery). In Alastruey et al. (2011), the importance

of wall visco-elasticity modeling is demonstrated in the comparison of numerical simulations with experimental in-vitro measurements. The inclusion of a Voigt-type visco-elastic wall reduces the underdamped high-frequency oscillations obtained using a purely elastic tube law, especially in peripheral vessels. These effects might therefore be important when fine details on peripheral sites are sought; including these properties could improve our model results in the lower-limb. Even though, increasing the complexity of the model might induce more uncertainty in the results as it requires the estimation of additional parameters.

Unlike in Steele et al. (2003); Reymond et al. (2009), tapering of arteries is not used here. Indeed, in our truncated model, the only vessel of considerable length is the bypass, which is often of constant diameter. We have shown that tapering of this vessel modifies the proximal and distal velocities, while pressure variations are negligible. In our case, we do not detect any small hemodynamic variation due to additional continuous wave reflections (distortion and sharpening of the pressure pulse) (Segers and Verdonck, 2000; Raines et al., 1974).

Our model is limited to the principal lower-limb arteries, because we aim at modeling patient-specific hemodynamics. Indeed, the acquisition of in-vivo data and the determination of elastic and geometrical properties of arteries is a difficult task. It requires the definition of a data acquisition protocol in accordance to the condition of the subjects considered. In this study, we analysed patients suffering from atherosclerosis and operated with bypass surgery. As described in Section 2.1 of Chapter 2, we used invasive measurements; indeed, non-invasive pressure acquisition (e.g. tonometry) is not efficient on the small, deep and calcified arteries of the leg. This invasive acquisition protocol needs therefore to be limited to the main arteries of the patient.

This study goes into details as it validates both pressure and velocity in all arteries of the leg. In comparison with literature, flow only was validated in Steele et al. (2003). In Reymond et al. (2009), blood flow was evaluated in the main aortic segments, lower-limb arteries, and in cerebral arteries; though, pressure was only considered in three arteries of the arterial network (radial, common carotid and temporal arteries). Notice also that Reymond et al.'s study performs a qualitative comparison of pressure and flow waveforms as it does not follow a subject-specific approach.

As presented in the process of transformation of data (Fig. 4.1), many steps are necessary from the raw measured data to the simulated waveforms. By associating an error estimate to each step of the process, each input to the model would be characterised by a combined error estimate, and a confidence interval on the simulated results could be drawn. Nevertheless, if one considers that these variations interact simultaneously, the number of simulations required to produce the confidence interval for one patient reaches 2^{18} runs! This approach is similar to a global sensitivity analysis and is not feasible with our computational resources.

Sensitivity analysis

In this work, we have rather conducted a local sensitivity analysis. Results are based on the analysis of one subject, though general observations are well reproduced for other subjects.

One objective of the SA is to determine the parameters which do not influence the outputs significantly. In our model, the length of the bypass presents a negligible influence on waveforms. The compliance of the 0D windkessel network is also poorly significant for velocity and pressure, and has only a small influence on the shape of the waveforms. Therefore, these two inputs do not need to be measured or computed with high precision.

The SA allows also to determine the parameters which influence significantly the model outputs. In our model, the vessel diameter has a great influence on both pressure and velocity results and should be measured precisely. In particular the diameter of the common femoral artery (the inlet artery) has a strong influence on the results. The windkessel resistance influences also significantly pressure and velocity waveforms. Finally, pressure is largely influenced by the rigidity of the vessel and its diastolic value. Again, the rigidity of the common femoral artery has more influence than the rigidity of other arteries.

The SA highlights the different behaviours of pressure and velocity under parameter variation: while the variation of the properties in one vessel are transmitted in all pressure waveforms, they have a local effect on velocity signals. This is particularly emphasized with the variation of the resistance and diameter inputs.

The SA also puts to the fore the way each input modifies the waveform contours. While variations of diameter, resistance and diastolic pressure induce mainly a translation of the pressure and velocity curves, variations of the PWV emphasize the pressure systolic peak and the velocity diastolic phase.

An unexpected result from the detailed sensitivity analysis in arteries is the relatively small influence of the structural properties (D_0 and c) of the bypass vessel on pressure and velocity waveforms. At the exception of a significant influence of D_{BP} on the velocity in the bypass u_{BP} , variation of D_{BP} and c_{BP} have only a small influence on the outputs, in comparison with D_0 and c of other arteries. At the exception of the direct relation between bypass diameter and velocity, the importance of the graft material and dimensions in a bypass surgery does not appear in this SA of our 1D-0D model. As a consequence, if one is interested in the extrapolation of the bypass surgery outcome with other graft properties, the 1D-0D model of wave propagation might not be sufficient and should be considered together with other models (e.g. 3D models of anastomoses).

The local SA performed in Leguy et al. (2010) focuses on the wave propagation in a model of the arm, based on patient-specific data. While the objective of that work is to estimate arterial mechanical properties, we obtain some similar conclusions in the present analysis: the large influence of resistance on

mean pressure, the significant influence of resistance and arterial wall rigidity on pulse pressure. They also observe the increased influence of the inlet artery of their truncated arterial network of the arm (i.e. the brachial artery), while this result is not particularly emphasized in their conclusions. Leguy et al. also report the need of higher precision when determining properties of small sized arteries with ultrasound registration methods.

Similarly than in Leguy et al. (2010); Ellwein et al. (2008), this local SA has demonstrated the complex relationship between the model parameters and the numerical simulations. A global sensitivity analysis (Leguy et al., 2011; Saltelli et al., 2008) or parametric uncertainty analysis (Xiu and Sherwin, 2007) could help to understand the variation of the model results to changes of multiple parameters in a defined range. Furthermore, as parameters act dependently on each other, it would be interesting to determine the correlation between parameters. A global SA approach is followed in Leguy et al. (2011): the main results are that output variables are significantly influenced by more than one system parameter, and that uncertainties in model parameters and input blood flow induce large variations in output variables. Furthermore, the global SA shows that the Young's modulus appears to have the largest influence and arterial length the smallest. Notice that the combined influence of the different parameters (i.e. correlations between input and output parameters) could not be determined due to the complexity of the results obtained.

Wave Intensity Analysis

One of the most important causes of graft failure is the development of myointimal hyperplasia at the anastomosis, especially in the distal location (Taylor et al., 1987; Sottiurai et al., 1983). The triggers for its formation are injury, circulating blood components, abnormal hemodynamics or impedance mismatch between the native vessel and the graft material (Toes, 2002). Three-dimensional studies have shown that abnormal hemodynamics may create zones of high or low wall shear stress that contribute to the development of plaque along the graft wall or at the distal anastomosis (Leuprecht et al., 2002; Pousset et al., 2006). Clinical studies have pointed out that the patency of the bypass in time depends on the nature of the bypass material and its ability to develop an endothelium along its inner wall (Albers et al., 2003; Norgren et al., 2007); venous material showing a higher 4-year bypass patency rate than synthetic ones. Nowadays, while clinical and 3D numerical studies are well-developed, the mechanisms responsible for bypass occlusion are not clearly understood yet.

In this work, we consider the wave-traveling approach in order to improve our understanding of the hemodynamics in the leg, after a bypass surgery. Formulated by Parker et al. (Parker and Jones, 1990), the wave intensity analysis (WIA) is an efficient tool for studying wave propagation and reflection and for quantifying wave power and energy. Based on the method of characteristics, this time-domain method presents the advantages to be intuitive and can be used in non-linear systems. It has been widely used to understand the physiology in the arterial system such as in the aorta (Parker and Jones, 1990; Jones et al., 2002; Khir et al., 2001a; Koh et al., 1998), the coronaries (Hughes et al., 2008; Davies et al., 2006a; Sun et al., 2000) or the pulmonary circulation (Hollander et al., 2001). It has also been applied to major systemic arteries: carotid and upper-limb arteries (Zambanini et al., 2005; Ohte et al., 2003) and femoral arte-

The content of this chapter will to be submitted in: Willemet M., Lacroix V., Khir. A., Marchandise E., Wave intensity analysis in the lower-limb arteries of human during peripheral bypass surgery. *American Journal of Physiology - Heart and Circulatory Physiology*.

ries (Borlotti et al., 2010) of healthy subjects. While wave intensity analysis has been used to understand some pathology (e.g. hypertension (Fujimoto et al., 2004; Manisty et al., 2009), heart failure (Curtis et al., 2007)), hemodynamics in atherosclerosed lower-limb arteries has never been analysed with this tool.

When designing a patient-specific bypass surgery, the clinician has many parameters to decide, e.g. the material and size of the bypass, the types and locations of anastomoses. In order to study the influence of his choice, one can use numerical simulations of the hemodynamics. Nowadays, the cardiovascular system can be efficiently described using mathematical models. Thanks to their accuracy, efficiency and reduced number of parameters, coupled one-dimensional and zero-dimensional models are widely used (cfr Chapter 3). Furthermore, numerous studies have validated these 1D-0D models against in-vivo data (cfr Chapter 4). In this study, we will apply the WIA theory to the results from a 1D-0D truncated arterial model of the bypassed lower-limb. The combination of these numerical tools offers the opportunity to study the influence of the bypass parameters (e.g. rigidity of the material, dimensions) and to model some hypothetical pathological conditions (e.g. blood leakage) from the point of view of the intensity of waves.

The first aim of this chapter is to study the wave propagation in bypassed and occluded lower-limb arteries. By applying the WIA to in-vivo experimental data, we describe the main features observed in the pathological leg arteries before and after bypass surgery, and compare them with healthy data. Emphasis is put on the reflections produced by the insertion of the graft vessel. Because of the pathological condition of the subjects analysed, we show that a larger and longer wave pattern is observed. The second aim of this work is to study the influence of the bypass parameters or abnormal hemodynamics on the wave propagation pattern. To do so, we use simulations from a numerical 1D-0D model and create hypothetical clinical cases.

In the first section of this work, the wave intensity theory, in-vivo data acquisition, and numerical model are presented. Results are then subdivided in two sections. In the first section of results, the in-vivo wave intensity in bypassed and occluded lower-limbs is described and discussed. In the second section of results, we analyse some in-vivo clinical cases in combination with the numerical model predictions. In particular, we describe the influence of reflections in the leg and the effect of blood leakage.

5.1 Materials and methods

5.1.1 Theoretical background of the WIA

The theoretical basis of the wave intensity analysis is the solution of the classical 1D conservation of mass and momentum non-linear equations (Parker et al., 1988). Wave intensity, dI , is defined as the amount of energy carried by

the wave per cross-sectional area of the vessel (SI units : $W/(m^2 s^2)$):

$$dI = \frac{dp}{dt} \frac{du}{dt} \quad (5.1)$$

where dp and du are the pressure and velocity differentials. In order to compare results acquired at different sampling time, it is convenient to normalize the derivatives by the sampling time dt (Ramsey and Sugawara, 1997). Besides its dimensional analysis, the main interest in the WIA is its ability to detect the importance of forward and backward propagating waves. While forward waves mainly result from the contraction and relaxation of the ventricle, backward waves are created by wave reflections at the vasculature. These forward (dp_f , du_f) and backward (dp_b , du_b) waves are described through Eqs. (3.23) and (3.24) in Chapter 3 and are derived from the theory of the method of characteristics (Parker and Jones, 1990; Parker, 2009). One can then compute the forward (dI_f) and backward wave intensities (dI_b):

$$dI_{f,b} = \frac{dp_{f,b}}{dt} \frac{du_{f,b}}{dt}. \quad (5.2)$$

with dI_f being positive and dI_b negative.

Four different types of waves might be observed, depending on the pressure and velocity variations (Table 5.1). In the aorta and in the main systemic arteries, the wave intensity presents three distinct waves. The first wave of significant intensity, a forward compression wave (FCW), arises with the systolic upstroke and is the result of the contraction of the left ventricle. During mid-systole, quickly after the FCW, a weak negative wave is observed. This backward compression wave (BCW) is the result of the reflection of the FCW at discontinuities, bifurcations and peripheral networks. The third wave, a forward expansion wave (FEW), is observed in late systole and is generated by the left ventricle just before the aortic valve closure.

	Acceleration $du > 0$	Deceleration $du < 0$
Compression $dp > 0$	Forward Compression (FCW) $dI > 0$	Backward Compression (BCW) $dI < 0$
Expansion $dp < 0$	Backward Expansion (BEW) $dI < 0$	Forward Expansion (FEW) $dI > 0$

Table 5.1 – Classification of waves as a function of the sign of dp and du

The wave energy (also called cumulative intensity) of an individual wave is described with the integral of the intensity, it takes into account both the duration and magnitude of each wave (SI units : $kJ m^{-2} s^{-2}$):

$$I = \int_{t_{start}}^{t_{end}} \left. \frac{dp}{dt} \frac{du}{dt} \right|_{wave} dt,$$

where t_{start} and t_{end} represent respectively the time of origin and end of the individual wave considered.

Many indicators have been defined in order to quantify the reflection of waves (Manisty et al., 2009; Mynard et al., 2008). In this study, we consider the reflection coefficient R_f and the reflection index $R_{|p|}$.

The reflection coefficient R_f is defined as the ratio of the change of pressure across the reflected wave to the change of pressure in the incident wave. It is computed on basis of the physical properties of arteries. At an arterial junction, R_f in the upstream vessel is computed as:

$$R_f = \frac{Y_{up} - \sum_j Y_{down(j)}}{Y_{up} + \sum_j Y_{down(j)}} \quad (5.3)$$

where Y is the characteristic admittance of the vessel in the upstream or downstream vessels: $Y = \frac{A}{\rho c}$ and A the area of the vessel. The reflection coefficient varies between -1 and 1 and a total reflection is observed at these extreme values. When $R_f = 0$, the arterial junction is said to be well-matched for forward-traveling waves.

The reflection index $R_{|p|}$ is defined as the ratio of amplitudes of backward to forward pressure waves $R_{|p|} = \frac{|p_b|}{|p_f|}$ (Khir and Parker, 2002). Notice that this coefficient is also referred to as reflection magnitude in Swillens and Segers (2008); Westerhof et al. (2006). Compared with other reflection indexes, $R_{|p|}$ is more appropriate as it is not sensitive to non-linearities (Mynard et al., 2008).

5.1.2 In-vivo data acquisition

Subjects. We have at our disposal in-vivo data from 9 subjects in order to perform a wave intensity analysis of bypassed legs hemodynamics. Amongst these 9 patients, we dispose of measurements of hemodynamics in the occluded leg, before insertion of the bypass, for 4 of them. Average clinical parameters of the subjects are presented in Subsection 2.1.3 of Chapter 2. For each patient analysed, in-vivo measurements and parameters, as well as bypass characteristics are presented in Appendix B. In the following, we refer to the state *PRE* as the patient's condition during surgery with occlusion of the superficial femoral artery; and to *POST* as the patient's condition during surgery with insertion of the bypass graft in the leg.

Data acquisition. As described in Section 2.1 of Chapter 2, in-vivo data was acquired during surgery, while patients were under anaesthesia in a stable hemodynamical state. Pressure and velocity were acquired simultaneously using invasive techniques at four locations in the leg (common femoral artery (CF), deep femoral artery (DF), bypass graft (BP) and popliteal artery (PO)). Ensemble average and filtering of the data is performed on the measured signals in order to obtain a representative set of simultaneous signals for each artery (see Subsection 2.1.2 of Chapter 2). Pulse wave velocities c of arteries and bypass graft are evaluated locally using the PU-loop, as described in Section 2.3 of Chapter 2.

5.1.3 1D-0D numerical model

The coupled 1D-0D numerical model is described in Chapter 3: it solves the 1D Euler equations of blood flow in arteries and is coupled with lumped 0D models describing the peripheral circulation. Our model focuses on a truncated arterial network of the lower-limb. It comprises the four vessels of the leg (CF, DF, BP, PO), modeled as one-dimensional segments (Fig. 4.2, Chapter 4). As inlet boundary condition, the forward component of the velocity in the CF is prescribed in an absorbing way. RCR-windkessel models are used as outlet boundary condition downwards of the DF and PO.

5.1.4 Statistical analysis

Results are presented as mean \pm standard deviation (SD). Differences in intensities between two arteries are compared using Student's unpaired t -test, combined with the Kolmogorov-Smirnov test for different distributions and small samples. Differences with P -values less than 0.05 are considered significant.

5.2 In-vivo wave intensity in bypassed and occluded lower-limbs

This first section of results aims at describing and analyzing the in-vivo wave intensity in bypassed and occluded legs. For all patients analysed, plots of wave intensity in the four vessels of the leg are displayed in Appendix B, for POST and PRE conditions (when available).

5.2.1 Results

In this section, we describe and discuss the wave pattern observed in the vessels of an occluded and bypassed leg. Average intensities and timings of

waves are described and compared between arteries. Mean PWV and reflection coefficients are presented in PRE and POST states.

Representative examples of the wave intensities observed in the four vessels of an occluded and of a bypassed leg are shown in Figure 5.1. Similarly to the aorta or healthy femoral artery, the three main waves are present: an initial FCW, a mid-systolic BCW and a late-systolic FEW. Nevertheless, their width and time of arrival differ. Furthermore, the introduction of the bypass increases greatly the intensity of waves in the distal vessels.

Intensities of waves

The average cumulative intensity I and peaks of dI in the four vessels of the bypassed legs in all patients are presented in Table 5.2. There is a great variability between patients, probably due to their different pathological conditions. Even though, the cumulative intensities of the FCW decrease significantly as the waves travel forwards towards the peripheral distal arteries ($P < 0.05$ between CF and PO). The cumulative intensity of the BCW presents an opposite evolution: as the reflected wave travels backwards from the periphery to the proximal leg, its intensity significantly increases ($P < 0.05$ between PO and CF). The intensity of the FEW also decreases, though this is not statistically significant ($P = 0.13$). Similar conclusions can be drawn for the peak magnitude of dI , with statistical significance observed for all 3 waves.

The average cumulative intensity I and peaks of dI in the three arteries of an occluded leg are presented in Table 5.3. There is a very strong decrease of wave intensity (both I and dI) in the popliteal artery, distal to the superficial femoral occlusion. Furthermore, while forward waves are of similar magnitudes

<i>POST state</i>				
	CF	DF	BP	PO
<i>I (kJm⁻²s⁻²)</i>				
FCW	45.8 ± 40.1	25.4 ± 22.3	17.6 ± 9.7	14.6 ± 9.1
BCW	-4.8 ± 6.0	-6.8 ± 9.3	-1.0 ± 0.7	-0.7 ± 0.6
FEW	15.1 ± 13.6	5.5 ± 4.9	4.9 ± 3.5	4.6 ± 4.0
<i>Peak dI (kWm⁻²s⁻²)</i>				
FCW	802.7 ± 818.0	517.7 ± 567.3	299.0 ± 166.2	249.2 ± 168.5
BCW	-87.8 ± 130.9	-112.4 ± 136.3	-37.7 ± 54.4	-12.9 ± 11.6
FEW	167.5 ± 125.3	65.7 ± 54.2	61.9 ± 52.2	55.7 ± 46.6

Table 5.2 – Average ± SD in all patients of cumulative intensity (I) and peak wave intensity (Peak dI) of the three main waves in the common femoral (CF), deep femoral (DF), bypass vessel (BP) and popliteal (PO) arteries of a bypassed leg.

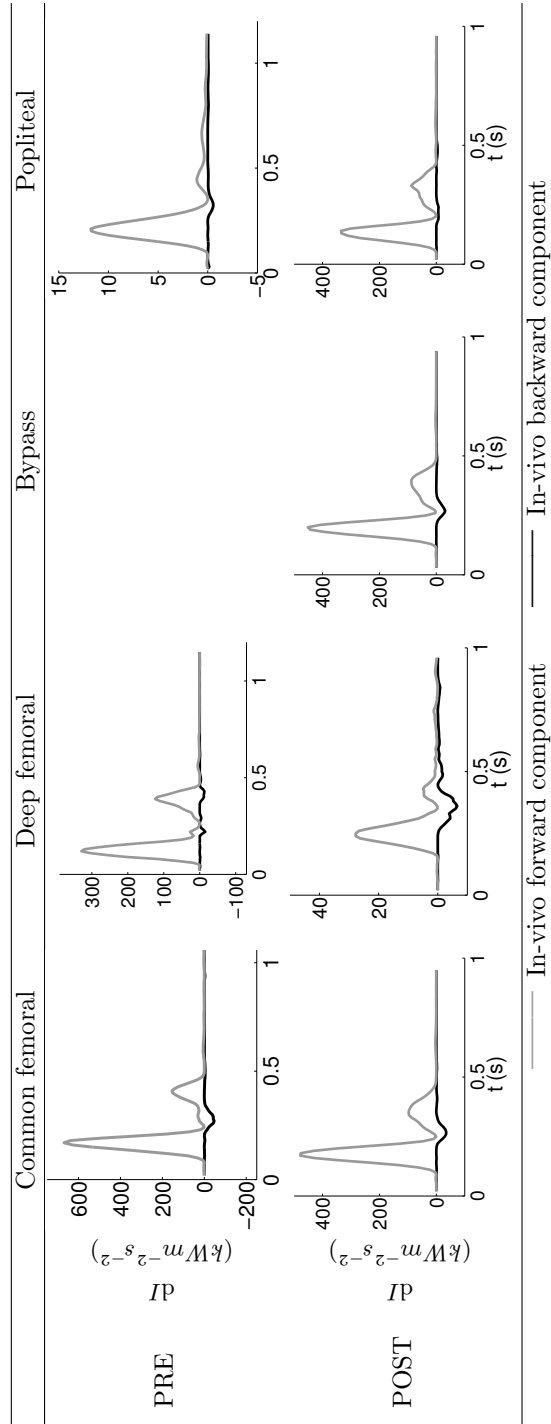


Figure 5.1 – Typical patterns of wave intensities in the 4 vessels of the lower-limb in PRE and POST states. Forward wave intensity dI_f is in grey line and backward wave intensity dI_b in black line. Data from patient #23 are presented.

<i>PRE state</i>			
	CF	DF	PO
<i>I (kJm⁻²s⁻²)</i>			
FCW	52.0 ± 32.5	24.9 ± 18.4	1.0 ± 0.7
BCW	-1.9 ± 1.6	-2.2 ± 2.1	-0.2 ± 0.4
FEW	12.4 ± 2.2	8.6 ± 5.4	0.2 ± 0.3
<i>Peak dI (kWm⁻²s⁻²)</i>			
FCW	959.3 ± 961.8	333.2 ± 263.1	9.4 ± 5.9
BCW	-28.0 ± 19.3	-28.0 ± 20.3	-2.2 ± 3.2
FEW	129.6 ± 22.2	83.7 ± 45.3	1.4 ± 1.5

Table 5.3 – Average ± SD in all patients of cumulative intensity (I) and peak wave intensity (Peak dI) of the three main waves in the common femoral (CF), deep femoral (DF) and popliteal (PO) arteries of occluded legs in all patients analysed.

between PRE and POST states, BCW are lower in the CF and DF in PRE state.

In comparison with the upper-limb, aorta and carotid arteries (Zambanini et al., 2005; Manisty et al., 2009; Curtis et al., 2007; Penny et al., 2008), the values of wave energy I reach the same order of magnitude. With the appropriate normalization by the time interval, the cumulative intensities (in $kJ m^{-2} s^{-2}$) of the main waves oscillate between 25 and 40 for the FCW, 3 and 7 for the BCW, 2 and 12 for the FEW.

Timings of waves

Table 5.4 presents the mean timing of start and end of the three waves in the common femoral artery, with respect to the onset of the FCW. In our population, the FEW arrives quickly after the FCW and overlays the BCW. In some subjects, the two forward waves follow each other without interruption, such that there is no “quiet” period without any significant wave intensity. In comparison with the carotid and upper-limb arteries (Zambanini et al., 2005), the FEW arrives earlier (194 ms in the CF versus 247 to 251 ms in upper-body arteries); while the BCW arrives later (90 ms in the CF versus 32 to 56 ms in upper-body arteries).

Compared with the PRE state, forward waves are wider, while the BCW arrives slightly later than in the bypassed leg.

No remarkable difference in intensities or timings are observed between above and below-knee bypasses.

		Timing of waves (<i>ms</i>)		
		start		end
<i>POST</i>	FCW	0	→	133 ± 25
	BCW	90 ± 19	→	213 ± 32
	FEW	194 ± 68	→	374 ± 48
<i>PRE</i>	FCW	0	→	158 ± 29
	BCW	137 ± 42	→	250 ± 35
	FEW	173 ± 21	→	395 ± 58

Table 5.4 – Average ± SD of the timing of the three waves in the common femoral artery of a bypassed leg (*POST*) and occluded leg (*PRE*): numeric values of start and end of waves.

Pulse wave velocity

Average PWV in the vessels of a bypassed leg are presented in Table 2.6 of Chapter 2. Values of wave speeds observed in the arteries of the leg are slightly higher than in healthy patients due to the presence of the pathology. Wave speeds increase along the leg of the patients, because of the reduction in arterial caliber. In the four patients with measurements before and after bypass suture, we observe a decrease of the PWV from the *PRE* to the *POST* state in the common femoral artery, while the opposite variation is observed in the popliteal.

Reflection coefficient

The average ± SD of reflection coefficient R_f computed with Eq. (5.3) equals 0.18 ± 0.38 at the CF bifurcation and 0.18 ± 0.36 at the distal anastomosis, in a bypassed leg. These large standard deviations illustrate the variability between patient's conditions. Values of these two reflection coefficients in each patient are displayed in Appendix B.

Table 5.5 presents the reflection index $R_{|p|}$ in the vessels of a bypassed and occluded leg. Similarly than for the intensities, the reflections are reduced in the *PRE* state.

5.2.2 Discussion

In the systemic circulation, waves are generated by the left ventricle (LV) ejecting blood into the aorta and therefore creating forward waves that propagate in the arterial network. While they propagate, waves are influenced by the surrounding tissues as well as by the morphology of the arteries. The typical pattern of waves observed in the main systemic arteries comprises three waves:

	CF	DF	BP	PO
$R_{ p }$ (%)				
<i>POST</i>	38.6 ± 14.5	49.3 ± 19.1	29.7 ± 18.6	29.9 ± 9.6
<i>PRE</i>	26.9 ± 5.0	33.1 ± 21.0	/	27.6 ± 19.0

Table 5.5 – Average \pm SD of the reflection index $R_{|p|}$ in the vessels of a bypassed (POST) and occluded (PRE) leg.

the FCW created by the LV contraction at the opening of the aortic valve, the BCW reflected by the vasculature and the FEW generated by the LV relaxation at closure of the aortic valve.

Subjects analysed

In order to fully understand the physiological signals treated in this work, let us recall the pathology of our subjects.

Our subjects are elderly people suffering from severe atherosclerosis; their distal arterial network presents an increased rigidity due to the arterial wall calcification (cfr Chapter 2). When a synthetic bypass material is used, because the graft material presents a smaller radial compliance (Daniele et al., 2003), the wall stiffness is increased as well. Thanks to the bypass, their peripheral run-off reaches normal values of flow. Indeed, vascular surgical literature demonstrated that a flow rate greater than 50 ml/min in the bypass is recommended for a bypass successful outcome (Stirnemann et al., 1994). These physiological conditions are particular to our subjects and are not met in normal conditions.

Furthermore, because of the vasodilation induced by anaesthesia, velocity waves present a biphasic waveform (Subsection 2.2.5, Chapter 2). Regarding the pressure, waveforms are similar to what is observed in old healthy subjects (Kelly et al., 1989). Contrary to the aorta, the dicrotic notch is not apparent in the femoral pressure waves, because of their location below the iliac bifurcation. In fact, the important reflection created at this point does not travel in the leg arteries.

Comparison with a healthy femoral artery

Recently, the wave intensity in healthy femoral arteries has been analysed using the logarithm of diameter and velocity data (*lnDU* method) (Borlotti et al., 2010; Feng and Khir, 2010). This method has been applied to in-vitro data and produced wave intensity patterns very close to those obtained with the classical *pu* analysis (Li and Khir, 2011). Even if intensity values may not be compared (m^2/s instead of W/m^2), times of arrival of waves as well as ratios between peaks remain very similar. A representative example of the diameter, velocity and wave intensity in the femoral artery of a healthy patient is shown

in Figure 5.2, left. Notice that this pattern of waves is similar to that observed in the aorta (Khir et al., 2001a; Koh et al., 1998).

The comparison of the wave intensity patterns between the healthy and pathological femoral arteries brings to the fore the influence of our pathological subjects (Figure 5.2). In order to emphasize the duration of each individual wave, areas under the pressure (or diameter), velocity and wave intensity signals are colored.

- In bypassed signals, waves are wider and extend over a longer period of time (Figure 5.3).
- In the pathological pressure, as soon as the systolic peak is reached, the pressure starts to decrease without reaching any plateau. As a result, pressure and velocity waves reach their systolic maxima nearly at the same time. The wave intensity pattern reflects this: the FEW (responsible for reducing p) arrives quickly after the FCW.
In the healthy femoral, once the systolic diameter is reached (at the end of the BCW), there is a period without any significant wave intensity. The diameter wave reaches some systolic plateau before decreasing at the beginning of the FEW. In that case, the velocity reaches its systolic peak (at the end of the FCW) earlier than the diameter signal (at the beginning of the FEW).
- While the reflected wave has a notable effect on the signals in the healthy subject (start of decrease of velocity, additional increase of diameter), its effect is more diffused in the pathological case, due to its simultaneous arrival to the FCW and FEW.

Comparison with a stented artery

We have studied wave intensity in a stenosed and stented leg (stent on the superficial femoral artery) during arteriography, on two subjects (Lacroix et al., 2012). Data were also acquired invasively using Volcano guide wire (cfr Section 2.1 of Chapter 2). Fig. 5.4 presents an example of patterns observed in the femoral artery above and below the stent, with stenosis and after dilatation and stenting.

We observe a large decrease of intensity downstream of the stenosis, similarly than in the occluded popliteal artery, even though the decrease is less marked in the stenosed artery. Regarding the pattern of waves, waves are wider than in the healthy condition like in the occluded and bypassed legs. The time delay between the FCW and the FEW in the stented artery seems to be longer than in the bypassed case.

The main observation from this clinical case is the similarity in width of waves with the bypassed condition, even if the pathology of these arteries is not as severe as the bypassed ones.

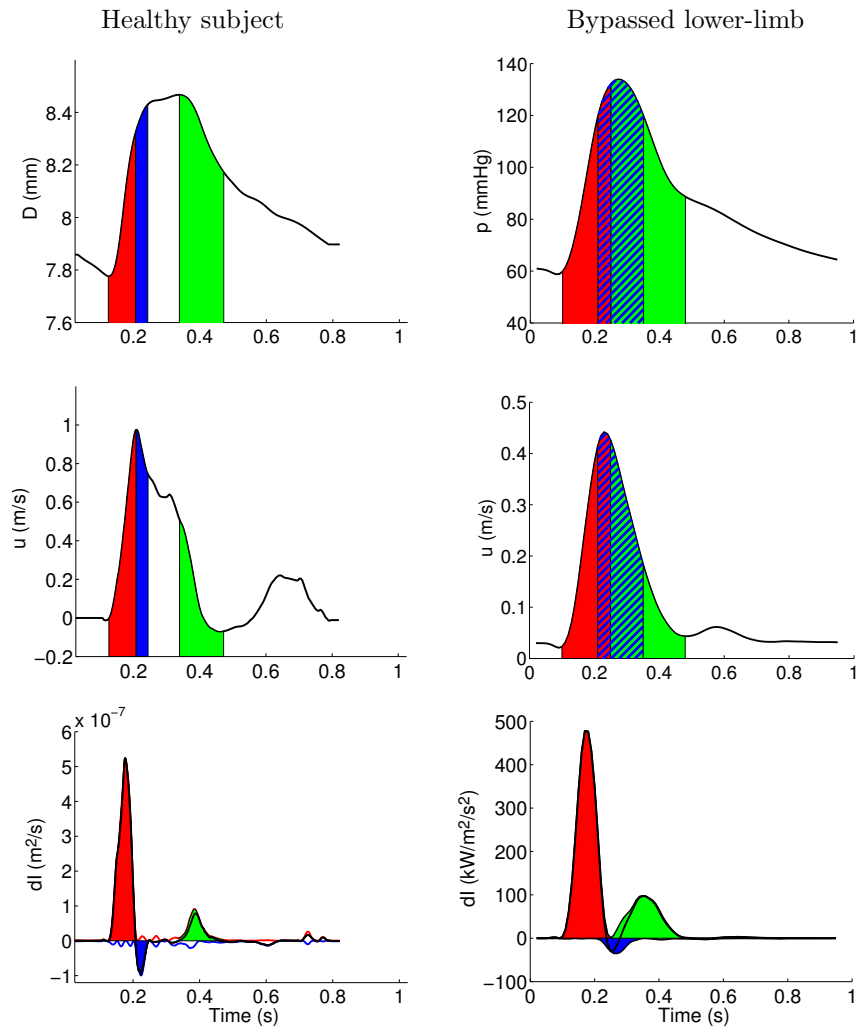


Figure 5.2 – Typical patterns of waves in the femoral artery of a healthy subject (left) and patient operated with femoro-popliteal bypass surgery (Patient #23) (right). From top to bottom: diameter D or pressure p , velocity u and wave intensity dI (total, forward and backward components). The pulse wave velocities measured by $\ln DU$ -loop or PU -loop are 6.7 m/s and 19.0 m/s respectively. The colored area under the D , p , u , dI signals represent the duration of each individual wave: FCW in red, BCW in blue and FEW in green. Healthy data provided by A. Borlotti and P. Segers (Borlotti et al., 2010).

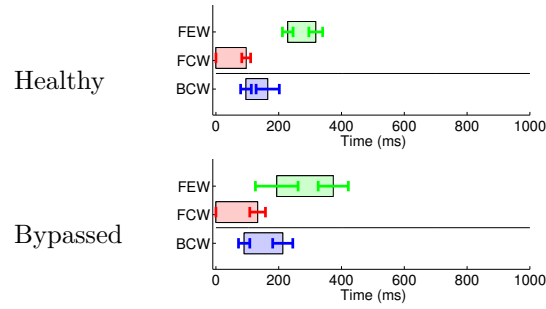


Figure 5.3 – Average timing of the three waves in the common femoral artery of a healthy (top) and a bypassed leg (bottom) over a cardiac cycle: FCW is in red, BCW in blue and FEW in green. Healthy data provided by A. Borlotti and P. Segers (Borlotti et al., 2010).

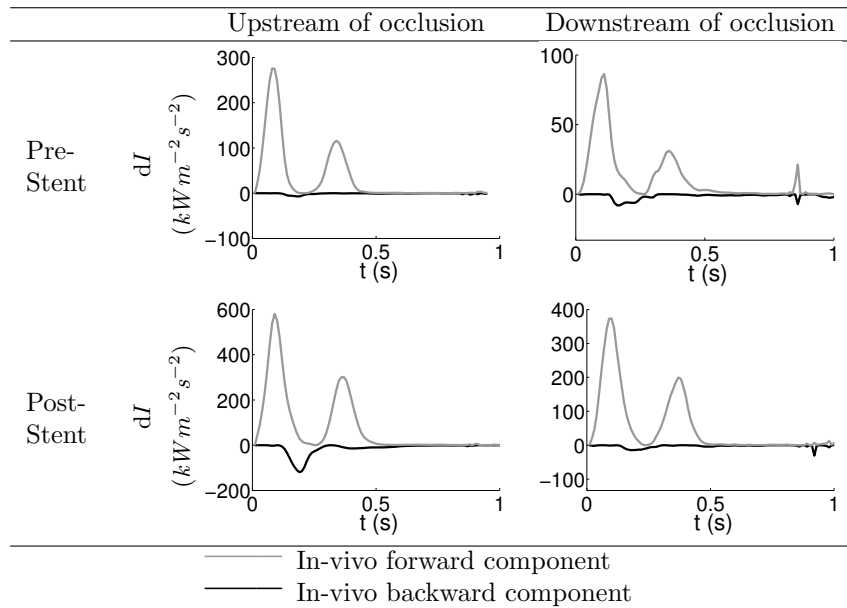


Figure 5.4 – Wave intensities upstream and downstream of an arterial stenosis in the superficial femoral artery, at occlusion (Pre-Stent) and after dilatation and stenting of the artery (Post-Stent). Forward wave intensity dI_f is in grey line and backward wave intensity dI_b in black line.

Longer and wider waves

Compared with healthy data, waves in the bypassed lower-limb arteries present a different timing that results from their longer duration. As observed in Figure 5.3, waves are not shifted in time; they are flattened: they start earlier and finish later. Because of this, the FEW arrives quickly after the FCW and the BCW superimposes with the forward waves. Two hypothesis could justify this particular pattern: either forward waves generated by the LV are wider, or waves widen while they propagate towards the lower-limb arteries. In both cases, we observe large FCW, the reflections of which are also large. As no measurements were taken in other systemic arteries than the lower-limbs during the bypass surgery, we can not reject for certain one of these hypotheses. Though, because the LV is influenced by the complete arterial vasculature while it ejects blood, it would seem more likely that the LV generates this particular pattern of wider waves. This longer and continuous effort generated by the heart could be due to the pathological condition of our patients: increased rigidity of the arterial wall and reduced cross-sectional area. These assumptions are verified with the study of stenosed and stented lower-limb artery, as a similar pattern of waves is observed in these pathological arteries. Though, they would need to be verified with further study focusing on other arteries from atherosclerosed subjects.

Comparison with upper-limb arteries

Because of the similarity of their location in the arterial network, it is interesting to compare the lower-limb with the upper-limb WIA (Zambanini et al., 2005). Indeed, both brachial and femoral arteries give rise to a closed peripheral network: the arm and the leg respectively. Though, besides the difference in timings previously stated, an additional wave is observed in the upper-limb: a FEW wave at mid-systole (X wave on Figure 2 in Zambanini et al. (2005)), responsible for an increased blood deceleration and rate of fall of pressure. The intensity of this wave increases in the more peripheral sites. Zambanini et al. suggested that the origin of this mid-systolic wave is the result of the reflection of the BCW from a proximal open-end type reflection site.

This additional wave is not observed in the bypassed lower-limb arteries, even in the distal vessels such as the posterior tibial artery. It might be comprised in the FEW of larger intensity and longer duration. Though, considering the very low intensities of the BCW observed in the distal vessels of the leg (Table 5.2), re-reflections would be hardly remarkable. In the hand, reflections arise from an open-type reflection site. An equivalent site could possibly be observed in the foot. Our observations are focusing on the arteries between the hip and the knee and are therefore located relatively far from this potential reflection site. Notice that this additional mid-systolic FEW is also not observed in the healthy femoral arteries.

In the arm, reflections increase as waves propagate distally towards the hand circulation. Zambanini et al. related this either to the anatomy of the hand circulation or to the level of resting vasoconstrictor tone in the hand. This is opposite to what is observed in the bypassed leg (Table 5.2).

Evolution of the wave energies throughout the leg

In bypassed leg, the wave energies of the FCW and FEW progressively decrease as waves travel towards the peripheral distal arteries. This dissipation of wave energy might be explained by the blood distribution through small collateral arteries. As we detail in the next section, an important dissipation of wave energy is observed in the presence of blood leakage.

The increase of the BCW intensity from the distal to the proximal artery results from the superimposition of multiple reflections that originate along the leg. These reflections might be small and diffuse or large and punctual, depending of their origin.

Reflection of waves

In comparison with the carotid and upper-limb arteries, we have observed that the BCW arrives later in bypassed arteries. Reflections are indeed generated at different sites: at the iliac bifurcation in the aorta, in the vasculature of the hand in the upper-limb or in the Circle of Willis of the head in the carotid. In lower-limbs, diffuse reflections originate at the distal peripheral network. Because the leg arteries run over longer distance than in the hand or head, the reflected waves arrive later. When a bypass is inserted, if the impedance mismatch with the surrounding arteries is great, it creates an additional punctual reflection, especially at the distal anastomosis where the popliteal artery is of smaller caliber. Considering the lengths of the bypasses (from 30 to 50 *cm*, see Table 2.3 of Chapter 2), the reflected wave arrives later than in other arteries.

We also observe that the introduction of the bypass increases the reflections: in PRE state in the CF, reflection index $R_{|p|}$ and wave intensities of the BCW are smaller than in the POST state. Furthermore, in an occluded leg, the BCW seems to arrive slightly later than in the bypassed condition. This indicates that the origin of reflections are different in these two situations. In the occluded case, the reflection seems to originate from the very distal vasculature, inducing the delay and damping. This is opposite to our expectations, there is no localized great reflection arising from the occlusion of the superficial femoral artery. In bypassed arteries, reflected waves result from the superimposition of multiple reflections along the leg: at the proximal and distal anastomosis, and at the peripheral network downstream of the deep femoral and tibial arteries.

5.3 Patient-specific results analysed with a numerical tool

In this second section of results, we analyse the variations of wave intensity that might be observed in bypassed lower-limbs by using the numerical model previously described. Initially motivated by patient-specific observations, we use simulations from the 1D-0D model to simulate hypothetical different bypass parameters and further understand some abnormal hemodynamics.

Two clinical cases will be considered: the influence of reflections and the effect of blood leakage.

5.3.1 Reflections

In this subsection, we analyse the reflections produced in the bypassed leg of one specific patient, resulting from the insertion of the bypass graft. Notice that achieving this analysis on average data is not pertinent, considering the different types of bypasses used and patient's conditions. With the use of the numerical model, we analyse the variation of reflections if another bypass type had hypothetically been used.

In-vivo results

The peripheral network of the patient of interest (patient #23) presents a severe pathology before surgery: arteries are diseased to such a point that their rigidity (high pulse wave velocity (2 to 3 times larger than normal) and low area compliance (10 times smaller than normal)) is close to the rigidity of the synthetic Gore-Tex bypass graft (see patient #23, Appendix B). As arteries and graft present similar diameters and rigidities, the reflection coefficient of the CF bifurcation (into the DF and BP) is close to zero ($R_{f,CF} = -0.094$), characterising a well-matched bifurcation. Thus, forward and backward waves are transmitted through this bifurcation without any new reflection (Figure 5.5 (top)). At the distal anastomosis of the bypass (BP-PO discontinuity), the reflection coefficient is positive ($R_{f,BP} = 0.30$) and some reflections are observed in the BP. The peripheral network distal to the popliteal is only responsible for weak and diffuse reflections that are produced by the capillaries.

Notice that a large wave energy drop is observed in the deep femoral artery. This is probably due to an error in the data acquisition (the guide wire might be too close to the arterial wall), as pressure and velocity both largely decrease. Velocity waveforms measured a few days after surgery do not present any particular drop.

Numerical model

The parameters of the 1D-0D model used to simulate the patient-specific results are listed in Appendix B for patient #23. Except for the deep femoral artery,

comparison of in-vivo data and numerical simulations reflects the accuracy of the numerical simulation (Figure 5.5). Similarly to in-vivo observations, the peripheral networks modeled by 0D windkessel models, produce weak reflections in the DF and PO arteries.

The numerical model allows to simulate the wave pattern if a softer bypass had been used. This softer bypass is characterised by $c = 10 \text{ m/s}$; reflection coefficients are then equal to $R_{f,CF} = -0.34$ and $R_{f,BP} = 0.62$. Notice though that this simulation will be approximate as we use the same signal at the inlet for both simulations, i.e. the forward component of the in-vivo velocity measured in the CF (while the stiffer bypass is inserted in the leg).

Figure 5.5 (bottom) compares these two numerical simulations. When a softer bypass is inserted, a large reflected wave is created at the BP distal anastomosis which propagates back in the CF while the forward waves in the CF remain nearly identical. In this case, a strong compliance mismatch between the graft and the surrounding arteries is a source of great reflections. Considering the negative impact of important reflections on the cardiovascular network, the compliance mismatch should be taken into account when choosing the bypass parameters, especially when the patient's arteries present increased rigidity.

5.3.2 Leakage

When studying hemodynamical outcomes of surgeries, there is a chance to analyse unexpected results. In the following, we describe the effect of blood leakage on the WIA.

In-vivo results

The bypass used for the patient #19 is made of a saphenous vein used in-situ. The vein is not removed from its natural surrounding but its valves are extracted in order to allow blood to flow downwards. Furthermore, side branch fistulae of the vein need to be ligated in order to avoid leakages.

The waves present an unexpected strong decrease in intensities as waves travel towards the distal network (see Figure and Table of Patient #19 in Appendix B). Also, the flow distribution through the upper-leg shows a drop of 33% of the local flow at the CF bifurcation and at the distal anastomosis. This is due to blood leakage through small collateral arteries and side branch fistulae which have not been properly ligated during surgery.

Numerical model

By using the numerical model, we confirm the wave intensities variation induced by leakages. To model leakages, we followed Leguy's approach (Leguy et al., 2010) and inserted two extra side branches at medium length of the CF and venous BP (as detailed in Subsection 4.1.3, Chapter 4).

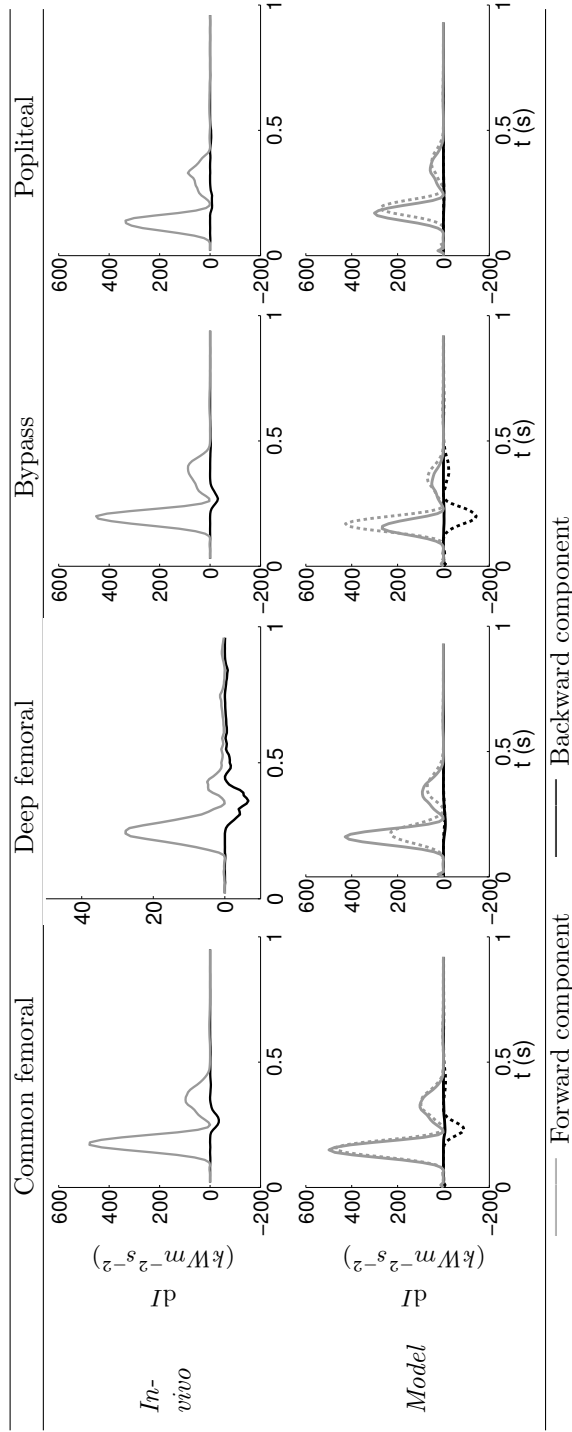


Figure 5.5 – Wave intensities dI of patient #23 in the four vessels of the bypassed leg: in-vivo measurements (top, $c = 23 \text{ m/s}$ in BP) compared to numerical simulations (bottom) with a rigid bypass ($c = 23 \text{ m/s}$, continuous line) and with a soft bypass ($c = 10 \text{ m/s}$, dashed line). Forward wave intensity dI_f is in grey line and backward wave intensity dI_b in black line.

Figure 5.6 presents the comparison of numerical waveforms in arterial networks with and without collateral vessels. We observe indeed, similarly to *in vivo* results, a decrease of wave intensity when leakages are present.

Even in the presence of abnormal hemodynamics, the WIA method allows an efficient analysis of waves in the arterial system. In clinical practice, when coupled with the classical ultrasound exams, this approach could become a useful confirmation tool that would help avoid post-surgery corrections.

5.4 Conclusion

In this chapter, we have shown that WIA could be efficiently applied to study bypassed and occluded lower-limb arteries. Due to the condition of the subjects (atherosclerosis, bypass surgery, elderly people), the pattern of waves is influenced: waves are wider and last longer than in healthy femoral arteries. One hypothesis to explain this physiological observation is that the heart needs to develop a longer effort in order to overcome the increased rigidity of the arterial network. This hypothesis would need to be verified in future works.

In the lower-limbs, reflections created by the peripheral vasculature are small and diffuse. Though, due to the insertion of the bypass, large and punctual reflections might be created if the bypass impedance differs strongly with the impedance of the surrounding arteries. While waves travel towards the peripheral distal arteries, their energy decrease. As observed in the presence of great leakages, such decrease is mainly due to blood distribution through small or large collateral arteries.

The insertion of the bypass modifies the reflections in the leg. In this analysis performed on 4 patients (with PRE and POST conditions), the reflections appear to increase and to arrive earlier with the introduction of the bypass. This shows that the origins of reflections differ. Surprisingly, it seems that the long arterial occlusion of the superficial femoral artery does not generate any great localized reflection. This result would need to be verified on a larger number of subjects in future works.

Limitations of the method.

Invasive data acquisition and local or general anaesthesia may alter blood hemodynamics, although no inotropic or vasodilatory drug were given at the time of measurements. The wave intensity analysis might differ quantitatively, but should not be qualitatively different from those obtained with non-invasive measurements obtained on conscious patients. Due to our data acquisition protocol, the number of studied patients was small; though the findings were consistent in all patients. Large standard deviations might be observed when averaging variables on all 9 subjects, which are explained by the variability in patient's conditions and pathologies.

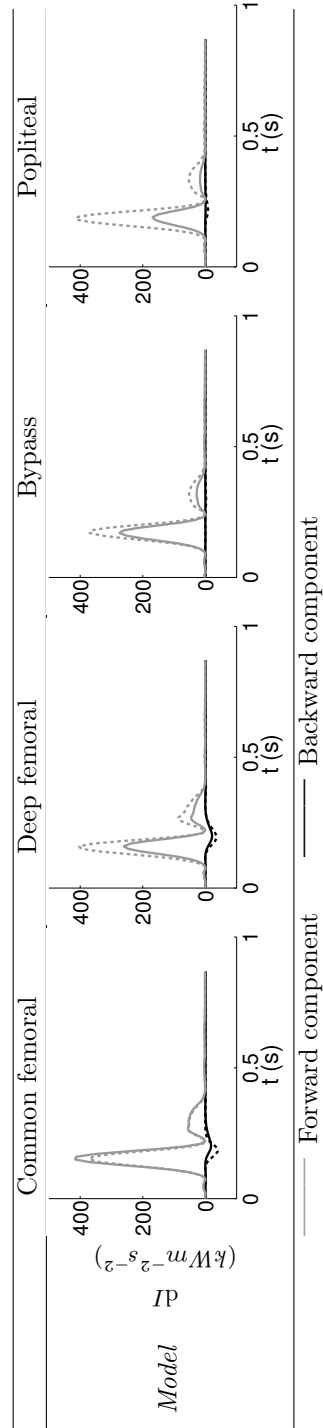


Figure 5.6 – Simulation of wave intensities dI of patient #19 in the four vessels of the bypassed leg: with leakage (continuous line), without leakage (dashed line). Forward wave intensity dI_f is in grey line and backward wave intensity dI_b in black line.

In cases of unsimultaneous measurements of pressure and velocity, care should be taken when aligning signals and applying filtering. As mentioned in previous works (Khir et al., 2007; Parker, 2009), incorrect temporal alignment might bias the determination of the linear part of the PU-loop, and therefore the wave speed. Also, WIA is rather sensitive to temporal delay and noise in experimental measurements since the method implies the multiplication of two derivatives.

Acknowledgments

The authors would like to acknowledge Patrick Segers (Ghent University, Belgium) who provided the velocity and distension waveforms acquired in lower-limbs of healthy subjects. Wave intensity analysis of these data was realised by Alessandra Borlotti (Brunel University, United Kingdom).

Reservoir-excess separation

In the separation of the pressure and velocity waveforms into their forward and backward components, Wang et al. (2003) pointed out non-logical explanation given by the wave theory for the behaviour of the separated waves during their diastolic decay. As illustrated in the left part of Fig. 6.1, large and simultaneous forward and backward waves are present during that period, while the aortic valve is closed and the left ventricle is not generating impulsion anymore. Therefore, the typical exponential pressure decay observed in diastole is obtained by adding these two pressure components, while the zero or low diastolic velocity results from velocity components canceling each other out.

In order to explain these diastolic observations, Wang et al. introduced the reservoir-excess hypothesis as an approach based on the windkessel theory and complementary to the wave propagation theory. It suggests that the pressure in the arteries is made of two components: a reservoir pressure $P(t)$ induced by the compliance of the arteries (windkessel effect, the arteries expand or contract themselves in order to reduce blood variation) and an excess pressure that drives the arterial waves $\tilde{p}(x, t)$:

$$p(x, t) = P(t) + \tilde{p}(x, t) . \quad (6.1)$$

In diastole, the reservoir pressure describes the pressure fall-off very well such that the forward and backward components of the excess pressure are almost nul, which is coherent with physiological observations (Fig. 6.1, right).

The reservoir-excess hypothesis has been successfully applied to the arterial (Wang et al., 2003) and the venous system (Wang et al., 2006). In the arterial circulation, while the approach was initially considering aortic waveforms, the work and its hypotheses have been extended to other large arteries of the cardiovascular system (Aguado-Sierra et al., 2008b; Vermeersch et al., 2009b; Aguado-Sierra et al., 2008a). This improved algorithm for pressure separation is based on assumptions which might become less valid in distal arteries because of the more significant effect of reflected waveforms.

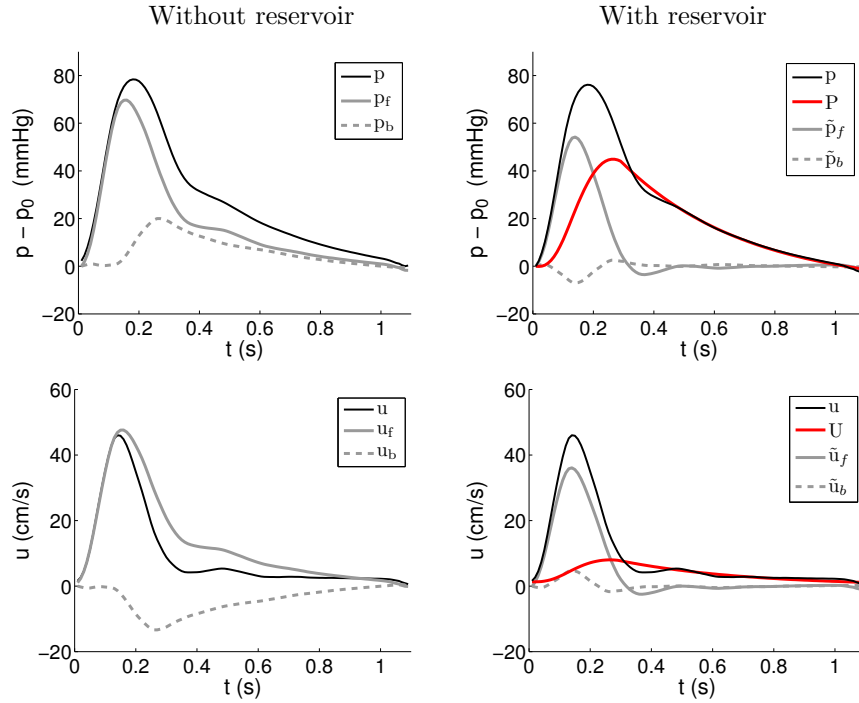


Figure 6.1 – Separation of the pressure (top) and velocity (bottom) into forward and backward components. Separation is performed on the measured signal p, u (left) and on the excess components \tilde{p}, \tilde{u} obtained after subtraction of the reservoir component (right). Wave speed used for separation is $c = 19 \text{ m/s}$ for both total and wave signals. Diastolic pressure p_0 is subtracted from pressure waveforms for ease of visualisation. Reservoir pressure P and velocity U are in red. Data were measured in the common femoral artery of a bypassed leg.

In order to bring a new interpretation of the hemodynamics in the bypassed lower-limbs, we apply the reservoir-excess separation to our database of pressure and velocity measurements (as presented in the Introduction and summarized in Appendix B). As the newly developed algorithm for computing the excess and reservoir components requires only the pressure measurement (Section 6.1), it could be applied to the in-vivo pressure signals acquired on the 25 patients of our database where measurements are taken along the leg, with the femoral artery occlusion and after insertion of the bypass graft (Section 6.2). Because we are considering a particular population, we also intend to point out the limitations of the method when applied to small, distal and pathological arteries. Using this new separation of waves, the importance of reflections will also be

discussed. Furthermore, the computation of the forward and backward wave intensity based on the excess pressure will be performed for the patients presenting a simultaneous acquisition protocol and these signals will be compared to the classical computation of wave intensity from total signals (Section 6.3).

6.1 Algorithm for pressure separation in an arbitrary artery

The reservoir-excess separation initially introduced by Wang et al. (2003), computed the reservoir pressure using the pressure and flow at the inlet of the arterial system. Recently, an extension of this algorithm to all arteries has been developed, which is based on empirical hypotheses and only requires pressure measurement alone in the artery of interest (Aguado-Sierra et al., 2008a). We briefly present the methodology in the following.

The reservoir pressure P at an arbitrary location can be determined from:

$$\frac{dP}{dt} = a(p - P) - b(P - P_\infty) \quad (6.2)$$

where $a = \gamma/C$ and $b = 1/\tau$ are the rate constants of the system. P_∞ is the constant pressure at which flow through the microcirculation is zero. This relation results from the conservation of mass at the inlet of the arterial system ($\frac{dV}{dt} = Q_{in} - Q_{out}$, with V the volume of the arterial system, Q_{in} and Q_{out} the flow at the inlet and outlet of the arterial system), together with the assumptions that the compliance of the whole arterial tree is constant ($C = \frac{dV}{dp}$) and that the outflow is driven by the gradient between P and the arterial asymptotic pressure P_∞ ($Q_{out} = \frac{P - P_\infty}{R}$). Furthermore it is based on the two following assumptions: (1) the pressure waveform decay behaviours measured at different locations within the arterial system are similar during diastole; (2) the excess component of pressure \tilde{p} measured in the ascending aorta is approximately proportional to the cardiac outflow ($Q_{in} = \gamma(p - P)$).

The solution of Eq. (6.2) is found by considering separately the diastolic and systolic phases. We define t_N as the time at which the aortic valve shuts at the end of systole. In aortic arteries, t_N can be found as the time of the dicrotic notch; but for pressure waveforms without a clearly marked notch such as in the lower-limbs, the determination of this time is very sensitive. Following Aguado-Sierra et al. (2008a), t_N is computed as the time of the first zero crossing of the second derivative of pressure at the end of systole. During diastole, the reservoir pressure is given by:

$$P - P_\infty = (P(t_N) - P_\infty) e^{-b(t - t_N)}, \quad t_N \leq t \leq T \quad (6.3)$$

where T is the cardiac cycle duration. During systole, P is given by

$$P = \frac{b}{a+b}P_\infty + e^{-(a+b)t} \left(\int_0^t a p(t') e^{(a+b)t'} dt' + P_0 - \frac{b}{a+b}P_\infty \right) \quad 0 \leq t \leq t_N \quad (6.4)$$

where P_0 corresponds to the start point of the onset of P . $P(t_N)$, P_∞ and b are estimated by fitting Eq. (6.3) to the measured pressure data, by using an unconstrained nonlinear optimization routine, minimizing the sum of squares of the error between fitted and measured pressure data. The parameter a is obtained by enforcing continuity between systole and diastole reservoir pressures, at t_N . Finally, P is determined for the entire period from Eqs. (6.3) and (6.4).

The velocity can also be resolved into a reservoir and excess components:

$$u = U(x, t) + \tilde{u}(x, t) \quad (6.5)$$

where the reservoir velocity U also depends upon position, contrarily to the reservoir pressure. U is directly proportional to $P - P_\infty$ at the end of diastole, when wave activity is expected to be minimal:

$$U = \frac{P - P_\infty}{\bar{R}} \quad (6.6)$$

where \bar{R} is the effective resistance of the vessels downstream of the measurement site. \bar{R} is computed from time-averaged pressure and velocity ($\langle p \rangle$ and $\langle u \rangle$ respectively) during diastole ($t_N \leq t \leq T$): $\bar{R} = \frac{\langle p \rangle - P_\infty}{\langle u \rangle}$. The excess velocity is then $\tilde{u} = u - U$.

In order to assess the success of the algorithm, we verified that the diastolic exponential decay of P was positive ($\tau > 0$) and that the asymptote of the exponential fit P_∞ was lower than the maximum of the input pressure ($P_\infty < \max(p)$).

We applied this algorithm on all pressure waveforms from our database (about 150 waveforms measured invasively on 25 patients, before and after bypass graft insertion). The algorithm failed in only four cases; all of them were taken in the popliteal artery (below the femoral occlusion or distally to a bypass with a poor run-off flow). These signals were very damped and noisy, with a diastolic decay convex rather than concave (Fig. 6.2). In these cases, by determining manually the time of start of diastole t_N , the algorithm produced valid results.

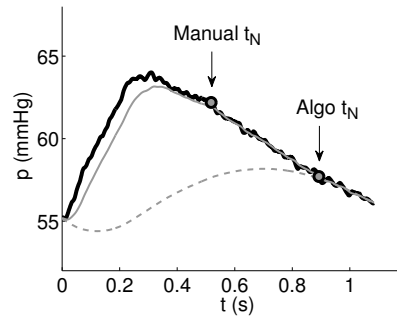


Figure 6.2 – Illustration of the failure of the algorithm applied to a popliteal signal of an occluded leg. The measured pressure is in black. When determining t_N with the algorithm, the reservoir pressure signal does not present a correct exponential decay (dashed grey line, $t_N = 0.89$ s, $\tau = -0.378$, $P_\infty = 60$ mmHg). A better result for P is obtained when t_N is determined manually (continuous grey line, $t_N = 0.53$ s, $\tau = 1.09$, $P_\infty = 47$ mmHg).

6.2 Pressure separation in bypassed lower-limbs

The following section presents the results of the separation into reservoir and excess components. We start by discussing the assumptions at the base of the algorithm. Observations about the reservoir and excess components in occluded and bypassed legs follow. Then, the pressure distribution of components puts to the fore the small influence of the reflected waves in the total signal. Finally, we discuss the values of the reflection coefficient in the four vessels of the leg.

6.2.1 Assumptions

From the two assumptions at the base of the algorithm, we will only be able to verify the first one (similar diastolic pressure decays in all arteries). Regarding the second one (proportionality between the excess pressure in the ascending aorta and the cardiac outflow), as we do not have cardiac measurements at our disposal, we will assume its validity for the rest of this work. Notice that achieving a comparison between the local arterial flow and excess pressure would not be efficient. Unlike the pressure which is well-matched at bifurcations, the flow waveform that propagates is greatly influenced by its division at bifurcations and by local reflections. The distal flow is therefore very different from the cardiac outflow.

The other assumption requires that the pressure waveform decays at different arterial locations are similar during diastole. In the bypassed leg, in about half of the patients analysed, this assumption is verified in all the arteries

of the leg. In the other cases, we observe a different diastolic decay in the popliteal artery, while it is similar in all arteries above. Discrepancies are also observed a few times within the deep femoral artery. In these cases, the artery is not considered for further analysis. We explain this difference in the popliteal diastolic decay by a decrease of the compliant elasticity of this distal network, induced by the atherosclerosed condition of the artery or by the insertion of the bypass graft. Notice that, in some patients on the contrary, even if a pressure drop is observed in the popliteal artery, its diastolic decay remains identical to above arteries (Fig. 6.3). In arteries of occluded legs, the popliteal pressure is strongly damped (see Section 2.2.3, Chapter 2) and its diastolic decay is always different from above arteries.

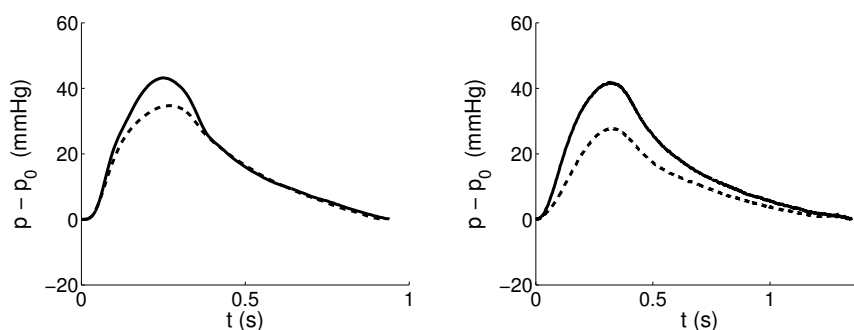


Figure 6.3 – Similar (left) versus different (right) diastolic decays between the common femoral (continuous line) and popliteal (dashed line) arteries in the bypassed leg of two patients. Diastolic pressure p_0 is subtracted from pressure waveforms for ease of comparison.

6.2.2 The reservoir components

The reservoir pressure is determined by the elastic compliance of systemic arteries. During systole, the aorta (the most compliant artery) is stretched by blood entering the vessel and the rise in pressure is restrained. During diastole, at the closure of the aortic valve, the elastic aorta loosens up and the reservoir effect avoids pressure to fall directly to the mean circulatory filling pressure (Davies et al., 2007). This effect is visible in the entire arterial system in diastole; indeed, the rate of decrease of diastolic pressure is almost identical in most arteries of the human body.

The reservoir pressure waveform was found to be common throughout the arteries. This conclusion follows from measurements in healthy subjects along the aorta and at the carotid and brachial arteries (Davies et al., 2007). Notice that reservoir pressures were similar even if these arteries have different

structures (elastic vs muscular arteries) and present different local resistances and compliances. Also, similar reservoir pressures were found when analysing numerical waveforms along the arterial tree, obtained with a coupled 1D-0D model of the arterial network (Aguado-Sierra et al., 2008a).

When analysing reservoir pressures in bypassed lower-limb arteries, we only took into account the signals respecting the first assumption of the algorithm, as described above. On basis of results described in the literature, reservoir signals at different arteries of a subject's leg were considered similar when the deviation of amplitudes between curves did not exceed 15%:

$$\frac{\max_{\text{leg}}(|P|) - \min_{\text{leg}}(|P|)}{\max_{\text{leg}}(|P|)} < 15 \% \quad (6.7)$$

where $|P|$ represents the amplitude of the reservoir pressure. In 15 patients out of 25, the reservoir pressures were similar in the vessels of the leg. Among those, we observed similarity between arteries including the popliteal artery in only 5 subjects. Fig. 6.4 presents an example of non-similar reservoir pressures. Notice that fixing an identical start of diastole t_N for all arteries of the leg does not modify the similarity between reservoir pressures.

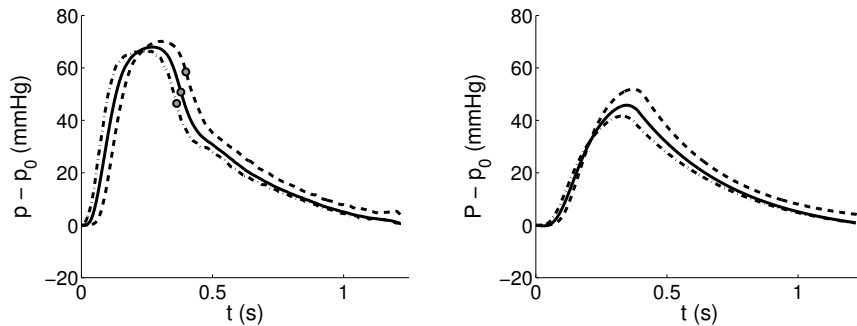


Figure 6.4 – Total pressure p (left) and reservoir pressure P (right) in the common femoral, deep femoral arteries and bypass graft. Diastolic pressure p_0 is subtracted from pressure waveforms. The grey points indicate t_N . Even if total pressure waveforms are relatively similar to each other, reservoir pressure components deviate of 20%.

Therefore, the conclusion that reservoir components of pressure are similar throughout the arterial network presents some restrictions when peripheral, pathological and grafted arteries are considered. The insertion of the bypass and the pathology of the lower-limbs modify the wave propagation in these vessels. New reflections might be created because of the bifurcation and junction at

anastomoses of the bypass. Above all, the graft material and the atherosclerosis disease modify the elastic compliance of the peripheral network of the leg.

From its definition, the reservoir velocity is proportional to the reservoir pressure. Even though, U presents a very flattened contour which fits the diastolic period quite well, even when diastolic fluctuations of u are observed (Fig. 6.1).

The average value of the fitted asymptote of the exponential decay P_∞ reaches 49 ± 14 mmHg, all valid arteries taken together. When considering arteries separately, P_∞ decreases from the common femoral (53 mmHg) to the popliteal artery (48 mmHg). According to the model at the base of the algorithm, this value represents the pressure at which flow through the microcirculation ceases; P_∞ is not necessarily the venous pressure but could be related to the tissue pressure surrounding the microcirculation. This value is indeed much higher than the venous pressure used in this work ($p_{out} = 20$ mmHg). As a result, the time constants of the diastolic decay computed with this model ($\triangleq \tau_{RW}$) are lower than those computed with the exponential fitting method based on the 2-element windkessel model ($\triangleq \tau_{exp}$, see Section 2.3.2, Chapter 2); mean values are $\tau_{exp} = 1.14 \pm 0.43$ s versus $\tau_{RW} = 0.46 \pm 0.25$ s. Notice that, in the Asklepios population study (Vermeersch et al., 2009b), a linear regression performed on τ_{RW} and τ_{exp} (computed from the 3-element windkessel model) found an excellent correlation between both parameters.

6.2.3 The excess components

Similarly to the central arteries, when accounting for the reservoir pressure in the lower-limb arteries, the excess pressure and velocity are only significant during systole, while they are almost zero during diastole, when wave activity is expected to be minimal (Fig. 6.5). This is also true for forward and backward excess components (Fig. 6.1).

Along the leg, the evolution of the excess pressure is similar to the evolution of the total pressure. In bypassed legs, no particular decrease is observed towards the distal arteries.

6.2.4 Pressure components distribution

When accounting for the reservoir pressure, the forward and backward components of pressure present a new distribution. Indeed, the reservoir pressure represents a larger contribution to the total pressure than the excess counterpart does (Aguado-Sierra et al., 2008a; Tyberg et al., 2009). Therefore, in contrast to widely held assumptions, the influence of reflected waves is largely reduced.

This is observed as well in the lower-limbs (Table 6.1). The contribution of the reservoir pressure to the total pressure (computed as the area under the curves) reaches about 72% in average for all valid arteries. The forward and backward components of \tilde{p} accounts for 22% and 6% respectively. If the

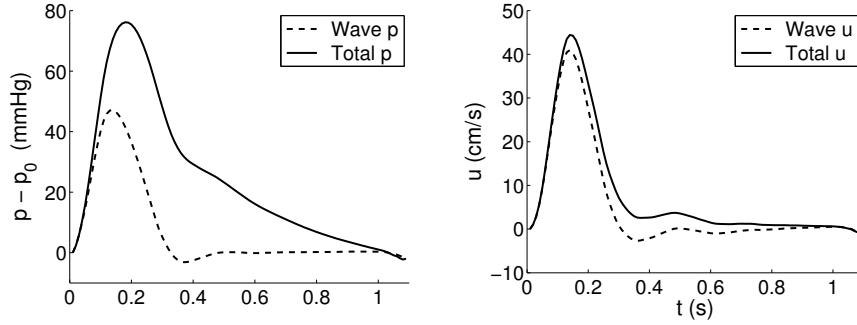


Figure 6.5 – Total and excess components of pressure (left) and velocity (right).

reservoir hypothesis is not considered, these values reach 73% and 27% instead. We see that the relative importances of reflections strongly varies depending on whether one considers the reservoir component or not.

	Ignoring reservoir	Accounting for reservoir
Reservoir	-	71.5 ± 10
Forward	72.7 ± 11.4	22.3 ± 14
Backward	27.3 ± 11.4	6.2 ± 11

Table 6.1 – Average pressure components distribution in % of the total pressure, in the arteries of bypassed legs.

Notice that we use the same wave speed (computed from pressure-velocity loop) for the separation of forward and backward components for both total and excess signals. When analysing the slopes of $\tilde{p}\tilde{u}$ and pu loops (Fig. 6.6), the wave speeds appear to be almost similar: the relative difference, computed as the mean ratio of the difference ($c_{pu} - c_{\tilde{p}\tilde{u}}$) to the average of both results, is limited to 2.6%. In carotid arteries, it was also observed that wave speeds computed from total or excess signals produced similar values (Aguado-Sierra et al., 2008b). While in the carotid, equivalent results were found when using the PU-loop or single-point methods, the reservoir-excess separation has a stronger impact on the single-point method when applied to the lower-limb arteries. If we compute the wave speeds using the single-point method, we observe a larger relative difference of 38% between total and excess signals. In the following, forward and backward separation will therefore use the PWV from the PU-loop method.

We obtain similar contribution of the reservoir pressure in occluded legs (before bypass grafting): the reservoir pressure accounts for 75% of the total

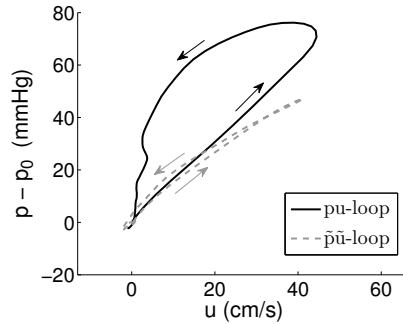


Figure 6.6 – Pressure-velocity loops: pu (continuous black line) and $\tilde{p}\tilde{u}$ (grey dashed line). Arrows indicate the direction of the curves. Slopes are similar in the initial part of systole.

pressure. The insertion of the bypass induces variations of the reservoir pressure P that greatly differ between patients. In only 25% of all subjects, we observe similar P in the common femoral artery (above the occlusion or proximal anastomosis) before and after bypass grafting; half of the rest of the subjects presents an increase of P after bypass (+33%), while a decrease in the other half (-40%). The compliance of the peripheral network is indeed modified thanks to the insertion of the bypass graft (see Section 2.3.2, Chapter 2). In the five patients whom evolution of the compliance from pre- to post-operative states is measured, we observe indeed a similar variation than the reservoir pressure (in these cases, decrease of P and C). In all patients, we would have expected an increase of the compliance of the network, and therefore an increase of the reservoir pressure as blood flows through a new conduit. This might also depend of the material of the graft, as synthetic materials present a reduced radial compliance. Even though, there is no clear relation between graft material and reservoir pressure variation. Notice that, as measurements on the occluded and bypassed leg are taken within an hour during surgery, the condition and central pressure of the patient might also have changed, inducing the variations observed.

Recent works also showed that the modification of the pressure profile with age is mainly due to the augmentation of the reservoir pressure (because of the decrease of the compliance of arteries) rather than the augmentation of the distal reflections (Davies et al., 2010; Vermeersch et al., 2009b). This conclusions also holds for the augmentation index AIx mainly determined by the reservoir pressure rather than the reflections (Davies et al., 2010).

6.2.5 Reflection coefficient

In Aguado-Sierra et al. (2008a), it is suggested that the empirical assumptions at the base of the algorithm become less valid when wave reflections become significant. In order to assess the reflections in distal arteries of the leg, we compute the reflection index or magnitude $R_{|p|}$, defined as the ratio of the amplitude of the backward to the forward pressure wave (Vermeersch et al., 2009b). This index can be computed with the forward and backward components of the total signals (p_f , p_b) and of the excess signals (\tilde{p}_f , \tilde{p}_b). Average results for the four vessels of the leg are resumed in Table 6.2 (only valid and bypassed arteries are considered). Because of the addition of backward-travelling reflections, the reflection index is smaller in the popliteal artery than in the common femoral artery. Even if less reflections are present in the distal leg, the algorithm is less easily applicable in distal arteries. This observation is in contradiction with the suggestion from Aguado-Sierra et al. (2008a). Our results show that the presence of important reflections does not necessarily implies that the algorithm becomes less valid.

	$R_{ p }$ (%)			
	CF	DF	BP	PO
Ignoring reservoir	37	50	28	26
Accounting for reservoir	32	40	23	28

Table 6.2 – Average reflection index $R_{|p|}$ in the four vessels of the bypassed leg, computed on the total signals (ignoring the reservoir component) or on the excess signals (accounting for the reservoir component).

CF: common femoral. DF: deep femoral. BP: bypass. PO: popliteal.

This conclusion is in agreement with Vermeersch et al. (2009b) who suggested that the greater $R_{|p|}$ becomes, the better the reservoir pressure concept holds. They suggested that the reservoir pressure concept shows large similarities with the classical 3-element windkessel model, and that this conclusion is particularly emphasized in subjects characterised by a high reflection magnitude and high 'windkesselness' of their arterial system.

When accounting for the reservoir pressure, the reflection index slightly decreases in each vessel, except in the popliteal artery (Table 6.2). Even if, when looking at pressure distribution, reflections are reduced in amplitude when accounting for the reservoir component, their ratio to the incident wave is almost similar. We suggest that the ratio of a reflected wave to the incident wave, induced by a morphological feature (e.g. bifurcation, junction) remains unchanged whether or not the reservoir pressure is considered. If one refers to the reflection coefficient R_f defined using the characteristic admittance of the vessels (see Eq. (5.3), Chapter 5), the amount of reflection is indeed computed from the morphological and structural parameters of the vessels.

In the aorta, unlike in the leg, Davies et al. (2010) showed that the reflection coefficient (R_p , defined as the ratio of the peak of the backward to the forward pressure wave) decreased by 71% when accounting for the reservoir. Some reasons might explain this difference. The definition of the reflection coefficient R_p might not be appropriate for excess signals: it does not consider the minimum of the reflected wave which might be negative (see Fig. 6.1). Also, the separation of forward and backward waves is computed using the single-point PWV which might be inaccurate for the excess signal, as discussed previously.

6.3 WIA applied to the excess component

The reservoir-excess theory suggests that the interaction of waves with the arterial system is described by the excess components of pressure \tilde{p} and velocity \tilde{u} . These components should therefore be used when analysing the wave intensity of curves, rather than the total signals.

On basis of the previous analysis from Chapter 5 (Sections 5.1), we compute the wave intensity $d\tilde{I}$ as follows:

$$d\tilde{I} = \frac{d\tilde{p}}{dt} \frac{d\tilde{u}}{dt} \quad (6.8)$$

and separate its forward $d\tilde{I}_f$ and backward components $d\tilde{I}_b$ using Eq. (5.2) (with \tilde{p} and \tilde{u} instead of p and u). As previously mentioned, we use the pulse wave velocity determined by the pu -loop to compute this wave separation.

Using the simultaneous measurements of pressure and velocity from our database (9 subjects), we analyse the modification of the wave intensity patterns induced by subtracting the reservoir component of the waves. Fig. 6.7 (left) presents typical variations observed in the common femoral artery of a bypassed leg. We observe in almost all datasets that the magnitudes of the three main waves of $d\tilde{I}$ (FCW, BCW, FEW) are modified differently. In the forward compression wave (FCW), the amplitude is reduced while it remains nearly constant (or slightly increases) in the forward expansion wave (FEW). The backward compression wave (BCW), of small amplitude already, is further reduced when the reservoir pressure is extracted from the signal. Fig. 6.7 (right) shows that the variation of $d\tilde{I}$ comes from the time variation of the excess pressure, as $d\tilde{u}$ is very similar to du (see also Fig. 6.5). Aguado-Sierra et al. (2008b) observed a reduction by 20% of the amplitude of $d\tilde{I}$ in carotid arteries, as well as small reflected waves. But they did not describe a different variation in the two forward waves.

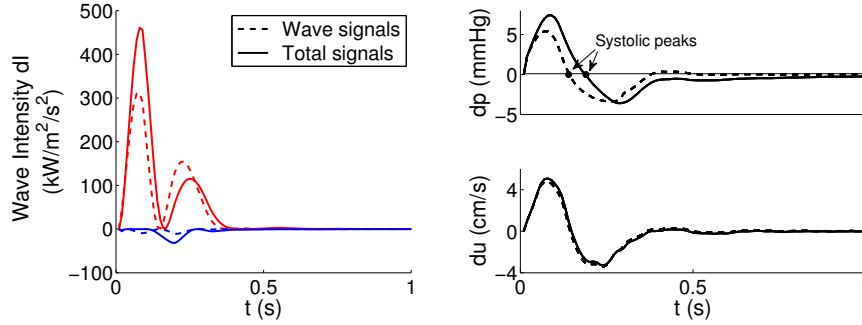


Figure 6.7 – On the left, wave intensity computed from the total signals p and u (dI , continuous line) and from the excess signals \tilde{p} and \tilde{u} ($d\tilde{I}$, dashed line). Forward components are in red, backward components in blue. On the right, variation in time of the total and excess pressure (dp , $d\tilde{p}$; top) and total and excess velocity (du , $d\tilde{u}$; bottom). Notice that these waveforms (same patient, same artery) also appear in Figs. 6.1, 6.5 and 6.6.

6.4 Conclusion

In this chapter, we have presented the application of the reservoir-excess separation to the in-vivo pressure and velocity signals acquired in occluded and bypassed lower-limbs. The work is based on the model proposed by Wang et al. (2003): this model states that waveforms are composed of a reservoir component accounting for the elastic compliance of large systemic arteries, and an excess component that propagates the arterial waves.

We have shown that the algorithm for reservoir-excess separation developed by Aguado-Sierra et al. (2008a) can be efficiently applied to our in-vivo data. Nevertheless, the validity of the results is not guaranteed in small and distal arteries of the occluded or bypassed leg (mainly in the popliteal artery) since the diastolic decay of the pressure waveforms in these vessels largely differ from the upstream arteries, thus not satisfying the first assumption of the algorithm. We were unable to assess the second assumption, since we did not have aortic in-vivo measurements at our disposal to test it.

Unlike results from other studies, the reservoir pressure was not always similar in all arteries of the subjects analysed. Keeping in mind that our reasoning is based on the assumption of validity of the algorithm, we suggest that the similarity in reservoir pressures is limited to healthy, large arteries. Distal arteries of the leg might indeed present small dimensions. Furthermore, the compliance of the peripheral leg is modified by the insertion of the bypass graft and by the increased stiffness of the atherosclerosed lower-limb arteries.

The introduction of the reservoir-excess model brings a new interpretation of the importance of the backward waves in the distal arteries. In the lower-limbs, we observe that the reservoir pressure consists of 70 to 75% of the total pressure, in occluded and bypassed legs. From the 30% of excess pressure, the backward wave represents only 6% of the total pressure. These observations support the suggestion from some authors that the backward wave is unlikely to account for the large changes in pressure increase with aging and disease, and that the global modification induced by age and disease results from variation of the compliant elasticity of the arterial network (Davies et al., 2010; Vermeersch et al., 2009b).

While the contribution of reflections to the total pressure is clearly reduced when accounting for the reservoir component, we observed that the relative importance of reflections against incident waves did not vary much with the reservoir theory. Furthermore, even if important reflection indexes are observed in the leg arteries, this does not seem to influence the validity of the reservoir-excess separation algorithm.

The computation of the wave intensity from the excess components of velocity and pressure highlighted the diminished contribution of backward waves. Furthermore, our results show that the amplitude of the FCW is decreased while the FEW remains identical; the intensity gap between the two forward waves is therefore reduced.

Conclusion and perspectives

This thesis concludes with a summary of the achievements presented in the previous chapters and with some directions of work for the future.

7.1 Summary and concluding remarks

This summary presents five aspects treated within this work: the acquisition of in-vivo data, the validation of the patient-specific 1D-0D model of hemodynamics in bypassed lower-limbs, its sensitivity analysis, the study of the origin and propagation of waves, and finally, some clinical conclusions.

7.1.1 In-vivo data acquisition

In the first two chapters of this work, a brief review of current techniques of data acquisition is presented, with a detailed description of the protocol of in-vivo data acquisition that we followed. In view of the pathological clinical cases treated, we had to cope with some constraints.

Considering the clinical and technical resources at our disposal, we have decided to consider an invasive data acquisition protocol. This limitation has restrained the number of subjects considered and analysed in this work. The repeatability of measurements has also therefore been restrained by the surgical setting. Our invasive data acquisition protocol did not allow measurements a few days before and after surgery, neither a follow-up months after months. Furthermore, measurements had to be realized while subjects were in surgery under anaesthesia, which might alter blood hemodynamics. Variations induced by vasodilation on the velocity waveforms have been described in Chapter 2 and were relatively limited; the pattern of waves remained almost similar with increase of mean flow. Notice also that this type of data acquisition has been used and validated in multiple studies without highlighting great variations (Parker and Jones, 1990; Khir et al., 2001a; Sun et al., 2000; Penny et al.,

2008; Hollander et al., 2001; Koh et al., 1998). One possible alternative to this invasive in-vivo data acquisition would be to consider the measurement of distension waveforms, as discussed in the outlook.

Within the NHEMO project, we have not been saved from the errors inherent to the elaboration of every experimental protocol. Many devices have been tested with success or failure, and many solutions have been developed to cope with the limitations of the clinical setting. Let us describe some of them.

- For the invasive pressure measurement by catheter, an electrical case has been built and installed in the surgery room, to allow splitting of the signal from the clinical device into the display screens of the surgery room and the recording on a personal computer.
- Velocity signals acquired by Doppler ultrasound could not be saved dynamically, but only as a static DICOM image with representation of about 4s of velocity cycles. A Matlab[®] routine performing image processing has been written in order to extract the velocity curve semi-automatically from DICOM images.
- Doppler ultrasound devices used to measure velocity during surgery had to cope with the invasive aspect of surgery. Water cushions had to be applied on open wound arteries in order to transfer the ultrasound waves.
- Erroneous measurements have been performed on 13 subjects. While pressure was measured during surgery (patient under anaesthesia, invasive measurement), velocity was acquired a few days after surgery, using Doppler ultrasound exams on an awake and resting patient. In view of the variability of the cardiovascular system, these two measurements did not correspond to the same physiological state. The current protocol of data acquisition has then been established.

Wiser with our experience, let us summarize here some advice for the setting-up of an efficient in-vivo data acquisition protocol.

- When evaluating the condition of a subject, hemodynamic measurements (pressure, velocity and diameter) should be realised simultaneously, or at least, under similar physiological conditions with constant heart rate (e.g. subject at rest, under anaesthesia, before or after surgical intervention). If measurements are not realised simultaneously, the ECG signal should be acquired together with the hemodynamical variables and used for synchronisation.
- Ideally, in-vivo measurements should be realised non-invasively, in order to easily widen the database of subjects and to allow multiple measurements at different times. The subject should be laying down and resting at the time of measurement.
- Stable signals should be acquired during at least five cardiac cycles, and with an acquisition frequency of at least 100 *Hz*.
- For the analysis of the hemodynamics of pathological subjects, measurements should be realised in a patent zone (avoid local stenosis or occlu-

- sions). Simultaneous imaging techniques might be needed to ensure the localisation of the probe.
- When choosing one acquisition technique, it should be verified that the level of precision is sufficient for the variable observed. For example, when acquiring distension waveforms, the spatial accuracy should be well smaller than the vessel diameter dimension (the pulsatility of the vessel is of the order of 10% of the diameter). Also, when performing 3D segmentations of small arteries, attention should be put on the spacing between slices and the spatial accuracy to ensure quality of the result.
 - In the case of invasive measurements, the probe (e.g. needle, guide wire) should preferably be oriented downstream to avoid the increase from dynamic pressure. The tip of the probe should be localised with imaging techniques in order to avoid errors and artefacts (e.g. tip along the wall).

7.1.2 Validation of the 1D-0D model

The first three chapters of this work have presented the different aspects of the patient-specific validation of the coupled 1D-0D model of the arterial hemodynamics in bypassed lower-limbs: the patient-specific determination of the model parameters, the definition of the 1D and 0D models with emphasis on the inlet boundary condition, and the validation of the numerical waveforms compared to the in-vivo measurements. The importance of the inlet boundary condition in truncated arterial networks has been discussed in Chapter 3: we have shown the efficiency of imposing the forward component of a wave in an absorbing way at the inlet.

In Chapter 4, we showed that the numerical simulations reproduce the physiological observations in a satisfactory way; we observed that the pressure simulations overestimate the pressure measurements. For some patients, important deviations of velocity and pressure curves were observed, and improvements of the model have been suggested. We summarize them in the outlook section. Two major improvements considered and applied in this work are the introduction of leakages in the distal arteries of the leg, and a more precise determination of the patient-specific parameters of the model.

The estimation of the patient-specific parameters is indeed a very important aspect of this work. In Chapter 2, as well as in the Introduction Chapter, we have presented and discussed different acquisition and computational methods for their evaluation. As the results of the different computational methods seemed to correlate relatively well, we rather suggest that the data precision needs to be refined. The main difficulty encountered comes from our pathophysiological application in the calcified, small and distal arteries of the leg.

Considering the imprecision inherent to every data acquisition protocol, we advise the researcher willing to do patient-specific modeling of pathological subjects to restrain to a truncated arterial network rather than to model the complete arterial tree patient-specifically. The ‘forward absorbing’ boundary

condition is also suggested at the inlet of the model, whether one considers 1D or 3D models. It is not surprising to notice that no study has validated yet the complete arterial tree on basis of patient-specific in-vivo data.

Finally, the one-dimensional modeling has proven to be relatively simple, fast-computing and efficient to reproduce arterial hemodynamics. Even though, this type of model presents limitations in the precise characterisation of the bypass conduit, and particularly at the anastomoses, the critical zones of the bypass where intimal hyperplasia is mostly observed after a few years. For example, the precise distribution of the wall shear stress along the wall can not be computed with this type of model. Also, the influence of the geometry (cuffs or patches) can not be determined.

7.1.3 Sensitivity analysis of the 1D-0D model

The second part of Chapter 4 considers the sensitivity analysis of our 1D-0D model. Even if this analysis is local (i.e. one parameter at a time fluctuates around its initial value), it allows to give a good overview of the influence of the different components of the model.

We have shown that the length of the bypass, as well as the compliance of the distal arterial network does not influence significantly the numerical results. Therefore, these parameters do not need to be measured with great precision. On the contrary, the parameters that influence the results the most are the diameter of the arteries and in particular the diameter of the common femoral artery, the resistance of the peripheral networks and, with a reduced influence, the rigidity of arteries with particular emphasis on the rigidity of the common femoral artery. Notice that the importance of the structural properties of the inlet artery of a truncated arterial network is a result that has never been emphasized before in studies of 1D-0D models.

While pressure variations seem to be global (a perturbation in a vessel propagates in the whole arterial tree), variations in velocity are local to the vessel. The way pressure or velocity waveforms vary depends on the input parameter. The directions and patterns of variation of pressure and velocity have been presented in this study: it consists mainly of translations of the whole curve and emphasis of the systole.

Another conclusion from the sensitivity analysis is the limited influence of the bypass parameters on the hemodynamical 1D results in the leg arteries. This observation points out another limitation of the 1D hemodynamics modeling: the structural nature of a vessel is only characterised by one parameter, the arterial stiffness. This type of model does not consider other important mechanisms which interfere in the development of hyperplasia intimal, such as the cellular adhesion along the endothelium, or the micro-structure of the synthetic graft.

7.1.4 Origin and propagation of waves

In Chapters 5 and 6, we still have studied 1D hemodynamics, but we have considered another point of view: the origin and propagation of waves. While Chapter 5 has studied the wave intensity analysis (WIA) (hemodynamics is considered as succession of waves from and towards the heart), Chapter 6 has focused on the reservoir-excess separation (hemodynamics results from the combination of a reservoir component due to the compliance of arteries and an excess component that drives the arterial waves). We have shown that both theories can be successfully applied to the pathological waves of bypassed lower-limb arteries.

Restrictions have been pointed out concerning the reservoir-excess separation. Under the assumption of proportionality between pressure and flow in the ascending aorta, the validity of the separation algorithm is not guaranteed in small and distal arteries, such as the popliteal artery. Also, we have shown that the pathological application of the reservoir-excess approach contradicts observations from previous studies: the reservoir component is not similar in all arteries of a patient. This comes from the modification of the vessel compliance due to the bypass surgery, atherosclerosis and insertion of the bypass graft. Notice also that the presence of reflections does not seem to impact the validity of the algorithm.

The application of WIA in bypassed vessels presents interesting results. The wave pattern generated by the heart presents great variations due to the pathology of arteries: the waves are wider and last longer than what is observed in healthy lower-limb arteries. On basis of similar and attenuated observations in stented arteries, we suggest that this pattern is due to the atherosclerosis and increased stiffness of the vessel walls.

Furthermore, the decomposition of the wave component alone (without its reservoir counterpart) into forward and backward wave intensities has been performed on our in-vivo data. Wave intensities (with and without the reservoir component) still present the same pattern but show weak variations of the amplitude.

Throughout this study, reflections of waves have played a significant role in the interpretation of results. While they are of importance in the discussion of the inlet boundary condition of the numerical model (reflections are responsible for the shape variations observed between simulated pressure and velocity waveforms), reflections from the distal vasculature of the leg appear to be of weak intensity in the WIA. Though, significant punctual reflections can be observed at marked discontinuities and bifurcations. In the reservoir-excess approach, the relative importance of reflections remained identical, with or without considering the reservoir component.

These different but simultaneous observations of reflections highlight the importance of the point of view of analysis. From a wave-propagation approach, the backward waves appear of weak intensity. Though, from the point of view

of the time evolution of waves at an arterial location, the backward component is far from negligible.

7.1.5 From a clinical point of view

Observations of the pathophysiology

In the first part of Chapter 2, pressure and velocity waveforms in the pathological bypassed arteries have been described in details, at locations proximal and distal to the occlusion, with their evolution from the healthy state to the occluded and bypassed condition. In comparison with healthy lower-limb vessels, pressure waveforms proximal to the occlusion present a single systolic wave with earlier peak and without diastolic fluctuations, as a result of the increased wall stiffness and earlier arrival of the reflected wave. Thanks to the insertion of the bypass graft, velocity waveforms in the upper leg present a triphasic contour, similarly to the healthy condition. Distal to the occlusion, waveforms might present a large pressure drop, probably due to blood leakages through collateral vessels, energy losses at the anastomoses or viscous dissipation. Leakages induce also reduced mean flows distal to the bypass.

The arterial wall stiffness of bypassed legs, which is described by the pulse wave velocity (PWV), presents increased values in comparison with healthy lower-limb arteries. The PWV in bypass grafts is larger than in arteries, especially in synthetic grafts. The peripheral networks of the leg also suffer from the pathology: the peripheral resistance is slightly increased while the peripheral compliance is reduced.

Influence of bypasses

By using numerical models of the hemodynamics, conclusions about the influence of bypasses on the hemodynamics have been suggested all along this work.

It is well-known among clinicians that the bypass success is supported by the diminution of the compliance mismatch between the native arteries and the bypass graft. In Chapter 5, the wave intensity analysis has shown that the insertion of a bypass graft of compliance largely different from the compliance of the patient's arteries created important new reflections in the leg, harmful for the cardiovascular system. We have highlighted that the compliance-mismatch might not systematically result from a too rigid graft vessel. In the clinical case considered, the compliance of the vessels is particularly large due to the stiffness of the diseased arteries, and seems to better tolerate a rigid bypass graft.

In another clinical case, blood leakages through collateral vessels and fistulae in the venous bypass graft have been observed. These should be avoided to

ensure success of the bypass surgery. This particular observation of hemodynamics can be easily noticed by looking at the wave intensity pattern (a strong decrease of the intensity of waves towards the distal arteries). Compared with the observations of pressure and velocity waveforms, WIA allows a quick detection of this abnormal flow. Flow leakage could also be observed in-vivo using flowmeters, though this technique presents great imprecisions due to the fixed size of probes. Furthermore, the observation of leakage is not direct, as the sum of flows in the deep femoral and popliteal arteries need to be computed.

In this work, no important difference in the hemodynamics has been observed between clinical cases treated with venous bypass or synthetic grafts. Similarly, no difference were found between the different types of synthetic materials. As discussed in the next section, we suggest to use 3D modeling to emphasize these differences observed in clinical practice.

Also, no conclusions could be drawn regarding the outcome of the 25 clinical cases followed, because most of them have been realized during the last two years and because detailed hemodynamic data is limited to the last 9 patients. For most subjects, vessels of the bypassed leg are still patent. Notice that in the population studied, the criteria of early graft failure did not correlate perfectly with the effective status of the bypass (occluded or patent).

From pre- to post-operative conditions

In our database of subjects, few patients present measurements before and after insertion of the bypass graft, i.e. with or without arterial occlusion. Nevertheless, these few results have shown that the surgery effectively modifies the characterisation of the physiology (the compliance and resistance of peripheral networks, the arterial stiffness). These modifications might result from the effective variation of the distal network, and also from the variation of the hemodynamic variables used for their computation. Reflections are also influenced by the insertion of the graft in the arterial network: reflections seem to increase in amplitude and to arrive earlier with the bypass graft. These few results seem to indicate that, unlike expected, no significant punctual reflection is generated by the arterial occlusion before bypass.

7.2 Outlook

In this research, approximations and estimations have been considered in the mathematical model.

Although the arterial wall behaves as a non-linear viscoelastic material, we have used a model of linear elasticity. As presented in Reymond et al. (2009), introducing a non-linear viscoelastic constitutive law for the arterial wall would induce relatively important variations of pressure and flow in the peripheral arteries. In Alastruey (2011); Alastruey et al. (2011), the influence

of the viscoelasticity (Voigt-type viscoelastic vessels) is also noted, and further models are suggested in Westerhof and Stergiopulos (2005). Two aspects need to be taken into account concerning the introduction of a viscoelastic law. Firstly, in atherosclerosed arteries, the viscoelastic behaviour of the wall is not guaranteed, as one effect of atherosclerosis is the stiffening of the vessel wall. Also, the behaviour of synthetic or venous bypasses should be studied in details. Secondly, within the scope of patient-specific modeling, introducing a more complex law comes along with the determination of the value of new parameters according to the patient's disease or bypass material. Further studies would need to evaluate if the gain in precision from the improved material law is not compromised by the uncertainty in the parameter value estimation.

We considered a simple flat velocity profile in the arteries of the numerical model. A more realistic approach would be to use the Womersley theory which takes into account the pulsatility of the velocity during the cardiac cycle (Reymond et al., 2009).

Our model simplifies the modeling of energy losses: we only included the energy losses from the viscous resistance of flow. Energy losses associated with secondary flows due to curvature and branching could be introduced in future works (Steele et al., 2003).

We have shown in the validation process that including leakages might improve numerical results in distal arteries, in some patients. Based on in-vivo observations, an objective criteria should be defined in order to decide whether leakages are needed or not for the clinical case analysed.

By considering the linear tapering of vessels, the 1D model can also assess the relevance of a tapered graft for bypass clinical practice. A tapered graft could present the advantage to reduce the mismatch in cross-sectional area between the bypass vessel and the native arteries. It also increases the peak systolic velocity at the distal anastomosis, which is favorable for the long-term patency. Even though, the increased velocity at this junction might lead to important intramural stresses, responsible for the development of intimal hyperplasia. The balance between these aspects would need to be further assessed with three-dimensional studies.

Regarding the wave intensity analysis, further in-vivo studies would need to be performed in order to verify our hypotheses regarding the WIA observed pattern (longer and wider waves). Central arteries of diseased patients with various levels of atherosclerosis should be analysed.

Within the framework of the NHEMO project, further remarks for future works can be formulated.

The data acquisition protocol is invasive and realized during surgery. While velocity acquisition can be performed non-invasively using Doppler ultrasound, the acquisition of pressure is more complex in small and calcified arteries. We suggest to investigate the use of calibrated diameter waveforms as indirect mea-

surement of the pressure waves. Arterial diameter can be determined very accurately by ultrasound (Hoeks et al., 1990), and is applicable to the pathological arteries considered in this work. Nevertheless, this method requires systolic and diastolic values of pressure for calibration, as well as the knowledge of the relation between pressure and diameter. While linear or exponential relations have efficiently been used in the carotid artery (Vermeersch et al., 2008; Meinders and Hoeks, 2004), this relation in atherosclerosed arteries of lower-limbs would need to be evaluated beforehand.

Regarding the predictive objective of the NHEMO project, we have shown in this work that the insertion of the bypass graft modifies the characterisation of the lower-limb (resistances and compliances of peripheral networks, arterial rigidity and wave reflections). Furthermore, the inlet velocity is based on a measured velocity signal in the common femoral artery, and these waveforms also slightly fluctuate before and after surgery. Therefore, using these pre-operative data as parameters of a predictive post-operative model would not lead to accurate results. Additional analysis of pre- and post-operative conditions should be considered in future work in order to clarify these relations. This task could be facilitated with the use on non-invasive data acquisition.

While the 1D-0D model is simple, efficient, and does not require much parameters computation, this model presents important limitations regarding the detailed characterisation of the hemodynamics at different zones of the bypass. Recirculations at the anastomoses, detailed wall shear stress along the bypass inner wall, characterisation of different cuffs and patches, streamlines in the bypass can only be visualised using 3D models. We therefore suggest to develop the mathematical and numerical model by using a coupling between 1D-0D and 3D models. While the distal and proximal anastomoses could be modeled using 3D geometry, the rest of the leg arterial network would be simulated with the model described in this work (i.e. similar 0D outlets and inlet boundary condition). Fluid-structure interaction laws as well as transfer of hemodynamic variables at the interfaces 3D-1D would then need to be defined.

Finally, while this work has considered the modeling of the arterial hemodynamics, one should keep in mind that other mechanisms and factors intervene in the bypass outcome. The most important one is probably the cellular adhesion along the endothelium of the vessel walls. Let us mention also the microstructure of the biomaterial of the graft or the transplant acceptance by the immune system. In the current model, structures of one-dimensional vessels are only characterised by their diameter and stiffness. Because the cellular adhesion is an important feature in the bypass outcome, it would be interesting to take this aspect into account in the characterisation of the materials, or in the model. Further research could be oriented to the evaluation of the cellular adhesion as a function of the local hemodynamics.

Appendices

APPENDIX **A**

Basic laws of hemodynamics

This appendix aims at presenting briefly some basic laws of hemodynamics used in this work. We refer the reader to Westerhof and Stergiopoulos (2005) for further information about their derivation.

Arterial resistance

The arterial resistance R describes the relation between pressure difference Δp and flow Q through a blood vessel:

$$R = \Delta p / Q. \quad (\text{A.1})$$

The resistance of a single vessel can be given by Poiseuille's law:

$$R = \frac{8\mu l}{\pi r_i^4} \quad (\text{A.2})$$

where μ is the dynamic blood viscosity, l is the length of the blood vessel and r_i is the internal radius of the vessel.

Two resistances in series result in a total resistance equal to their sum:

$$R_{total} = R_1 + R_2. \quad (\text{A.3})$$

Two resistances in parallel add up in an inverse fashion; the inverses of individual resistances (the conductances) add up to equal the parallel conductance:

$$\frac{1}{R_{total}} = \frac{1}{R_1} + \frac{1}{R_2}. \quad (\text{A.4})$$

Arterial compliance

Arterial volume compliance quantifies the pressure-volume relation in biological organs and arterial networks:

$$C = \Delta V / \Delta p \quad (\text{A.5})$$

For biological organs, the relation is generally not straight but convex to the volume axis. Compliance is not a material parameter but a structural parameter, that can be derived from material properties.

Volume compliance is usually determined from pressure and diameter measurements. Assuming a circular cross-sectional area $A = \pi D^2/4$, the area compliance is defined as

$$C_A = \Delta A / \Delta p \quad (\text{A.6})$$

and C_A is related to the volume compliance by $C = l C_A$, with l the length of the vessel.

The diameter compliance quantifies the diameter to the pressure change

$$C_D = \Delta D / \Delta p, \quad (\text{A.7})$$

and is related to the area compliance by:

$$C_A = \frac{\pi D}{2} C_D. \quad (\text{A.8})$$

Two compliances in series result in a total compliance equal to their sum; while two compliances in parallel add up in an inverse way (the sum of the inverses of the individual compliances equals the inverse of the total compliance).

Arterial elasticity

The elastic Young's modulus E is a material property and is a measure of the stiffness of the material. Its units are the units of force per area (N/m^2), i.e. (Pa) or ($mmHg$) in medical units.

From Laplace's law, one can compute the elastic Young's modulus on basis of the assumptions of a homogeneous and isotropic material. The law of Laplace relates transmural pressure p_t with wall stress σ in a cylindrical vessel of radius r_i and thickness h , and can be formulated as

$$\sigma = \frac{p_t r_i}{h}. \quad (\text{A.9})$$

Recalling Hooke's law $E = \sigma / \epsilon$, with the strain $\epsilon = \Delta r / r$, and assuming that the arterial wall is relatively thin and incompressible, the incremental elastic modulus can be computed as

$$E = \frac{r_i^2}{h} \frac{\Delta p_t}{\Delta r_i} = \frac{D_i^2}{2h} \frac{\Delta p_t}{\Delta D_i}, \quad (\text{A.10})$$

where Δp_t is the change in transmural pressure and Δr_i and ΔD_i are the changes in internal radius and diameter. In practice, the diameter is rather measured than the radius.

Using the definitions of compliances (Eqs. (A.7) and (A.8)), the elastic modulus can be written as:

$$E = \frac{D}{h} \frac{A}{C_A}. \quad (\text{A.11})$$

Moens-Korteweg equation

The Moens-Korteweg equation relates the wave speed c to the elastic modulus of the wall material E :

$$c_0(x) = \sqrt{\frac{E h}{\rho D (1 - \sigma^2)}}, \quad (\text{A.12})$$

with h the wall thickness, D the vessel diameter, ρ the blood density and σ the Poisson's ratio. This equation is derived for non-viscous fluid but is a good approximation for conduit filled with blood.

Bramwell-Hill equation

Also called the Newton-Young, or Frank equation, the Bramwell-Hill equation is derived from the Moens-Korteweg equation. It relates wave speed c to the volume compliance C , or area compliance C_A :

$$c = \sqrt{\frac{dp}{\rho} \frac{V}{dV}} = \sqrt{\frac{V}{\rho C}} = \sqrt{\frac{A}{\rho C_A}}. \quad (\text{A.13})$$

APPENDIX B

In-vivo parameters, waveforms and results of simulations

This appendix presents the database of in-vivo measurements and simulations of hemodynamics in bypassed lower-limb arteries in the 9 patients analysed.

The number of the patient, the type of bypass material used and the location of the distal anastomosis are displayed in the title. For each patient, a table summarizes the values of in-vivo measured parameters (length L , diastolic diameter D_0 , diastolic pressure p_0 , mean flow rate \bar{Q}) and computed parameters (pulse wave velocity c , reflection coefficient R_f , peripheral resistance R , peripheral compliance C , pressure diastolic decay τ) in the four vessels of the leg (CF: common femoral, DF: deep femoral, BP: bypass, PO: popliteal). Each table also includes the forward component of velocity u_f in the CF used as inlet boundary condition in the numerical simulation. The first reflection coefficient refers to the CF bifurcation while the second to the BP distal anastomosis. For all patients, these parameters are evaluated in the *POST* condition, i.e. during surgery, once the bypass is sutured to the native arteries. Notice that, for all patients the venous pressure p_{out} is set to 20 *mmHg*. Also, because measurements were not available in the bypass of patient #22, it has not been possible to compute the BP parameters R_f , c , \bar{Q} . For 4 patients (#21, #23, #24, #25), these parameters are also evaluated in the *PRE* condition, i.e. during surgery, before bypass grafting, once the superficial femoral artery is occluded.

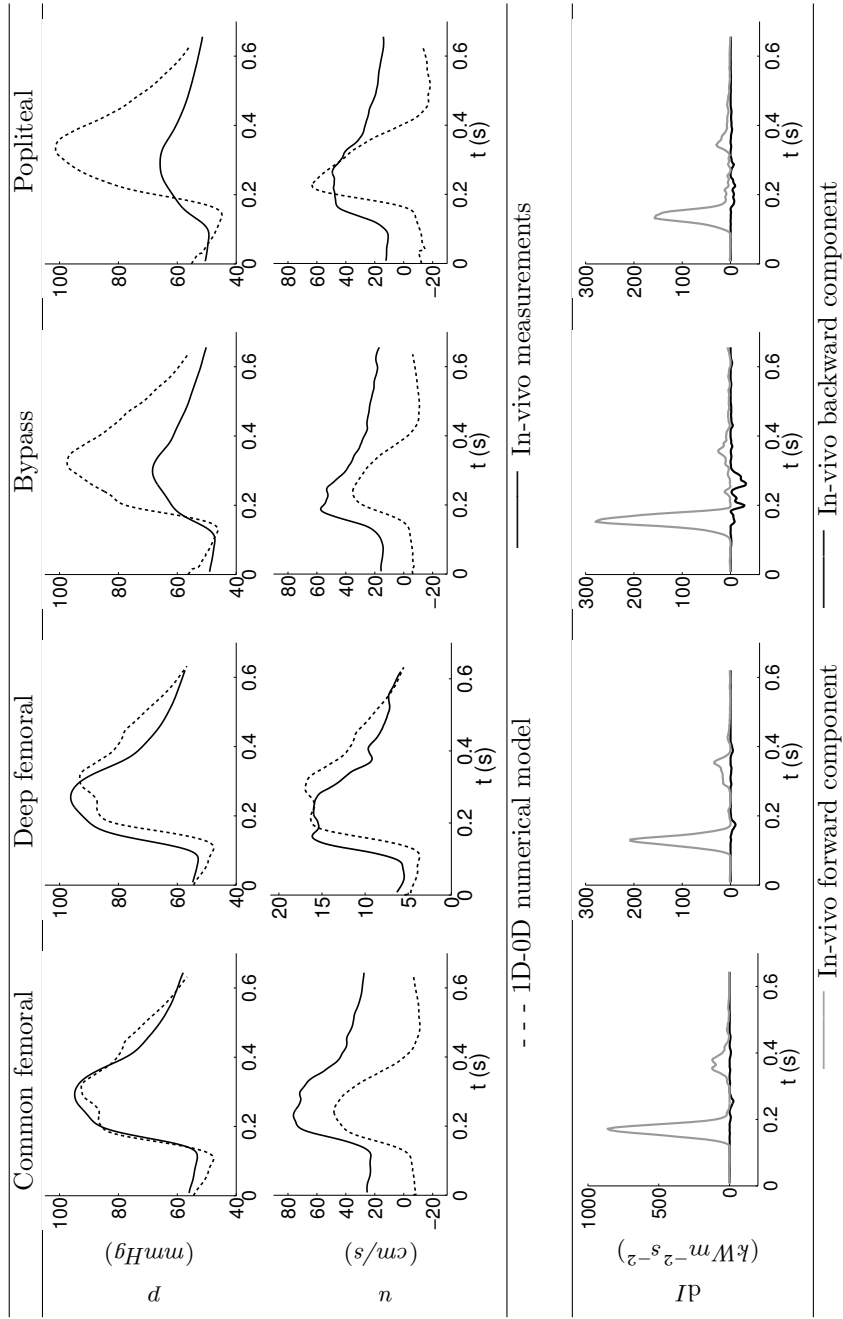
For each patient, a figure labeled “POST observations” presents the comparison of pressure p and velocity u between in-vivo measurements and results from the numerical model, in the *POST* condition. The third line of the figure presents the computation of the forward and backward wave intensity dI in the four vessels, on basis of in-vivo measurements. No comparison with the numerical wave intensity is performed for ease of visualisation.

For the four patients with in-vivo data in the PRE condition, the measurements of p and u , together with the computation of dI , are also presented in the figure labeled “PRE observations”. These waveforms only represent in-vivo data in the three arteries (CF, DF, PO), and are not compared with numerical simulations.

Patient 14, Gore-Tex bypass (6 mm), Below-knee

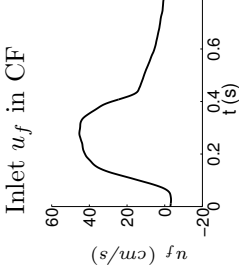
	Artery				Inlet u_f in CF
	CF	DF	BP	PO	
L (cm)	1	2	55	1	
D_0 (cm)	0.6	0.4	0.66	0.22	
p_0 (mmHg)			49		
R_f /		-0.33		0.72	
c (m/s)	8	37	5	3.5	
POST					
\bar{Q} (ml/s)	12.3	1.27	9.75	1.03	
R ($cm^{-4}gs^{-1}$)	-	$5.35e^4$	-	$5.25e^4$	
C ($cm^4g^{-1}s^2$)	-	$1.26e^{-5}$	-	$1.98e^{-5}$	
τ (s)	-	0.676	-	1.04	

Patient 14, POST observations

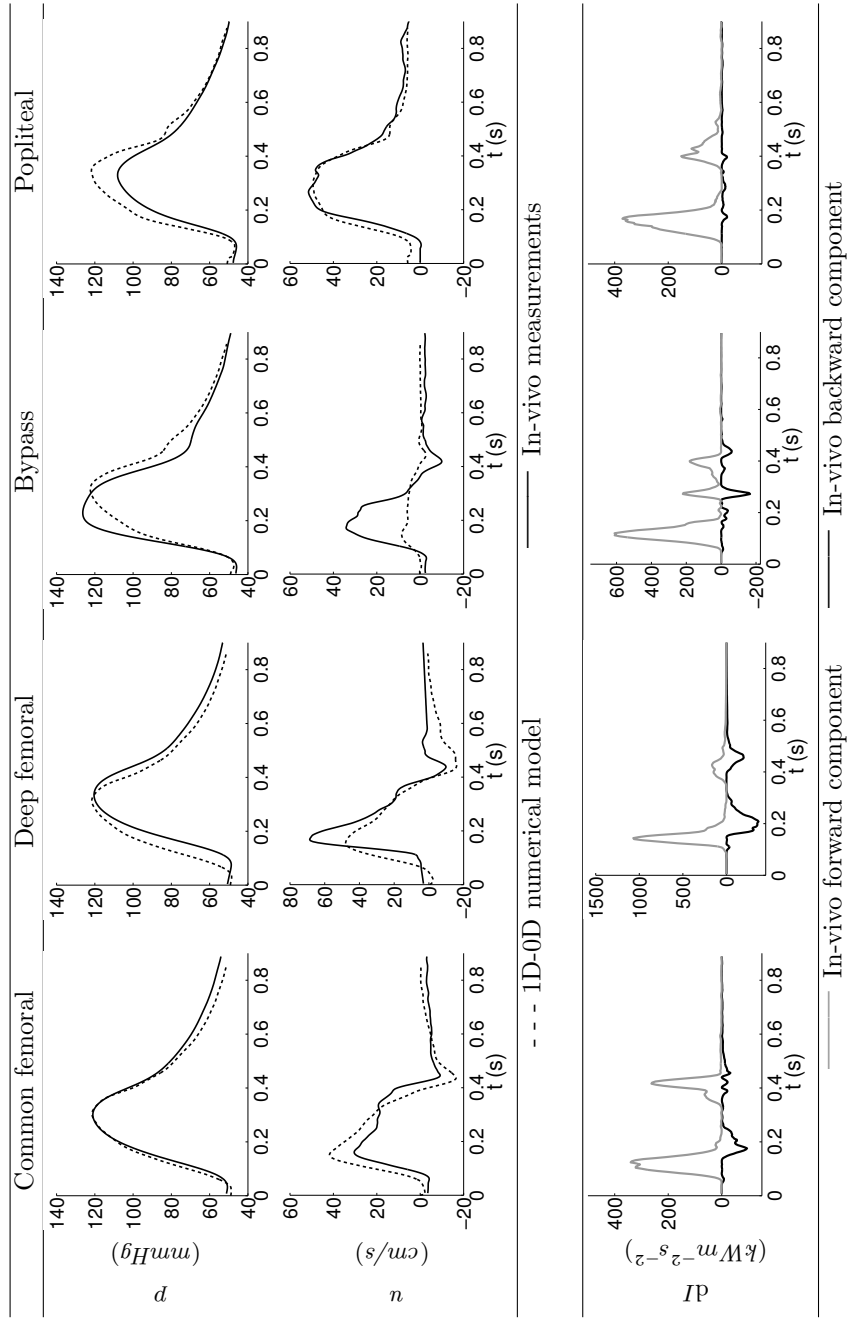


Patient 15, Gore-Tex bypass (6 mm), Below-knee

	Artery			
	CF	DF	BP	PO
L (cm)	1.5	1	55	1.5
D_0 (cm)	0.63	0.41	0.7	0.2
p_0 (mmHg)		47		
R_f /		-0.33	0.79	
c (m/s)	12	4.2	20	14
\bar{Q} (ml/s)	1.39	1.55	1.5	0.612
R ($cm^{-4}gs^{-1}$)	-	$5.65e^4$	-	$11.4e^4$
C ($cm^4g^{-1}s^2$)	-	$1.15e^{-5}$	-	$0.57e^{-5}$
τ (s)	-	0.65	-	0.65

Inlet u_f in CF	
u_f (cm/s)	
t (s)	

Patient 15, POST observations

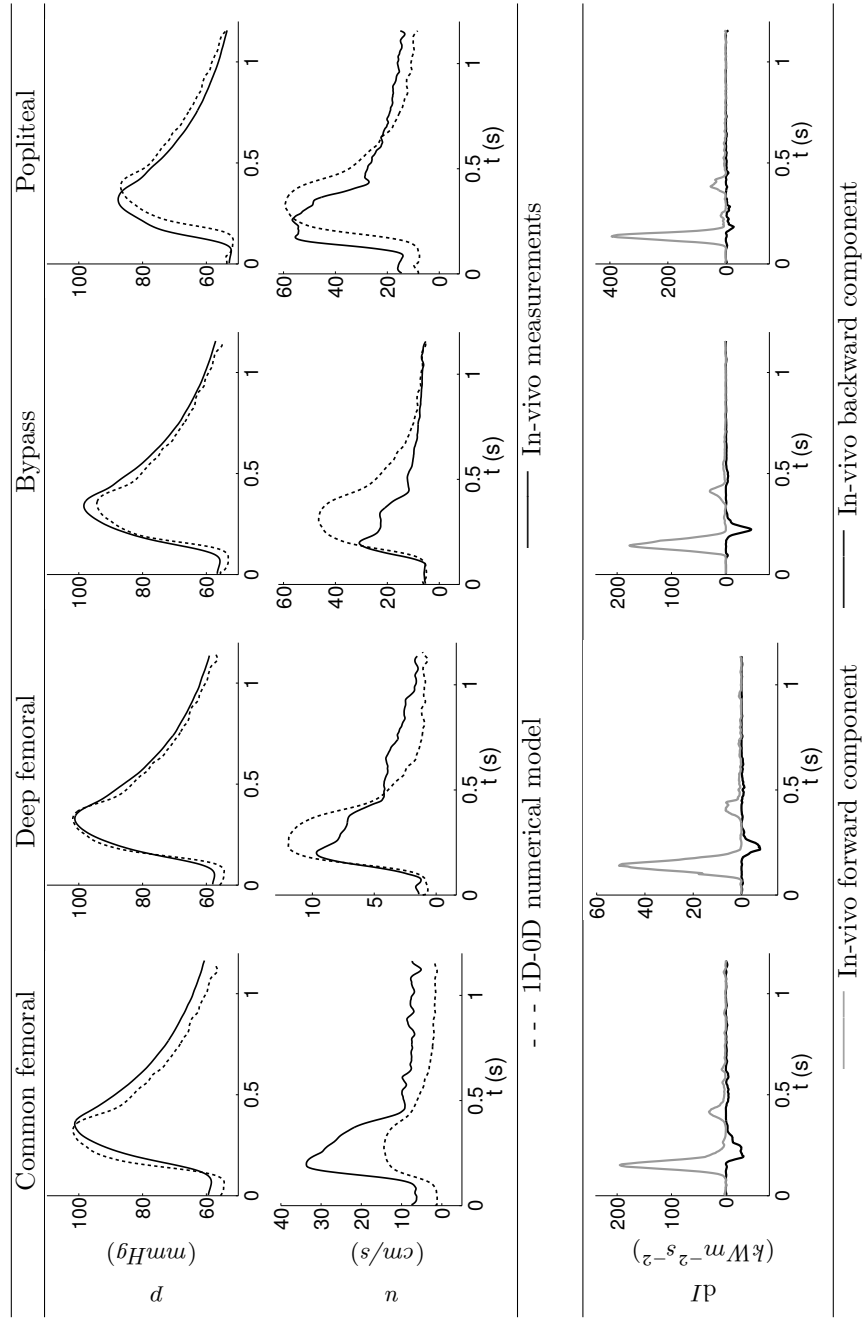


Patient 16, In-situ vein bypass, Below-knee

	Artery			
	CF	DF	BP	PO
L (cm)	1	1	51	2
D_0 (cm)	0.81	0.54	0.36	0.31
p_0 ($mmHg$)		57		
R_f /		0.60	-0.14	
c (m/s)	8.5	40	11	6
\bar{Q} (ml/s)	6.38	0.921	1.24	2.01
R ($cm^{-4}gs^{-1}$)	-	$8.32e^4$	-	$3.13e^4$
C ($cm^4g^{-1}s^2$)	-	$1.56e^{-5}$	-	$4.15e^{-5}$
τ (s)	-	1.3	-	1.3

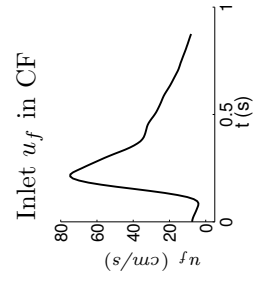
Inlet u_f in CF

Patient 16, POST observations

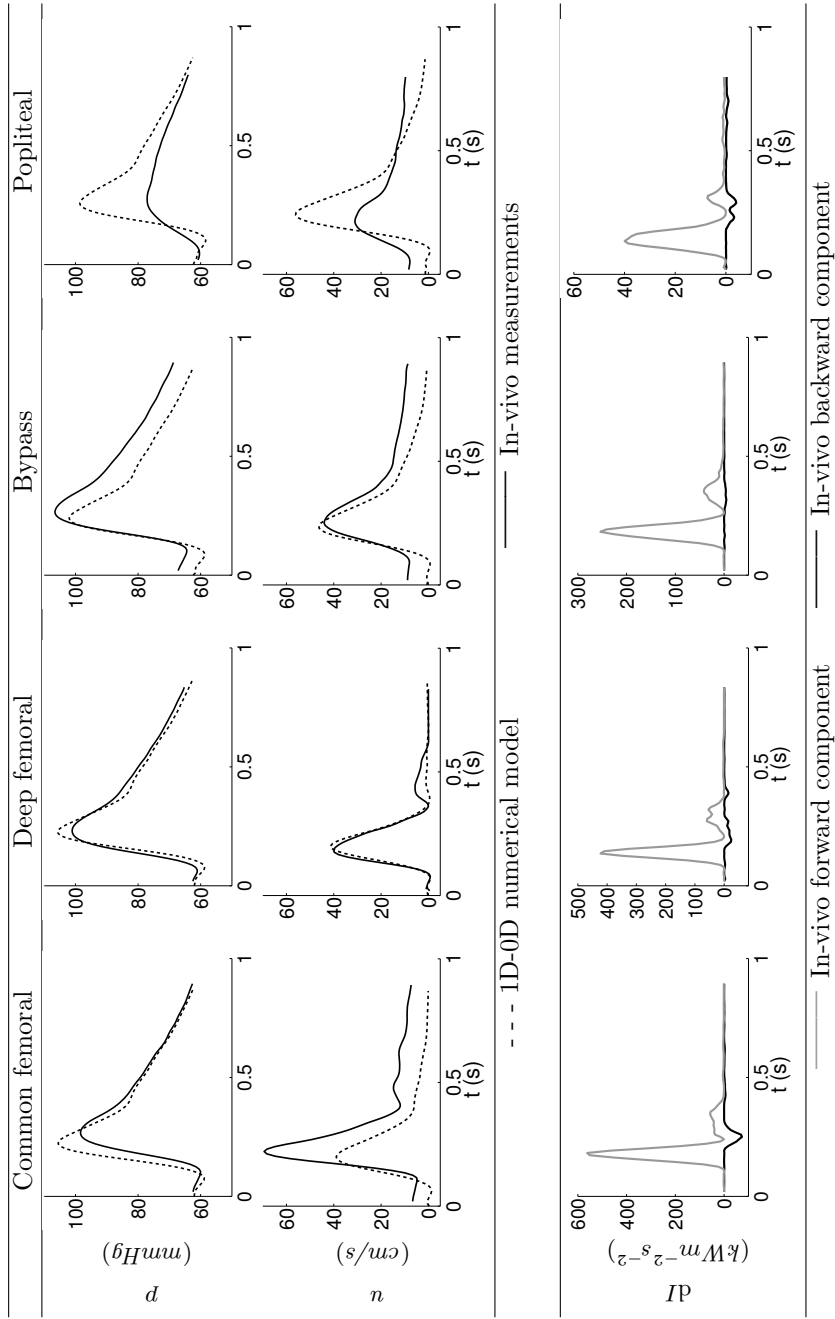


Patient 19, In-situ vein bypass, Above-knee

	Artery			
	CF	DF	BP	PO
L (cm)	3	1	30	1
D_0 (cm)	0.61	0.43	0.43	0.38
p_0 ($mmHg$)			61	
R_f /		0.33		-0.23
c (m/s)	5.8	8.9	15	7.2
\bar{Q} (ml/s)	5.53	1.12	2.63	1.76
R ($cm^{-4}gs^{-1}$)	-	$7.5e^4$	-	$3.93e^4$
C ($cm^4g^{-1}s^2$)	-	$1.58e^{-5}$	-	$4.17e^{-5}$
τ (s)	-	1.19	-	1.64



Patient 19, POST observations

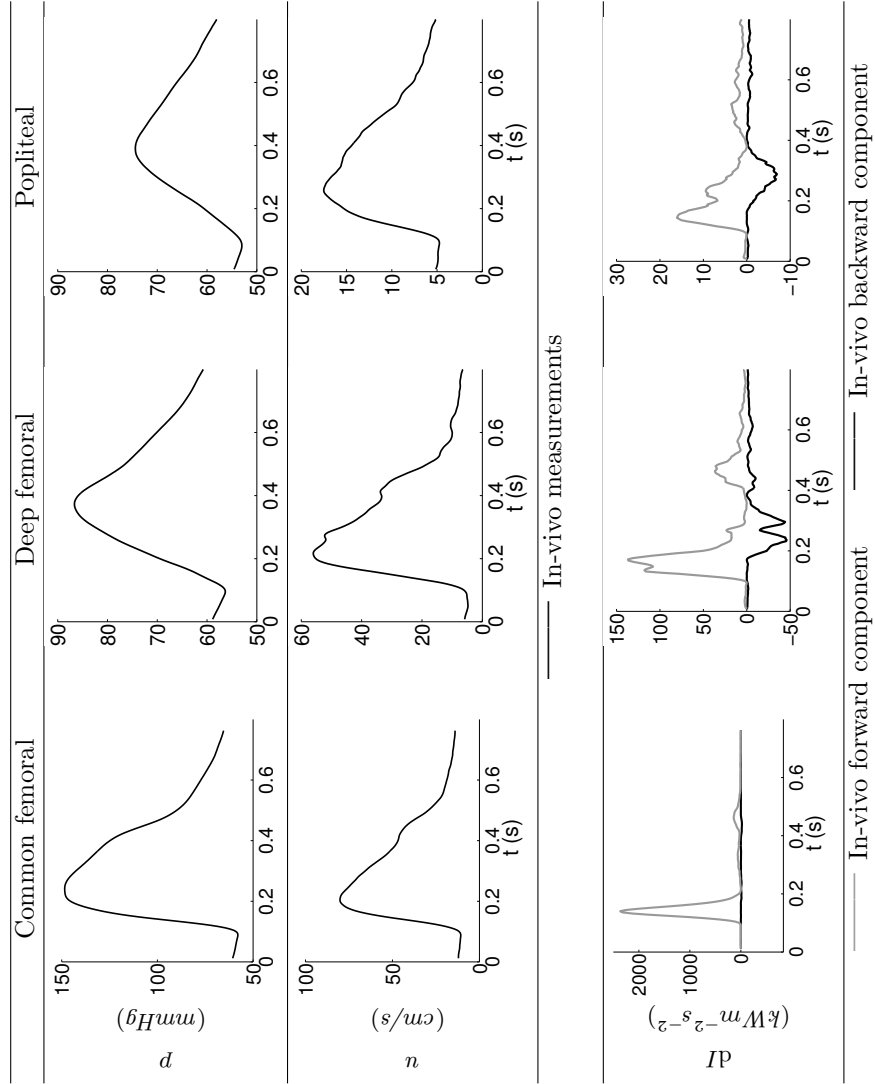


Patient 21, Dacron bypass (6 mm), Above-knee

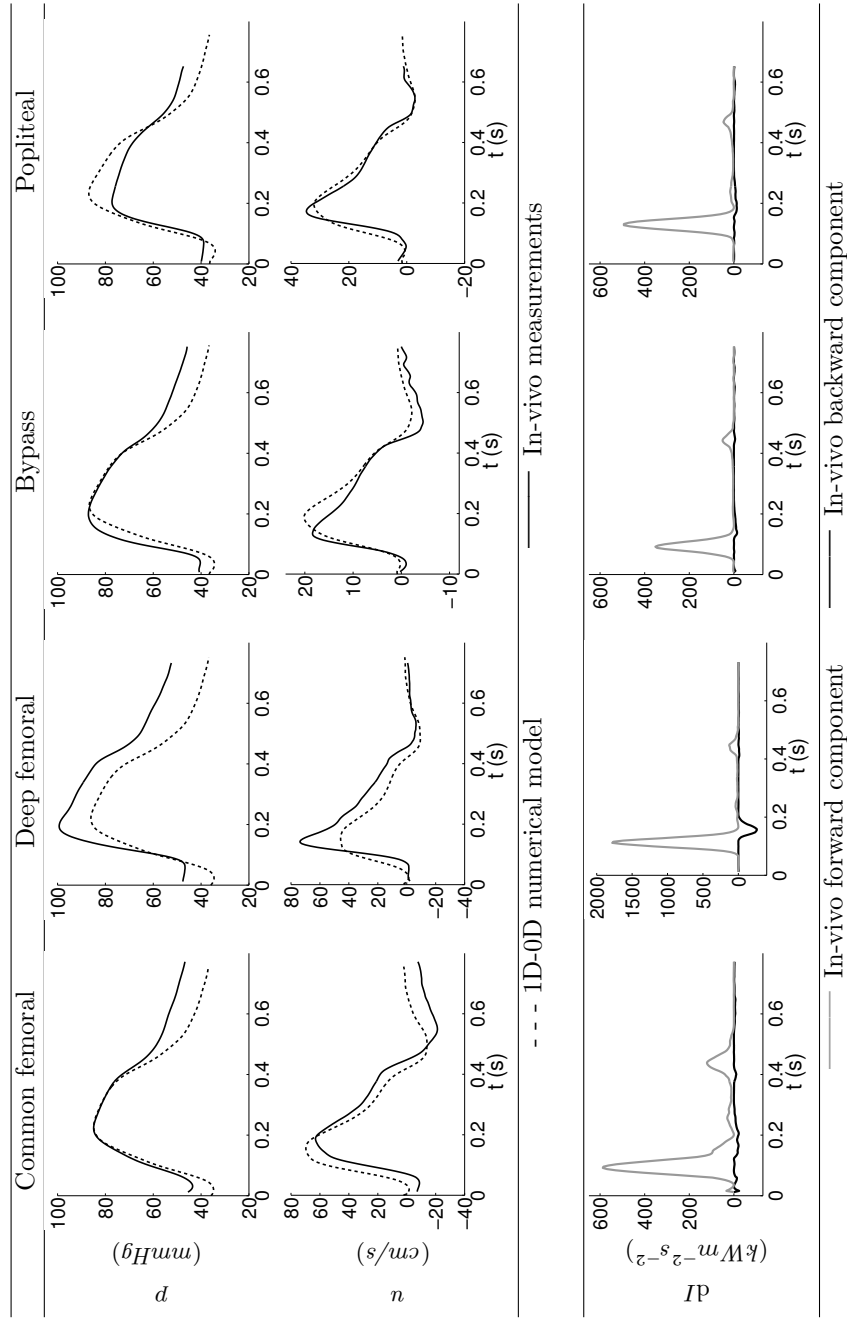
	Artery			
	CF	DF	BP	PO
L (cm)	3	1	34	3
D_0 (cm)	0.56	0.58	0.56	0.43
p_0 (mmHg)			44	
R_f /	-0.06			-0.06
c (m/s)	5	5.8	24	12.5
\bar{Q} (ml/s)	2.77	4.2	1.05	1.5
R ($cm^{-4}gs^{-1}$)	-	$1.69e^4$	-	$3.6e^4$
C ($cm^4g^{-1}s^2$)	-	$2.53e^{-5}$	-	$1.17e^{-5}$
τ (s)	-	0.428	-	0.419
c (m/s)	15	3	-	7
\bar{Q} (ml/s)	9.11	5.94	-	1.48
R ($cm^{-4}gs^{-1}$)	-	$1.37e^4$	-	$8.1e^4$
C ($cm^4g^{-1}s^2$)	-	$6.88e^{-5}$	-	$1.33e^{-5}$
τ (s)	-	0.941	-	1.08

Inlet u_f in CF

Patient 21, PRE observations

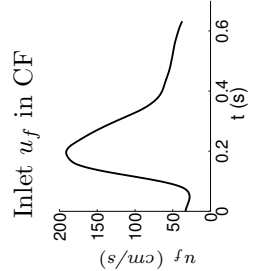


Patient 21, POST observations

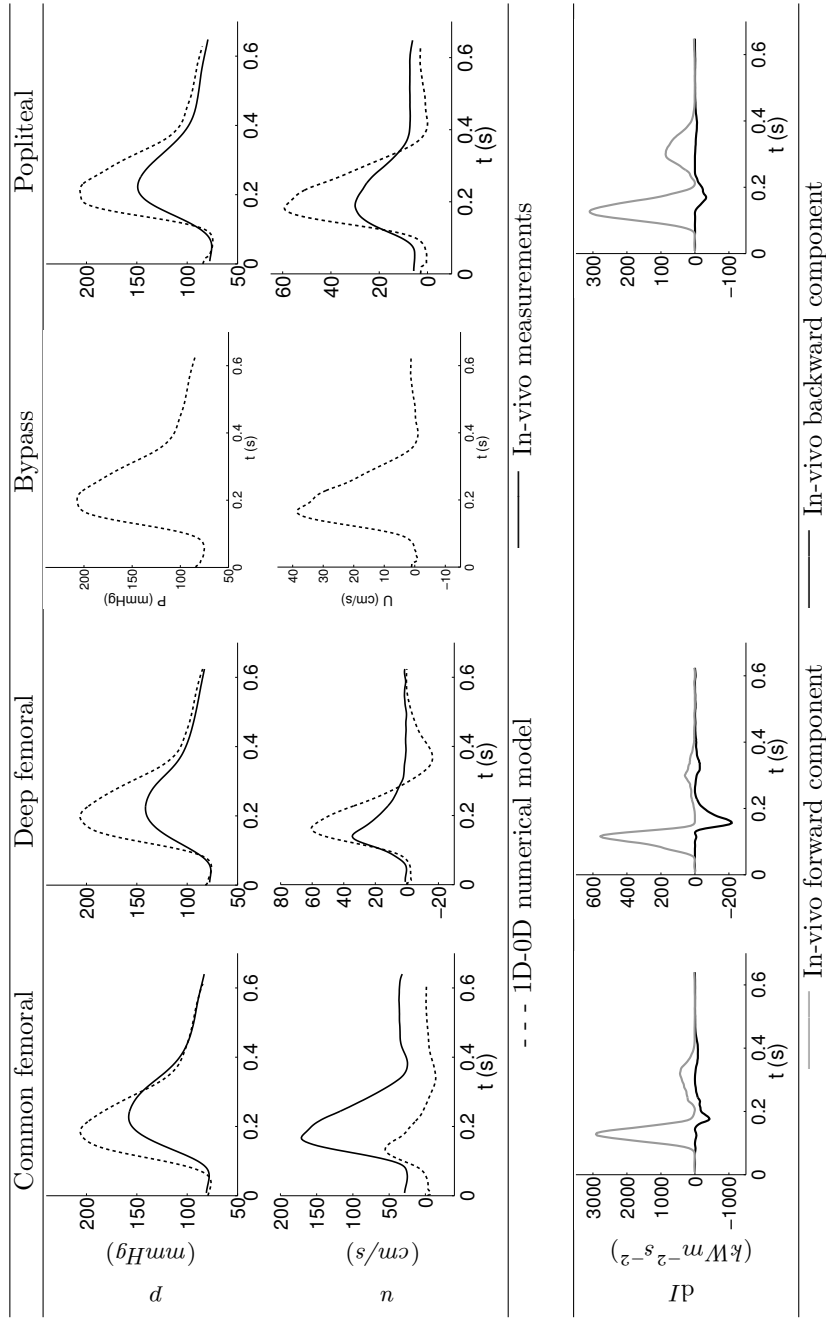


Patient 22, Gore-Tex bypass (6 mm), Above-knee

	Artery			
	CF	DF	BP	PO
L (cm)	2	3	35	2
D_0 (cm)	0.82	0.42	0.6	0.46
p_0 ($mmHg$)		80		
R_f /		-		-
c (m/s)	5	14.9	-	24
\bar{Q} (ml/s)	32.5	0.947	-	2.16
R ($cm^{-4}gs^{-1}$)	-	$12.2e^4$	-	$5.22e^4$
C ($cm^4g^{-1}s^2$)	-	$0.637e^{-5}$	-	$1.45e^{-5}$
τ (s)	-	0.776	-	0.755



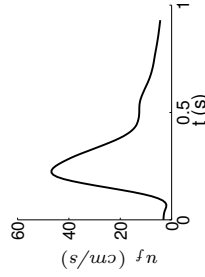
Patient 22, POST observations



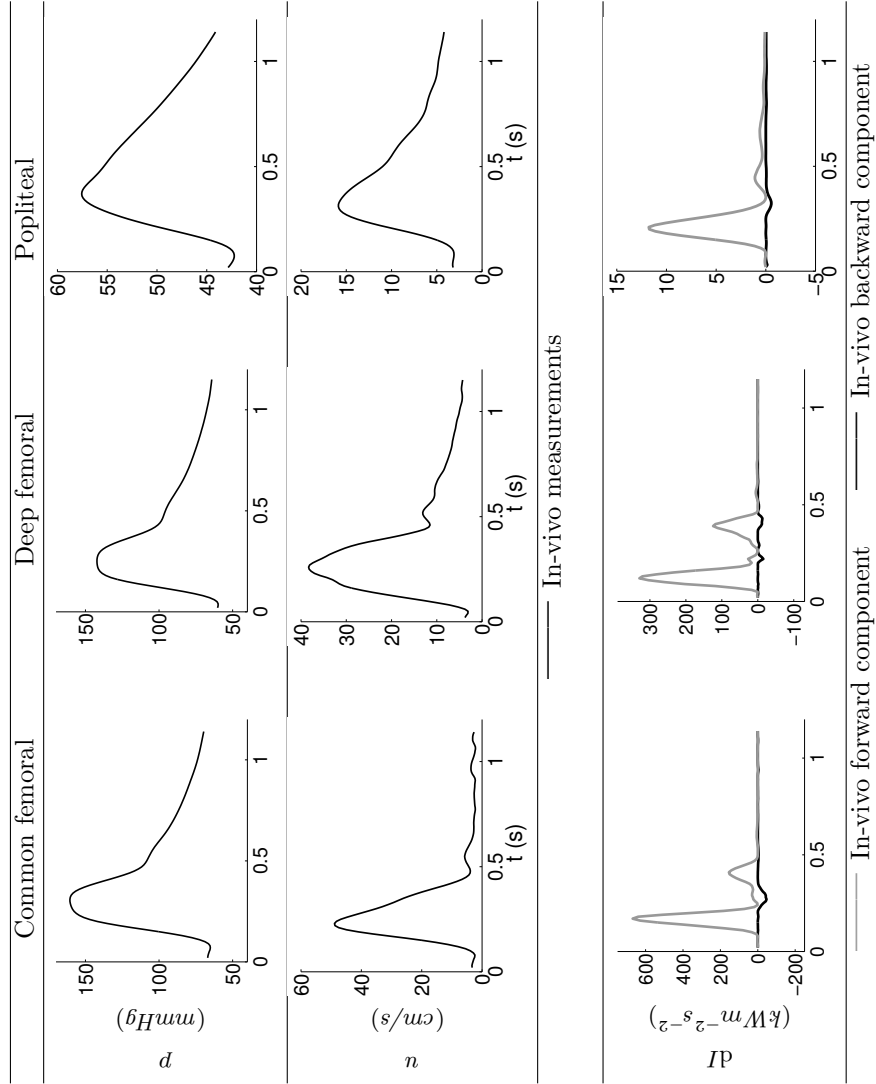
Patient 23, Gore-Tex bypass (6 mm), Above-knee

		Artery			
		CF	DF	BP	PO
L	(cm)	1.5	3	34	2
D_0	(cm)	0.68	0.55	0.6	0.55
p_0	(mmHg)		59		
R_f	/	-0.094		0.30	
c	(m/s)	19	22	23	36
\bar{Q}	(ml/s)	3.94	1.53	1.77	2.21
R	($cm^{-4}gs^{-1}$)	-	$4.61e^4$	-	$4.55e^4$
C	($cm^4g^{-1}s^2$)	-	$2.56e^{-5}$	-	$2.5e^{-5}$
τ	(s)	-	1.18	-	1.14
c	(m/s)	23	34	-	12
\bar{Q}	(ml/s)	3.91	3.31	-	1.92
R	($cm^{-4}gs^{-1}$)	-	$2.85e^4$	-	$2.08e^4$
C	($cm^4g^{-1}s^2$)	-	$3.74e^{-5}$	-	$7.39e^{-5}$
τ	(s)	-	1.07	-	1.54

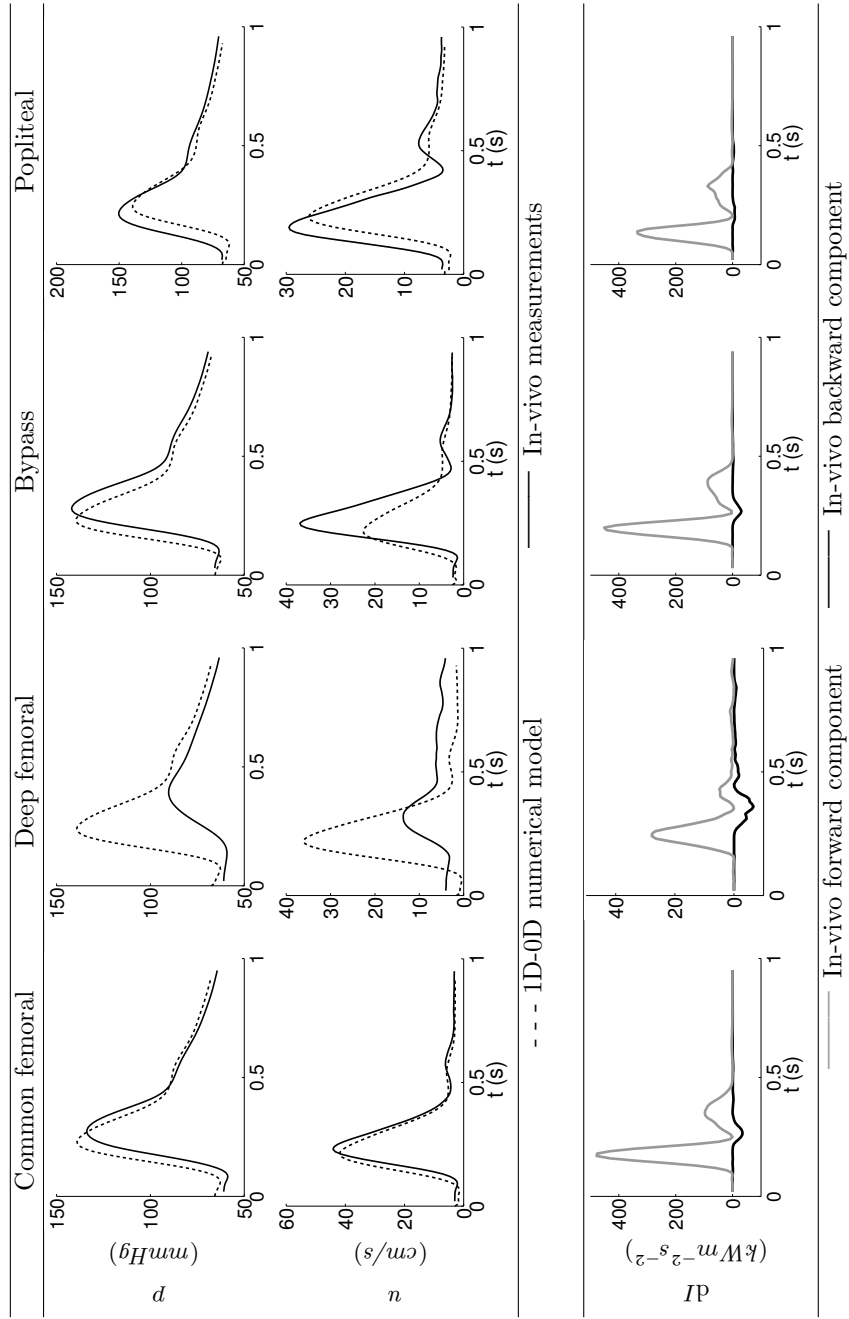
Inlet u_f in CF



Patient 23, PRE observations

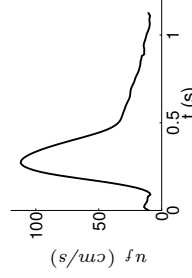


Patient 23, POST observations

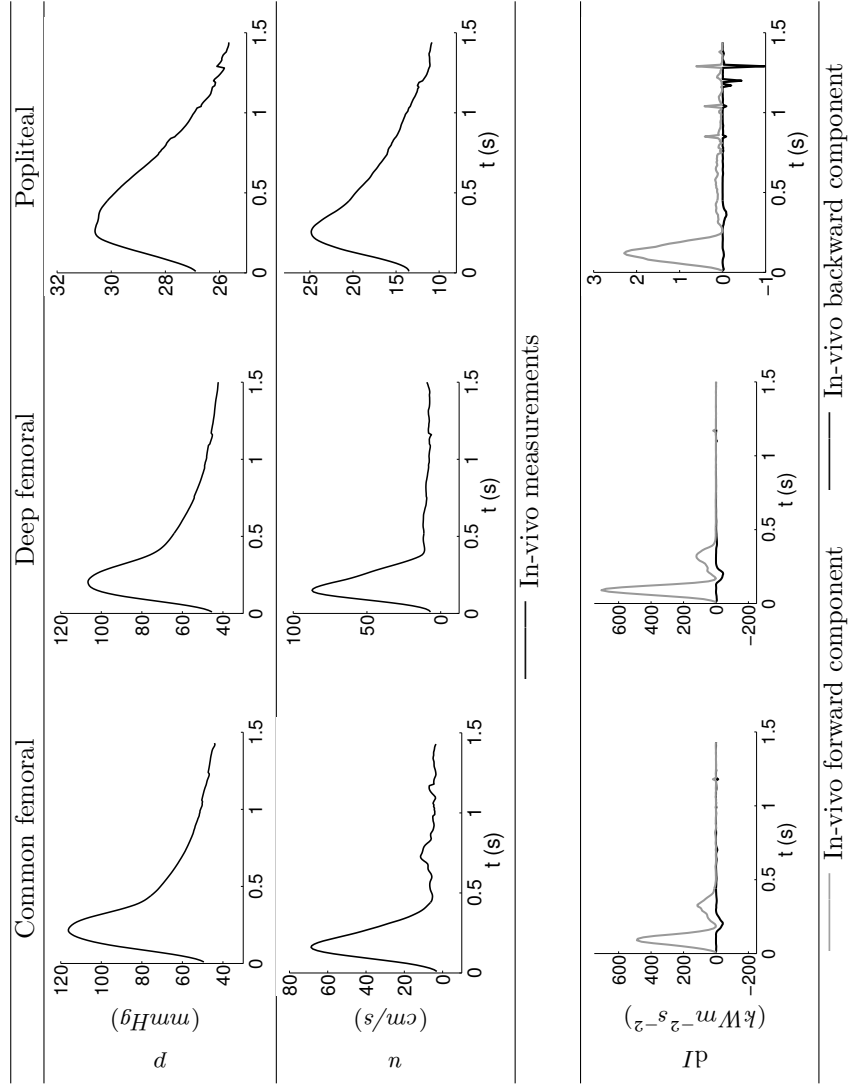


Patient 24, Dacron bypass (6 mm), Below-knee

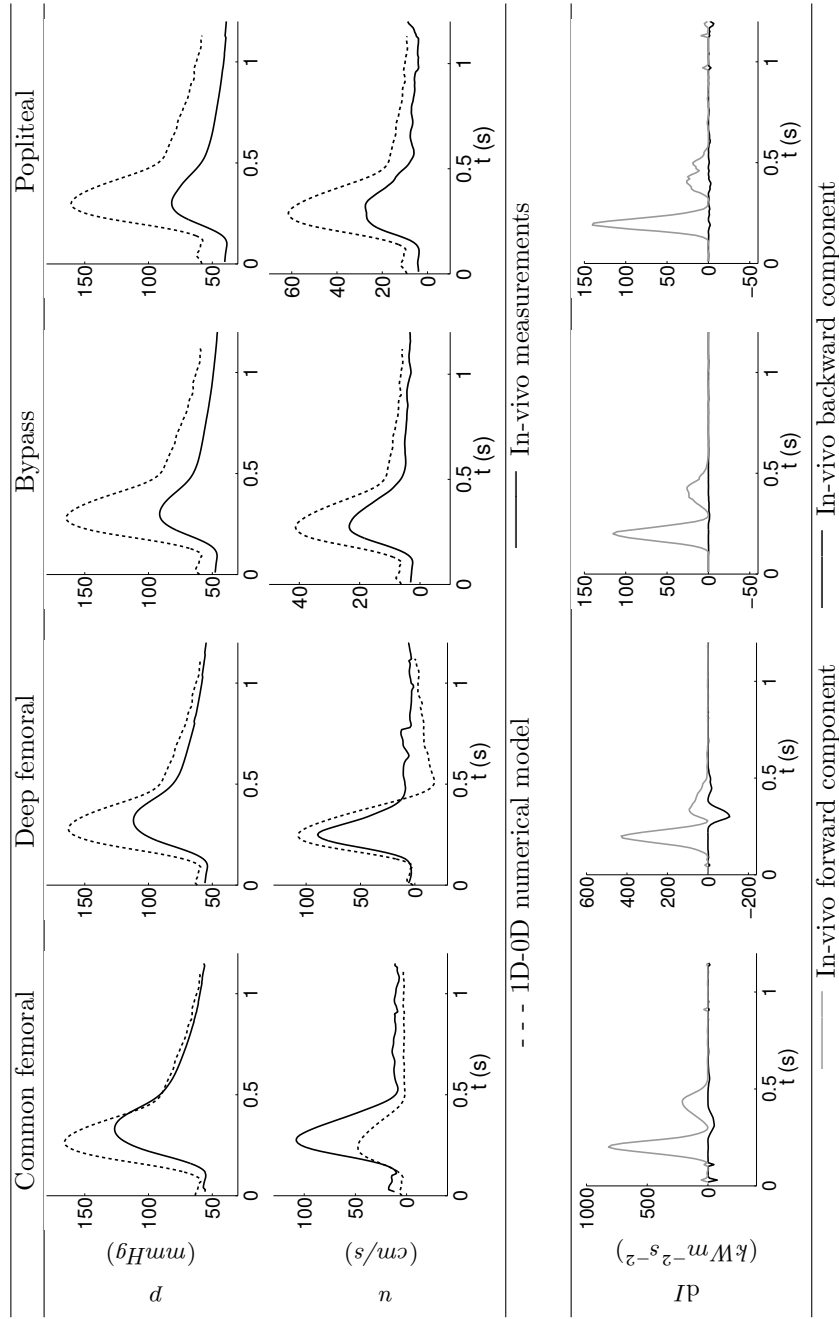
		Artery			
		CF	DF	BP	PO
L	(cm)	2	3	42	5
D_0	(cm)	0.71	0.33	0.55	0.45
p_0	(mmHg)		50		
R_f	/	0.46		0.14	
c	(m/s)	7.9	9.8	25	22
\bar{Q}	(ml/s)	10.9	1.18	1.53	1.42
R	($cm^{-4}gs^{-1}$)	-	$5.81e^4$	-	$2.61e^4$
C	($cm^4g^{-1}s^2$)	-	$2.4e^{-5}$	-	$4.7e^{-5}$
τ	(s)	-	1.39	-	1.23
c	(m/s)	10.5	8	-	4.2
\bar{Q}	(ml/s)	5.64	1.6	-	2.6
R	($cm^{-4}gs^{-1}$)	-	$3.4e^4$	-	$0.415e^4$
C	($cm^4g^{-1}s^2$)	-	$4.02e^{-5}$	-	$37e^{-5}$
τ	(s)	-	1.37	-	1.54

Inlet u_f in CF

Patient 24, PRE observations



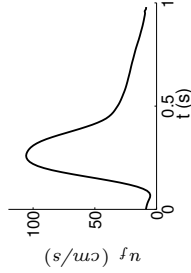
Patient 24, POST observations



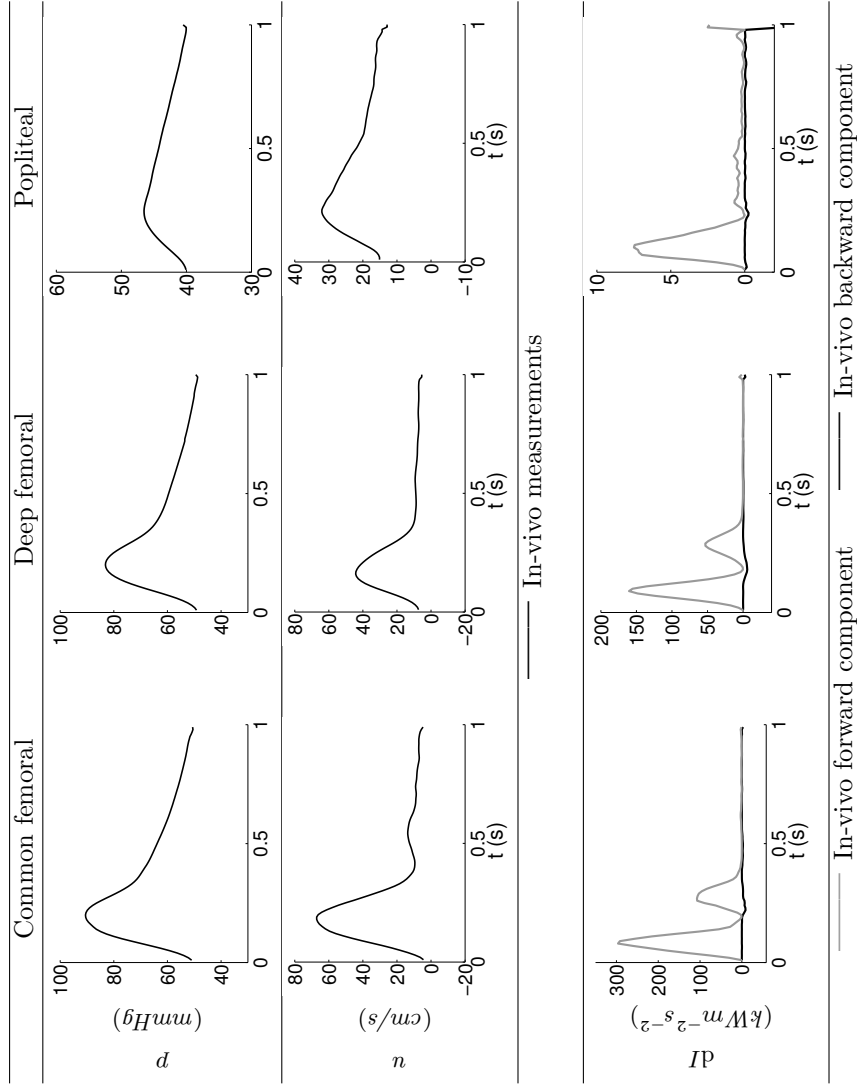
Patient 25, Gore-Tex bypass (6 mm), Above-knee

		Artery			
		CF	DF	BP	PO
L	(cm)	3	3	42	3
D_0	(cm)	0.83	0.5	0.6	0.53
p_0	(mmHg)			58	
R_f	/		0.35		-0.05
c	(m/s)	5	9.7	9	6.4
\bar{Q}	(ml/s)	15.5	1.95	5.57	6.01
R	($cm^{-4}gs^{-1}$)	-	$3.54e^4$	-	$0.736e^4$
C	($cm^4g^{-1}s^2$)	-	$4.16e^{-5}$	-	$24.3e^{-5}$
τ	(s)	-	1.47	-	1.79
c	(m/s)	7.7	10	-	4.2
\bar{Q}	(ml/s)	11.1	2.93	-	4.71
R	($cm^{-4}gs^{-1}$)	-	$1.86e^4$	-	$0.66e^4$
C	($cm^4g^{-1}s^2$)	-	$7.91e^{-5}$	-	$38.4e^{-5}$
τ	(s)	-	1.47	-	2.53

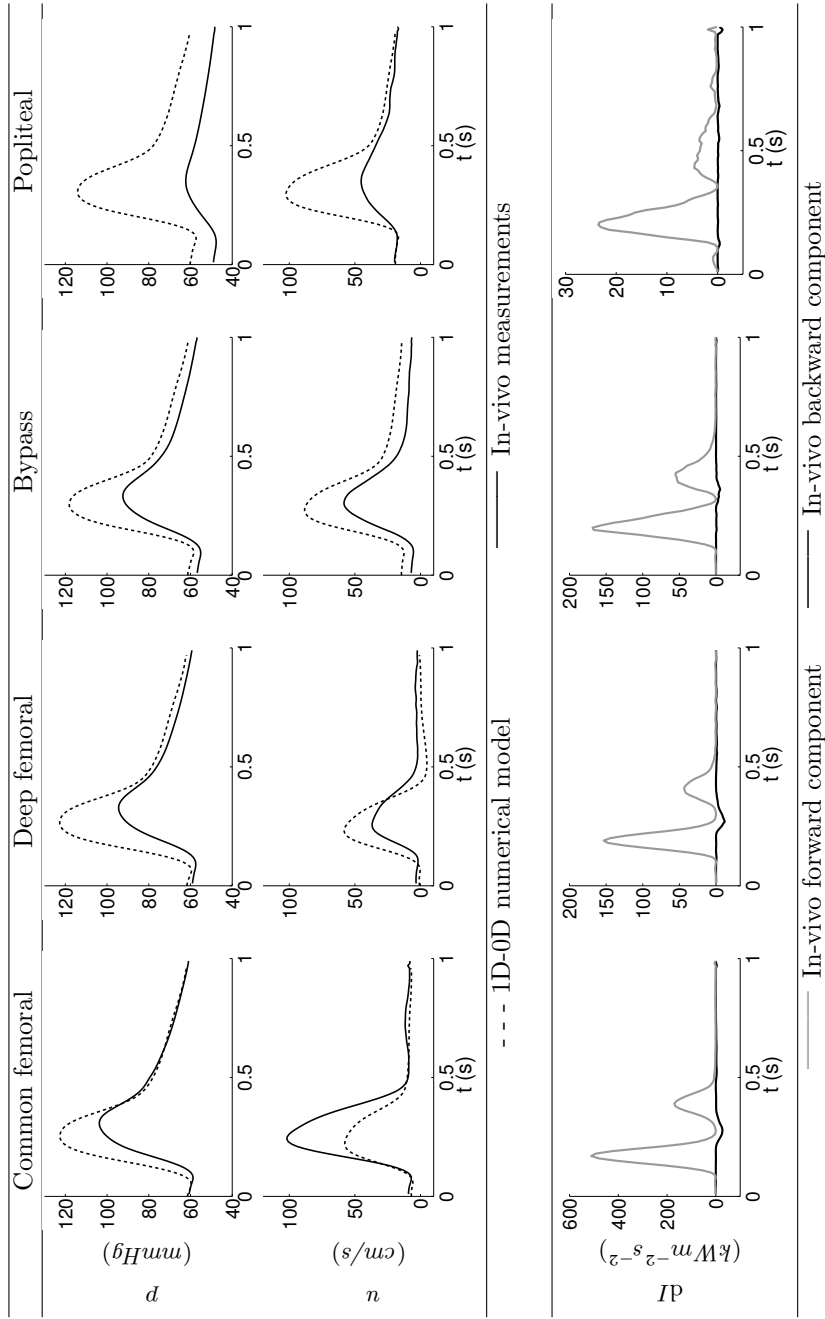
Inlet u_f in CF



Patient 25, PRE observations



Patient 25, POST observations



Additional results of the sensitivity analysis

This appendix presents additional plots relative to the sensitivity analysis of Chapter 4. As a reminder, one figure represents the mean relative sensitivity indexes ($\bar{I}_{i,k}$) for one output as a function of different inputs.

The 9 outputs considered are

- the root-mean-square error of pressure ($\tilde{\epsilon}_p$) and velocity ($\tilde{\epsilon}_u$),
- the pulse pressure (PP),
- the slope of the systolic increase (\dot{p}),
- the peak systolic velocity (PSV),
- the end diastolic velocity (EDV),
- the velocity at one third of diastole (u^*),
- the time of the systolic peak ($t(PSV)$),
- the mean flow rate over a cardiac cycle (\bar{Q}).

The input variables taken into account in this analysis are:

- the length of the bypass (L_{BP}),
- the vessel diameter (D),
- the pulse wave velocity in a vessel (c),
- the resistance of the windkessel model (R),
- the compliance of the windkessel model (C),
- the diastolic pressure (p_0).

We also study the sensitivity of the outputs to the diameter and PWV from the four vessels (D_{CF} , D_{DF} , D_{BP} , D_{PO} , c_{CF} , c_{DF} , c_{BP} , c_{PO}), as well as to the resistance and compliance from the DF and PO windkessel models (R_{DF} , R_{PO} , C_{DF} , C_{PO}).

All bar plots presented in this appendix refer to pressure, velocity or flow in the four vessels of the leg: the common femoral artery (CF), the deep femoral artery (DF), the bypass (BP) or the popliteal artery (PO).

Additional plots for subject #23 are shown, followed by results of subject #15.

Results from subject #23

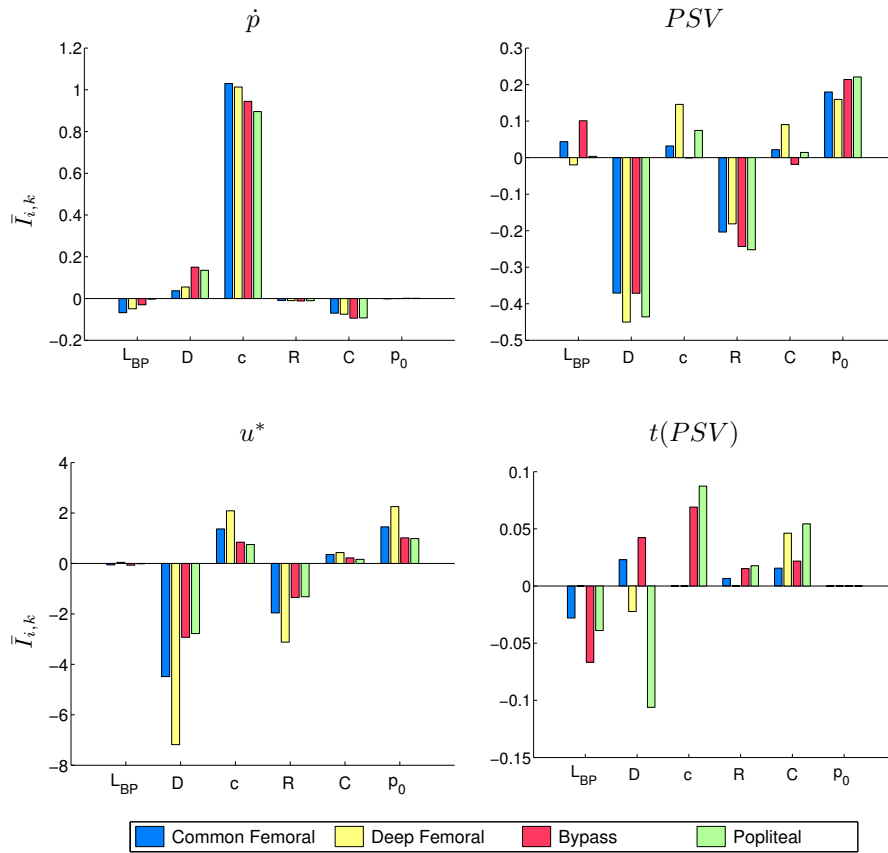


Figure C.1 – Mean relative sensitivity index $\bar{I}_{i,k}$ of the outputs \dot{p} , PSV , u^* and $t(PSV)$ as a function of the 6 input variables (L_{BP} , D , c , R , C and p_0) in the four leg vessels (subject #23).

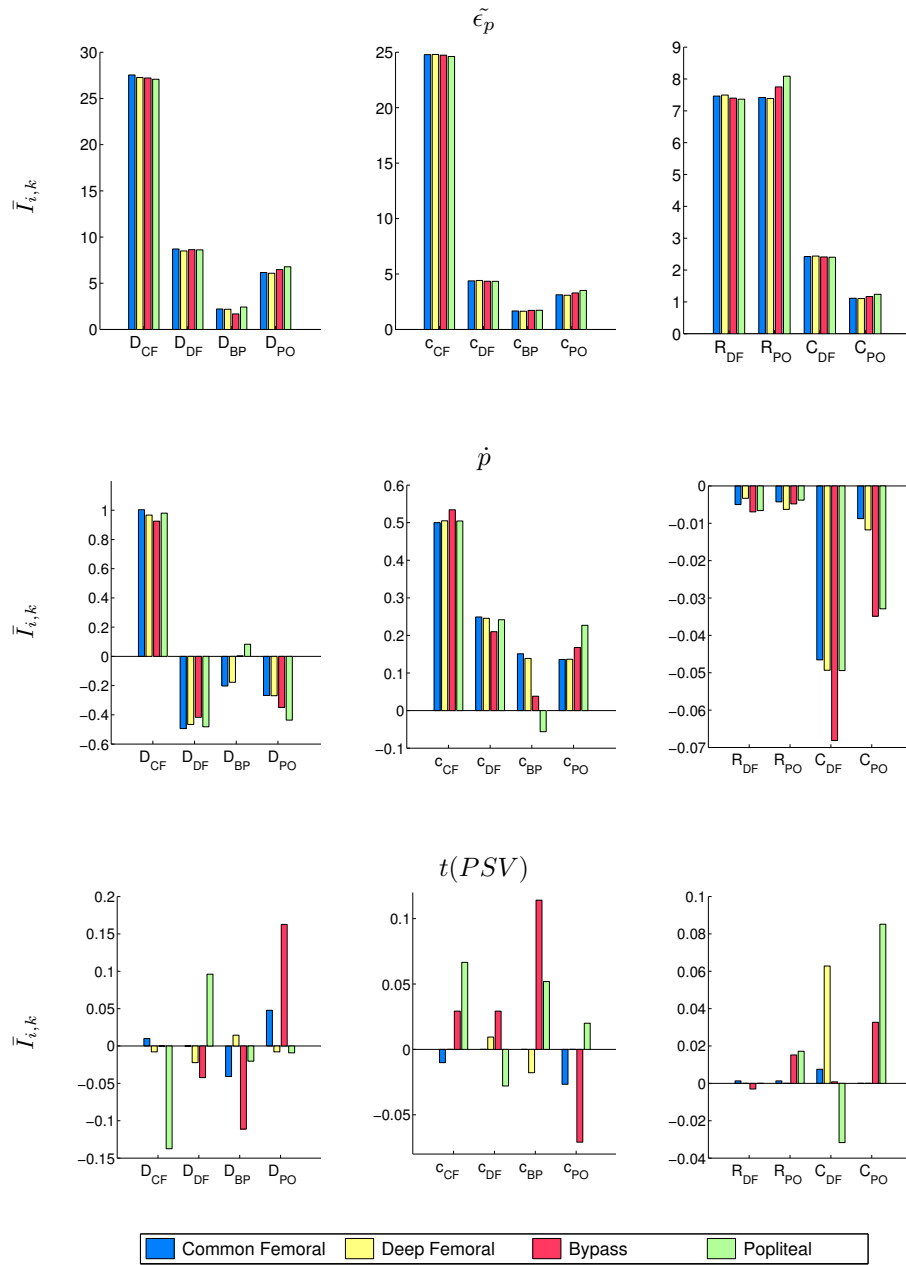


Figure C.2 – Mean relative sensitivity index $\bar{I}_{i,k}$ of the outputs $\tilde{\epsilon}_p$ (1st line), \dot{p} (2nd line) and $t(PSV)$ (3rd line) as a function of the inputs D (1st column), c (2nd column), R and C (3rd column) of the different arteries (subject #23).

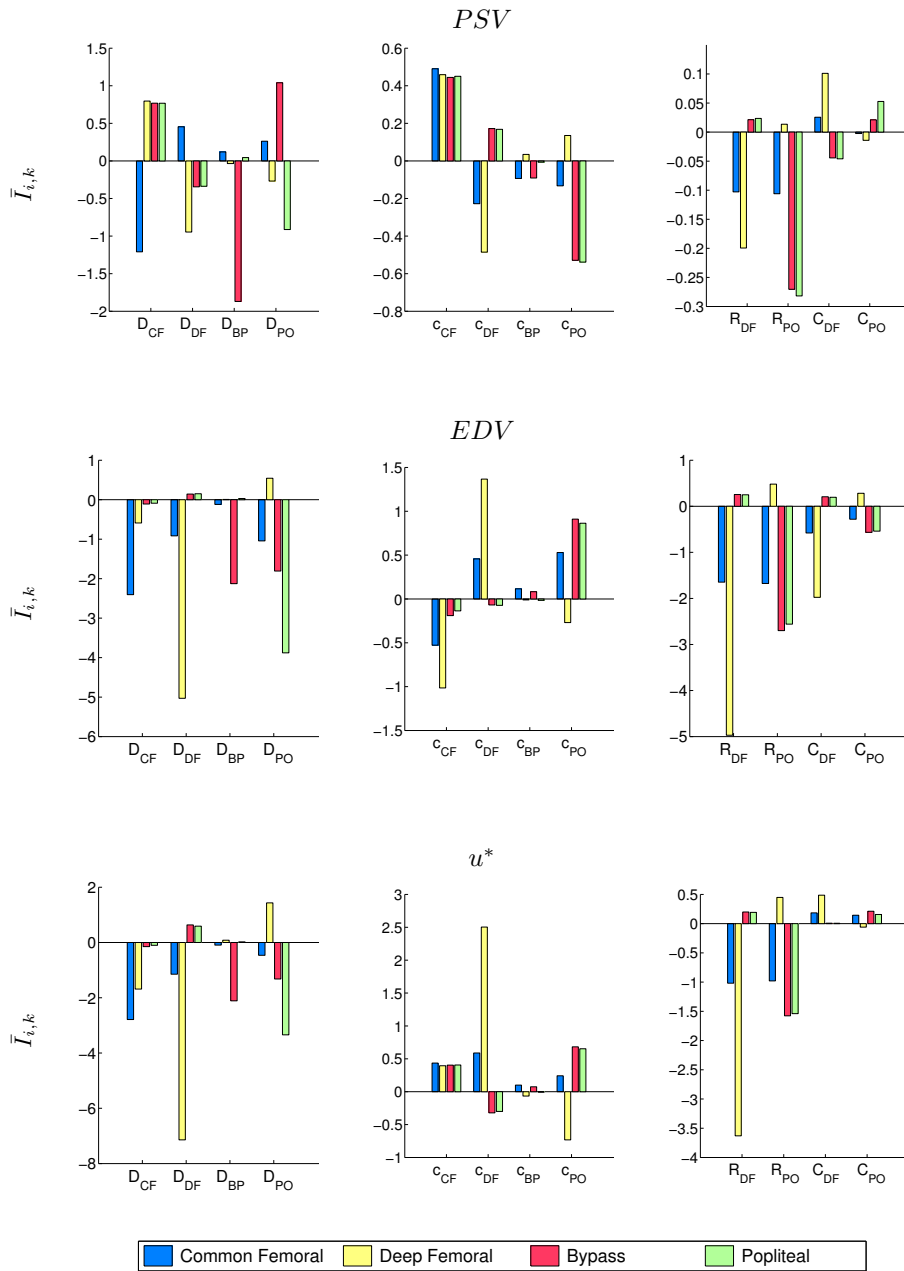


Figure C.3 – Mean relative sensitivity index $\bar{I}_{i,k}$ of the outputs PSV (1st line), EDV (2nd line) and u^* (3rd line) as a function of the inputs D (1st column), c (2nd column), R and C (3rd column) of the different arteries (subject #23).

Results from subject #15

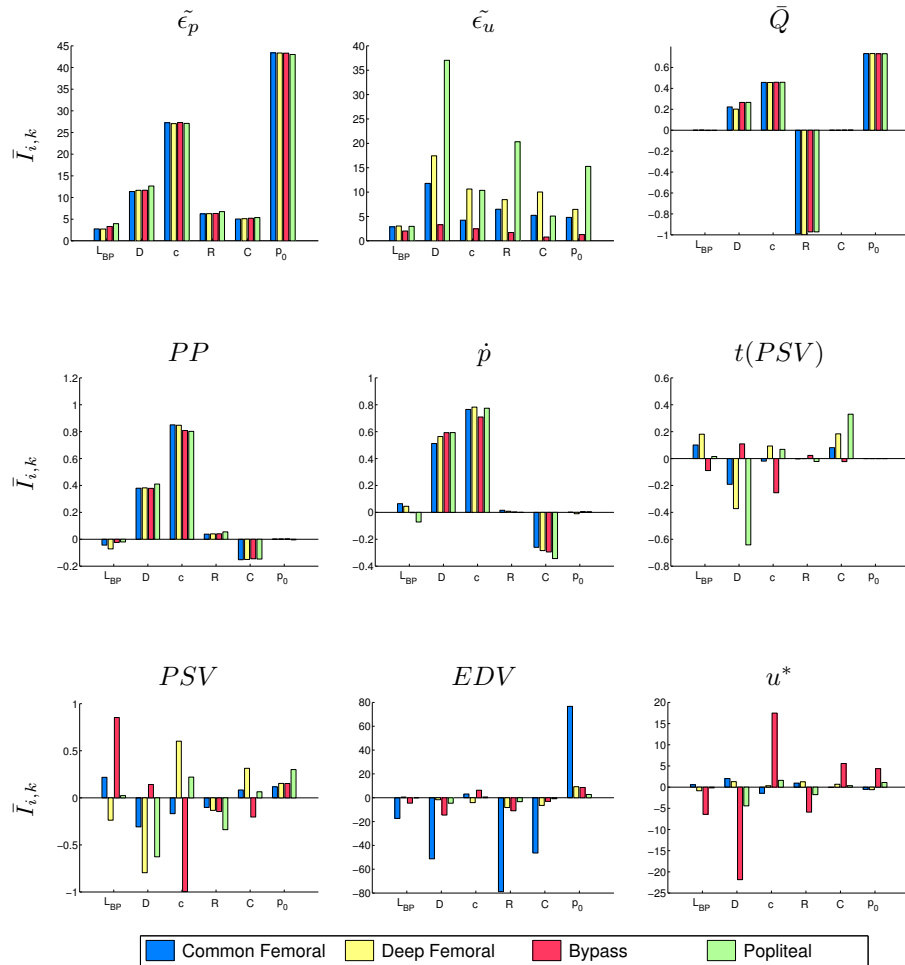


Figure C.4 – Mean relative sensitivity index $\bar{I}_{i,k}$ of the 9 outputs as a function of the 6 input variables (L_{BP} , D , c , R , C and p_0) in the four leg vessels (subject #15).

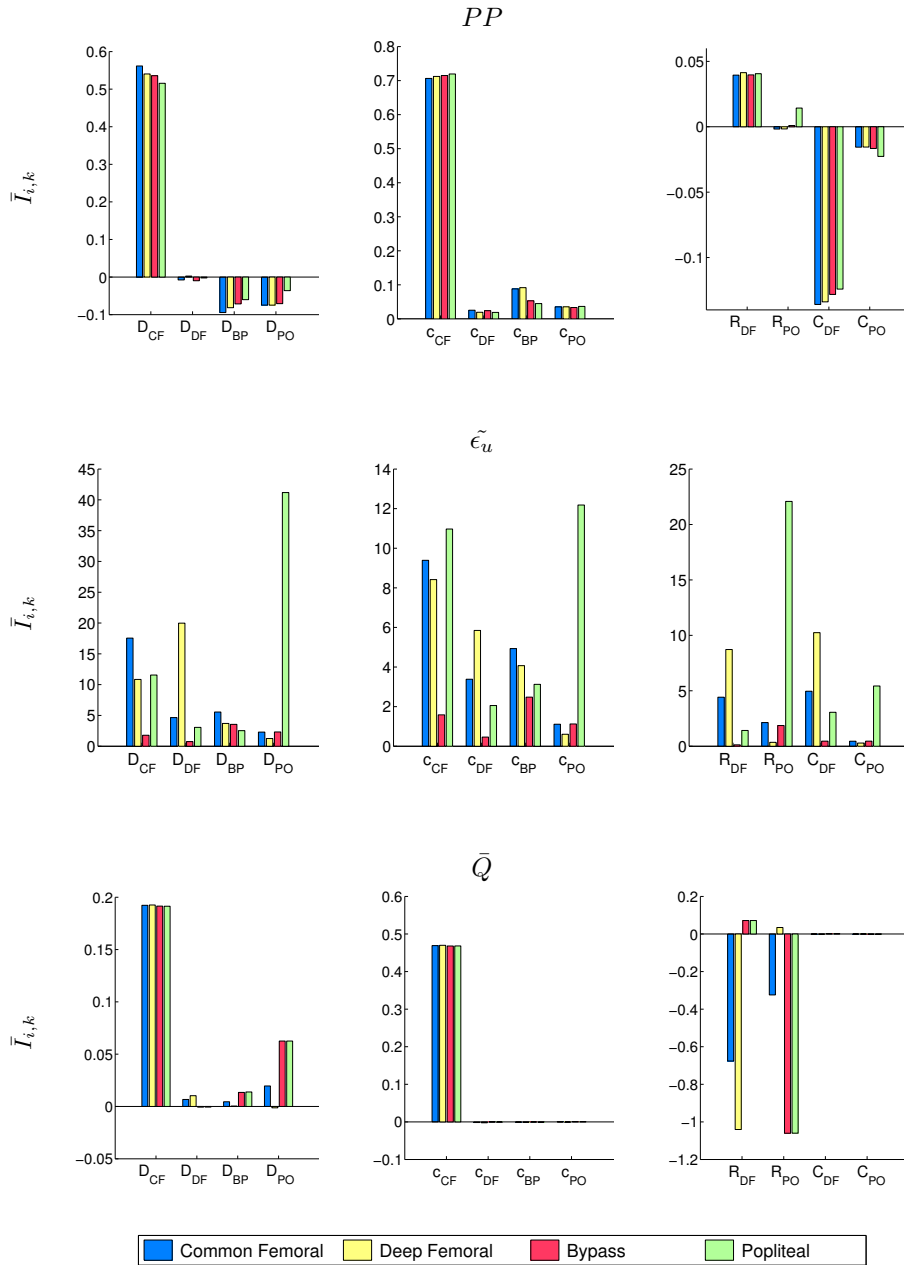


Figure C.5 – Mean relative sensitivity index $\bar{I}_{i,k}$ of the outputs PP (1st line), $\tilde{\epsilon}_u$ (2nd line) and \bar{Q} (3rd line) as a function of the inputs D (1st column), c (2nd column), R and C (3rd column) of the different arteries (subject #15).

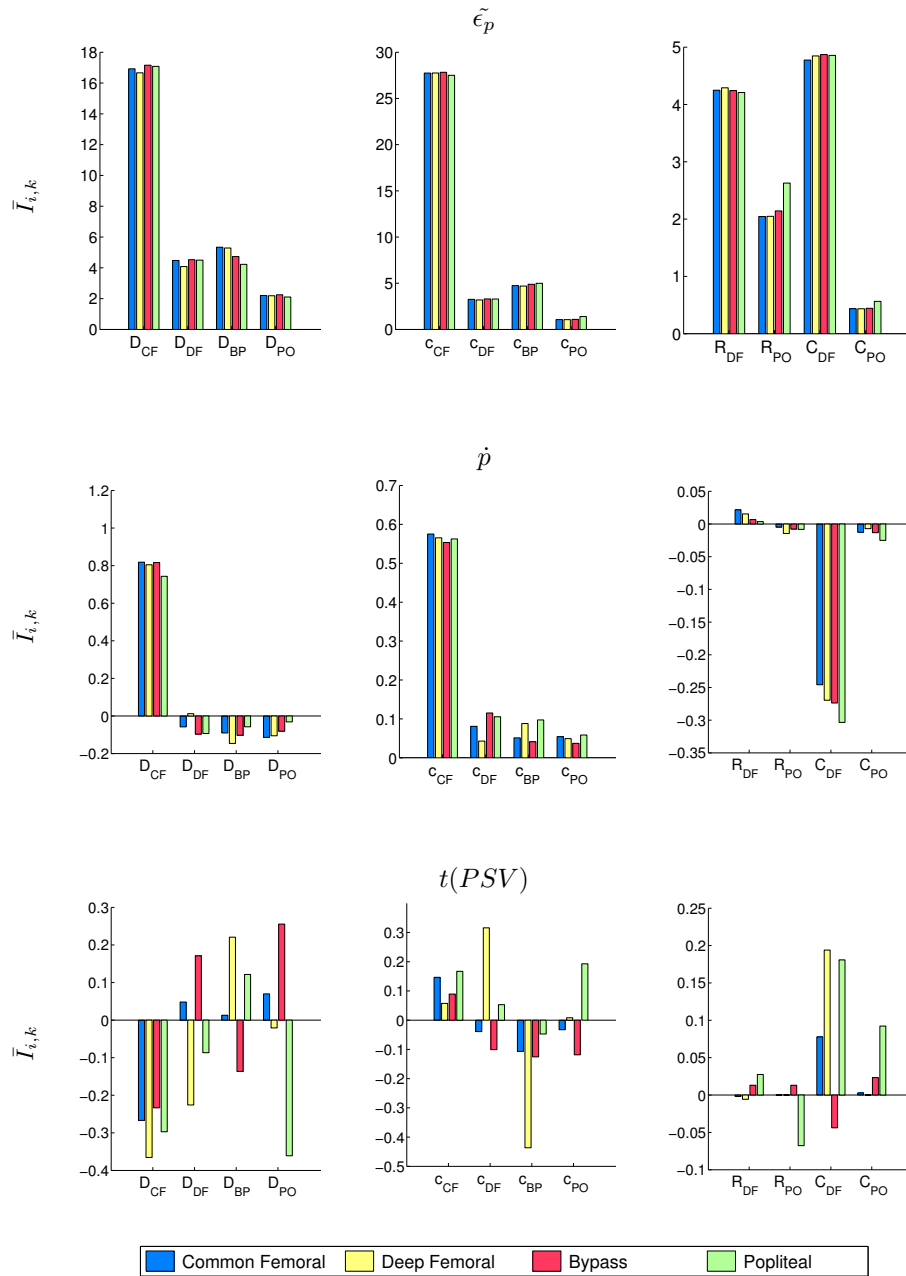


Figure C.6 – Mean relative sensitivity index $\bar{I}_{i,k}$ of the outputs $\tilde{\epsilon}_p$ (1st line), \dot{p} (2nd line) and $t(PSV)$ (3rd line) as a function of the inputs D (1st column), c (2nd column), R and C (3rd column) of the different arteries (subject #15).

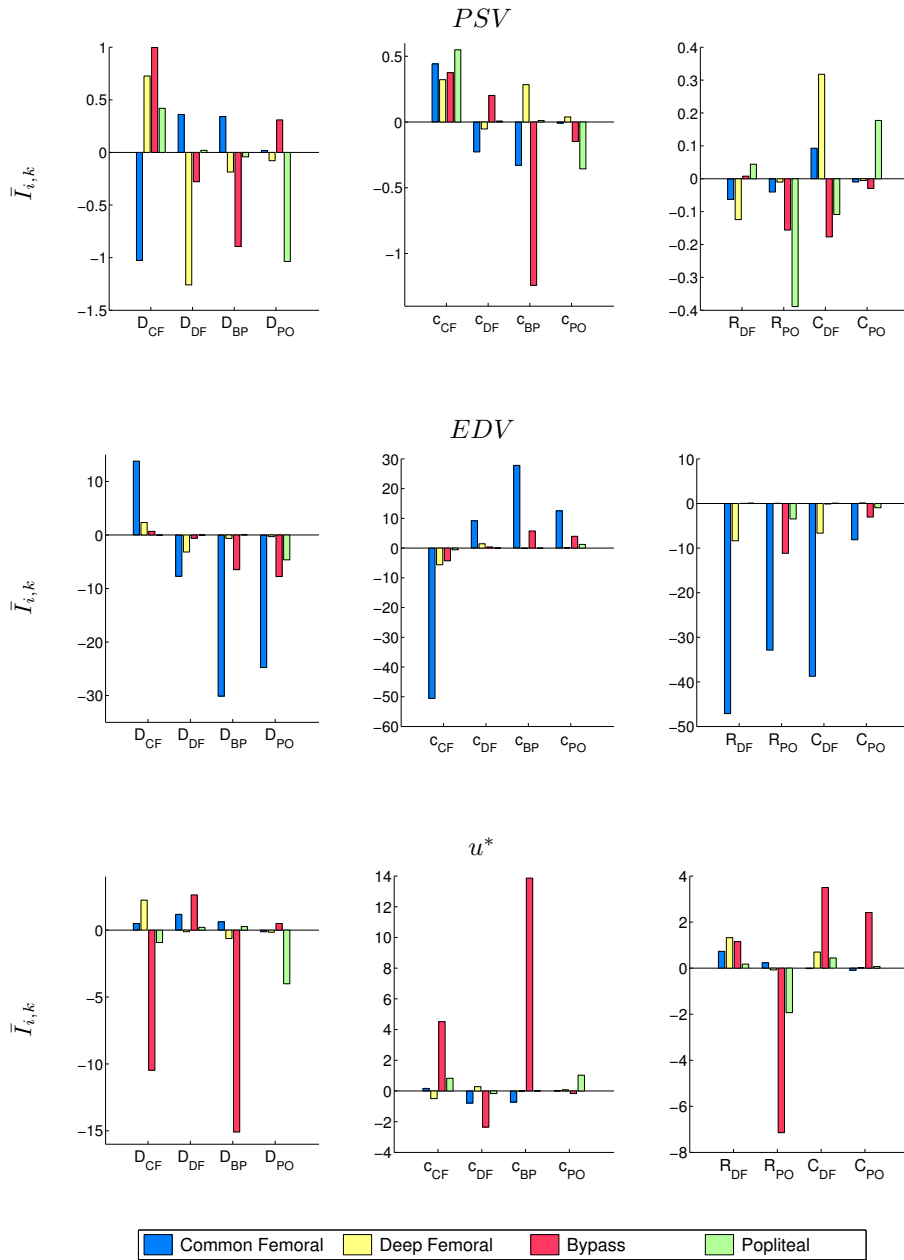


Figure C.7 – Mean relative sensitivity index $\bar{I}_{i,k}$ of the outputs *PSV* (1st line), *EDV* (2nd line) and u^* (3rd line) as a function of the inputs *D* (1st column), *c* (2nd column), *R* and *C* (3rd column) of the different arteries (subject #15).

Bibliography

- Aguado-Sierra, J., Alastruey, J., Wang, J., Hadjiloizou, N., Davies, J., Parker, K., 2008a. Separation of the reservoir and wave pressure and velocity from measurements at an arbitrary location in arteries. *Proceedings of the Institution of Mechanical Engineers. Part H, Journal of engineering in medicine* 222 (4), 403–416.
- Aguado-Sierra, J., Davies, J. E., Hadjiloizou, N., Francis, D., Mayet, J., Hughes, A. D., Parker, K. H., 2008b. Reservoir-wave separation and wave intensity analysis applied to carotid arteries: A hybrid 1D model to understand haemodynamics. In: *30th Annual International IEEE EMBS Conference*, Vancouver, British Columbia, Canada.
- Al-Qaisi, M., Nott, D., King, D., Kaddoura, S., 2009. Ankle brachial pressure index (ABPI): An update for practitioners. *Vascular Health and Risk Management* 5, 833–41.
- Alastruey, J., 2006. Numerical modeling of pulse wave propagation in the cardiovascular system: development, validation and clinical applications. Ph.D. thesis, Imperial College London.
- Alastruey, J., 2011. Numerical assessment of time-domain methods for the estimation of local arterial pulse wave speed. *Journal of Biomechanics* 44 (5), 885–891.
- Alastruey, J., Khir, A. W., Matthys, K. S., Segers, P., Sherwin, S. J., Verdonck, P. R., Parker, K. H., Peiro, J., 2011. Pulse wave propagation in a model human arterial network: Assessment of 1-D visco-elastic simulations against in vitro measurements. *Journal of Biomechanics* 44 (12), 2250–2258.
- Alastruey, J., Parker, K. H., Peiró, J., Byrd, S. M., Sherwin, S. J., 2007. Modelling the circle of Willis to assess the effects of anatomical variations and occlusions on cerebral flows. *Journal of Biomechanics* 40 (8), 1794–1805.
- Alastruey, J., Parker, K. H., Peiró, J., Sherwin, S., 2008. Lumped parameter outflow models for 1-D blood flow simulations: Effect on pulse waves and parameter estimation. *Communications in Computational Physics* 4, 317–336.

- Alastruey, J., Parker, K. H., Peiró, J., Sherwin, S. J., 2006. Can the modified Allen's test always detect sufficient collateral flow in the hand? A computational study. *Computer Methods in Biomechanics and Biomedical Engineering* 9 (6), 353–361.
- Alastruey, J., Parker, K. H., Peiró, J., Sherwin, S. J., 2009. Analysing the pattern of pulse waves in arterial networks: a time-domain study. *Journal of Engineering Mathematics* 64, 331–351.
- Albers, M., Battistella, V., Romiti, M., Rodrigues, A., Pereira, C., 2003. Meta-analysis of polytetrafluoroethylene bypass grafts to infrapopliteal arteries. *Journal of Vascular Surgery* 37, 1263–1269.
- Asmar, R., Benetos, A., Topouchian, J., Laurent, P., Pannier, B., Brisac, A., Target, R., Levy, B., 1995. Assessment of arterial distensibility by automatic pulse wave velocity measurement. validation and clinical application studies. *Hypertension* 35, 637–642.
- Avolio, A., 1980. Multi-branched model of the human arterial system. *Medical and Biological Engineering and Computing* 18 (6), 709–718.
- Avolio, A., Chen, S., Wang, R., Zhang, C., Li, M., O'Rourke, M., 1983. Effects of aging on changing arterial compliance and left ventricular load in a northern Chinese urban community. *Circulation* 68, 50–58.
- Avolio, A., Deng, F., Li, W., Luo, Y., Huang, Z., Xing, L., O'Rourke, M., 1985. Effects of aging on arterial distensibility in populations with high and low prevalence of hypertension: comparison between urban and rural communities in China. *Hypertension* 71 (2), 202–210.
- Balar, S. D., Rogge, T. R., Young, D. F., 1989. Computer simulation of blood flow in the human arm. *Journal of Biomechanics* 22 (6-7), 691–697.
- Bandyk, D., Cato, R., Towne, J., 1985. A low flow velocity predicts failure of femoropopliteal and femorotibial bypass grafts. *Surgery* 89 (4), 799–809.
- Bertolotti, C., Deplano, V., 2000. Three-dimensional numerical simulations of flow through a stenosed coronary bypass. *Journal of Biomechanics* 33 (8), 1011–1022.
- Bessemers, D., 2006. On the propagation of pressure and flow waves through the patient specific arterial system. Ph.D. thesis, Technische Universiteit Eindhoven.
- Bessemers, D., Giannopapa, C. G., Rutten, M. C., van de Vosse, F. N., 2008. Experimental validation of a time-domain-based wave propagation model of blood flow in viscoelastic vessels. *Journal of Biomechanics* 41, 284–291.

- Blanco, P., Pivello, M., Urquiza, S., Feijóo, R., 2009. On the potentialities of 3D-1D coupled models in hemodynamics simulations. *Journal of Biomechanics* 42(7), 919–930.
- Bland, J. M., Altman, D. G., 1986. Statistical methods for assessing agreement between two methods of clinical measurement. *Lancet* 1, 307–310.
- Borlotti, A., Vermeersch, S., Rietzschel, E., Segers, P., Khir, A., 2010. A comparison between local wave speed in the carotid and femoral arteries in healthy humans: application of a new method. *IEEE Engineering in Medicine and Biology Society Conference Proceedings*, 2857–2860.
- Bosiers, M., Deloose, K., Verbist, J., Schroë, H., Lauwers, G., Lansink, W., Peeters, P., 2006. Heparin-bonded expanded polytetrafluoroethylene vascular graft for femoropopliteal and femorocrural bypass grafting: 1-year results. *Journal of vascular surgery* 43 (2), 313–318.
- Boutouyrie, P., Briet, M., Collin, C., Vermeersch, S., Pannier, B., 2009. Assessment of pulse wave velocity. *Artery Research* 3, Issue 1, 3–8.
- Brands, P., Willigers, J., Ledoux, L., Reneman, R., Hoeks, A., 1998. A non-invasive method to estimate pulse wave velocity in arteries locally by means of ultrasound. *Ultrasound in Medicine & Biology* 24 (9), 1325–1335.
- Chang, K., Davis, R., 1993. Propofol produces endothelium-independent vasodilation and may act as a Ca²⁺ channel blocker. *Anesthesia and analgesia* 76 (1), 24–32.
- Cole, J., Watterson, J., O'Reilly, M., 2002. Is there a haemodynamic advantage associated with cuffed arterial anastomoses? *Journal of Biomechanics* 35, 1337–1346.
- Cossmann, D. V., Ellison, J. E., Wagner, W. H., Carroll, R. M., Treiman, R. L., Foran, R. F., Levin, P. M., Cohen, J. L., 1989. Comparison of contrast arteriography to arterial mapping with color-flow duplex imaging in the lower extremities. *Journal of Vascular Surgery* 10, 522–529.
- Crosetto, P., Deparis, S., Fourestey, G., Quarteroni, A., 2011. Parallel algorithms for fluid-structure interaction problems in haemodynamics. *Siam Journal on Scientific Computing* 33 (4), 1598–1622.
- Cruickshank, K., Riste, L., Anderson, S. G., Wright, J. S., Dunn, G., Gosling, R. G., 2002. Aortic pulse-wave velocity and its relationship to mortality in diabetes and glucose intolerance: an integrated index of vascular function? *Circulation* 106 (16), 2085–2090.

- Curtis, S., Zambanini, A., Mayet, J., Thom, S. M., Foale, R., Parker, K., Hughes, A., 2007. Reduced systolic wave generation and increased peripheral wave reflection in chronic heart failure. *American Journal of Physiology - Heart and Circulatory Physiology* 293, H557–H562.
- Daenens, K., Schepers, S., Fourneau, I., Houthoofd, S., Nevelsteen, A., 2009. Heparin-bonded ePTFE grafts compared with vein grafts in femoropopliteal and femorocrural bypasses: 1- and 2-year results. *Journal of vascular surgery* 49 (5), 1210–1216.
- Daniele, C., Grigioni, M., D’Avenio, G., Barbaro, V., 2003. Characterization of graft’s mechanical properties relevant for hemodynamics. WIT Press, Ch. 3, pp. 83–126.
- Davies, J., Baksi, J., Francis, D., Hadjiloizou, N., Whinnett, Z., Manisty, C., Aguado-Sierra, J., Foale, R., Malik, I., Tyberg, J., Parker, K., Mayet, J., Hughes, A., 2010. The arterial reservoir pressure increases with aging and is the major determinant of the aortic augmentation index. *American Journal of Physiology - Heart and Circulatory Physiology* 298 (2), H580–H586.
- Davies, J. E., Hadjiloizou, N., Leibovich, D., Malaweera, A., Alastruey-Armon, J., Whinnett, Z. I., Manisty, C. H., Francis, D. P., Aguado-Sierra, J., Foale, R. A., Malik, I. S., Parker, K. H., Mayet, J., Hughes, A. D., 2007. Importance of the aortic reservoir in determining the shape of the arterial pressure waveform - The forgotten lessons of Frank. *Artery Research* 1 (2), 40–45.
- Davies, J. E., Whinnett, Z. I., Francis, D. P., Manisty, C. H., Aguado-Sierra, J., Willson, K., Foale, R. A., Malik, I. S., Hughes, A. D., Parker, K. H., Mayet, J., 2006a. Evidence of a dominant backward-propagating "suction" wave responsible for diastolic coronary filling in humans, attenuated in left ventricular hypertrophy. *Circulation* 113, 1768–1778.
- Davies, J. E., Whinnett, Z. I., Francis, D. P., Willson, K., Foale, R. A., Malik, I. S., Hughes, A. D., Parker, K. H., Mayet, J., 2006b. Use of simultaneous pressure and velocity measurements to estimate arterial wave speed at a single site in humans. *American Journal of Physiology - Heart and Circulatory Physiology* 290, 878–885.
- Duprez, D., Buyzere, M. D., Bruyne, L. D., Clement, D., Cohn, J., 2001. Small and large artery elasticity indices in peripheral arterial occlusive disease (PAOD). *Vascular Medicine* 6, 211–214.
- Ellwein, L., Tran, H., Zapata, C., Novak, V., Olufsen, M., 2008. Sensitivity analysis and model assessment: Mathematical models for arterial blood flow and blood pressure. *Cardiovascular Engineering* 8 (2), 94–108.

- Ethier, C. R., Simmons, C. A., 2007. *Introductory Biomechanics. From Cells to organisms*. Cambridge University Press.
- Euler, L., 1775. *Principia pro motu sanguinis per arterias determinando. Opera posthuma mathematica et physica anno 1844 detecta 2* (Ediderunt PH Fuss et N Fuss Petropoli; Apud Eggers et Socios), 814–823.
- Feng, J., Khir, A., 2010. Determination of wave speed and wave separation in the arteries using diameter and velocity. *Journal of Biomechanics* 43 (3), 455–62.
- Formaggia, L., Lamponi, D., Tuveri, M., Veneziani, A., 2006. Numerical modeling of 1D arterial networks coupled with a lumped parameters description of the heart. *Computer Methods in Biomechanics and Biomedical Engineering* 9, 273–288.
- Formaggia, L., Nobile, F., Quarteroni, A., 2002. A one dimensional model for blood flow: application to vascular prosthesis. In: Babuska, I., Miyoshi, T., Ciarlet, P. (Eds.), *Lecture Notes in Computational Science and Engineering*. Springer-Verlag, Ch. 19, pp. 137–153.
- Formaggia, L., Nobile, F., Quarteroni, A., Veneziani, A., 1999. Multiscale modelling of the cardiovascular system: a preliminary analysis. *Computing and Visualization in Science* 2 (2-3), 75–83.
- Frank, O., 1920. Die elastizität der blutgefäße. *Zeitschrift für Biologie* 71, 255–272.
- Fujimoto, S., Mizuno, R., Saito, Y., Nakamura, S., 2004. Clinical application of wave intensity for the treatment of essential hypertension. *Heart Vessels* 19 (1), 19–22.
- Geuzaine, C., Remacle, J.-F., 2009. Gmsh: a three-dimensional finite element mesh generator with built-in pre- and post-processing facilities. *International Journal for Numerical Methods in Engineering* 79 (11), 1309–1311.
- Giordana, S., Sherwin, S. J., Peiro, J., Doorly, D. J., Crane, J. S., Lee, K., Cheshire, N. J. W., Caro, C. G., 2005. Local and global geometric influence on steady flow in distal anastomoses of peripheral by-pass grafts. *J. Biomech. Eng.* 127 (7), 1087–1098.
- Harada, A., Okada, T., Niki, K., Chang, D., Sugawara, M., 2002. On-line non-invasive one-point measurements of pulse wave velocity. *Heart Vessels* 17, 61–68.
- Hayashi, K., 1980. Stiffness and elastic behavior of human intracranial and extracranial arteries. *Journal of Biomechanics* 13 (2) (175-184).

- Hedstrom, G. W., 1979. Nonreflecting boundary conditions for nonlinear hyperbolic systems. *Journal of Computational Physics* 30, 222–237.
- Hoeks, A., Brands, P., Smeets, F., Reneman, R., 1990. Assessment of the distensibility of superficial arteries. *Ultrasound in Medicine & Biology* 16 (2), 121–128.
- Hollander, E., Wang, J., Dobson, G., Parker, K., Tyberg, J., 2001. Negative wave reflections in pulmonary arteries. *American Journal of Physiology - Heart and Circulatory Physiology* 281, H895–902.
- Horváth, I., Németh, A., Lenkey, Z., Alessandri, N., Tufano, F., Kis, P., Gaszner, B., Cziráki, A., 2010. Invasive validation of a new oscillometric device (Arteriograph) for measuring augmentation index, central blood pressure and aortic pulse wave velocity. *Journal of Hypertension* 28 (10), 2068–2075.
- Hron, J., Mádlík, M., 2007. Fluid-structure interaction with applications in biomechanics. *Nonlinear Analysis: Real World Applications* 8 (5), 1431–1458.
- Hughes, A. D., Parker, K. H., Davies, J. E., 2008. Waves in arteries: A review of wave intensity analysis in the systemic and coronary circulations. *Artery Research* 2 (2), 51–59.
- Jiang, B., Liu, B., McNeill, K. L., Chowienczyk, P., 2008. Measurement of pulse wave velocity using pulse wave doppler ultrasound: comparison with arterial tonometry. *Ultrasound in Medicine and Biology* 34, 509–512.
- Johnson, B. L., Bandyk, D. F., Back, M. R., Avino, A. J., Roth, S. M., 2000. Intraoperative duplex monitoring of infrainguinal vein bypass procedures. *Journal of Vascular Surgery* 31 (4), 678–690.
- Jones, C. J. H., Sugawara, M., Kondoh, Y., Uchida, K., Parker, K. H., 2002. Compression and expansion wavefront travel in canine ascending aortic flow: wave intensity analysis. *Heart and Vessels* 16, 91–98.
- Kelly, R., Hayward, C., Avolio, A., O'Rourke, M., 1989. Noninvasive determination of age-related changes in the human arterial pulse. *Circulation* 80, 1652–1659.
- Khiri, A., Parker, K. H., 2002. Measurements of wave speed and reflected waves in elastic tubes and bifurcations. *Journal of Biomechanics* 35, 775–783.
- Khiri, A., Swalen, M., Feng, J., Parker, K., 2007. Simultaneous determination of wave speed and arrival time of reflected waves using the pressure-velocity loop. *Medical & Biological Engineering & Computing* 45 (12), 1201–1210.
- Khiri, A., Zambanini, A., Parker, K. H., 2004. Local and regional wave speed in the aorta: effects of arterial occlusion. *Medical Engineering & Physics* 26 (1), 23–29.

- Khair, A. W., Henein, M. Y., Koh, T., Das, S. K., Parker, K. H., Gibson, D. G., 2001a. Arterial waves in humans during peripheral vascular surgery. *Clinical Science* 101(6), 749–57.
- Khair, A. W., O'Brien, A., Gibbs, J. S., Parker, K. H., 2001b. Determination of wave speed and wave separation in the arteries. *Journal of Biomechanics* 34(9), 1145–55.
- Kingwell, B. A., Berry, K. L., Cameron, J. D., Jennings, G. L., Dart, A. M., 1997. Arterial compliance increases after moderate-intensity cycling. *American Journal of Physiology* 273 (5 Pt 2), H2186–H2191.
- Koh, T. K., Pepper, J. R., DeSouza, A. C., Parker, K. H., 1998. Analysis of wave reflections in the arterial system using wave intensity: a novel method for predicting the timing and amplitude of reflected waves. *Heart Vessels* 13, 103–113.
- Kolachalama, V.B.and Bressloff, N., Nair, P., Shearman, C., 2008. Predictive haemodynamics in a one-dimensional human carotid artery bifurcation. Part II: Application to graft design. *IEEE Transactions on Biomedical Engineering* 55 (3), 1176–1184.
- Kolyva, C., Spaan, J. A. E., Piek, J. J., Siebes, M., 2008. Windkesselness of coronary arteries hampers assessment of human coronary wave speed by single-point technique. *American Journal of Physiology - Heart and Circulatory Physiology* 295, 482–490.
- Ku, D. N., 1997. Blood flow in arteries. *Annual Review of Fluid Mechanics* 29, 399–434.
- Lacroix, V., Willemet, M., Marchandise, E., Beauloye, C., Verhelst, R., 2012. Using per-operative wave intensity analysis for assessing adequate peripheral arterial reconstruction: lesson from cases study. *EuroIntervention*, To be submitted.
- Lacroix, V., Willemet, M., Verhelst, R., Beauloye, C., Jacquet, L., Astarci, P., Persu, A., Marchandise, E., 2011. Central and peripheral pulse wave velocities are associated with ankle-brachial pressure index. *Artery Research*, Corrected proof.
- Langewouters, G. J., Wesseling, K. H., Goedhard, W. J. A., 1984. The static elastic properties of 45 human thoracic and 20 abdominal aortas in vitro and the parameters of a new model. *Journal of Biomechanics* 17 (6), 425–435.
- Laurent, S., Boutouyrie, P., Asmar, R., Gautier, I., Laloux, B., Guize, L., Ducimetiere, P., Benetos, A., 2001. Aortic stiffness is an independent predictor of all-cause and cardiovascular mortality in hypertensive patients. *Hypertension* 37 (5), 1236–1241.

- Laurent, S., Cockcroft, J., Van Bortel, L., Boutouyrie, P., Giannattasio, C., Hayoz, D., Pannier, B., Vlachopoulos, C., Wilkinson, I., Struijker-Boudier, H., 2006. Expert consensus document on arterial stiffness: methodological issues and clinical applications. *European Heart Journal* 27 (21), 2588–2605.
- Leguy, C., Bosboom, E., Gelderblom, H., Hoeks, A., van de Vosse, F., 2010. Estimation of distributed arterial mechanical properties using a wave propagation model in a reverse way. *Medical Engineering & Physics* 32 (9), 957–967.
- Leguy, C. A. D., Bosboom, E. M. H., Belloum, A. S. Z., Hoeks, A. P. G., van de Vosse, F. N., 2011. Global sensitivity analysis of a wave propagation model for arm arteries. *Medical Engineering & Physics* 33 (8), 1008–1016.
- Leguy, C. A. D., Bosboom, E. M. H., Hoeks, A. P. G., van de Vosse, F. N., 2009. Model-based assessment of dynamic arterial blood volume flow from ultrasound measurements. *Medical and Biological Engineering and Computing* 47, 641–648.
- Leuprecht, A., Perktold, K., Prosi, M., Berk, T., Trubel, W., Schima, H., 2002. Numerical study of hemodynamics and wall mechanics in distal end-to-side anastomoses of bypass grafts. *Journal of Biomechanics* 35, 225–236.
- Li, Y., Khir, A. W., 2011. Experimental validation of non-invasive and fluid density independent methods for the determination of local wave speed and arrival time of reflected wave. *Journal of Biomechanics* 44 (7), 1393–1399.
- Liu, Z., Brin, K., Yin, F., 1986. Estimation of total arterial compliance: an improved method and evaluation of current methods. *American Journal of Physiology - Heart and Circulatory Physiology* 251, H588–H600.
- Loth, F., Fischer, P. F., Bassiouny, H. S., 2008. Blood flow in end-to-side anastomoses. *Annual Reviews of Fluid Mechanics* 40, 367–393.
- Lundell, A., Bergqvist, D., 1993. Prediction of early graft occlusion in femoropopliteal and femorodistal reconstructions by measurement of volume flow with a transit time flowmeter and calculation of peripheral resistance. *European Journal of Vascular Surgery* 7, 704–709.
- Manisty, C. H., Zambanini, A., Parker, K. H., Davies, J. E., Francis, D. P., Mayet, J., McG Thom, S. A., Hughes, A. D., on behalf of the Anglo-Scandinavian Cardiac Outcome Trial Investigators, 2009. Differences in the magnitude of wave reflection account for differential effects of Amlodipine-versus Atenolol-based regimens on central blood pressure. *Hypertension* 54, 724–730.

- Marchandise, E., Compère, G., Willemet, M., Bricteux, G., Geuzaine, C., Remacle, J.-F., 2010. Quality meshing based on STL triangulations for biomedical simulations. *International Journal For Numerical Methods In Biomedical Engineering* 83, 876–889.
- Marchandise, E., Flaud, P., 2010. Accurate modelling of unsteady flows in collapsible tubes. *Computer Methods in Biomechanics and Biomedical Engineering* 13 (2), 279–290.
- Marchandise, E., Remacle, J., Chevaugnon, N., 2006. A quadrature-free discontinuous Galerkin method for the level set equation. *Journal of Computational Physics* 212, 338–357.
- Marchandise, E., Willemet, M., Lacroix, V., 2009. A numerical hemodynamic tool for predictive vascular surgery. *Medical Engineering & Physics* 31, 131–144.
- Marieb, E. N., 2005. *Anatomie et physiologie humaines*. Pearson Education.
- Matthys, K., Alastruey, J., Peiró, J., Khir, A., Segers, P., Verdonck, P., Parker, K., Sherwin, S., 2007. Pulse wave propagation in a model human arterial network: Assessment of 1-D numerical simulations against in vitro measurements. *Journal of Biomechanics* 40 (15), 3476–3486.
- Meinders, J. M., Hoeks, A. P. G., 2004. Simultaneous assessment of diameter and pressure waveforms in the carotid artery. *Ultrasound in Medicine & Biology* 30 (2), 147–154.
- Millasseau, S. C., Stewart, A. D., Patel, S. J., Redwood, S. R., Chowienczyk, P. J., 2005. Evaluation of carotid-femoral pulse wave velocity: influence of timing algorithm and heart rate. *Hypertension* 45 (2), 222–226.
- Miller, J., Walsh, J. A., Foreman, R. K., Dupont, P. A., Luethke, R., James, M. J., Iannos, J., 1990. Vascular outflow resistance and angiographic assessment of lower limb arterial reconstructive procedures. *The Australian and New Zealand Journal of Surgery* 60 (4), 275–281.
- Murgo, J., Westerhof, N., Giolma, J., Altobelli, S., 1980. Aortic input impedance in normal man: relationship to pressure wave forms. *Circulation* 62, 105–116.
- Mynard, J., Penny, D. J., Smolich, J. J., 2008. Wave intensity amplification and attenuation in non-linear flow: implications for the calculation of local reflection coefficients. *Journal of Biomechanics* 41(16), 3314–3321.
- Mynard, J. P., Davidson, M. R., Penny, D. J., Smolich, J. J., 2010. A numerical model of neonatal pulmonary atresia with intact ventricular septum and RV-dependent coronary flow. *International Journal For Numerical Methods In Biomedical Engineering* 26(7), 843–861.

- Mynard, J. P., Nithiarasu, P., 2008. A 1D arterial blood flow model incorporating ventricular pressure, aortic valve and regional coronary flow using the locally conservative galerkin (LCG) method. *Communications in Numerical Methods in Engineering* 24 (5), 367–417.
- Nichols, W. W., O'Rourke, M. F., 2005. McDonald's blood flow in arteries. Theoretical, experimental and clinical principles. Fifth edition. Hodder Arnold.
- Nobile, F., 2009. Coupling strategies for the numerical simulation of blood flow in deformable arteries by 3D and 1D models. *Mathematical and Computer Modelling* 49, 2152–2160.
- Noori, N., Scherer, R., Perktold, K., Czerny, M., Karner, G., Trubel, W., Polteraue, P., Schima, H., 1999. Blood flow in distal end-to-side anastomoses with PTFE and a venous patch: Results of an in vitro flow visualisation study. *European Journal Vascular Endovascular Surgery* 18, 191–200.
- Norgren, L., Hiatt, W., Dormandy, J., Nehler, M., Harris, K., Fowkes, F., 2007. Inter-society consensus for the management of peripheral arterial disease (TASC II). *European Journal of Vascular and Endovascular Surgery* 33, S1–75.
- Ohte, N., Narita, H., Sugawara, M., Niki, K., Okada, T., Harada, A., Hayano, J., Kimura, G., 2003. Clinical usefulness of carotid arterial wave intensity in assessing left ventricular systolic and early diastolic performance. *Heart Vessels* 18, 107–111.
- Olufsen, M., 1999. Structured tree outflow condition for blood flow in larger systemic arteries. *American Journal of Physiology - Heart and Circulatory Physiology* 276, 257–268.
- Olufsen, M., Peskin, C., Kim, W., Pedersen, E., Nadim, A., Larsen, J., 2000. Numerical simulation and experimental validation of blood flow in arteries with structured-tree outflow conditions. *Annals of Biomedical Engineering* 28 (11), 1281–99.
- Olufsen, M. S., Ottesen, J. T., Tran, H. T., Ellwein, L. M., Lipsitz, L. A., Novak, V., 2005. Blood pressure and blood flow variation during postural change from sitting to standing: model development and validation. *Journal of Applied Physiology* 99 (4), 1523–1537.
- O'Rourke, M., Staessen, J., Vlachopoulos, C., Duprez, D., Plante, G., 2002. Clinical applications of arterial stiffness; definitions and reference values. *American Journal of Hypertension* 15, 426–444.
- O'Rourke, M. F., Avolio, A. P., 1980. Pulsatile flow and pressure in human systemic arteries. *Circulation Research* 46, 363–372.

- O'Rourke, M. F., Taylor, M. G., 1966. Vascular impedance of the femoral bed. *Circulation Research* 18, 126–139.
- Pannier, B., Avolio, A., Hoeks, A., Mancia, G., Takazawa, K., 2002. Methods and devices for measuring arterial compliance in humans. *American Journal of Hypertension* 15, 743–753.
- Parker, K., Jones, C., 1990. Forward and backward running waves in the arteries: analysis using the method of characteristics. *Journal of Biomechanics* 112(3), 322–326.
- Parker, K. H., 2009. An introduction to wave intensity analysis. *Medical and Biological Engineering and Computing* 47, 175–188.
- Parker, K. H., Jones, C. J. H., Dawson, J. R., Gibson, D. G., 1988. What stops the flow of blood from the heart? *Heart and Vessels* 4, 241–245.
- Peeters, P., Verbist, J., Deloose, K., Bosiers, M., 2006. Results with heparin bonded polytetrafluoroethylene grafts for femorodistal bypasses. *The journal of cardiovascular surgery* 47 (4), 407–13.
- Penny, D., Mynard, J., Smolich, J., 2008. Aortic wave intensity analysis of ventricular-vascular interaction during incremental dobutamine infusion in adult sheep. *American Journal of Physiology - Heart and Circulatory Physiology* 294 (1), H481–9.
- Pope, S., Ellwein, L., Zapata, C., Novak, V., Kelley, C., Olufsen, M., 2009. Estimation and identification of parameters in a lumped cerebrovascular model. *Mathematical Biosciences and Engineering* 6 (1), 93–115.
- Pousset, Y., Lermusiaux, P., Berton, G., Le Gouez, J.-M., Leroy, R., 2006. Numerical model study of flow dynamics through an end-to-side anastomosis: choice of anastomosis angle and prosthesis diameter. *Annals of Vascular Surgery* 20 (6), 773–779.
- Pukacki, F., Jankowski, T., Gabriel, M., Oszkinis, G., Krasinski, Z., Zapalski, S., 2000. The mechanical properties of fresh and cryopreserved arterial homografts. *European Journal of Vascular and Endovascular Surgery* 20, 21–24.
- Pythoud, F., Stergiopoulos, N., Meister, J., 1996. Separation of arterial pressure waves into their forward and backward running components. *Journal of Biomechanical Engineering* 118 (3), 295–301.
- Quarteroni, A., Formaggia, L., 2003. Mathematical Modelling and Numerical Simulation of the Cardiovascular System. In: *Modelling of Living Systems. Handbook of Numerical Analysis Series.*

- Rabben, S., Stergiopoulos, N., Hellevik, L., Smiseth, O., Slørdahl, S., Urheim, S., Angelsen, B., 2004. An ultrasound-based method for determining pulse wave velocity in superficial arteries. *Journal of Biomechanics* 37 (10), 1615–1622.
- Raines, J. K., Jaffrin, M., Shapiro, A., 1974. A computer simulation of arterial dynamics in the human leg. *Journal of Biomechanics* 7, 77–91.
- Ramsey, M., Sugawara, M., 1997. Arterial wave intensity and ventriculoarterial interaction. *Heart and Vessels Suppl* 12, 128–134.
- Reymond, P., Merenda, F., Perren, F., Rüfenacht, D., Stergiopoulos, N., 2009. Validation of a one-dimensional model of the systemic arterial tree. *American Journal of Physiology - Heart and Circulatory Physiology* 297, 208–222.
- Robinson, B., Ebert, T., O'Brien, T., Colinco, M., Muzi, M., 1997. Mechanisms whereby propofol mediates peripheral vasodilation in humans. Sympatho-inhibition or direct vascular relaxation? *Anesthesiology* 86 (1), 64–72.
- Roll, S., Müller-Nordhorn, J., Keil, T., Scholz, H., Eidt, D., Greiner, W., Willich, S. N., 2008. Dacron® vs. PTFE as bypass materials in peripheral vascular surgery - systematic review and meta-analysis. *BMC Surgery* 8:22.
- Rzucidlo, E., Walsh, D., Powell, R., 2002. Prediction of early graft failure with intraoperative completion duplex ultrasound scan. *Journal of Vascular Surgery* 36, 975–981.
- Saltelli, A., Ratto, M., Andres, T., Campolongo, F., Cariboni, J., Gatelli, D., Saisana, M., Tarantola, S., 2008. *Global sensitivity analysis: the primer*. John Wiley.
- Saltelli, A., Tarantola, S., Campolongo, F., Ratto, M., 2004. *Sensitivity analysis in practice. A guide to assessing scientific models*. John Wiley & Sons.
- Savitzky, A., Golay, M., 1964. Smoothing and differentiation of data by simplified least squares procedures. *Analytical Chemistry* 36 (8), 1627–1639.
- Segers, P., Stergiopoulos, N., Verdonck, P., Verhoeven, R., 1997. Assessment of distributed arterial network models. *Med Biol Eng Comput* 35 (6), 729–736.
- Segers, P., Verdonck, P., 2000. Role of tapering in aortic wave reflection: hydraulic and mathematical model study. *Journal of Biomechanics* 33, 299–306.
- Shaalán, W. E., French-Sherry, E., Castilla, M., Lozanski, L., Bassiouny, H. S., 2003. Reliability of common femoral artery hemodynamics in assessing the severity of aortoiliac inflow disease. *Journal of Vascular Surgery* 37 (5), 960–969.

- Sherwin, S., Formaggia, L., Peiró, J., Franke, V., 2003a. Computational modelling of 1D blood flow with variable mechanical properties and its applications to the simulation of wave propagation in the human arterial system. *International Journal for Numerical Methods in Fluids* 43 (6-7), 673–700.
- Sherwin, S., Franke, V., Peiró, J., Parker, K., 2003b. One-dimensional modelling of a vascular network in space-time variables. *Journal of Engineering Mathematics* 47, 217–250.
- Simon, A. C., Safar, M. E., Levenson, J. A., London, G. M. and Levy, B. I., Chau, N. P., 1979. An evaluation of large arteries compliance in man. *American Journal of Physiology* 237 (5), 550–554.
- Sottiurai, V., Yao, J., Flinn, W., Batson, R., 1983. Intimal hyperplasia and neointima: An ultrastructural analysis of thrombosed grafts in humans. *Surgery* 93 (6), 809–817.
- Steele, B. N., Wan, J., Ku, J. P., Hughes, T. J. R., Taylor, C. A., 2003. In vivo validation of a one-dimensional finite-element method for predicting blood flow in cardiovascular bypass grafts. *IEEE Transactions on Biomedical Engineering* 50 (6), 649–656.
- Stergiopoulos, N., Young, D., Rogge, T., 1992. Computer simulation of arterial flow with application to arterial and aortic stenoses. *Journal of Biomechanics* 25 (12), 1477–1488.
- Stergiopoulos, N., Meister, J., Westerhof, N., 1995. Evaluation of methods for estimation of total arterial compliance. *American Journal of Physiology - Heart and Circulatory Physiology* 268 (4), 1540–1548.
- Stergiopoulos, N., Meister, J.-J., Westerhof, N., 1994. Simple and accurate way for estimating total and segmental arterial compliance: The pulse pressure method. *Annals of Biomedical Engineering* 22, 392–397.
- Stirnemann, P., Ris, H. B., Do, D., Hammerli, R., 1994. Intraoperative flow measurement of distal runoff: a valid predictor of outcome of infrainguinal bypass surgery. *European Journal of Vascular Surgery* 160, 431–436.
- Sun, Y.-H., Anderson, T. J., Parker, K. H., Tyberg, J. V., 2000. Wave-intensity analysis: a new approach to coronary hemodynamics. *Journal of Applied Physiology* 89, 1636–1644.
- Swalen, M. J., Khir, A. W., 2009. Resolving the time lag between pressure and flow for the determination of local wave speed in elastic tubes and arteries. *Journal of Biomechanics* 42 (10), 1574–1577.
- Swillens, A., Segers, P., 2008. Assessment of arterial pressure wave reflection : methodological considerations. *Artery Research* 2, 122–131.

- Taylor, R., McFarland, R., Cox, M., 1987. An investigation into the causes of failure of PTFE grafts. *European Journal of Vascular Surgery* 1 (5), 335–343.
- Thompson, K. W., 1987. Time dependant boundary conditions for hyperbolic systems. *Journal of Computational Physics* 68, 1–24.
- Toes, G. J., 2002. Intimal hyperplasia, the obstacle in bypass grafts. Ph.D. thesis, University of Groningen.
- Toorop, G. P., Westerhof, N., Elzinga, G., 1987. Beat-to-beat estimation of peripheral resistance and arterial compliance during pressure transients. *American Journal of Physiology* 252 (6), H1275–1283.
- Torii, R., Wood, N., Hughes, A., Thom, S., Aguado-Sierra, J., Davies, J., Francis, D., Parker, K., Xu, X., 2007. A computational study on the influence of catheter-delivered intravascular probes on blood flow in a coronary artery model. *Journal of Biomechanics* 40 (11), 2501–2509.
- Tyberg, J. V., Davies, J. E., Wang, Z., Whitelaw, W. A., Flewitt, J. A., Shrive, N. G., Francis, D. P., Hughes, A. D., Parker, K. H., Wang, J.-J., 2009. Wave intensity analysis and the development of the reservoir-wave approach. *Medical and Biological Engineering and Computing* 47, 221–232.
- Urquiza, S., Blanco, P., Venere, M., Feijoo, R., 2006. Multidimensional modelling for the carotid artery blood flow. *Computer Methods In Applied Mechanics and Engineering* 195, 4002–4017.
- Van Bortel, L. M., Duprez, D., Starmans-Kool, M. J., Safar, M. E., Giannattasio, C., Cockcroft, J., Kaiser, D. R., Thuillez, C., 2002. Clinical applications of arterial stiffness, task force iii: Recommendations for user procedures. *American Journal of Hypertension* 15, 445–452.
- Vermeersch, S., Rietzschel, E., De Buyzere, M., Van Bortel, L., Gillebert, T., Verdonck, P., Laurent, S., Segers, P., Boutouyrie, P., 2009a. Distance measurements for the assessment of carotid to femoral pulse wave velocity. *Journal of Hypertension* 27 (12), 2377–2385.
- Vermeersch, S. J., Rietzschel, E. R., De Buyzere, M. L., De Bacquer, D., De Backer, G., Van Bortel, L. M., Gillebert, T. C., Verdonck, P. R., Segers, P., 2008. Determining carotid artery pressure from scaled diameter waveforms: comparison and validation of calibration techniques in 2026 subjects. *Physiological Measurement* 29(11), 1267–1280.
- Vermeersch, S. J., Rietzschel, E. R., De Buyzere, M. L., Van Bortel, L. M., Gillebert, T. C., Verdonck, P. R., Segers, P., 2009b. The reservoir pressure concept: the 3-element windkessel model revisited? Application to the Asklepios population study. *Journal of Engineering Mathematics* 64 (4), 417–428.

- Vignon-Clementel, I. E., Figueroa, C. A., Jansen, K. E., Taylor, C., 2006. Outflow boundary conditions for three-dimensional finite element modeling of blood flow and pressure in arteries. *Computer Methods in Applied Mechanics and Engineering* 195 (29-32), 3776–3796.
- Vignon-Clementel, I. E., Taylor, C., 2004. Outflow boundary conditions for one-dimensional finite element modeling of blood flow and pressure waves in arteries. *Wave Motion* 39 (7), 361–374.
- Vlachopoulos, C., O'Rourke, M., 2000. Genesis of the normal and abnormal arterial pulse. *Current Problems in Cardiology* 25 (5), 297–367.
- Wang, J.-J., Flewitt, J. A., Shrive, N. G., Parker, K. H., Tyberg, J. V., 2006. Systemic venous circulation. waves propagating on a windkessel: relation of arterial and venous windkessels to systemic vascular resistance. *American Journal of Physiology - Heart and Circulatory Physiology* 290, H154–162.
- Wang, J.-J., O'Brien, A. B., Shrive, N. G., Parker, K. H., Tyberg, J. V., 2003. Time-domain representation of ventricular-arterial coupling as a windkessel and wave system. *American Journal of Physiology - Heart and Circulatory Physiology* 284 (4), 1358–68.
- Westerhof, N., Elzinga, G., Sipkema, P., 1971. An artificial arterial system for pumping hearts. *Journal of Applied Physiology* 31 (5), 776–81.
- Westerhof, B. E., Guelen, I., Westerhof, N., Karemaker, J. M., Avolio, A., 2006. Quantification of wave reflection in the human aorta from pressure alone. a proof of principle. *Hypertension* 48, 595–601.
- Westerhof, N., Jan-Willem, L., Westerhof, B. E., 2009. The arterial windkessel. *Medical and Biological Engineering and Computing* 47 (2), 131–141.
- Westerhof, N., Stergiopoulos, N., 2005. *Snapshots of hemodynamics*. Springer.
- Wilkinson, I., Fuchs, S., Jansen, I., Spratt, J., Murray, G., Cockcroft, J., Webb, D., 1998. Reproducibility of pulse wave velocity and augmentation index measured by pulse wave analysis. *Journal of Hypertension* 16 (12), 2079–2084.
- Wilson, S. E., Hobson, R. W., Veith, F. J., 2003. *Vascular Surgery: Principles and Practice*. Informa Healthcare.
- Wright, J., Cruickshank, J., Kontis, S., Doré, C., Gosling, R., 1990. Aortic compliance measured by non-invasive doppler ultrasound: description of a method and its reproducibility. *Clinical Science* 78, 463–468.
- Xiu, D., Sherwin, S., 2007. Parametric uncertainty analysis of pulse wave propagation in a model of a human arterial networks. *Journal of Computational Physics* 226 (1), 1385–1407.

-
- Zambanini, A., Cunningham, S., Parker, K., Khir, A., Thom, S. M., Hughes, A., 2005. Wave-energy patterns in carotid, brachial, and radial arteries: a non-invasive approach using wave-intensity analysis. *American Journal of Physiology - Heart and Circulatory Physiology* 289, H270–276.
- Zhao, S. Z., Xu, X. Y., Hughes, A. D., Thom, S. A., Stanton, A. V., Ariff, B., Long, Q., 2000. Blood flow and vessel mechanics in a physiologically realistic model of a human carotid arterial bifurcation. *Journal of Biomechanics* 33(8), 975–984.

Publications related to this thesis

Journal articles

Willemet M., Lacroix V., Marchandise E., 2011. Inlet boundary conditions for blood flow simulations in truncated arterial networks. *Journal of Biomechanics*, **44**(5), 897-903.

Willemet M., Lacroix V., Marchandise E., 2012. Validation and sensitivity analysis of a coupled 1D-0D model of the arterial hemodynamics in bypassed lower-limbs. *Medical Engineering & Physics*. To be submitted.

Willemet M., Lacroix V., Khir. A., Marchandise E., 2012. Wave intensity analysis in the lower-limb arteries of human during peripheral bypass surgery. *American Journal of Physiology - Heart and Circulatory Physiology*. To be submitted.

Marchandise, E., Willemet, M., Lacroix, V., 2009. A numerical hemodynamic tool for predictive vascular surgery. *Medical Engineering & Physics* **31**, 131-144.

Lacroix, V., Willemet, M., Verhelst, R., Beauloye, C., Jacquet, L., Astarci, P., Persu, A., Marchandise, E., 2011. Central and peripheral pulse wave velocities are associated with ankle-brachial pressure index. *Artery Research*. **Corrected proof**.

Lacroix, V., Willemet, M., Marchandise, E., Beauloye, C., Verhelst, R., 2012. Using per-operative wave intensity analysis for assessing adequate peripheral arterial reconstruction: lesson from cases study. *EuroIntervention*. To be submitted.

Marchandise, E., Compère, G., Willemet, M., Bricteux, G., Geuzaine, C., Remacle, J.-F., 2010. Quality meshing based on STL triangulations for biomedical simulations. *International Journal For Numerical Methods In Biomedical Engineering* **83**, 876-889.

Published proceedings and abstracts

Willemet, M., Compère, G., Remacle, J.-F., Marchandise, E., 2009. Simulation-based femoro-popliteal bypass surgery, in *IFMBE Proceedings, 4th European Conference of the International Federation for Medical and Biological Engineering*, **22**, 2568–2570.

V. Lacroix, M. Willemet, E. Marchandise, and R. Verhelst, 2008. An hemodynamic study of the lower limb arterial network and its application in a model for predictive bypass surgery. *Artery Research* **2(3)**, 96.